UNIVERSITY OF IOANNINA
SCHOOL OF PHYSICAL SCIENCES
PHYSICS DEPARTMENT

Cosmological Implications of Scalar Tensor Theories

Lavrentios Kazantzidis

PH.D. THESIS

This research is co-financed by Greece and the European Union (European Social Fund- ESF) through the Operational Programme «Human Resources Development, Education and Lifelong Learning» in the context of the project "Strengthening Human Resources Research Potential via Doctorate Research – 2nd Cycle" (MIS-5000432), implemented by the State Scholarships Foundation (ΙΚΥ).

IOANNINA 2022

ΠΑΝΕΠΙΣΤΗΜΙΟ ΙΩΑΝΝΙΝΩΝ
ΣΧΟΛΗ ΘΕΤΙΚΩΝ ΕΠΙΣΤΗΜΩΝ
ΤΜΗΜΑ ΦΥΣΙΚΗΣ

Κοσμολογικές Εφαρμογές Βαθμοτανυστικών Θεωριών Βαρύτητας

Λαυρέντιος Καζαντζίδης

ΔΙΔΑΚΤΟΡΙΚΗ ΔΙΑΤΡΙΒΗ

Το έργο συγχρηματοδοτείται από την Ελλάδα και την Ευρωπαϊκή Ένωση (Ευρωπαϊκό Κοινωνικό Ταμείο) μέσω του Επιχειρησιακού Προγράμματος «Ανάπτυξη Ανθρώπινου Δυναμικού Εκπαίδευση και Διά Βίου Μάθηση», στο πλαίσιο της Πράξης «Ενίσχυση του ανθρώπινου ερευνητικού δυναμικού μέσω της υλοποίησης διδακτορικής έρευνας - 2ος κύκλος» (MIS-5000432), που υλοποιεί το Ίδρυμα Κρατικών Υποτροφιών (ΙΚΥ)

ΙΩΑΝΝΙΝΑ 2022

Three-member advisory committee:

- L. Perivolaropoulos, Professor, Department of Physics, University of Ioannina (Supervisor), Greece.
- P.Kanti, Professor, Department of Physics, University of Ioannina, Greece.
- G. Leontaris, Emeritus Professor, Department of Physics, University of Ioannina, Greece.

Seven-member PhD thesis examination committee:

- L. Perivolaropoulos, Professor, Department of Physics, University of Ioannina (Supervisor), Greece.
- P. Kanti, Professor, Department of Physics, University of Ioannina, Greece.
- A. Dedes, Professor, Department of Physics, University of Ioannina, Greece (substituting Emeritus Professor G. Leontaris due to legal constraints).
- C. Tsagas, Professor, Department of Physics, Aristotle University of Thessaloniki, Greece.
- S. Nesseris, Associate Professor, Instituto de Fisica Teorica (IFT UAM-CSIC), Spain.
- E. Saridakis, Senior Researcher (Researcher Grade B), Institute for Astronomy, Astrophysics, Space Applications and Remote Sensing (IAASARS), National Observatory of Athens, Greece.
- C. Charmousis, Professor Laboratoire de Physique Theorique, CNRS, Universite Paris-Sud, Universite Paris-Saclay, France.

"I wish it need not have happened in my time," said Frodo. *"So do I,"* said Gandalf, *"and so do all who live to see such times. But that is not for them to decide. All we have to decide is what to do with the time that is given to us"*

The Fellowship of The Ring, J.R.R. Tolkien

Acknowledgements

First and foremost, I would like to express my deep gratitude to my supervisor Professor Leandros Perivolaropoulos. He gave me an amazing opportunity to study on the latest challenges of modern Cosmology. His unwavering professionalism, his guidance and plenty advice were of paramount importance for the completion of the current thesis. Moreover, I would like to thank the Professors David Polarski, Radouane Gannouji, Arman Shafieloo, Valerio Marra, Christos Tsagas as well as the postdoctoral fellow Eleonora Di Valentino for our flawless cooperation in the various projects that I was involved during my PhD studies. A big thank you goes to the Associate Professor Savvas Nesseris for being always there. His help and guidance all these years were truly invaluable. Moreover, I would like to thank all the department's theoretical division faculty members for their help and support throughout my undergraduate and my graduate years.

It would be amiss from my part to not thank my friends (and colleagues) George Alestas, Angelos Lykkas, Theodoros Nakas, Paris Gianneios, Kostantinos Violaris, Ilias Tavellaris and Kerkyra Asvesta for the countless hours that we spent together discussing about (non)physical matters. In addition I would like to specially thank the PhD candidate Zinovia Eleme. Her patience, love and support all these years made my life much brighter. I am also grateful to my family and especially my sister Chrysa that always stood behind my choices and supported me financially and emotionally all these years.

Last but not least I would like to thank the Greek State Scholarship Foundation (IKY) as well as the Hellenic Foundation for Research and Innovation (HFRI) for financially supporting me during my PhD studies.

Contents

Publication List

Within the context of my PhD studies, nine peer-reviewed articles have been published. They are listed here in descending chronological order

1. **Evolution of the $f\sigma_8$ tension with the Planck15/ΛCDM Determination and Implications for Modified Gravity**,
   Lavrentios Kazantzidis and Leandros Perivolaropoulos,
   Published in *Phys. Rev. D97 (2018) no.10, 103503*,
   DOI: 10.1103/PhysRevD.97.103503.
   The numerical analysis files for the reproduction of the figures can be downloaded from the "Growth-Tomography repository."

2. **Consistency of Modified Gravity Theories with a Decreasing $G_{\text{eff}}(z)$ in a ΛCDM Background**,
   Radouane Gannouji, Lavrentios Kazantzidis, David Polarski and Leandros Perivolaropoulos,
   Published in *Phys. Rev. D98 (2018) no.10, 104044*,
   DOI: 10.1103/PhysRevD.98.104044

3. **Constraining Power of Cosmological Observables: Blind Redshift Spots and Optimal Ranges**,
   Lavrentios Kazantzidis, Leandros Perivolaropoulos and Foteini Skara,
   Published in *Phys. Rev. D99 (2019), 063537*
   DOI: 10.1103/PhysRevD.99.063537
   The numerical analysis files for the reproduction of the figures can be downloaded from the "Optimum-Redshift repository."

4. **Hints of Modified Gravity in Cosmos and in the Lab?**
   Leandros Perivolaropoulos and Lavrentios Kazantzidis,
   Published in *Int.J.Mod.Phys. D28 (2019) no.05, 1942001*,
   DOI: 10.1142/S021827181942001X

5. **Hints of a Local Matter Underdensity or Modified Gravity in the Low z Pantheon data**,
   Lavrentios Kazantzidis and Leandros Perivolaropoulos
   Published in *Phys.Rev. D102 (2020) 023520*,
   DOI: 10.1103/PhysRevD.102.023520

The numerical analysis files for the reproduction of the figures can be downloaded from "Pantheon-Tomography repository."

6. H_0 **Tension, Phantom Dark Energy and Cosmological Parameter Degeneracies**,
George Alestas, Lavrentios Kazantzidis and Leandros Perivolaropoulos,
Published in *Phys.Rev. D101 (2020) 12, 123516*,
DOI: 10.1103/PhysRevD.101.123516
The numerical analysis files for the reproduction of the figures can be downloaded from the "H0-Tension-Data repository."

7. **Hints for Possible Low Redshift Oscillation around the best fit ΛCDM model in the Expansion History of the Universe**,
Lavrentios Kazantzidis, Hanwool Koo, Leandros Perivolaropoulos and Arman Shafieloo,
Published in *Mon.Not.Roy.Astron.Soc. 501 (2021) 3, 3421-3426*,
DOI: 10.1093/mnras/staa3866

8. **A** $w-M$ **Phantom Transition at** $z_t < 0.1$ **as a Resolution of the Hubble Tension**,
George Alestas, Lavrentios Kazantzidis and Leandros Perivolaropoulos,
Published in *Phys.Rev.D 103 (2021) 083517*,
DOI: 10.1103/PhysRevD.103.083517
The numerical analysis files for the reproduction of the figures can be downloaded from the "LwMPT repository."

9. **Late Transition vs Smooth** $H(z)$ **Deformation Models for the Resolution of the Hubble Crisis**,
George Alestas, David Camarena, Eleonora Di Valentino, Lavrentios Kazantzidis, Valerio Marra, Savvas Nesseris and and Leandros Perivolaropoulos,
Published in *Phys.Rev.D 105 (2022) 6, 063538*,
DOI: 10.1103/PhysRevD.105.063538
The numerical analysis files for the reproduction of the figures can be downloaded from the "H0_Model_Comparison repository."

During the last stages of my PhD studies, I worked in parallel on the following article

- **Observational Constraints on the Deceleration Parameter in a Tilted Universe,**
Kerkyra Asvesta, Lavrentios Kazantzidis, Leandros Perivolaropoulos and Christos G. Tsagas
Accepted for publication in *Mon.Not.Roy.Astron.Soc.*, arxiv: 2202.00962
The numerical analysis files for the reproduction of the figures can be downloaded from the "tilted-cosmology repository."

Also, I was a team member of the CANTATA and SNOWMASS collaborations working on the following reviews writing small contributions:

1. **Modified Gravity and Cosmology: An Update by the CANTATA Network,**
Funded Under CA15117 CANTATA COST Action
CANTATA Collaboration: Emmanuel N. Saridakis et al.
Review in the framework of the COST European Action "Cosmology and Astrophysics Network for Theoretical Advances and Training Actions"

Published Chapter Title: σ_8 Tension: Is Gravity Getting Weaker at Low z? Observational Evidence and Theoretical Implications.
DOI: 10.1007/978-3-030-83715-0

2. **Cosmology Intertwined: A Review of the Particle Physics, Astrophysics, and Cosmology Associated with the Cosmological Tensions and Anomalies,**
Snowmass Collaboration: Eleonora Di Valentino et al.
Contribution to the 2022 Snowmass Summer Study
arxiv: 2203.06142

Abstract

In this PhD dissertation we study the cosmological consequences of modified theories of gravity. Motivated by the theoretical and observational challenges of the concordance model ΛCDM, we use up to date cosmological data from both geometric and dynamical probes to constrain modified gravity theories and extract the relevant best fit parameters. In particular, we first introduce the reader to the mathematical formalism of standard cosmology and then focusing on one of the two major tensions that ΛCDM faces (σ_8 tension), we introduce a purely phenomenological parametrization for the evolving Newton's constant $G_{\rm eff}$ and constructing an up to date compilation of growth data we extract its best fit parameters. Then, we study viable modified theories of gravities (such as $f(R)$ and scalar tensor theories) in order to see if they have the potential to support the observed behavior the evolving Newton's constant. Moreover, we examine other cosmological data (such as the low l cosmic microwave background data as well as the Pantheon compilation, *i.e.* the latest publicly available Type Ia supenovae compilation that is publicly available) to impose strong constraints on the phenomenological parametrization for $G_{\rm eff}$. Next, we study the constraining power (sensitivity) of a wide range of cosmological observables on cosmological parameters, showing that the sensitivity is actually a rapidly varying function of the redshift where the observable is measured and not a monotonically increasing function. In addition, we consider two late time gravitational transition dark energy models that have the ability to simultaneously tackle both the H_0 and growth problems and using the full cosmic microwave background data as well as some other up to date cosmological data, we obtain their quality of fit and compare it with the quality of fit provided by other well studied dark energy models that have been proposed as possible solutions in the literature as well as with the concordance model of standard cosmology. Finally, we study the impact of various modified gravity models in the sub-mm scales using the data of the Washington experiment.

Σύνοψη

Στην παρούσα Διδακτορική Διατριβή μελετάμε τις κοσμολογικές συνέπειες τροποποιημένων θεωριών βαρύτητας. Ορμώμενοι από τις θεωρητικές και παρατηρησιακές προκλήσεις του καθιερωμένου κοσμολογικού προτύπου ΛCDM, χρησιμοποιούμε πρόσφατες γεωμετρικές και δυναμικές παρατηρήσεις για την ταυτοποίηση χαρακτηριστικών προβλέψεων συγκεκριμένων θεωριών τροποποιημένης βαρύτητας και τον υπολογισμό των αντίστοιχων βέλτιστων τιμών των παραμέτρων τους. Αρχικά, εισάγουμε τον αναγνώστη στον μαθηματικό φορμαλισμό της Κοσμολογίας και έπειτα επικεντρωνόμενοι στη μία από τις δύο παρατηρησιακές ασυμβατότητες που αντιμετωπίζει το ΛCDM ("σ_8 ασυμβατότητα"), εισάγουμε μια φαινομενολογική παραμετροποίηση για την δυναμικά εξελισσόμενη σταθερά του Νεύτωνα $G_{\rm eff}$. Κατασκευάζοντας μία εκτεταμένη συλλογή δεδομένων που περιγράφουν Παραμορφώσεις στον Χώρο της Ερυθράς Μετατόπισης, υπολογίζουμε τις βέλτιστες τιμές των παραμέτρων της παραμετροποίησης της $G_{\rm eff}$ και μελετάμε συγκεκριμένες τροποποιημένες θεωρίες βαρύτητας (όπως $f(R)$ και βαθμοτανυστικές θεωρίες βαρύτητας), για να δούμε, εάν μπορούν να υποστηρίξουν τη συγκεκριμένη παρατηρήσιμη συμπεριφορά της. Έπειτα, εξετάζουμε και άλλου τύπου παρατηρησιακά δεδομένα (όπως για παράδειγμα δεδομένα Κοσμικής Ακτινοβολίας Υποβάθρου και τα δεδομένα Pantheon, δηλαδή τα πιο προσφατα δημοσιευμένα δεδομένα Υπερκαινοφανών Αστέρων Τύπου Ia) για την εύρεση των βέλτιστων τιμών των παραμέτρων της φαινομενολογικής παραμετροποίησης $G_{\rm eff}$. Στο πλαίσιο της παρούσας Διδακτορικής Διατριβής ερευνήθηκε επιπλέον η ευαισθησία ερευνητικών αποστολών στην ανίχνευση ενός μεγάλου εύρους κοσμολογικών παραμέτρων και αποδείχθηκε οτι η ευαισθήσια τους δεν αυξάνει γραμμικά με την τιμή της ερυθράς μετατόπισης, αλλά παρουσιάζει μια μεταβολή ανάλογα με την περιοχή της ερυθράς μετατόπισης που πραγματοποιείται η μέτρηση/ανίχνευση. Ακόμα, μελετήθηκαν μοντέλα σκοτεινής ενέργειας που παρουσιάζουν μια απότομη μεταβολή της απόλυτης λαμπρότητας M σε συγκεκριμένη τιμή της ερυθράς μετατόπισης, τα οποία έχουν τη δυνατότητα να λύσουν τόσο την "H_0 ασυμβατότητα" όσο και τη "σ_8 ασυμβατότητα" που αντιμετωπίζει το μοντέλο ΛCDM. Ειδικότερα, υπολογίσαμε την ποιότητα προσαρμογής αυτών των μοντέλων σε διάφορα προσφατα κοσμολογικά δεδομένα (μεταξύ αυτών και τα πλήρη δεδομένα Κοσμικής Ακτινοβολίας Υποβάθρου) και την συγκρίναμε με την ποιότητα προσαρμογής που παρέχει τόσο το μοντέλο ΛCDM, όσο και άλλα εναλλακτικά μοντέλα σκοτεινής ενέργειας που έχουν προταθεί στη βιβλιογραφία ως λύσεις των παρατηρούμενων ασυμβατοτήτων στο πλαίσιο του μοντέλου ΛCDM. Τέλος, μελετήθηκαν οι επιπτώσεις παραμετροποιήσεων που προκύπτουν από τροποποιημένες θεωρίες βαρύτητας στις κλίμακες χιλιοστού, με την αξιοποίηση δεδομένων του πειράματος Washington.

Preface

Cosmology is undoubtedly one of the most intriguing and important branches of modern Physics. Along with Quantum Field Theory, the theory that combines quantum mechanics and special relativity, Cosmology is established as one of the two pillars of modern Physics. In the beginning of the 20th century, Cosmology hardly existed as a scientific discipline. Nowadays, on the contrary, the tremendous progress of technology has led to a plethora of cosmological observations establishing the branch of Cosmology as one of the most dazzling and active areas of scientific research.

The first step towards a mathematical formulation for Cosmology, was General Theory of Relativity (GR) that was first introduced by Albert Einstein in 1915 revolutionizing the idea of space and time. Einstein proposed that both space and time are actually interwoven into one entity known as continuum (or spacetime) and that gravity is a geometric property of the continuum itself. In particular, he realized that the more massive an object is the more it distorts the continuum around it. At its core, GR implies that the spacetime curvature can be related directly to the energy and momentum of a fluid, through a system of partial differential equations that are called "*Einstein's Field Equations*". GR is nowadays considered the most widely accepted gravitational theory mainly due to its ability to make extremely accurate predictions in a wide variety of phenomena that Newtonian gravity fails to explain, such as the "anomalous" perihelion of Mercury's orbit [1], which according to GR should change by approximately 44 arcsec every century, the gravitational lensing effect caused by the Sun's gravity which was confirmed by Arthur Eddington in 1919 during a solar eclipse [2] *etc.* Moreover, GR predicts the existence of objects such as black holes [3–8] as well as the existence of gravitational waves that was confirmed a few years ago [9–11].

The discovery of GR was a major step towards the constitution of the Standard Cosmological Model which is widely known as "*Concordance Model*" or "ΛCDM" that corresponds to the mathematical parametrization of the Big Bang Cosmology [12–14] that accurately explains how the Universe expanded from an initial infinitely hot and dense singularity almost 13.8 billion years ago to the Universe that we observe today. According to ΛCDM, there are only three major ingredients that account for the composition of the observed Universe. These are the following:

- Baryonic Matter and Radiation: The baryonic (or ordinary matter) corresponds to the baryons and leptons, while the radiation describes particles with zero mass such as photons. Surprisingly, only a small fraction of the Universe (4%) corresponds to the observable matter.

- Dark Matter: The Dark Matter constitutes about 22% of the total mass energy density of the Universe. Even though Dark Matter is a well established idea [15–18] and it is of paramount importance for the ΛCDM model, its true nature remains one of the greatest

mysteries of modern Cosmology. It is believed, that it corresponds to an unknown non-relativistic, stable particle that interacts with ordinary matter only gravitationally. A great number of models have been proposed in the literature as possible candidates to embody Dark Matter including (but not limited to) Weakly Interacting Massive Particles [19, 20], Massive Astrophysical Compact Halo Objects [21, 22], Primordial Black Holes [23–26], Quantum Chromodynamics Axions [27,28], Neutralinos [29], Strongly Interacting Massive Particles [30, 31] *etc.*

- Dark Energy: The other 74% corresponds to another unknown quantity that is dubbed "Dark Energy" and exhibits repulsive properties in contrast to baryonic matter or radiation. This mysterious form of energy, is responsible for the observed accelerated expansion of the Universe. In the context of ΛCDM the role of Dark Energy is embodied by the famous cosmological constant [32].

The cosmological constant was first introduced by Albert Einstein in 1917 [33] in an attempt to achieve a static Universe, an idea that was favored during this period. However, due to serious stability issues of such a Universe [34, 35] as well as the experimental confirmation that the galaxies of the Milky Way are straying from each other by Edwin Hubble [36], it was dismissed approximately fourteen years later[1].

Nevertheless, it was reintroduced in 1998 when two different teams, namely the Supernova Cosmology Project [37] and the High-Redshift Supernova Search Team [38], confirmed using Type Ia Supernovae that our Universe is indeed accelerating[2]. Currently, the cosmological constant is considered to be the prime candidate to explain the observed accelerating expansion determining the "*Concordance Model*" to be ΛCDM (Λ stands for the cosmological constant, while the acronym CDM corresponds to the Cold Dark Matter).

Since then, numerous different probes using different cosmological data (such as Cosmic Microwave Background data [17, 18, 39], Type Ia Supernovae [40, 41], Cosmic Chronometers [42–44], Baryon Acoustic Oscillations data [45, 46], Redshift Space Distortions that probe large scale matter perturbations [18, 47, 48], Weak Lensing data [49, 50], Cluster Count data [51–55] and many more) have provided evidence supporting the existence of the cosmological constant. Nonetheless, despite its simplicity and its extremely good fit to observational data, ΛCDM is not flawless and encounters a number of challenges both at the theoretical and the observational level

Prominent among the theoretical challenges are the cosmological constant [56–60] and the coincidence problems [61, 62]. The former refers to the divergence between the quantum field theory prediction of the energy density of the vacuum ρ_Λ with its observed value[3]. This mismatch is approximately 122 orders of magnitude, making it one of the worst predictions in the history of modern Physics! The latter is associated with the fact that even though the matter density ρ_m evolves proportionally to the inverse cubic power of the scale factor, nowadays is of the same order of magnitude as the energy density of the cosmological constant ρ_Λ. This problem can also be seen as a fine-tuning problem, since in the context of ΛCDM the cosmological constant should dominate at the exact time as it did in order to obtain an expanding

[1] Einstein characterised the cosmological constant as the "*biggest blunder of my life.*"

[2] Adam Riess, Saul Perlmutter and Brian Schmidt won the 2011 Nobel Prize for this particular discovery.

[3] The cosmological constant and the vacuum energy share the same behaviour dynamically in the context of GR, so at a first level the assumption that the two quantities are different sides of the same coin is valid.

Universe with structures such as galaxies and stars [62]. Therefore, the ratio ρ_m/ρ_Λ should take an incredible accurate value for this to happen.

Since 1998 and the confirmation that the Universe is accelerating, the accuracy of the cosmological observations constantly increases, revealing a series of "tensions" in the context of ΛCDM. When a "tension" for a specific parameter in the context of a particular model is identified in the literature, then it is implied that the best fit measurements of the specific parameter obtained from independent probes disagree at level of at least 2σ. The most serious observational tension in the context of ΛCDM is the so called "H_0 *tension*" and is currently at a 5σ level. This arises in the case of the Hubble parameter H_0 when comparing its indirect measurement from the Cosmic Microwave Background and Baryon Acoustic Oscillations, using the inverse distance ladder method ($H_0 = 67.36 \pm 0.54$ km s^{-1} Mpc^{-1}) [18] with the direct measurement from Type Ia supernovae measurement using the standard distance ladder method ($H_0 = 73.04 \pm 1.04$ km s^{-1} Mpc^{-1}) [63]. However, the tension level rises even further approaching the 6σ mark depending on the data combination of local measurement that are used [64, 65]. Another (but milder) tension that unveiled itself in the last couple of years is the so called "σ_8 or S_8 or *growth tension*". This tension refers to the mismatch in the measurement of the growth rate of cosmological perturbations using peculiar velocities through Redshift Space Distortions data [66–74], Weak Lensing cosmological data [75–82] as well as Cluster Count data [17, 83, 84]. These type of data favor a lower growth rate than the observed Planck18/ΛCDM value, expressed via the lower density rms matter fluctuations within spheres of radius $8h^{-1}$ Mpc, σ_8 and/or the matter density $\Omega_{\rm m,0}$. The "*growth tension*" is currently at a $2\sigma - 3\sigma$ level but it raises to approximately a 5σ level when the E_G statistic data are adopted [85]. For more detailed overviews on the main problems and tensions in the context of ΛCDM see also Refs. [73, 86–94].

Motivated by these difficulties, cosmologists search on both the galactic as well as in the sub-mm scales for hints towards a more complete theory of gravity that explains these challenges in a more fundamental manner. As a result, throughout the years many extensions of ΛCDM have been proposed that address some of the aforementioned problems. These extensions may involve the anthropic principle [95–98], dynamical dark energy models in which the energy density of the cosmological constant is promoted to a dark energy density ρ_{DE} that presents a dynamical evolution [99–105], running vacuum models in which the vacuum energy density is a time dependent quantity [106–114], theories where some sort of scalar field represents the dark energy (*e.g.* quintessence dark energy models [115–130], phantom dark energy models [131–136], k-essence dark energy models [137, 138], scalar tensor theories [139–150] *etc.*) or some sort of a perfect fluid (*e.g.* chaplygin gas [151–155]), modified theories of gravity where the action of ΛCDM is modified introducing extra terms (that may depend on the Ricci scalar R [156–180], or on the torsion T [181–190] *etc.*) or even more complicated modifications such as extra dimensions [191–193], braneworld models [194–202], Brans Dicke models [203], interacting dark energy with dark matter models [204–211], interacting dark matter with neutrinos [212], holographic dark energy models [213–216], early dark energy models [217–223], decaying dark matter models [224], topological defects [225–227], evaporating primordial black holes [228], exotic dark energy models [229–243] and many more.

The basic goal of the present thesis is to contribute to this long term effort in identifying a more complete theory of gravity focusing on the main observational problems of ΛCDM and studying some of the viable alternative theories proposed above pinpointing their observational predictions.

Πρόλογος

Η Κοσμολογία αποτελεί αναμφίβολα έναν από τους πιο ενδιαφέροντες και σημαντικούς κλάδους της Φυσικής. Μαζί με την Κβαντική Θεωρία Πεδίου, η οποία συνδυάζει την Κβαντική Μηχανική και τη Γενική Σχετικότητα, έχει καθιερωθεί ως ένας από τους δύο βασικούς πυλώνες της Σύγχρονης Φυσικής. Όμως, στις αρχές του 20ου αιώνα, η Κοσμολογία δεν είχε καθιερωθεί ως κλάδος της Φυσικής. Αντιθέτως, στις μέρες μας, η τεράστια εξέλιξη της τεχνολογίας έχει οδηγήσει σε μια πληθώρα κοσμολογικών παρατηρήσεων καθιερώνοντάς την ως έναν από τους πιο εντυπωσιακούς και ενεργούς κλάδους των σύγχρονων επιστημών.

Το πρώτο βήμα προς τη μαθηματική διατύπωση της Κοσμολογίας, αποτέλεσε η διατύπωση της Γενικής Θεωρίας της Σχετικότητας (ΓΣ) από τον Άλμπερτ Αϊνστάιν το 1915 φέρνοντας την επανάσταση στον τρόπο που αντιλαμβανόμαστε τις έννοιες του χώρου και του χρόνου. Ο Αϊνστάιν πρότεινε οτι ο χώρος και ο χρόνος είναι συνυφασμένοι σε μια κοινή οντότητα γνωστή ως χωροχρόνος ή συνεχές, στην οποία η βαρύτητα αποτελεί μια γεωμετρική ιδιότητά της. Ειδικότερα, συνειδητοποίησε ότι όσο βαρύτερο είναι ένα αντικείμενο, τόσο περισσότερο παραμορφώνει τον χωροχρόνο γύρω του και ότι η καμπυλότητα του χωροχρόνου μπορεί να συνδεθεί άμεσα με την ενέργεια και την ορμή ενός ρευστού, μέσα από ένα σύστημα μερικών διαφορικών εξισωσέων γνωστών ως *Εξισώσεις του Βαρυτικού Πεδίου του Αϊνστάιν*. Στις μέρες μας, η ΓΣ ειναι η ευρύτερα αποδεκτή θεωρία βαρύτητας εξαιτίας της ικανότητάς της να κάνει ακριβείς προβλέψεις σε μια πληθώρα βαρυτικών φαινομένων τα οποία η Νευτώνεια Θεωρία αποτυγχάνει να εξηγήσει, όπως για παράδειγμα η γωνία μετάθεσης του περιηλίου του Ερμή [1], η οποία με βάση τη ΓΣ μετατίθεται κατά περίπου 44 arcsec κάθε αιώνα, το φαινόμενο της καμπύλωσης των φωτεινών ακτίνων που οφείλεται στη βαρύτητα του Ηλίου όπως αποδείχθηκε από τον Αρθουρ Έντιγκντον το 1919 κατά τη διάρκεια μια ηλιακής έκλειψης [2] *κ.α.* Επιπλεόν, η ΓΣ προβλέπει τόσο την ύπαρξη εξωτικών αντικείμενων όπως οι μαύρες τρύπες [3–8] όσο και των βαρυτικών κυμάτων, η ύπαρξη των οποίων επιβεβαιώθηκε πειραματικά πριν από μερικά χρόνια [9–11].

Η ανακάλυψη της ΓΣ αποτέλεσε ένα καθοριστικό βήμα προς τη διαμόρφωση του Καθιερωμένου Κοσμολογικού Προτύπου, το οποίο είναι ευρέως γνωστό ως "*μοντέλο* ΛCDM" (όπου το Λ αντιστοιχεί στην Κοσμολογική Σταθερά ενώ το ακρώνυμο CDM στην Ψυχρή Σκοτεινή Ύλη) και αντιστοιχεί στη μαθηματική παραμετροποίηση της Θεωρίας της Μεγάλης Έκρηξης [12–14]. Η συγκεκριμένη θεωρία εξηγεί με εξαιρετικά μεγάλη ακρίβεια, πως το Σύμπαν μας, πριν από περίπου 13.8 δισεκατομμύρια χρόνια διαστάλθηκε από μια αρχική απείρως θερμή και πυκνή ανωμαλία στο Σύμπαν που παρατηρούμε σήμερα. Σύμφωνα, λοιπόν, με το μοντέλο ΛCDM, υπάρχουν τρία βασικά συστατικά που απαρτίζουν το παρατηρούμενο Σύμπαν. Αυτά είναι:

- Η Βαρυονική Ύλη και η Ακτινοβολία: Η βαρυονική (ή συνηθισμένη ύλη) αντιστοιχεί στα βαρυόνια και τα λεπτόνια, ενώ η ακτινοβολία περιγράφει σωματίδια με μηδενική μάζα ηρεμίας, όπως είναι για παράδειγμα τα φωτόνια. Παραδόξως, μόνο ένα πολύ μικρό μέρος του Σύμπαντος (4%) αντιστοιχεί στην ορατή ύλη.

- Η Σκοτεινή Ύλη: Η Σκοτεινή Ύλη αποτελεί περίπου το 22% του Σύμπαντος. Αν και η Σκοτεινή Ύλη είναι μια καλά καθορισμένη ιδέα [15–18] και είναι εξαιρετικά μεγάλης σημασίας για το μοντέλο ΛCDM, η πραγματική της φύση παραμένει μέχρι και σήμερα ένα από τα μεγαλύτερα μυστήρια της Σύγχρονης Κοσμολογίας. Οι Κοσμολόγοι θεωρούν ότι η Σκοτεινή Ύλη αντιστοιχεί σε ένα άγνωστο, μη σχετικιστικό, σταθερό σωματίδιο, που αλληλεπιδρά μόνο βαρυτικά με τη συνηθισμένη ύλη. Ως πιθανές εξηγήσεις της Σκοτεινής Ύλης έχουν προταθεί μια πληθώρα εναλλακτικών θεωριών στη βιβλιογραφία, όπως για παραδειγμα τα Weakly Interacting Massive Particles (Ασθενώς Αλληλεπιδρώντα Μαζικά Σωματίδια) [19,20], τα Massive Astrophysical Compact Halo Objects (Μαζικά Συμπαγή Αντικείμενα της Άλω) [21,22], οι Primordial Black Holes (Αρχέγονες Μαύρες Τρύπες) [23–26], τα Quantum Chromodynamics Axions (Κβαντικά Χρωμοδυναμικά Αξιόνια) [27,28], τα Neutralinos [29], τα Strongly Interacting Massive Particles (Ισχυρά Αλληλεπιδρώντα Μαζικά Σωμάτια) [30, 31] *κ.α.*

- Σκοτεινή Ενέργεια: Το υπόλοιπο 74% αποτελείται από μία ακόμα άγνωστη ποσότητα που ονομάζεται "Σκοτεινή Ενέργεια" και παρουσιάζει αντιβαρυτικές ιδιότητες σε αντίθεση με την βαρυονική ύλη ή την ακτινοβολία. Αυτή η μυστηριώδης μορφή ενέργειας είναι υπεύθυνη για την παρατηρούμενη διαστολή του Σύμπαντος. Στο πλαίσιο του ΛCDM, η Σκοτεινή Ενέργεια ταυτίζεται με την Κοσμολογική Σταθερά [32].

Η Κοσμολογική Σταθερά εισήχθη για πρώτη φορά από τον Άλμπερτ Αϊνστάιν το 1917 [33], σε μια προσπάθεια να επιτύχει ένα στατικό Σύμπαν, μία ιδέα που εκείνη την εποχή αποτελούσε την επικρατούσα θεωρία για την περιγραφή του Σύμπαντος. Όμως, λόγω των προβλημάτων σταθερότητας που αντιμετώπιζε το συγκεκριμένο μοντέλο [34,35], καθώς και της παρατηρησιακής επιβεβαίωσης από τον Έντγουιν Χαμπλ ότι οι γαλαξίες απομακρύνονται μεταξύ τους [36], η ιδέα εγκαταλείφθηκε περίπου δεκατέσσερα χρόνια αργότερα[4].

Παρόλα αυτά, η Κοσμολογική Σταθερά επανήλθε το 1998, όταν δύο διαφορετικές ερευνητικές ομάδες, η ομάδα Supernova Cosmology Project [37] και η ομάδα High-Redshift Supernova Search Team [38], επιβεβαίωσαν με τη χρήση δεδομένων Type Ia Supernovae (Υπερκαινοφανών Αστέρων Τύπου Ια) ότι το Σύμπαν μας, πράγματι, επιταχύνεται[5]. Σήμερα, η Κοσμολογική Σταθερά θεωρείται ως ο βασικός υποψήφιος για την εξήγηση της επιταχυνόμενης διαστολής καθιερώνοντας στη βιβλιογραφία το "Καθιερωμένο Κοσμολογικό Πρότυπο" ως ΛCDM (το Λ αναφέρεται στην Κοσμολογική Σταθερά, ενώ το ακρώνυμο CDM αντιστοιχεί στη Σκοτεινή Ύλη).

Από τότε, ένας μεγάλος αριθμός διαφορετικών αποστολών χρησιμοποιώντας εναλλακτικού τύπου κοσμολογικά δεδομένα [όπως για παράδειγμα δεδομένα Cosmic Microwave Background (Κοσμικής Ακτινοβολίας Υποβάθρου) [17,18,39], δεδομένα Type Ia Supernovae (Υπερκαινοφανών Αστέρων Τύπου Ια) [40,41], δεδομένα Cosmic Chronometers (Κοσμικών Χρονομέτρων) [42–44], δεδομένα Baryon Acoustic Oscillations (Βαρυονικών Ακουστικών Ταλαντώσεων) [45, 46], δεδομένα Redshift Space Distortions (Παραμορφώσεων στον Χώρο της Ερυθράς Μετατόπισης) [18, 47, 48], δεδομένα Weak Lensing (Ασθενών Βαρυτικών Φακών) [49, 50], δεδομένα Cluster Count (Αρίθμησης Σμηνών Γαλαξιών) [51–55] *κ.α.*] συγκλίνουν στην υπάρξη της Κοσμολογικής Σταθεράς. Όμως, το μοντέλο αυτό, παρά την απλότητα του και την πολύ καλή συμφωνία του

[4] Ο ίδιος ο Αϊνστάιν χαρακτήρισε την εισαγωγή της Κοσμολογικής Σταθεράς ως "το μεγαλύτερο σφάλμα της ζωής μου."

[5] Οι ερευνητές Adam Riess, Saul Perlmutter και Brian Schmidt κέρδισαν το 2011 το βραβείο Νόμπελ για την συγκεκριμένη ανακάλυψη.

με τα κοσμολογικά δεδομένα, παρουσιάζει ορισμένα προβλήματα τόσο σε θεωρητικό όσο και σε παρατηρησιακό επίπεδο.

Τα θεωρητικά προβληματά του μοντέλου ΛCDM αποτελούν τα προβλήματα της κοσμολογικής σταθεράς (cosmological constant problem) [56–60] καθώς και αυτό της σύμπτωσης (coincidence problem) [61, 62]. Το πρώτο αναφέρεται στην απόκλιση της πρόβλεψης της ενέργειας κενού ρ_Λ η οποία προκύπτει από την Κβαντική Θεωρία Πεδίου με την παρατηρήσιμη τιμή της[6]. Η απόκλιση αυτή είναι περίπου 122 τάξεις μεγέθους και θεωρείται μία από τις χειρότερες θεωρητικές προβλέψεις στην ιστορία της Σύγχρονης Φυσικής! Το δεύτερο πρόβλημα συνδέεται με το γεγονός ότι εαν και η πυκνότητα ενέργειας της ύλης ρ_m εξελίσσεται αντιστρόφως ανάλογα της τρίτης δύναμης του παράγοντα κλίμακας, στις μέρες μας είναι της ίδιας τάξης μεγέθους με την πυκνότητα ενέργειας της Κοσμολογικής Σταθεράς ρ_Λ. Αυτό το πρόβλημα μπορούμε να το δούμε και ως ένα πρόβλημα μιας λεπτομερούς ρύθμισης (fine-tuning problem), καθώς στο πλαίσιο του ΛCDM, η Κοσμολογική Σταθερά θα πρέπει να κυριαρχεί κάποια συγκεκριμένη χρονική στιγμή ώστε να έχουμε ένα Σύμπαν σαν το δικό μας, ένα Σύμπαν δηλαδή το οποίο βρίσκεται σήμερα σε μια περίοδο επιταχυνόμενης διαστολής και παρουσιάζει δομές, όπως γαλαξίες και αστέρια [62]. Επομένως, ο λόγος ρ_m/ρ_Λ πρέπει να έχει μία πολύ συγκεκριμένη τιμή για να συμβεί αυτό.

Από το 1998 και την επιβεβαίωση ότι το Σύμπαν μας βρίσκεται σε μία φάση επιταχυνόμενης διαστολής, η ακρίβεια των κοσμολογικών παρατηρήσεων συνεχώς αυξάνεται, αποκαλύπτοντας έτσι μια σειρά από "ασυμβατότητες" στο πλαίσιο του μοντέλου ΛCDM. Η ανίχνευση μιας "ασυμβατότητας" για μία συγκεκριμένη παράμετρο σε κάποιο κοσμολογικό μοντέλο ισοδυναμεί με το γεγονός ότι η εύρεση των βέλτιστων τιμών της συγκεκριμένης παραμέτρου με τη χρήση εναλλακτικών μεθόδων διαφέρει σε στατιστικό επίπεδο μεγαλύτερο του 2σ. Η πιο σοβαρή παρατηρησιακή ασυμβατότητα του μοντέλου ΛCDM αφορά την παράμετρο Hubble, καλείται "*H_0 ασυμβατότητα*" και βρίσκεται σε στατιστικό επίπεδο 5σ. Η ασυμβατότητα αυτή εμφανίζεται, όταν συγκρίνουμε την τιμή της παραμέτρου Hubble που προκύπτει έμμεσα από δεδομένα Κοσμικής Ακτινοβολίας Υποβάθρου και Βαρυονικών Ακουστικών Ταλαντώσεων με τη χρήση της inverse distance ladder method (αντίστροφης μεθόδου κλίμακας-αποστάσεων) της αποστολής Planck ($H_0 = 67.36 \pm 0.54$ km s^{-1} Mpc^{-1}) [18] με την τιμή της που προκύπτει άμεσα από δεδομένα Υπερκαινοφανών Αστέρων Τύπου Ia με τη χρήση της standard distance ladder method (μεθόδου κλίμακας-αποστάσεων) ($H_0 = 73.04 \pm 1.04$ km s^{-1} Mpc^{-1}) [63]. Όμως, η ασυμβατότητα αυτή προσεγγίζει τα 6σ ανάλογα με τον συνδυασμό των τοπικών δεδομένων που χρησιμοποιούνται [64, 65]. Ακόμα μία ασυμβατότητα που αποκαλύφθηκε τα τελευταια χρόνια (η οποία όμως είναι λιγότερο στατιστικά σημαντική) είναι η λεγόμενη "σ_8 ή S_8 ασυμβατότητα". Αυτή η ασυμβατότητα αναφέρεται στην ασυνέπεια της τιμής της παραμέτρου του πλάτους του φάσματος ισχύος κοσμικών δομών στην κλίμακα $8h^{-1}$ Mpc, σ_8 ή/και της αδιάστατης παραμέτρου πυκνότητας της ύλης $\Omega_{\mathrm{m},0}$. Συγκεκριμένα μετρήσεις με τη χρήση δεδομένων που αφορούν Παραμορφώσεις στο Χώρο της Ερυθράς Μετατόπισης [66–74], δεδομένων Ασθενών Βαρυτικών Φακών [75–82] καθώς και δεδομένων Αρίθμησης Σμηνών Γαλαξιών [17, 83, 84] ευνοούν χαμηλότερες τιμές για τις συγκεκριμένες παραμέτρους από τις τιμές που αναφέρει η αποστολή του Planck. Η "σ_8 ασυμβατότητα" βρίσκεται σε στατιστικό επίπεδο $2\sigma - 3\sigma$ αλλά προσεγγίζει τα 5σ, όταν χρησιμοποιούνται τα E_G δεδομένα [85]. Για περισσότερες λεπτομέρειες σχετικά με τα βασικά προβλήματα που αντιμετωπίζει το μοντέλο ΛCDM, ο αναγνώστης μπορεί να ανατρέξει στις ακόλουθες αναφορές [73, 86–94].

Ορμώμενοι από αυτές τις δυσκολίες, οι Κοσμολόγοι ερευνούν τόσο τις κοσμολογικές όσο και τις κλίμακες χιλιοστού για πιθανές ενδείξεις ύπαρξης μιας πληρέστερης θεωρίας βαρύτητας η οποία

[6] Η Κοσμολογική Σταθερά και η ενέργεια του κενού παρουσιάζουν την ίδια δυναμική συμπεριφορά στα πλαίσια της ΓΣ, οπότε σε μια πρώτη προσέγγιση, η υπόθεση οτι οι δύο αυτές έννοιες ταυτίζονται είναι εύλογη.

να εξηγεί τα προβλήματα αυτά με έναν πιο θεμελιώδη τρόπο. Αυτή η αναζήτηση έχει οδηγήσει τα τελευταία χρόνια στη διατύπωση πολλών θεωριών, οι οποίες αποτελούν επεκτάσεις του μοντέλου ΛCDM και έχουν ως σκοπό την πιθανή επίλυση αυτών των προβλημάτων. Αυτές οι προτεινόμενες επεκτάσεις/λύσεις μπορεί να περιλαμβάνουν την ανθρωπική αρχή [95–98], δυναμικά εξελισσόμενα μοντέλα σκοτεινής ενέργειας στα οποία η πυκνότητα ενέργειας της κοσμολογικής σταθεράς προάγεται σε μια πυκνότητα ενεργειας σκοτεινής ενέργειας ρ_{DE} και παρουσιάζει δυναμική εξέλιξη [99–105], μοντέλα κλιμακωτού μεταβολλόμενου κενού, στα οποία η πυκνότητα ενέργειας του κενού είναι μία χρονικά εξαρτώμενη ποσότητα [106–114], θεωρίες στις οποίες τον ρόλο της σκοτεινής ενέργειας παίζει ένα βαθμωτό πεδίο [όπως για παράδειγμα στις θεωρίες πεμπτουσίας (quintessence dark energy models) [115–130], στις θεωρίες phantom, στις οποίες το βαθμωτό πεδίο έχει αρνητικό πρόσημο στον κινητικό όρο (phantom dark energy models) [131–136], θεωρίες k-essence, στις οποίες εμφανίζονται βαθμωτά πεδία με γενικευμένους κινητικούς όρους (k-essence dark energy models) [137, 138], στις βαθμοτανυστικές θεωρίες πεμπτουσίας (scalar tensor theories) [139–150] *κ.α.*], κάποιου είδους τέλειου ρευστού (όπως για παράδειγμα το μοντέλο chaplygin [151–155]), τροποποιημένες θεωρίες βαρύτητας στις οποίες η δράση του μοντέλου ΛCDM μεταβάλλεται με την εισαγωγή επιπλέον όρων (οι οποίοι μπορεί να εξαρτώνται από το βαθμωτό Ricci R [156–180] ή τη στρέψη T [181–190] *κ.α.*) ή και ακόμα πιο περίπλοκες τροποποιήσεις, όπως για παράδειγμα θεωρίες στις οποίες εισάγονται έξτρα διαστάσεις [191–193], μοντέλα μεμβρανών [194–202], μοντέλα τύπου Brans Dicke [203], μοντέλα στα οποία η Σκοτεινή Ενέργεια και η Σκοτεινή Ύλη αλληλεπιδρούν (interacting dark energy with dark matter models) [204–211], μοντέλα στα οποία η Σκοτεινή Ύλη αλληλεπιδρά με νετρίνα (interacting dark matter with neutrinos) [212], μοντέλα ολογραφικής Σκοτεινής Ενέργειας (holographic dark energy models) [213–216], μονέλα πρώιμης σκοτεινη ενεργειας (early dark energy) [217–223], μοντέλα διασπώμενης Σκοτεινής Ύλης (decaying dark matter) [224], μοντέλα με τοπολογικές ατέλειες [225–227], μοντέλα αρχέγονων μαύρων τρυπών που εξαφανίζονται (evaporating primordial black holes) [228], μοντέλα εξωτικής σκοτεινής ενέργειας (exotic dark energy) [229–243] *κ.α.*

Αυτός ακριβώς είναι και ο στόχος της παρούσας Διδακτορικής Διατριβής. Να συνεισφέρει σε αυτη τη μακροπρόθεσμη προσπάθεια ανίχνευσης μιας πλήρους θεωρίας βαρύτητας, επικεντρωνόμενη στα βασικά παρατηρησιακά προβλήματα του μοντέλου ΛCDM και ερευνώντας ορισμένα από τα εναλλακτικά μοντέλα που έχουν αναφερθεί παραπάνω, να ταυτοποιήσει πιθανές παρατηρησιακές τους προβλέψεις.

Chapter 1

Introduction

1.1 Mathematical Formulation of ΛCDM

1.1.1 Cosmological Principle

A key concept of General Theory of Relativity (GR) is the Cosmological Principle which postulates that even though at small scales the Universe contains structures, at large scales, *i.e.* scales greater than 100 Mpc, the Universe is actually homogeneous and isotropic. This means that two different observers independently on which point or which direction they are looking, they are going to receive the same observational evidence. The Cosmological Principle is a generalization of the Copernican Principle which was a basic assumption of the Copernican heliocentrism model that was first developed by Nicolaus Copernicus in 1543 [244] and states that there are no privileged observers on the Universe.

The Cosmological Principle is currently under intense investigation using a variety of different cosmological data [245–259], however up to date, no conclusive evidence against the Cosmological Principle have been provided. The concept of a homogeneous and isotropic spacetime, is incorporated in the context of ΛCDM through the so called *Friedmann-Lemaitre-Robertson-Walker* metric which we will discuss later on in this chapter. However, if the Cosmological Principle is indeed violated, then the concept of homogeneity is also violated. Therefore, the observed accelerated expansion of the Universe is not due to a mysterious component such as dark energy as we discussed earlier, but it can be due to a local underdense region that dwindles at large scales [260–267].

The idea that we currently live in an underdense region could also, in principle, explain the observed H_0 tension in a more generic manner, since locally we would measure an H_0 value that is higher than the true H_0 measured globally. However, the scale and depth needed for this cosmic variance seems to be strongly disfavored by current observations [268–275]. Even so, in the last couple of years some groups presented evidence of a local underdensity of a few Mpc (which is approximately three order of magnitudes smaller than the Gpc scale required to fully resolve the H_0 tension) using different galaxy survey catalogues such as the 2 Micron All Sky Survey catalogue [276, 277], the UKIRT Infrared Deep Sky Large Area Survey [278] as well as galaxy samples galaxies samples created by the 6-degree Field Galaxy, Sloan Digital Sky and Galaxy and Mass Assembly surveys [279, 280]. Furthermore, there have been reports studying the latest Type Ia Supernovae dataset that is publicly available (Pantheon) [281–285] and a sample of galaxy X-ray galaxy clusters [286] that stress that a local underdensity should

not yet excluded.

Clearly, even though the concept of the Cosmological Principle is currently under debate, the idea that we live in an isotropic and homogeneous Universe remains arguably the most popular until today, since no vividly evidence against it have been discovered.

1.1.2 Metric and Energy Momentum Tensor

Einstein's goal was to formulate an equation that connected the energy and matter distribution of spacetime to its geometry. The concept of geometry is embodied in the metric described by the symmetric second rank tensor $g_{\mu\nu}$. A metric tensor is the most important tensor that can be defined on a manifold, since it allows the transformation of the observer dependent coordinate distance to be transformed into physical distance. The invariant line element in the context of GR is defined as

$$ds^2 = g_{\mu\nu} dx^\mu dx^\nu \,, \tag{1.1}$$

where $x^\mu = (x^0, x^1, x^2, x^3) = (ct, \vec{x})$. Clearly, this is a rather tedious situation however it can be drastically simplified by imposing the aforementioned symmetry as well as the cosmological principle. In this case, the line element in spherical coordinates is written as

$$ds^2 = (c\,dt)^2 - a^2(t) \left[\frac{dr^2}{1 - k\,r^2} + r^2 (d\theta^2 + \sin^2\theta\, d\phi^2) \right] , \tag{1.2}$$

where $a(t)$ corresponds to the scale factor which is determined by solving the Einstein's Field Equations and k to the spatial curvature, a constant parameter that determines the geometry of the studied Universe. This spacetime is known as Friedmann-Lemaitre-Robertson-Walker (FLRW) [287].

The spatial curvature k is a constant parameter, independent of the selected coordinates that its exact value is irrelevant since it can be normalized by a redefinition of the scale factor $a(t)$ and of the radial distance coordinate r. So, the spatial curvature has the following three eligible values describing three different geometries for the Universe. For $k = 0$ a flat Universe is represented, for $k = 1$ a closed Universe is described, while the value $k = -1$ correspond to an open Universe. The associated topological geometries are illustrated below

Figure 1.1: The three different geometric manifolds for zero, positive and negative spatial curvature. From Ref. [288].

Furthermore, in order to be able to resolve the Einstein's Field Equations the representation of the energy distribution at large scales in the context of GR is needed. This problem was first

studied by Herman Weyl in 1923 [289]. Using the Cosmological Principle, Weyl proposed that the Universe contains a uniform substratum with a four-velocity u^μ and that its contents, *i.e.* the galaxies, behave like "particles" inside a perfect fluid. Each point of the fluid is characterized by a density ρ and a pressure p and the relative velocities of the "particles" that move inside the substratum can be ignored. Despite the fact that this is not a perfect assumption, this hypothesis can be adopted in the context of GR, since the relative velocities of the galaxies are much smaller compared to the cosmic expansion. Therefore, the second rank tensor that describes the matter and energy distribution of the Universe is of the following form [287]

$$T_{\mu\nu} = (\rho + p)u_\mu u_\nu - p\, g_{\mu\nu}\,. \tag{1.3}$$

Eq. (1.3) defines another extremely useful quantity, the energy momentum tensor. Obviously, since this tensor describes the energy it should also obey a conservation law.

However, we can not simply use the partial derivative as usual. In the context of GR a new symbol is defined and the conservation law for the energy momentum tensor is written as $\nabla^\mu T_{\mu\nu} = 0$. The partial derivative in this case is generalized to the *covariant derivative*, which for a vector A_ν takes the following form

$$\nabla_\mu A_\nu \equiv \partial_\mu A_\nu + \Gamma^\lambda_{\mu\nu}\, A_\lambda\,, \tag{1.4}$$

while for a vector A^ν it is written as

$$\nabla_\mu A^\nu \equiv \partial_\mu A^\nu - \Gamma^\nu_{\mu\lambda}\, A^\lambda\,. \tag{1.5}$$

In Eqs. (1.4) and (1.5) the $\Gamma^\lambda_{\mu\nu}$ symbols correspond to the well known *Christoffel symbols* which are defined as

$$\Gamma^\rho_{\mu\nu} \equiv \frac{1}{2} g^{\lambda\rho}\left(\partial_\mu g_{\lambda\nu} + \partial_\nu g_{\lambda\mu} - \partial_\lambda g_{\mu\nu}\right) \tag{1.6}$$

1.1.3 Einstein's Field Equations

Armed with the results of the previous section, we are ready to compute the famous Einstein's Field Equations. Since the Newtonian gravity should be included in GR, Einstein realized that the basic step towards a mathematical formulation was to supersede the Poisson's law. Poisson's law for a gravitational potential $\phi(r)$ is given by

$$\nabla^2\phi(r) = 4\,\pi\, G_{\rm N}\,\rho\,, \tag{1.7}$$

where $G_{\rm N}$ corresponds to Newton's constant and ρ is the mass density. So, in order to generalize this equation to the GR corresponding one we need to understand its characteristics. On the left hand side of Eq. (1.7) there is a second order differential operator which acts upon the gravitational field, while on the right hand side we have a measure of the mass distribution. The right hand side of Eq. (1.7) is generalized easily to the energy momentum tensor. However, things are a little more complicated regarding the left hand side. For its generalization, a tensor with second order derivatives of $g_{\mu\nu}$ is needed. The obvious answer would be the Riemann's curvature tensor, which is defined as

$$R^\rho_{\sigma\mu\nu} \equiv \partial_\mu\Gamma^\rho_{\nu\sigma} - \partial_\nu\Gamma^\rho_{\mu\sigma} + \Gamma^\rho_{\mu\lambda}\Gamma^\lambda_{\nu\sigma} - \Gamma^\rho_{\nu\lambda}\Gamma^\lambda_{\mu\sigma}\,, \tag{1.8}$$

but unfortunately it is not of the same rank as the energy momentum tensor $T_{\mu\nu}$. On the contrary, the Ricci tensor that is derived by contracting two indices, is of the correct order, *i.e.* of the same order as the energy momentum tensor. The Ricci tensor is defined as

$$R_{\mu\nu} \equiv g^{\lambda\rho} R_{\lambda\mu\rho\nu} = R^{\rho}_{\mu\rho\nu} = \partial_\rho \Gamma^{\rho}_{\mu\nu} - \partial_\mu \Gamma^{\rho}_{\rho\nu} + \Gamma^{\rho}_{\rho\lambda}\Gamma^{\lambda}_{\mu\nu} - \Gamma^{\rho}_{\mu\lambda}\Gamma^{\lambda}_{\rho\nu} \tag{1.9}$$

and based on (1.9), the Ricci scalar can be defined

$$R = g^{\mu\nu} R_{\mu\nu} \,. \tag{1.10}$$

At a certain point, Einstein did consider that the correct gravitational field equations are

$$R_{\mu\nu} = \kappa\, T_{\mu\nu} \,, \tag{1.11}$$

where $\kappa \equiv (8\pi G_{\rm N})/c^4$ is a constant. But, taking into account the conservation of energy, Eq. (1.11) faces severe problems. Even though the energy momentum tensor obeys the relation $\nabla^\mu T_{\mu\nu} = 0$, this is not true for $R_{\mu\nu}$ considering an arbitrary geometry, breaking as a result the equality. Therefore, Einstein constructed the following tensor

$$G_{\mu\nu} \equiv R_{\mu\nu} - \frac{1}{2} g_{\mu\nu} R \,, \tag{1.12}$$

proved that $\nabla^\mu G_{\mu\nu} = 0$ [287] based on the Bianchi identity and showed that the correct gravitational field equations are (for $c = 1$) [287]

$$G_{\mu\nu} = 8\pi G_{\rm N} T_{\mu\nu} \,. \tag{1.13}$$

The constant κ was chosen by Einstein so at the limit of the weak gravitational field the above equation leads to the Poisson law (1.7) as expected.

A more mathematical way to obtain the Einstein's Field Equations (1.13), is by applying the stationary action principle in the full Einstein-Hilbert action. Even though this approach is trivial for the full Einstein-Hilbert action, it is extremely useful in more complicated actions. The action consists of two terms, one that incorporates the geometry and one that describes the matter fields of the theory and is of the following form

$$S_{EH} = \int d^4x \sqrt{-g} \left[\frac{1}{2\kappa} R + \mathcal{L}_{matter} \right] \,, \tag{1.14}$$

where $g \equiv det(g_{\mu\nu})$ is the determinant of the metric tensor matrix. Following the stationary action principle, we demand that the variation of the action with respect to the inverse metric is zero for any $\delta g^{\mu\nu}$, so it is straightforward to obtain the following equation

$$\frac{\delta S_{EH}}{\delta g^{\mu\nu}} = 0 \Rightarrow \frac{\delta R}{\delta g^{\mu\nu}} + \frac{R}{\sqrt{-g}} \frac{\delta \sqrt{-g}}{\delta g^{\mu\nu}} = -\frac{2\kappa}{\sqrt{-g}} \frac{\delta \left(\mathcal{L}_{matter} \sqrt{-g} \right)}{\delta g^{\mu\nu}} \,, \tag{1.15}$$

The right hand side of (1.15) is by definition the energy momentum tensor multiplied by κ. Regarding the left hand side of (1.15) using the fact that

$$\frac{\delta R}{\delta g^{\mu\nu}} = R_{\mu\nu} \,, \tag{1.16}$$

$$\delta \left(\sqrt{-g} \right) = -\frac{1}{2} \sqrt{-g} g_{\mu\nu} \delta g^{\mu\nu} \,, \tag{1.17}$$

then Eq. (1.15) reduces to

$$R_{\mu\nu} - \frac{1}{2} g_{\mu\nu} R = \kappa T_{\mu\nu} \overset{c=1}{\Longrightarrow} G_{\mu\nu} = 8\pi G_{\rm N}\, T_{\mu\nu} \,,$$

i.e. the Einstein's Field Equations (1.13).

1.1.4 Friedmann Equations

The Einstein's Field Equations may be used to relate the evolution of the scale factor $a(t)$ with the pressure and energy of the matter for a plethora of different gravitational systems. So, a basic question that arises is the following: "Can we achieve an exact solution of the Einstein's Field Equations for our Universe?" As we discussed earlier our Universe at large scales is homogeneous and isotropic, so the metric that incorporates both of these concepts is the FLRW metric with (1.2) as the line element.

For the FLRW metric the non-zero components of the metric are

$$g_{00} = c^2 = 1, \qquad g_{11} = -\frac{a^2}{1-kr^2}, \qquad g_{22} = -a^2 r^2, \qquad g_{33} = -a^2 r^2 \sin^2\theta\,,$$

leading to the following non-zero Christoffel symbols

$$\begin{aligned}
\Gamma^0_{11} &= \frac{a\dot{a}}{1-kr^2}, & \Gamma^0_{22} &= a\dot{a}r^2, & \Gamma^0_{33} &= a\dot{a}r^2\sin^2\theta\,,\\
\Gamma^1_{11} &= \frac{kr}{1-kr^2}, & \Gamma^1_{22} &= -r(1-kr^2), & \Gamma^1_{33} &= -r\,\sin^2\theta(1-kr^2)\,,\\
\Gamma^1_{01} &= \Gamma^2_{02} = \frac{\dot{a}}{a}, & \Gamma^3_{03} &= \frac{\dot{a}}{a}, & \Gamma^2_{12} &= \frac{1}{r}\,,\\
\Gamma^3_{13} &= \frac{1}{r}, & \Gamma^2_{33} &= -\sin\theta\,\cos\theta, & \Gamma^3_{23} &= \frac{\cos\theta}{\sin\theta}\,,
\end{aligned}$$

where the dot represents derivation with respect to time. Armed with the non-vanishing Christoffel symbols, the Ricci scalar (1.9) can be computed immediately as

$$R = g^{\mu\nu}R_{\mu\nu} = g^{00}R_{00} + g^{11}R_{11} + g^{22}R_{22} + g^{33}R_{33} \Rightarrow R = -6\left(\frac{\ddot{a}}{a} + \frac{\dot{a}^2}{a^2} + \frac{k}{a^2}\right). \tag{1.18}$$

Now using the definitions (1.3) and (1.13) we can calculate the non-zero components of the Einstein Field Equations. The (00)-component gives [287]

$$G_{00} = 8\pi G_{\rm N}\,T_{00} \Rightarrow \left(\frac{\dot{a}}{a}\right)^2 = \frac{8\pi G_{\rm N}}{3}\rho - \frac{k}{a^2}\,, \tag{1.19}$$

an equation that is known as the *Friedmann equation* that connects the geometry with the density ρ and the spatial curvature k. The spatial components (ii) give

$$2\frac{\ddot{a}}{a} + \frac{\dot{a}^2}{a^2} + \frac{k}{a^2} = -8\pi G_{\rm N}\,p\,. \tag{1.20}$$

Usually, Eq. (1.20) is not used in its current form, but we substitute the second term with (1.19), yielding [287]

$$\frac{\ddot{a}}{a} = -\frac{4\pi G_{\rm N}}{3}(\rho + 3p)\,. \tag{1.21}$$

This equation is known as the *Raychaudhuri equation* or the *acceleration equation* since it includes the second derivative of the scale factor $a(t)$. The minus sign of this equation is of paramount significance, since for $\rho > 0$ and $p > 0$ (ordinary matter), the right hand side of (1.21) is always negative, leading to a deceleration of the expansion. However, as we discussed

earlier, current observations confirmed that the Universe nowadays is actually accelerating. Therefore, we can either completely omit (1.21)[1] or consider a mysterious component (such as the cosmological constant) with negative pressure.

So far we have two differential equations with three unknown functions, the scale factor $a(t)$, the density $\rho(t)$ and the pressure $p(t)$ that depend on time. Therefore, in order to be able to solve the differential system another equation is needed. Naively, one could think that this equation is the continuity equation which is the following [287]

$$\dot{\rho} + 3\frac{\dot{a}}{a}(\rho + p) = 0\,. \tag{1.22}$$

However, (1.22) is derivable from Eqs. (1.19) and (1.21) by differentiating the first one with respect to time and substituting the $\ddot{a}$ from the Raychaudhuri equation[2]. So, the needed equation is none other than the equation of state [287]

$$p = w\,\rho\,, \tag{1.23}$$

where the proportionality factor w can be constant or it can be a function of time. Typically, Eqs. (1.19) and (1.21) are expressed in terms of the Hubble rate $H \equiv \frac{\dot{a}}{a}$ and its first derivative. In this case, the Friedmann equation takes the form [287, 290]

$$H^2 = \frac{8\pi G_{\rm N}}{3}\rho - \frac{k}{a^2}\,, \tag{1.24}$$

while the Raychaudhuri equation is written as [287, 290]

$$\dot{H} + H^2 = -\frac{4\pi G_{\rm N}}{3}(\rho + 3p) \tag{1.25}$$

1.1.5 Cosmological Constant and ΛCDM

Several decades ago, when Einstein was formulating GR, the Universe was though to be static, infinite and mainly composed of matter. This was a valid assumption, since at that time it was not even clear that galaxies outside our own Milky Way existed. Therefore, the Friedmann equations presented in the previous subsection need to be modified since they can not provide a static solution. This belief severely puzzled many scientists as well as Einstein himself. In an attempt to "solve" this problem, Einstein proposed the cosmological constant in 1917 [33]. Einstein decided to modify his original field equations (1.13) by adding a small constant term Λ multiplied by the metric tensor, slightly modifying the geometry of the Universe as [287, 290]

$$G_{\mu\nu} - \Lambda\, g_{\mu\nu} = 8\pi G_{\rm N}\, T_{\mu\nu}\,, \tag{1.26}$$

This extra term preserves the symmetry of GR since it is a small Lorentz invariant term that affects the Friedmann equations. Eqs. (1.24) and (1.25) with the addition of the cosmological constant take the form [32, 287, 290, 291]

$$H^2 = \frac{8\pi G_{\rm N}}{3}\rho - \frac{k}{a^2} + \frac{\Lambda}{3}\,, \tag{1.27}$$

$$\dot{H} + H^2 = -\frac{4\pi G_{\rm N}}{3}(\rho + 3p) + \frac{\Lambda}{3}\,. \tag{1.28}$$

[1] In this context, GR should be modified to a new more complete theory at cosmological scales that includes as a limit GR.

[2] The continuity equation can also be derived using the conservation of the energy momentum tensor $\nabla^\mu T_{\mu\nu} = 0$.

Einstein showed that the value of Λ needed to cancel the attractive gravitational force of matter was $\Lambda = 4\,\pi\,G_{\rm N}\,\rho_m$. This model is known as the "*Einstein's Static Universe Model*".

However, this particular model suffers from serious stability issues as it was proven later on [34, 35]. The final blow for Einstein's Static Universe Model was given by Edwin Hubble in 1929 [36]. Edwin Hubble after years of observing distant galaxies, confirmed that they stray from us, with a velocity u proportional to each object's distance d, leading to the relation

$$u = H_0 \cdot d\,. \tag{1.29}$$

Eq. (1.29) is known as the *Hubble law* and provided the first estimate of the Hubble parameter H_0 as the slope of the diagram. The corresponding value obtained was $H_0 = 500\ km\,s^{-1}\,Mpc^{-1}$. The diagram was presented in [36] is known as Hubble diagram and is illustrated in Fig. 1.2.

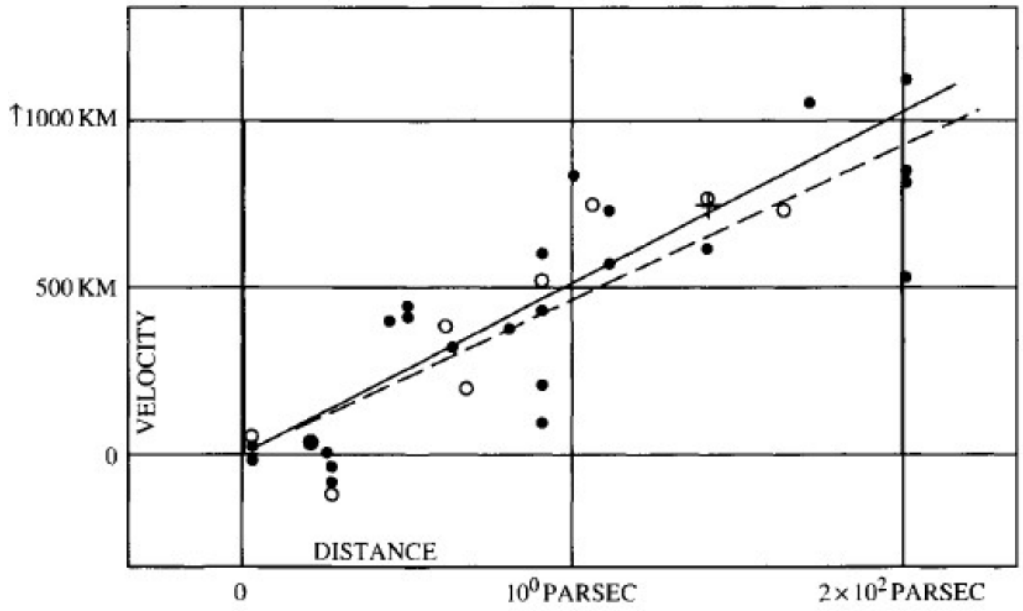

Figure 1.2: The famous Hubble diagram presented in Ref. [36] that illustrates the velocity of distant galaxies as a function of the distance. The dots represent the solution for solar motion using the galaxies separately, while the circles represent the solution mixing the galaxies in groups.

The first confirmation that the Universe is indeed accelerating naturally shocked the scientific world. This discovery forced Einstein to completely abandon the idea of the cosmological constant and that of a static Universe. In the following years, the considered models that attempted to explain the accelerated expansion of the Universe considered the cosmological constant to be equal to zero.

However, the concept of cosmological constant was resurrected for good in 1998. The Supernova Cosmology Project [37] and the High-Redshift Supernova Search Team [38] using Type Ia Supernovae (SnIa) proved independently, that the Universe is indeed accelerating as it is illustrated in Fig. 1.3. Nowadays, the concept of the accelerated expansion is encoded to a repulsive force that exhibits properties of anti-gravity that opposes the self-attraction of matter and dilutes much more slowly than matter as the Universe expands. This mysterious quantity is called dark energy, and the prime candidate is considered to be the cosmological constant. In

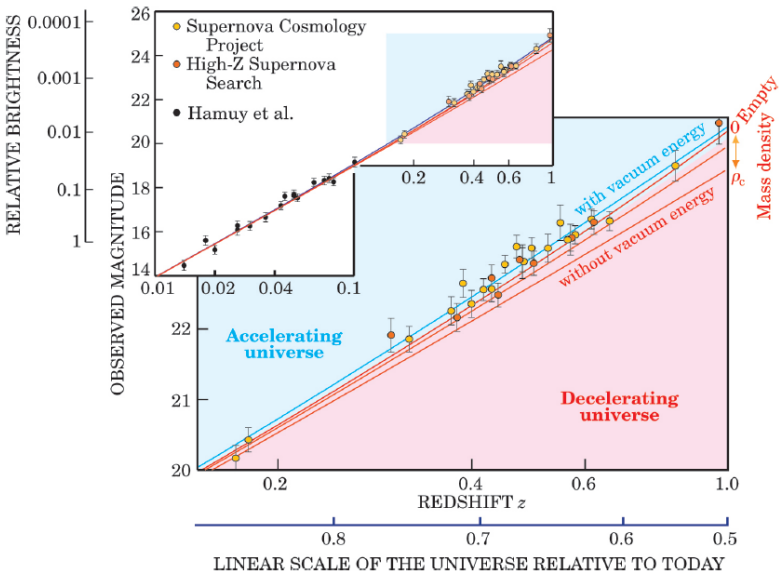

Figure 1.3: The measured magnitude as a function of redshift. The red lines represent different models with zero cosmological constant and mass densities from the critical density ρ_{crit} to zero. The blue line corresponds to a non-zero cosmological constant with a mass density $\rho_{crit}/3$ implying an accelerating expansion. The yellow, orange and black points correspond to the SnIa presented in Refs. [37, 38, 292] respectively. From Ref. [293].

the following years, a plethora of independent observations have provided evidence supporting the existence of cosmological constant establishing the current standard model of cosmology to be the ΛCDM model that has Eqs. (1.27) and (1.28) as background equations[3]. In the context of ΛCDM, the cosmological constant has a constant energy density of the following form [32, 290, 291]

$$\rho_\Lambda = -p_\Lambda = \frac{\Lambda}{8\,\pi\,G_{\rm N}}\,, \tag{1.30}$$

where p_Λ corresponds to the pressure of the cosmological constant and $c = 1$. Eq. (1.30) leads to a constant equation of state parameter [32, 290, 291]

$$w_\Lambda = \frac{p_\Lambda}{\rho_\Lambda} = -1\,. \tag{1.31}$$

Nevertheless, the job is far from done. Despite the simplicity of the model and the excellent fit provided by the data, ΛCDM faces a series of challenges at both the theoretical and the observational level that will be discussed later on leading scientists to search for a more complete theory of gravity that is free of such problems.

[3]In the acronym ΛCDM, Λ stands for the cosmological constant, while CDM describes the cold dark matter described in the Preface.

1.2 Cosmological Observables

1.2.1 Cosmological Redshift

Before proceeding to the main challenges of ΛCDM let us make a small detour to review some useful and important observables in Cosmology that will be extensively used throughout the present thesis. The first concept that we will discuss is that of the redshift. Redshift is an elementary quantity for Cosmology and can be directly associated with the emitted and received photons from an astrophysical object. Suppose that we have a photon that is emitted at a time t_E and is received at a time t_R. Using the FLRW metric (1.2), we set for the photon $ds^2 = 0$ and after an integration we derive [290]

$$\int_{t_E}^{t_R} \frac{c\,dt}{a(t)} = -\int_{r_E}^{0} \frac{dr}{\sqrt{1-k\,r^2}}\,, \tag{1.32}$$

where r_E corresponds to the radial distance of the source. Now, if the emitter sends another photon at a time $t_E + \delta t_E$ and this photon is received at a time $t_R + \delta t_R$, then, since the two photons need to cover the same radial distance, we have [290]

$$\int_{t_E}^{t_R} \frac{c\,dt}{a(t)} = -\int_{r_E}^{0} \frac{dr}{\sqrt{1-k\,r^2}} = \int_{t_E+\delta t_E}^{t_R+\delta t_R} \frac{c\,dt}{a(t)}\,. \tag{1.33}$$

Omitting the middle part of (1.33) and considering that δt_E and δt_R are small so that $a(t)$ can assumed to be constant, we deduce that

$$\frac{\delta t_E}{a(t_E)} = \frac{\delta t_R}{a(t_R)}\,. \tag{1.34}$$

Furthermore, considering the light pulses to be successives of an electromagnetic wave, we derive for the redshift z that

$$1 + z \equiv \frac{\delta t_R}{\delta t_E} = \frac{a(t_R)}{a(t_E)}\,. \tag{1.35}$$

Usually, we neglect the subscripts R and E and consider that t_R corresponds to the present time t_0. So, setting $a(t_0) = 1$ as usual, (1.35) reduces to

$$a(t) = \frac{1}{1+z} \tag{1.36}$$

1.2.2 Geometrical and Dynamical Probes

It is known that the observed accelerated expansion of the Universe is attributed to a mysterious component dubbed dark energy. This dark energy can be due to the existence of a cosmological constant or it can emerge in the context of some more complete theory of gravity. Both of these possibilities leave some characteristic predictions on specific parameters that can be probed using different cosmological data that allow to compare different theories. In general, these probes can be divided [73, 294–296] in the following two broad categories:

- Geometric Probes: The geometric probes refer to cosmological data that probe directly the cosmic metric through cosmological distances, *i.e.* independently of the underlying theory. Examples of such probes include the luminosity distance, the angular diameter distance, the scale of the sound horizon, the cluster gas mass fraction *etc.*

- Dynamical Probes: The dynamical probes refer to cosmological data that probe at the same time the metric as well as the growth rate of cosmological perturbations in the linear and nonlinear regime. An example of a dynamical probe includes the linear matter overdensity growth factor.

In the present thesis, we will study a variety of different cosmological data that belong to both categories, so it would be useful to be more thorough with the examples that were discussed above.

First, let us clarify the concept of distance in Cosmology. Distances are extremely useful in order to study the scale factor $a(t)$ using distant cosmological objects. In Cosmology we can identify the following two basic types of distances:

- Physical Distance d: The physical (or proper) distance d corresponds to the distance between two cosmological objects which could theoretically be measured using a ruler at a constant cosmological time. The concept of this distance is of course theoretical, since we can not freeze the expansion at the time of the measurement.

- Comoving Distance χ: The comoving distance χ is a distance expressed in comoving coordinates and it is by definition fixed at all times. We can associate the physical distance d with the comoving distance χ through the following equation

$$d = a(t)\,\chi\,. \tag{1.37}$$

  Clearly, if we measure the physical distance at the present time t_0, then the two distances coincide since we can set $a(t_0) = 1$.

Using the definition of the comoving distance, we can write an alternative form for the FLRW metric (1.2). Introducing the following variable

$$r \equiv S(\chi) = \begin{cases} \sin\chi, & \text{for } k = +1, \\ \chi, & \text{for } k = 0, \\ \sinh\chi, & \text{for } k = -1\,, \end{cases} \tag{1.38}$$

we can easily redefine the FLRW metric as [297]

$$ds^2 = (c\,dt)^2 - a^2(t)\left[d\chi^2 + S^2(\chi)\left(d\theta^2 + \sin^2\theta\,d\phi^2\right)\right]\,. \tag{1.39}$$

For example for $k = +1$, the r coordinate is redefined as $r = sin\chi$ leading the spatial part of the invariant line element ds^2 to take the form

$$d\sigma^2 = d\chi^2 + \sin^2\chi(d\theta^2 + \sin^2\theta\,d\phi^2)\,, \tag{1.40}$$

which corresponds to the metric of a three dimensional sphere. So how can we associate the comoving distance with the scale factor $a(t)$? In any universe with a FLRW metric (such as ours) we derive the comoving distance to be

$$\chi = c\int_{t_E}^{t_0}\frac{dt}{a(t)} = c\int_{t_E}^{t_0}\frac{1}{a}\frac{dt}{da}da = c\int_{a(t_E)}^{a(t_0)}\frac{1}{a}\frac{1}{\dot{a}}da \xrightarrow[a(t_0)=1]{c=1} \chi = \int_0^z\frac{dz'}{H(z')}\,. \tag{1.41}$$

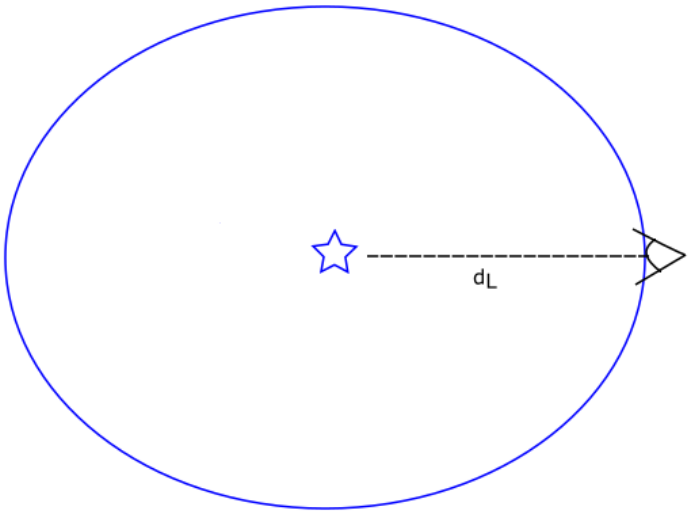

Figure 1.4: A graphic representation of the luminosity distance d_L of a distant astrophysical object.

Even though we can directly associate the comoving distance with the geometry through $H(z)$, the comoving distance is also a non observable quantity. Therefore, we are obligated to define two new quantities in terms of the comoving distance χ and then identify the geometry of the Universe through $H(z)$. These new observables are the luminosity distance d_L and the angular diameter distance d_A.

Suppose that we have an astrophysical distant object, such as a SnIa, that has a known intrinsic luminosity L which is constant in a spherical shell of radius d_L as it is demonstrated in Fig. 1.4. Measuring its flux f, we can define the luminosity distance d_L through the following relation [290, 298, 299]

$$f = \frac{L}{4\,\pi\,d_L^2}\,. \tag{1.42}$$

In a static Euclidean Universe, the luminosity distance would coincide with the actual distance from the astrophysical object. However, we know that we live in an expanding Universe described by the FLRW metric (1.38) [or equivalently (1.2)]. In this case, the energy of the incoming photons from the astrophysical object is reduced by a factor $\frac{a(t_0)}{a(t)}$ [290, 298, 299], so the flux f is written as

$$f = \frac{L}{4\,\pi\,a^2(t_0)\,S^2(\chi)\,(1+z)^2} \xrightarrow{a(t_0)=1} f = \frac{L}{4\,\pi\,S^2(\chi)\,(1+z)^2}\,. \tag{1.43}$$

Comparing (1.42) with (1.43), we easily derive that in the context of an expanding Universe, the luminosity distance is

$$d_L = S(\chi)\,(1+z) = \begin{cases} (1+z)\,\sin\chi, & \text{for } k=+1,\\ (1+z)\,\chi, & \text{for } k=0,\\ (1+z)\,\sinh\chi, & \text{for } k=-1 \end{cases} \tag{1.44}$$

where χ is given by (1.41).

Concerning the angular diameter distance d_A, we consider a distant astrophysical object with a known proper diameter l. Assuming that the studied object is perpendicular to the line

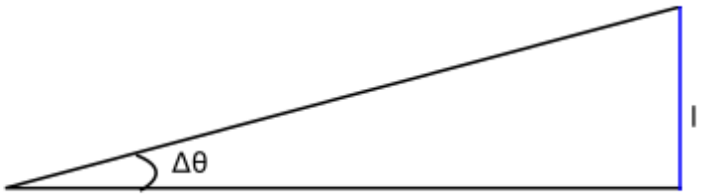

Figure 1.5: A graphic representation of the angular diameter distance d_A of a distant astrophysical object.

of sight as it is illustrated in Fig. 1.5, we can define that in a Euclidean space for small angles, the angular diameter distance is given by [290, 298, 299]

$$d_A \equiv \frac{l}{\Delta\theta}\,. \tag{1.45}$$

For the angular part of the FLRW metric we know that $l = a(t_E)\,S(\chi)\,\Delta\theta$ [290], so using Eq. (1.35), the definition (1.45) is written as

$$d_A = a(t_E)\,S(\chi) = a(t_0)\,\frac{a(t_E)}{a(t_0)}\,S(\chi) = a(t_0)\,\frac{S(\chi)}{1+z} \xrightarrow{a(t_0)=1} d_A = \frac{S(\chi)}{1+z}\,. \tag{1.46}$$

From (1.44) and (1.46) we can easily extract the relation that connects d_L with d_A which is known as the *distance duality relation* and has the following form

$$d_L = (1+z)^2\,d_A\,. \tag{1.47}$$

Clearly, since both the luminosity distance d_L and the angular diameter distance d_A depend on the comoving distance $S(\chi)$ they will differ for different cosmological models. Therefore, both of these distance are extremely helpful (geometrical) probes to identify the correct geometry of the Universe.

Regarding the dynamical probes, we focus on the linear matter overdensity growth factor. The linear matter growth factor is defined as

$$\delta \equiv \frac{\delta\rho_m}{\rho_m}\,, \tag{1.48}$$

with ρ_m describing the matter density and $\delta\rho_m$ corresponding to its first order perturbation. In the context of GR as well as in the majority of modified gravity theories, the evolution of the linear matter growth factor is given as [68, 172, 300–303]

$$\ddot{\delta} + 2H\dot{\delta} - 4\pi G_{\rm eff}\,\rho_m\,\delta \approx 0 \tag{1.49}$$

where $G_{\rm eff}$ is the effective Newton's constant, that for the GR case reduces to the usual Newton's constant $G_{\rm N}$ and in modified theories of gravity, it may depend on both the scale factor a and the scale k. In terms of the scale factor, Eq. (1.49) takes the following form

$$\delta''(a) + \left(\frac{3}{a} + \frac{H'(a)}{H(a)}\right)\delta'(a) - \frac{3}{2}\frac{\Omega_{\rm m,0}\,G_{\rm eff}(a,k)/G_{\rm N}}{a^5 H^2(a)/H_0^2}\,\delta(a) = 0\,, \tag{1.50}$$

where primes denote differentiation with respect to a and $\Omega_{\rm m,0}$ is the present value of the matter density parameter which we will discuss in detail in the following subsection. It is important to note that in Eq. (1.50) we neglect the neutrinos as well as the dark energy perturbations and that this equation is only valid on subhorizon scales. The effective Newton's constant emerges from generalizing Poisson's equation as [146, 147]

$$\nabla^2\phi \approx 4\pi G_{\rm eff}\rho_m\,\delta\,, \tag{1.51}$$

where ϕ is the perturbed metric potential in the Newtonian gauge defined via the perturbed FLRW metric [147, 304, 305]

$$ds^2 = (1+2\psi)dt^2 - a^2(1-2\phi)d\vec{x}^{\,2} \tag{1.52}$$

and ϕ, ψ are referred as Bardeen potentials [305]. Therefore, given a background $H(a)$, the matter density parameter $\Omega_{\rm m,0}$ and a parametrization for $G_{\rm eff}(a,k)/G_{\rm N}$, Eq. (1.50) can be solved either numerically or analytically and construct the theoretical prediction for the growth factor δ. Using the linear matter growth factor δ, the growth rate of perturbations

$$f(a) \equiv \frac{dln\delta(a)}{dlna}\,, \tag{1.53}$$

which can be used for the construction of the product

$$f\sigma_8(a) \equiv f(a)\cdot\sigma(a) = \frac{\sigma_8}{\delta(1)}\,a\,\delta'(a)\,, \tag{1.54}$$

where σ_8 is the density rms fluctuations within spheres of radius on scales of about $8h^{-1}\,Mpc$. This product is reported by various independent surveys that probe the growth rate of cosmological perturbations, so we have an immediate comparison between observations with different cosmological models.

1.3 Cosmological Models and Age of the Universe

The Friedmann equations (1.27) and (1.28) constitute a major tool, since they can be used for a large variety of cosmological models. Depending on the studied cosmological model, the Friedmann equations take different forms, leading to different solutions for the scale factor $a(t)$. The quantities that appear in Friedmann equations, ρ and p correspond in reality, to the total energy density and pressure. Hence, they can be written as sums of the contributions of the individual components as follows

$$\rho \equiv \rho_{total} = \sum_i \rho_i, \qquad\qquad p \equiv p_{total} = \sum_i p_i\,. \tag{1.55}$$

In this case, we can solve the continuity equation (1.22) for each individual contribution

$$\dot\rho + 3\frac{\dot a}{a}(\rho+p) = 0 \Rightarrow \dot\rho_i + 3\frac{\dot a}{a}(\rho_i+p_i) = 0 \xrightarrow{(1.23)} \dot\rho_i = -3\frac{\dot a}{a}\,\rho_i(1+w_i) \Rightarrow$$
$$\frac{d\rho_i}{\rho_i} = -\frac{3}{a}\,da\,(1+w_i) \overset{\int}{\Rightarrow} \rho_i(a) = \rho_{i,0}\left(\frac{a_0}{a}\right)^{3(1+w_i)}\,, \tag{1.56}$$

where $\rho_{i,0}$ describes the current density of each individual component and the sum symbols are neglected. As we know the basic ingredients of our Universe are the ordinary matter for which $w = 0$, the radiation for which $w = 1/3$ and if the dark energy corresponds to cosmological constant then $w = -1$. Therefore (1.56) for each case is written as

$$\rho = \begin{cases} \rho_{m,0} \left(\frac{a_0}{a}\right)^3, & \text{for matter} \\ \rho_{r,0} \left(\frac{a_0}{a}\right)^4, & \text{for radiation} \\ \rho_{\Lambda,0} \left(\frac{a_0}{a}\right)^0 \equiv \rho_\Lambda, & \text{for cosmological constant.} \end{cases} \tag{1.57}$$

Usually, the Friedmann equation (1.27) is expressed using dimensionless quantities that are called density parameters. Defining the critical density $\rho_{crit,0}$, *i.e.* the energy density of the cosmic fluid in a flat Universe, as

$$\rho_{crit,0} = \frac{3\,H_0^2}{8\,\pi\,G_{\rm N}}\,,$$

we can define the density parameters for each individual component via

$$\Omega_{\rm i,0} \equiv \frac{\rho_{i,0}}{\rho_{crit,0}} = \frac{8\,\pi\,G_{\rm N}}{3H_0^2}\rho_{i,0}\,. \tag{1.58}$$

Then, Eq. (1.27) (for $c = 1$) takes the form

$$H^2 = \frac{8\pi G_{\rm N}}{3}\rho - \frac{k}{a^2} + \frac{\Lambda}{3} \xrightarrow{(1.30)} H^2 = \frac{8\pi G_{\rm N}}{3}(\rho + \rho_\Lambda) - \frac{k}{a^2} \Rightarrow H^2 = H_0^2\Big[\Omega_{\rm r,0}\left(\frac{a_0}{a}\right)^4 + \\ +\Omega_{\rm m,0}\left(\frac{a_0}{a}\right)^3 + \Omega_{\rm k,0}\left(\frac{a_0}{a}\right)^2 + \Omega_{\Lambda,0}\Big] \xrightarrow{a_0=1} H^2 = H_0^2\left[\Omega_{\rm r,0}\,a^{-4} + \Omega_{\rm m,0}\,a^{-3} + \Omega_{\rm k,0}\,a^{-2} + \Omega_{\Lambda,0}\right]\,, \tag{1.59}$$

where we introduce the so called curvature density $\Omega_{\rm k,0} \equiv -k/(a_0\,H_0)^2$. The density parameters at present time obey the following relation

$$\Omega_{\rm r,0} + \Omega_{\rm r,0} + \Omega_{\rm k,0} + \Omega_{\Lambda,0} = 1\,. \tag{1.60}$$

The last two equations are extremely useful in Cosmology, since they can be used in order to calculate the form of the scale factor $a(t)$. In complicated systems the form of $a(t)$ is calculated numerically, but there is a number of special cases for specific values of the density parameters $\Omega_{\rm i,0}$ for which $a(t)$ can be solved analytically through Eq. (1.59). In general, we can divide the cosmological models in two broad categories. The ones where the contribution of the cosmological constant is zero ($\Omega_{\Lambda,0} = 0$) which are called *Friedmann models* and the ones with a non-zero cosmological constant ($\Omega_{\Lambda,0} \neq 0$) that are known as *Lemaitre models*.

1.3.1 Friedmann Models

All the Friedmann models have a big bang singularity at a finite time in the past and can be characterized by the fact that the predicted age of the Universe is less than the Hubble time, so [290]

$$t_0 < H_0^{-1}\,. \tag{1.61}$$

Analytical solutions can be derived for the following Friedmann cases:

- Dust Only Models: In this case, we set $\Omega_{\Lambda,0} = \Omega_{\mathrm{r},0} = 0$ in Eq. (1.59) and obtain

$$H^2 = H_0^2 \left[\Omega_{\mathrm{m},0}\, a^{-3} + \Omega_{\mathrm{k},0}\, a^{-2}\right] \xrightarrow{\times a^2} \dot{a}^2 = H_0^2 \left(\Omega_{\mathrm{m},0}\, a^{-1} + 1 - \Omega_{\mathrm{m},0}\right) .$$

Setting $\Omega_{\mathrm{m},0} = 1$, the solution is rather simple [290]

$$a(t) = \left(\frac{3}{2} H_0\, t\right)^{2/3} .$$

For such a universe it straightforward to calculate its age by fixing $t = t_0$ in the previous equation and solving it with respect to t_0. So, the current age of such a universe is [290]

$$t_0 = \frac{2}{3\, H_0} \Rightarrow t_0 \approx 9.3 \times 10^9 \,\text{years}\,,$$

an age significantly lower than the age of some of the oldest stars existing in some globular clusters. For the dust only models with $\Omega_{\mathrm{m},0} > 1$ and $\Omega_{\mathrm{m},0} < 1$ the scale factor is derived to be [290]

$$a = \frac{\Omega_{\mathrm{m},0}}{2(\Omega_{\mathrm{m},0} - 1)} \left(1 - \cos\psi\right),$$
$$a = \frac{\Omega_{\mathrm{m},0}}{2(1 - \Omega_{\mathrm{m},0})} \left(\cosh\psi - 1\right),$$

respectively, where ψ corresponds to the development angle. The $\Omega_{\mathrm{m},0} = 1$ case is known in the literature as the *Einstein–de-Sitter model*.

- Radiation Only Models: In a similar manner, we set $\Omega_{\Lambda,0} = \Omega_{\mathrm{m},0} = 0$ in Eq. (1.59) and obtain a similar equation as in the dust only models of the form

$$H^2 = H_0^2 \left[\Omega_{\mathrm{r},0}\, a^{-4} + \Omega_{\mathrm{k},0}\, a^{-2}\right] \xrightarrow{\times a^2} \dot{a}^2 = H_0^2 \left(\Omega_{\mathrm{r},0}\, a^{-2} + 1 - \Omega_{\mathrm{r},0}\right) .$$

Setting $\Omega_{\mathrm{r},0} = 1$ the solution that we obtain is also trivial [290]

$$a(t) = \left(2\, H_0\, t\right)^{1/2} ,$$

while solving with respect to $t = t_0$ as we did before, we compute the age of such a universe to be

$$t_0 = \frac{1}{2\, H_0} \Rightarrow t_0 \approx 7 \times 10^9 \,\text{years}\,,$$

an age that is even smaller than the one that we calculated for the dust only models. For $\Omega_{\mathrm{r},0} \neq 1$ the solution for the scale factor is [290]

$$a(t) = \left(2\, H_0\, \Omega_{\mathrm{r},0}^{1/2}\, t\right)^{1/2} \left(1 + \frac{1 - \Omega_{\mathrm{r},0}}{2\Omega_{\mathrm{r},0}^{1/2}}\, H_0\, t\right)^{1/2}$$

and the corresponding age of such a Universe is generalized to

$$t_0 = \frac{1}{H_0} \frac{1}{\Omega_{\mathrm{r},0}^{1/2} + 1}$$

1.3.2 Lemaitre Models

The Lemaitre Models correspond to models with $\Omega_{\Lambda,0} \neq 0$. In this subsection we will review the matter only models, *i.e.* models with $\Omega_{\mathrm{r},0} = 0$ that have embed a Big Bang origin and expand forever. This assumption is not far from the truth, since current observations suggest that the radiation density $\Omega_{\mathrm{r},0}$ is significantly lower than $\Omega_{\mathrm{m},0}$ or $\Omega_{\Lambda,0}$. However, the results can be easily extended to models with $\Omega_{\mathrm{r},0} \neq 0$.

Analytical solutions can be obtained for the following Lemaitre models:

- Matter Only Lemaitre Models: In this case, we set $\Omega_{\mathrm{r},0} = 0$ in Eq. (1.59) and calculate

$$H^2 = H_0^2 \left[\Omega_{\mathrm{m},0}\, a^{-3} + \Omega_{\mathrm{k},0}\, a^{-2} + \Omega_{\Lambda,0}\right] \xrightarrow{\times a^2} \dot{a}^2 = H_0^2 \left(\Omega_{\mathrm{m},0}\, a^{-1} + \Omega_{\mathrm{k},0} + \Omega_{\Lambda,0}\, a^2\right) \Rightarrow$$
$$\xrightarrow{(1.60)} \dot{a}^2 = H_0^2 \left(\Omega_{\mathrm{m},0}\, a^{-1} + \Omega_{\Lambda,0}\, a^2 + 1 - \Omega_{\mathrm{m},0} - \Omega_{\Lambda,0}\right) .$$

  This equation is rather complicated and the elliptic functions are needed for the solution of the integral, so we break the solution to small and large values of time. Doing so, we can easily solve the integral and acquire [290]

$$\begin{cases} a(t) = \left(\frac{3}{2}\, H_0 \sqrt{\Omega_{\mathrm{m},0}}\, t\right)^{3/2}, & \text{for small } t \\ a(t) \propto e^{H_0 \sqrt{\Omega_{\Lambda,0}}\, t}, & \text{for large } t\,. \end{cases}$$

- Spatially Flat Matter Only Models: In a similar manner, we set $\Omega_{\mathrm{r},0} = 0$ and $\Omega_{\mathrm{k},0} = 0$ in Eq. (1.59) and derive

$$H^2 = H_0^2 \left[\Omega_{\mathrm{m},0}\, a^{-3} + \Omega_{\Lambda,0}\right] \xrightarrow{\times a^2} \dot{a}^2 = H_0^2 \left(\Omega_{\mathrm{m},0}\, a^{-1} + \Omega_{\Lambda,0}\, a^2\right) .$$

  Solving the integral, we find the following two solutions for the cosmic time of such case [290]

$$t = \frac{2}{3\, H_0 \sqrt{|\Omega_{\Lambda,0}|}} \times \begin{cases} sinh^{-1}\left(\sqrt{\frac{a^3\,|\Omega_{\Lambda,0}|}{1-\Omega_{\Lambda,0}}}\right), & \text{for } \Omega_{\Lambda,0} > 0 \\ sin^{-1}\left(\sqrt{\frac{a^3\,|\Omega_{\Lambda,0}|}{1-\Omega_{\Lambda,0}}}\right), & \text{for } \Omega_{\Lambda,0} < 0\,. \end{cases}$$

  Inverting this equation, it is straightforward to obtain the solution for the scale factor.

However, not all the Lemaitre models have a Big Bang origin. In Fig. 1.6 we summarize various Lemaitre universes in the parametric space $(\Omega_{\mathrm{m},0}, \Omega_{\Lambda,0})$. In this graphic we have different dividing lines that split the graph in various regions, so depending on the different values of $\Omega_{\mathrm{m},0}$ and $\Omega_{\Lambda,0}$ we can identify useful properties for each universe case. The line that divides the "open-closed" universes has the following simple form [290]

$$\Omega_{\Lambda,0} = 1 - \Omega_{\mathrm{m},0}\,,$$

while the dividing line that splits the "accelerating-decelerating" universes is given by [290]

$$\Omega_{\Lambda,0} = \frac{\Omega_{\mathrm{m},0}}{2}\,.$$

The form of the other two lines (the "No Big Bang - Big Bang" and "Expand forever - Recollapse" lines) can be obtained after some tedious calculations (see Ref. [290] for more details).

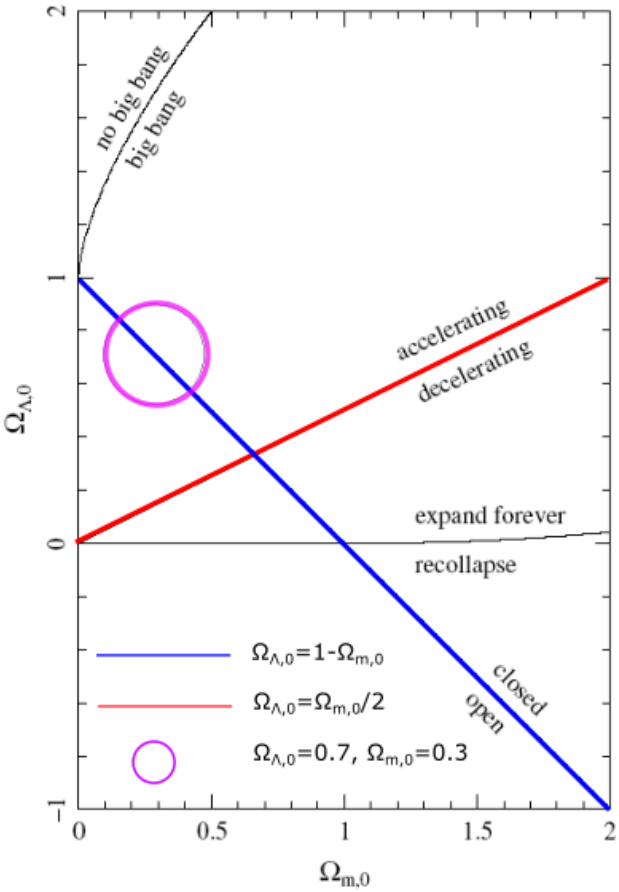

Figure 1.6: Different Lemaitre universes with matter and cosmological constant as a function of $\Omega_{\mathrm{m},0}$ and $\Omega_{\Lambda,0}$. The red line divides the accelerating with the decelerating universes, the blue line separates the open and closed universes, while the purple circle corresponds to our Universe (note also the additional black lines in "no Big Bang - Big Bang" and the "Expansion forever - Recollapse") that divide the graph. Partially adopted from Ref. [290]

Current observations indicate that $\Omega_{\mathrm{m},0} = 0.3$, $\Omega_{\Lambda,0} = 0.7$ and $\Omega_{\mathrm{k},0} = 0$ (the purple circle in Fig. 1.6) highly excluding the possibility that we live in a decelerating Universe. Moreover, it is clear that our Universe has a Big Bang origin and that it will expand forever in the future. "And what about the age of this kind of Universe?" In this case, assuming that the contribution from radiation is negligible, Eq. (1.59) is written as

$$H^2 = H_0^2 \left[\Omega_{\mathrm{m},0}\, a^{-3} + \Omega_{\Lambda,0}\right] \Rightarrow H^2 = H_0^2 \left[\Omega_{\mathrm{m},0}\, a^{-3} + (1 - \Omega_{\mathrm{m},0})\right] \Rightarrow$$
$$\Rightarrow \frac{da}{dt}\frac{1}{H_0} = \sqrt{\frac{\Omega_{\mathrm{m},0}}{a}}\sqrt{1 + \frac{1-\Omega_{\mathrm{m},0}}{\Omega_{\mathrm{m},0}}a^3} \overset{\int}{\Rightarrow} \int_0^a da' \frac{\sqrt{a'}}{\sqrt{\Omega_{\mathrm{m},0}}\sqrt{1 + \frac{1-\Omega_{\mathrm{m},0}}{\Omega_{\mathrm{m},0}}a'^3}} = H_0 \int_0^t dt\,, \quad (1.62)$$

where we used that $\Omega_{\mathrm{m},0} + \Omega_{\Lambda,0} = 1$. The integral of the left hand is quite complicated but it can be solved making the following change of variables

$$\frac{1 - \Omega_{\mathrm{m},0}}{\Omega_{\mathrm{m},0}}\, a^3 = x^3\,. \quad (1.63)$$

Then, we immediately derive that the age of the Universe is

$$t_0 = \frac{2}{3\,H_0\,\sqrt{1-\Omega_{\rm m,0}}}\,ln\left[\frac{\sqrt{1-\Omega_{\rm m,0}}+1}{\sqrt{\Omega_{\rm m,0}}}\right] \Rightarrow t_0 \approx 13.5\times 10^9\,{\rm years}\,, \tag{1.64}$$

assuming that $H_0 = 70\ {\rm km\,s^{-1}\,Mpc^{-1}}$.

1.4 Triumphs and Challenges of ΛCDM

Since 1998 an immense number of different cosmological data have provided evidence that support ΛCDM as the standard cosmological model [17, 18, 39–55]. The basic assumptions of ΛCDM include the viability of the Cosmological Principle and GR at cosmological scales, the existence of the Cold Dark Matter and of the cosmological constant as the driving force of the accelerated expansion of our Universe, the flatness of spacetime as well as the existence of a primitive rapid inflation phase that is essential to tackle the horizon, flatness and magnetic monopole problems [290, 306–310]. Furthermore, ΛCDM depends only on six basic parameters that have been significantly constrained by the Planck mission [18] and are illustrated in the following Table 1.1, where h is the dimensionless Hubble parameter defined as $H_0 = 100\,h\ {\rm km\,s^{-1}\,Mpc^{-1}}$.

Parameter	Name	Value
$\Omega_{\rm b,0}\,h^2$	Baryon Density	0.02237 ± 0.00015
$\Omega_{\rm c,0}\,h^2$	Cold Dark Matter Density	0.1200 ± 0.0012
$100\,\theta_{MC}$	Angular Size of the Sound Horizon at Recombination	1.04092 ± 0.00031
τ	Optical Depth	0.0544 ± 0.0073
$ln(10^{10}\,A_s)$	Amplitude of Curvature Primordial Perturbations	3.044 ± 0.014
n_s	Spectral Index	0.9649 ± 0.0042

Table 1.1: The values of the six independent parameters of ΛCDM constrained by the Planck mission [18] using the TT,TE,EE+lowE+lensing likelihoods. Based on the six independent parameters the best fits of the other parameters needed to describe our Universe can be calculated.

The six independent parameters of ΛCDM are the present value of the baryon density $\Omega_{\rm b,0}\,h^2$, the present value of the cold dark matter density $\Omega_{\rm c,0}\,h^2$, the angular size of the sound horizon at recombination $100\,\theta_{MC}$, the optical depth τ, the marginalized amplitude of curvature primordial perturbations $ln(10^{10}\,A_s)$ as well as the spectral index n_s. Based on these values, one can calculate basically all the other parameters, such as the present value of the matter density parameter $\Omega_{\rm m,0}$, the Hubble constant H_0 *etc.*, needed to describe our Universe.

However, despite its simplicity, consistency with the data and accurately predicting a variety of different phenomena, such as the accelerated expansion of the Universe [37, 38], the form and properties of the power spectrum of the Cosmic Microwave Background (CMB) [17, 18, 39], observations in the large scale regime [311], as well as the primordial abundances of light elements (hydrogen, deuterium, helium and lithium) [312–315], ΛCDM faces a number of challenges both at the theoretical and the observational level.

1.4.1 Theoretical Challenges

From the point of view of particle physics, the cosmological constant naturally emerges as an energy density of the vacuum, since both the cosmological constant and the vacuum energy present the same dynamical behaviour in the context of GR. In Quantum Field Theory (QFT) empty space is not empty, but it is composed of fundamental quantum fields that oscillate at different frequencies $\omega_{\vec{k}}$. These oscillations can be represented by Feynman loop diagrams that add an infinite amount of quantities to the total energy of a quantum system. The so called "ground state" of the vacuum in QFT, *i.e.* the state with zero real particles, can be characterized by an energy density of the form [60]

$$\rho_{vac} = \int \frac{d^3\vec{k}}{(2\pi)^3}\frac{\omega_{\vec{k}}}{2} = \frac{1}{2}\int_0^\infty \frac{d^3\vec{k}}{(2\pi)^3}\sqrt{k^2+m^2} = \frac{1}{4\pi^2}\int_0^\infty dk\, k^2\,\sqrt{k^2+m^2}\,. \tag{1.65}$$

However, we anticipate that the QFT calculation is valid up to a reasonable cut off scale, so the upper limit of the integral goes to a certain k_{max} value. Furthermore, we naturally except GR to be valid up to the Planck scale, hence we can also assume that $k_{max} = M_{pl} \equiv 8\,\pi\,G_{\rm N}^{-1} = 1.22\times10^{19}\,\text{GeV}$. In this case, the integral (1.65) is trivially solved to give [60]

$$\rho_{vac} \approx \frac{k_{max}^4}{16\,\pi^2} = \frac{M_{pl}^4}{16\,\pi^2} \Rightarrow \rho_{vac} \approx 10^{74}\,\text{GeV}^4\,, \tag{1.66}$$

where we used that for large k's, $\sqrt{k^2+m^2}\to\sqrt{k^2}=k$. Observationally, since the cosmological constant dominates at the present epoch we have [60]

$$\Lambda \approx H_0^2 \Rightarrow 8\,\pi\,G_{\rm N}\,\rho_\Lambda \approx H_0^2 \Rightarrow \rho_\Lambda \approx (H_0\,M_{pl})^2 \Rightarrow \rho_\Lambda \approx 10^{-47}\,\text{GeV}^4\,. \tag{1.67}$$

Comparing Eq. (1.66) with (1.67) one can see that ρ_{vac} is 10^{121} orders of magnitude larger than the observed value of ρ_Λ[4]. This is known as the *cosmological constant* (or *smallness*) *problem* [56–60] and remains up to date a major theoretical issue for ΛCDM.

Another theoretical problem is encountered when considering the matter energy density ρ_m and the cosmological constant energy density ρ_Λ. Even though ρ_m is evolving with redshift and ρ_Λ is constant, these totally independent quantities appear to be comparable (of the same order of magnitude) at present time. For this to happen, their ratio should be fine tuned to a very specific infinitesimal value in the early Universe. Unfortunately, ΛCDM offers no physical mechanism to explain this remarkable coincidence and the problem is referred to the bibliography as *cosmic coincidence problem* [61, 62].

Some authors in the field, discuss if these theoretical challenges constitute actual problems [316]. They appear to be problematic only if we consider that we could find ourselves with equal probability in any of the periods of the cosmic evolution. So, necessarily anthropic arguments enter the discussion and the anthropic principle is naturally considered to be a possible solution to these problems [95–98]. In the context of the anthropic principle, a group of different universes exists each one with a specific value of Λ. From this group, the universes with larger Λ than the observed do not form galaxies and as a result they do not have any intelligent life. Therefore, the most likely Universe that has intelligent life is the one that has a value of Λ that is big enough to form galaxies, *i.e.* our Universe.

[4] This difference significantly improves with the addition of other fields or in the context of Supersymmetry (see for instance Refs. [59, 60]).

1.4.2 Observational Challenges

Observationally, a number of different cosmological datasets analyzed in the last decade seem to prefer different values (at a level of 2σ or more) for some of the basic parameters of ΛCDM. The most important "tensions" of ΛCDM include the following (see Ref. [92] for a more extensive discussion on the subject):

- The H_0 Tension: This tension is the most statistically significant and refers to the mismatch of the value of the Hubble constant. Indirect measurements from the Planck mission from CMB data, Baryon Acoustic Oscillations (BAO) as well as uncalibrated SnIa data using the inverse distance ladder method in the context of a ΛCDM model calculate the Hubble constant to be $H_0 = 67.36 \pm 0.54\ \mathrm{km\,s^{-1}\,Mpc^{-1}}$ [18]. This value is in a 5σ level tension with the direct measurement published from Type Ia supernovae data, using the standard distance ladder method $H_0 = 73.04 \pm 1.04\ \mathrm{km\,s^{-1}\,Mpc^{-1}}$ [63]. Similar values with the direct measurement of SnIa data for the Hubble constant have been reported using Tully Fisher data [317,318], Type II supernovae data [319] as well as strong lens systems and time-delay measurements [64,320,321]. Nevertheless, H_0 measurements coming from a calibration of the Tip of the Red Giant Branch method (instead of the usual Cepheid calibration one) on SnIa data [322,323], HII galaxy measurements [324] as well as various low redshift data combinations [325] report a value that lies in the intermediate area of these two. Finally, recent independent measurements from gravitational waves give a Hubble constant value with significantly large errors, failing to tip the balance in favour of either side [326–329]. The H_0 measurements are summarized in Fig. 1.7.

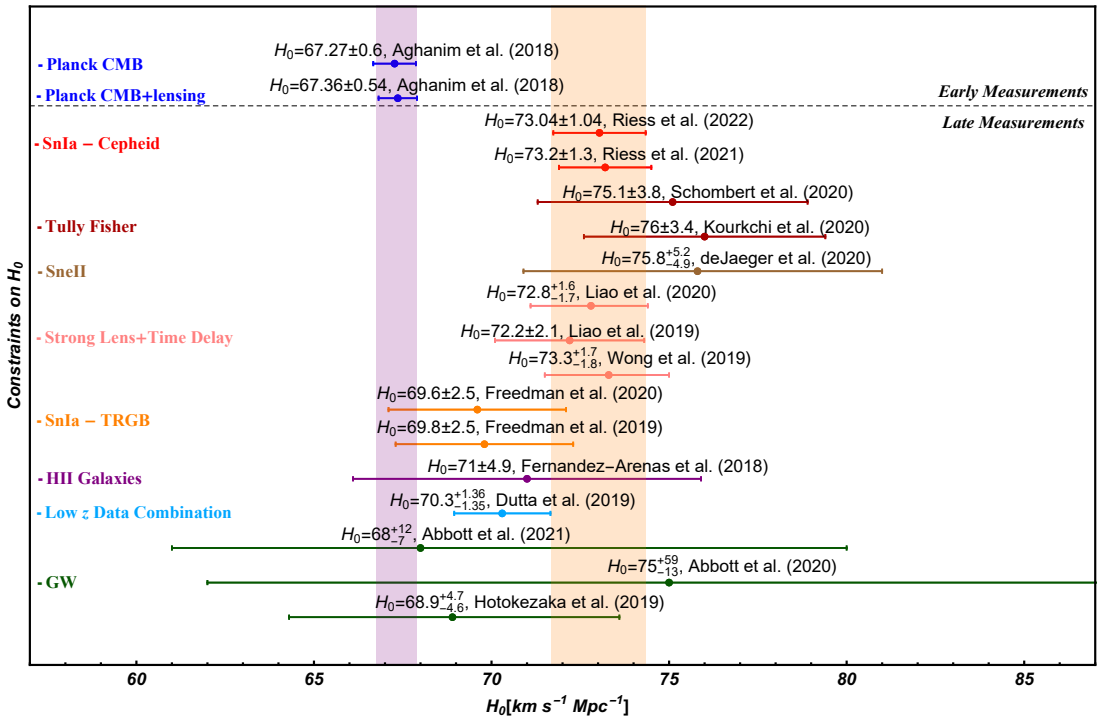

Figure 1.7: The Hubble constant H_0 constraints superimposed with the 1σ errors derived by different datasets (Partially adopted from Ref. [92]). For the reproduction of this figure visit the following dropbox link.

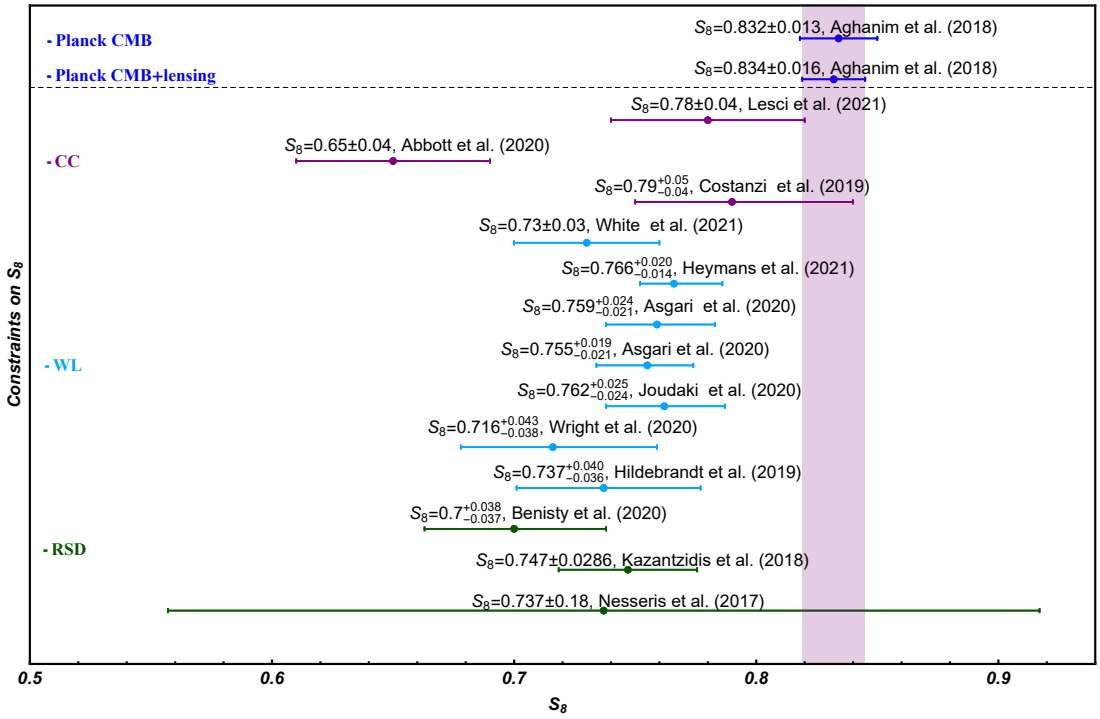

Figure 1.8: The S_8 constraints superimposed with the 1σ errors derived by different datasets (Partially adopted from Ref. [92]). For the reproduction of this figure visit the following dropbox link.

- The σ_8 or S_8 or Growth Tension: This is a milder tension and refers to mismatch of the values of the $\sigma_8/\Omega_{\rm m,0}$ parameters. Frequently, for convenience, the S_8 parameter is used that is defined as $S_8 \equiv \sigma_8 \sqrt{\Omega_{\rm m,0}/0.3}$, *i.e.* a combination of the present value of the matter density parameter and the root mean square density fluctuations. In particular, in the context of ΛCDM, dynamical probes such as the Weak Lensing (WL) [75–78, 80, 82, 330–334], the Redshift Space Distortions (RSD) [68, 70, 74] as well as Cluster Count (CC) data [53–55, 81, 335] predict lower values for S_8 compared to the corresponding values predicted by the CMB data and the Planck mission [18]. This tension is currently at a $2\sigma - 3\sigma$ level but it can reach the 5σ threshold, if the E_G statistic data are adopted [85]. The specific values from different probes are illustrated in the following Fig. 1.8.

- Low–High l CMB Power Spectrum Anomaly: Another mild anomaly that has been extensively discussed in the context of ΛCDM, is the mismatch of the best fit of the cold dark matter density parameter $\Omega_{\rm c,0}\, h^2$ that is derived using high ($l > 1000$) and low multipoles ($l < 1000$). This tension is currently at a 2.5σ level [336, 337] and seems to be relaxed if one introduces by hand the phenomenological parameter A_L, that changes the level of lensing in the power spectrum. In the context of ΛCDM, this phenomenological parameter should take the value $A_L = 1$, but the Plank mission reports a value of $A_L = 1.243 \pm 0.096$ [337].

- BAO Low-High z Anomaly: This anomaly is at a similar level with the low l–high l CMB power spectrum tension and corresponds to the predicted value of $\Omega_{\rm m,0}$ obtained by Ly-α BAO that is $\Omega_{\rm m,0} \approx 0.19 \pm 0.7$ for $z > 2.4$, while galaxy BAO measurements for $z < 0.6$ support $\Omega_{\rm m,0} \approx 0.37 \pm 0.7$ [338, 339].

Of course, a possible explanation for these tensions would be the existence of some unknown systematic effect which affects the results. However, if this is not true, we have severe observational evidence that ΛCDM should be extended to a more complete theory of gravity which will be free of these problems. Moving towards this direction a vast variety of ideas have been proposed as possible solutions to address the aforementioned (theoretical or observational) tensions.

These physical mechanisms, include dynamical dark energy models [99–105], running vacuum models in which the vacuum energy density is a time dependent quantity [106–114], theories where some sort of scalar field represents the dark energy (*e.g.* quintessence dark energy models [115–130], phantom dark energy models [131–136], k-essence dark energy models [137, 138], scalar tensor theories [139–150] *etc.*) or some sort of a perfect fluid (*e.g.* Chaplygin gas [151–155]), modified theories of gravity that may depend on the Ricci scalar R [156–158, 160, 161, 168, 170, 172, 173], or on the torsion T [181–190], or even more complicated modifications such as extra dimensions [191–193], braneworld models [194, 195, 199], Brans Dicke models [203], interacting dark energy with dark matter models [204–211], interacting dark matter with neutrinos [212], holographic dark energy models [213–216], early dark energy models [217–223], decaying dark matter models [224], and many more. Nevertheless, none of them, up to date, provide a solution that naturally explains the accelerated expansion of the Universe as well as providing a more fundamental mechanism to resolve the aforementioned problems of the concordance model. Perhaps ΛCDM is a limiting case of a more complete theory of gravity.

1.5 ΛCDM Alternative Theories

In this section we present some of the most well known alternative theories that deviate from its theoretical framework and have been proposed over the years in an attempt to better handle the challenges of ΛCDM. Obviously, the alternative theories should not depart far from it due to the tremendous success of ΛCDM in explaining most of the cosmological observations.

1.5.1 Dynamical Dark Energy Models

The most obvious extension of ΛCDM corresponds to a dark energy component, where the energy density ρ_{DE} presents a dynamical evolution and obeys the usual continuity equation

$$\dot{\rho}_{DE} + 3H\,\rho_{DE}\,(1 + w_{DE}) = 0\,. \tag{1.68}$$

Clearly, it is possible to construct many complex forms for w_{DE}, but in this section our goal is just to review the simplest cases, namely the wCDM and the Chevallier-Polarski-Linder (CPL) [101, 103] dark energy models (for more complicated forms of w_{DE} see *e.g.* Refs. [340, 341]). Common feature of the studied dark energy models are that they also share the fine tuning problem of ΛCDM, but the extra degrees of freedom may explain the accelerated expansion of the Universe in a more natural way.

The first of them corresponds to a model with a constant equation of state parameter $w_{DE} \equiv w$ that differs from the concordance one, since $w \neq w_\Lambda = -1$. For $w = -1$ this model reduces to the standard one and in the context of a flat Universe, the Hubble parameter for wCDM takes the form

$$H(z) = H_0\sqrt{\Omega_{\mathrm{m},0}(1+z)^3 + \Omega_{\mathrm{r},0}(1+z)^4 + (1 - \Omega_{\mathrm{m},0} - \Omega_{\mathrm{r},0})\,(1+z)^{3(1+w)}}\,. \tag{1.69}$$

Another quite interesting dark energy parametrization, corresponds to the CPL model. This model assumes a slowly varying equation of state of the form

$$w_{DE}(z) = w_0 + w_1 \frac{z}{1+z} \,. \tag{1.70}$$

For this model we have two degrees of freedom instead of one and this parametrization has the advantage that the equation of state does not increase indefinitely with redshift. The Hubble parameter for this case is the following

$$H(z) = H_0 \sqrt{\Omega_{\mathrm{m},0}(1+z)^3 + \Omega_{\mathrm{r},0}(1+z)^4 + (1-\Omega_{\mathrm{m},0}-\Omega_{\mathrm{r},0})\,(1+z)^{3(1+w_0+w_1)} e^{-3\frac{w_1 z}{1+z}}} \,. \tag{1.71}$$

There is no good reason to believe that these purely phenomenological parametrizations approach the real form of dark energy, but due to their simplicity, they have been extensively used in the literature as baseline models before advancing to more sophisticated dark energy forms for the equation of state.

1.5.2 Modified Matter Models

This class of models [342] adopts GR at cosmological scales and attributes the observed accelerated expansion of the Universe to a dark energy component with negative pressure. Since GR is considered to be a valid theory, the Einstein's Field Equations (1.13) that were derived from the Einstein Hilbert action determine the dynamics of the Universe. However, the right hand side of (1.13) is slightly different because the energy momentum tensor $T_{\mu\nu}$ is altered to include the dark energy component with the negative pressure. Important examples of this class include (but not limited to) the quintessence dark energy models [115–130], the phantom dark energy models [131–136], k-essence models [137, 138], chaplygin gas models [151–155], topological defects [225–227] *etc.* In this subsection we focus on the first three examples and we briefly outline the main characteristics of each one below.

1.5.2.1 Quintessence/Phantom Dark Energy Models

In the Quintessence dark energy models, the role of the dark energy that drives the accelerated expansion is embodied by a scalar filed ϕ, with a corresponding slowly varying potential $V(\phi)$. In particular, the energy density of the scalar field ρ_ϕ is evolving slowly (due to its dependence from the potential) until it dominates, generating the observed accelerated expansion. The total action for this case is given as [130, 343]

$$S_{tot} = S_{EH} + S_\phi = \int d^4x \sqrt{-g} \left[\frac{1}{2\kappa} R + \frac{1}{2} g^{\mu\nu}\, \partial_\mu \phi\, \partial_\nu \phi - V(\phi) + \mathcal{L}_{matter} \right] . \tag{1.72}$$

Following the stationary action principle, we find the energy momentum tensor of the scalar field ϕ to be

$$T_{\mu\nu} = \partial_\mu \phi\, \partial_\nu \phi - g_{\mu\nu} \left[\frac{1}{2} g^{\alpha\beta} \partial_\alpha \phi\, \partial_\beta \phi - V(\phi) \right] . \tag{1.73}$$

From (1.73), the energy density ρ_ϕ and the pressure of the scalar field p_ϕ can be inferred leading to an equation of state parameter of the form [130, 343]

$$w_\phi = \frac{p_\phi}{\rho_\phi} = \frac{\frac{1}{2}\dot{\phi}^2 - V(\phi)}{\frac{1}{2}\dot{\phi}^2 + V(\phi)} \,. \tag{1.74}$$

In the context of a flat FLRW metric, the scalar field obeys the following Klein-Gordon

$$\ddot{\phi} + 3H\,\dot{\phi} + \frac{dV}{d\phi} = 0 \tag{1.75}$$

In order to produce the accelerated expansion of the Universe, the condition $w_\phi < -1/3$ should be satisfied which entails that $\dot{\phi}^2/2 \ll V(\phi)$ and that the scalar field also violates the strong energy condition [343]. Clearly, the form of the potential $V(\phi)$ defines the way that the scalar field reproduces the accelerated expansion of the Universe. Hence, over the years, many forms for the potential forms have been studied [115, 116, 124, 125, 343–348] and some of them have the ability to explain the cosmological data with great efficiency and more effectively than ΛCDM. However, quintessence models are not without shortcomings. The most severe and puzzling drawback for this class of models is that they share the same fine tuning problem as ΛCDM. The required energy density today is $\rho_\phi \approx 10^{-47}\,\mathrm{GeV}^4$, corresponding to a particle with a mass $m_\phi \approx 10^{-33}\,\mathrm{eV}$, a value many order of magnitudes smaller than any known particle [60, 341].

The phantom dark energy models are identical to the quintessence dark energy models but with a negative kinetic term [343]. Therefore, changing the kinetic term sign in Eq. (1.72), it is straightforward to show that the equation of state parameter takes the form

$$w_\phi = \frac{p_\phi}{\rho_\phi} = \frac{-\frac{1}{2}\dot{\phi}^2 - V(\phi)}{-\frac{1}{2}\dot{\phi}^2 + V(\phi)}\,. \tag{1.76}$$

A characteristic of the phantom dark energy models is that the energy density keeps growing with time leading to even more acceleration and an equation of state parameter $w_\phi < -1$, a value that is not excluded by current observational data (*e.g.* the Planck mission reports $w = -1.028 \pm 0.031$ for a combination of CMB, SnIa and BAO data [18]). This value leads the Universe to a Big Rip singularity in the far future, *i.e.* a state that the Universe (even atoms) is ripped apart and physical laws break [343, 349].

1.5.2.2 k-Essence Dark Energy Models

Another interesting class of the modified matter models that we briefly discuss is the k-essence class of dark energy models. The action of the k-essence models is in general given by [350]

$$S_{tot} = S_{EH} + S_\phi = \int d^4x\,\sqrt{-g}\left[\frac{1}{2\kappa}R + p(\phi, X) + \mathcal{L}_{matter}\right]\,, \tag{1.77}$$

where $p(\phi, X)$ is a general function of the kinetic term of the scalar field $X = \frac{1}{2}g^{\mu\nu}\,\partial_\mu\,\phi\,\partial_\nu\,\phi$. Following the stationary action principle, the energy momentum tensor of the scalar field is

$$T_{\mu\nu} = \frac{dp}{dX}\,\partial_\mu\,\phi\,\partial_\nu\,\phi + g_{\mu\nu}\,p\,, \tag{1.78}$$

leading to an equation of state parameter of the form [350]

$$w_\phi = \frac{p_\phi}{\rho_\phi} = \frac{p}{2X\,\frac{dp}{dX} - p}\,. \tag{1.79}$$

In order to achieve $w_\phi \approx -1$, as it is indicated by the cosmological data, the condition $|2X\,\frac{dp}{dX}| \ll |p|$ should be satisfied. However, even the k-essence models constructed to solve some issues of ΛCDM, such as the coincidence problem face other challenges *e.g.* lead to a sound speed of the field that is superluminal [350].

1.5.3 Modified Gravity Models

The third class that we briefly review, corresponds to modified gravity models. In contrast to modified matter models, the modified gravity models attribute the accelerated expansion of the Universe to modifications of GR leading to alternative descriptions of gravity itself. Prominent examples of this class of models include (but not limited to) scalar tensor theories [139–150], $f(R)$ gravity theories [156–180], $f(T)$ gravity theories [181–190], braneworld models [194–202], inhomogeneities [261–266,283,351–358] mainly in the context of Lemaıtre-Tolman-Bondi models [359–361], massive gravities [362–365] *etc.* As in the previous subsection we briefly discuss the main characteristics of the first three below.

1.5.3.1 Scalar Tensor Theories

An important class of modified gravity theories that remain a viable possibility for the explanation of the observed accelerated expansion of the Universe are the scalar tensor theories. These theories have all the advantages of the quintessence dark energy models but have the additional advantage of a more natural explanation for the physical origin of the scalar field. In particular, the scalar field ϕ with a corresponding potential $V(\phi)$, is non-minimally coupled with gravity, a characteristic that naturally emerges in Supergravity or M theories [366, 367].

Throughout this thesis, we will focus on the most general form of the scalar tensor theories (up to two derivatives) that was firstly presented in Refs. [146, 147]. In this case, the scalar field dependence is given by an arbitrary function $F(\phi)$ and the corresponding action has the following form [146, 147]

$$S_{ST} = \int d^4x\sqrt{-g}\left[\frac{F(\phi)}{2}R - \frac{1}{2}\,Z(\phi)\,g^{\mu\nu}\partial_\mu\phi\partial_\nu\phi - V(\phi)\right] + S_m\,, \tag{1.80}$$

where R is the Ricci scalar, S_m is the matter action term of some arbitrary matter source and the arbitrary functions $F(\phi)$ and $Z(\phi)$ determine the dynamics of the scalar field along with its potential. This form includes a wide variety of different theories, such as the classical Brans Dicke model for $F(\phi) = \phi$ and $Z(\phi) = \omega_{BD}/\phi$, or some $f(R)$ theories is the arbitrary function depends also in the Ricci scalar. The simplest choice corresponds to $Z(\phi) = 1$ and $F(\phi)$ to remain arbitrary [147], which will adopt throughout the present thesis. However, despite its arbitrariness, the function $F(\phi)$ needs to be consistent with observations. Therefore, from solar system observations we have that $dF/d\phi < 4\times10^{-4}$, while at the same time $F(\phi)$ should be positive so that gravitons have positive energy.

In the context of a homogeneous scalar field and a flat FLRW metric, the corresponding dynamical equations derived using the stationary action principle are [146]

$$3F(\phi)\,H^2 = \rho_m + \frac{\dot\phi^2}{2} + V(\phi) - 3H\,\dot F\,, \tag{1.81}$$

$$-2F(\phi)\,\dot H = \rho_m + \dot\phi^2 + \ddot F - H\dot F\,, \tag{1.82}$$

$$\ddot\phi + 3\frac{\dot a}{a}\dot\phi - 3\,\dot H\,\frac{dF}{d\phi} + \frac{dV}{d\phi} = 0\,. \tag{1.83}$$

Usually, the first two equations are expressed in terms of the redshift. So, eliminating the potential from Eqs. (1.81) and (1.82), we find [147, 150]

$$\left(\frac{d\phi}{dz}\right)^2 = -\frac{d^2F}{dz^2} - \left[\frac{dlnH}{dz} + \frac{2}{1+z}\right]\frac{dF}{dz} + 2\frac{\frac{dlnH}{dz}}{1+z}F - 3(1+z)\,\Omega_{\rm m,0}\left(\frac{H_0}{H}\right)^2 F_0\,, \tag{1.84}$$

where F_0 corresponds to the present value of $F(\phi)$. Finally, in scalar tensor theories, as in all modified gravity theories, the effective Newton's constant $G_{\rm eff}$ presents a dynamical evolution. For the action (1.80), $G_{\rm eff}$ is given as

$$G_{\rm eff}(z) = G_{\rm N}\left[\frac{1}{F(z)}\frac{F(z)+2\left(\frac{dF}{d\phi}\right)^2}{F(z)+\frac{3}{2}\left(\frac{dF}{d\phi}\right)^2}\right] \tag{1.85}$$

1.5.3.2 $f(R)$ Gravity Theories

The second class that we briefly discuss corresponds to $f(R)$ gravity theories. This class of theories generalizes the Ricci scalar of the Einstein-Hilbert action to a more general function $f(R)$. This form is preferred over more complicated forms that include higher order curvature invariants (*e.g.* $R_{\mu\nu}R^{\mu\nu}$) to avoid the Ostrogradski instability [170, 368]. So, the general action for the $f(R)$ modified theories of gravity is the following [161, 170, 176]

$$S_{f(R)} = \frac{1}{2\kappa}\int d^4x\sqrt{-g}\, f(R) + S_m\,, \tag{1.86}$$

where S_m is the matter action term of some arbitrary matter source. In the context of a flat FLRW metric, the corresponding dynamical equations derived using the stationary action principle are[5]

$$3H^2\frac{df}{dR} - \frac{\frac{df}{dR}R - f}{2} + 3H\frac{d^2f}{dR^2}\dot{R} = 8\,\pi\,G_{\rm N}\,\rho_m\,, \tag{1.87}$$

$$-2\frac{df}{dR}\dot{H} = 8\,\pi\,G_{\rm N}\,\rho_m + \frac{d^2}{dt^2}\left(\frac{df}{dR}\right) + H\frac{d}{dt}\left(\frac{df}{dR}\right)\,. \tag{1.88}$$

Of course for $f(R) = R - 2\Lambda$ we revert to the usual ΛCDM case.

However, not all $f(R)$ models are viable [168–170]. Similar to what we considered in scalar tensor theories, the gravitons should have positive energy leading to the condition $df/dR > 0$. Furthermore, in this case we have the additional condition $d^2f/dR^2 > 0$ in order to ensure the stability of scalar perturbations, since the mass of the $f(R)$ gravity model is approximated as [169]

$$M^2_{f(R)} \approx \frac{1}{3}\left(\frac{d^2f}{dR^2}\right)^{-1}\,. \tag{1.89}$$

Even though these two stability conditions limit the eligible $f(R)$ forms, a plethora of alternatives have been studied. Two of the most popular models include the Hu-Sawicki [168] and the Starobinski $f(R)$ models [169]. These models not only satisfy the above conditions but they can provide at the same time accurate predictions for the presence of matter era, the current accelerated expansion as well as the stability of cosmological perturbations.

[5] It is important to note here that two different approaches are followed in the literature to extract the dynamical equations from the action (1.86). The first one is the metric formalism and the second one is the Palatini formalism where the Christoffel symbols and the metric tensor are considered independent quantities. These two methods in the context of $f(R)$ theories are non equivalent at the level of the equations of motion. In the present thesis we choose to adopt the usual metric formalism. For an extensive discussion on this subject see Ref. [170].

Despite the similar predictions between ΛCDM and viable $f(R)$ theories they have some key differences, such as the nature of Newton's constant. In the context of the $f(R)$ theories, the effective Newton's constant under the sub-horizon/quasi-static approximation is calculated to be [300]

$$G_{\rm eff}(k,z) = G_{\rm N}\left\{\left(\frac{df}{dR}\right)^{-1}\left[\frac{1+4\left(\frac{d^2f}{dR^2}/\frac{df}{dR}\right)\cdot k^2\,(1+z)^2}{1+3\left(\frac{d^2f}{dR^2}/\frac{df}{dR}\right)\cdot k^2\,(1+z)^2}\right]\right\}\,. \tag{1.90}$$

Therefore, considering a specific form for $f(R)$ we can easily derive the corresponding dynamical equations as well as the effective Newton's constant for each $f(R)$ form, using the above formulas.

1.5.3.3 $f(T)$ Gravity Theories

Another class of models that has gained a lot of attention over the years is $f(T)$ gravity theories. In this class, instead of the Ricci scalar R, the geometry manifests itself with the torsion T. So, similarly to $f(R)$ gravity theories where the Ricci scalar is promoted to an arbitrary function $f(R)$, in $f(T)$ gravity theories the torsion T is promoted to an arbitrary function $f(T)$.

In $f(T)$ gravities it is convenient instead of the metric tensor $g_{\mu\nu}$, to use the vierbeins fields $\mathbf{e}_A(x^\mu)$ that at each point of the manifold form an orthonormal basis for the tangent space [186, 369]

$$\mathbf{e}_A\cdot\mathbf{e}_B = \eta_{AB} = diag(1,-1,-1,-1)\,. \tag{1.91}$$

In coordinate basis, the vierbeins fields are expressed as $\mathbf{e}_A = e^\mu_A\partial_\mu$, leading to a metric of the following form

$$g_{\mu\nu}(x) = \eta_{AB}\,e^A_\mu(x)\,e^B_\nu(x)\,. \tag{1.92}$$

Now, introducing the curvature-less Weitzenböck connection as

$$\overset{\mathbf{w}}{\Gamma}{}^\lambda_{\nu\mu} \equiv e^\lambda_A\,\partial_\mu e^A_\nu\,,$$

the torsion tensor can be defined as [186]

$$T^\lambda_{\mu\nu} = \overset{\mathbf{w}}{\Gamma}{}^\lambda_{\nu\mu} - \overset{\mathbf{w}}{\Gamma}{}^\lambda_{\mu\nu} = e^\lambda_A\left(\partial_\mu e^A_\nu - \partial_\nu e^A_\mu\right). \tag{1.93}$$

Using Eq. (1.93), it is straightforward to construct the torsion scalar

$$T \equiv \frac{1}{4}T^{\rho\mu\nu}\,T_{\rho\mu\nu} + \frac{1}{2}T^{\rho\mu\nu}\,T_{\nu\mu\rho} - T_{\rho\mu}{}^\rho\,T^{\nu\mu}_{\ \ \nu}\,, \tag{1.94}$$

that is utilized for various $f(T)$ models.

The most commonly used action for the $f(T)$ theories of gravity corresponds to [183, 186]

$$S = \frac{1}{2\kappa}\int d^4x\,e\,\left[T + f(T)\right] + S_m\,, \tag{1.95}$$

where $e \equiv \sqrt{-g}$ and S_m corresponds to the matter action term of some arbitrary matter source. In the context of a flat FLRW metric and using the stationary action principle (varying this

time with respect to the vierbeins) the corresponding dynamical equations are [183, 186]

$$H^2 = \frac{8\,\pi\,G_{\rm N}}{3}\rho_m - \frac{f}{6} + \frac{T\,f_T}{3}\,, \tag{1.96}$$

$$\dot{H} = -\frac{4\,\pi\,G_{\rm N}\,\rho_m}{1 + df/dT + 2T\,d^2f/dT^2}\,, \tag{1.97}$$

with $T = -6H^2$. Finally, from (1.96), one can define the corresponding energy density and pressure, leading to an equation of state parameter of the form [183, 186]

$$w = -\frac{f/T - df/dT + 2T\,d^2f/dT^2}{[1 + df/dT + 2T\,d^2f/dT^2]\,[f/T - 2\,df/dT]}\,. \tag{1.98}$$

Obviously for $f(T) = -2\Lambda$, we revert to the usual ΛCDM case.

1.5.4 "Tilted" Universes

Another quite interesting approach that has been discussed in the literature [370–372], corresponds to the concept of the "tilted Universe". These types of cosmological models are equipped with two families of observers. The first one, follows the smooth Hubble expansion, whereas the second family of observers live in a galaxy in the interior of a bulk flow that moves with respect to the Hubble flow with a non relativistic peculiar velocity. With the term bulk flow we mean large regions of a few hundred Mpc which move coherently with a velocity of a few hundred km/s [373–376]. The observers that follow the smooth Hubble expansion are the fictitious (idealised) observers while the other observers are called tilted. Even though the majority of the other solutions ignore peculiar velocities, in this class of cosmological models the peculiar motions play a key role and can successfully reproduce both the early deceleration and the late acceleration phases of the Universe as we discuss in the current Subsection.

Suppose that the fictitious observers have a four-velocity u_a that is normalised as $u^a u_a = -1$, the tilted observers have a four-velocity $\tilde{u}_a$ that is normalised as $\tilde{u}_a\tilde{u}^a = -1$ and that $\tilde{v}_a$ which is normalised as $\tilde{v}^2 = \tilde{v}_a\tilde{v}^a \ll 1$ corresponds to the peculiar velocity of the tilted observers with respect to the Hubble flow. Then, the three velocities are connected through the reduced Lorentzian boost [370]

$$\tilde{u}_a = u_a + \tilde{v}_a\,. \tag{1.99}$$

The mean kinematics of the observers are determined by their volume scalar of motion, namely their expansion/contraction rate. Adopting the 1+3 covariant approach [377–380], the spatial divergence of Eq. (1.99) gives [381]

$$\tilde{\Theta} = \Theta + \tilde{\theta}\,, \tag{1.100}$$

in the linear regime, with $\Theta = \mathrm{D}^a u_a$, $\tilde{\Theta} = \tilde{\mathrm{D}}^a\tilde{u}_a$ and $\tilde{\theta} = \tilde{\mathrm{D}}_a\tilde{v}_a$. Although $\tilde{\Theta}$ and Θ are always positive, this is not the case for $\tilde{\theta}$ which can be either positive or negative corresponding to expanding or contracting bulk flows respectively.

Hence, it is clear that the measured expansion rates in the two frames may differ simply due to their relative motion. As a result, these differences affect the measurement of the deceleration parameter in the two frames. Denoting the deceleration parameter of the fictitious observer as q and of the tilted observer as $\tilde{q}$, then it is straightforward to show, after some algebra, that the two quantities are connected through [370–372]

$$\tilde{q} = q + \frac{1}{9}\left(\frac{\lambda_H}{\lambda}\right)^2\frac{\tilde{\theta}}{H}\,, \tag{1.101}$$

where $\lambda_H = 1/H$ is the Hubble radius and λ corresponds to the size of the bulk flow. It is important to note that the second term of Eq. (1.101) is a correction that emerges only when the peculiar motions are taken into consideration. So, in principle, it is possible for the fictitious observer to measure positive values of q, while the tilted one measures negatives values of $\tilde{q}$. This indicates that the tilted observers may believe that they live in an accelerating Universe, while in reality the Universe is decelerating. This is only a local effect and happens due to the presence of the peculiar motions.

From (1.101) it is easy to define the transition scale λ_T, *i.e.* the scale in which the sign of $\tilde{q}$ changes as [382]

$$\lambda_T = \sqrt{\frac{1}{9q}\frac{|\tilde{\theta}|}{H}}\lambda_H \,, \tag{1.102}$$

which is called "the peculiar Jeans length" (the name is given due to its similarity with the standard Jeans length). On scales well inside this length, the peculiar velocities dominate over the background expansion. Focusing on contracting bulk flows where $\tilde{\theta} < 0$, then Eqs. (1.101) and (1.102) are easily combined to give

$$\tilde{q} = q\left[1 - \left(\frac{\lambda_T}{\lambda}\right)^2\right] . \tag{1.103}$$

So, the value of $\tilde{q}$ is actually determined by the form of the local volume scalar $\tilde{\theta}$. In the previous equations, the form of $\tilde{\theta}$ is considered to be constant. However, it is only natural to expect it to be a scale dependent expression. More specifically, we anticipate the value of $\tilde{\theta}$ to decrease as λ increases and when dealing with contracting bulk motions, we expect faster contraction rates near the outskirts of the flow and slower towards its center. These qualitative characteristics can be parametrised by the form [383]

$$\tilde{\theta} = \tilde{\theta}(\lambda) = \frac{m\,\lambda^2}{p + r\,\lambda^3} \,, \tag{1.104}$$

where m, p and r correspond to free parameters. Substituting this equation in Eq. (1.103) we deduce

$$\tilde{q} = \tilde{q}(\lambda) = \frac{1}{2}\left(1 - \frac{m}{p + r\,\lambda^3}\right) , \tag{1.105}$$

with the term $1/2$ in front of the parenthesis corresponds to a decelerating Universe measured in the Hubble frame. This form is quite useful since after some rearrangement, it can be directly confronted with cosmological data. In particular, following the analysis of Ref. [383] one can set $\lambda \equiv \bar{\chi}(z)$, where $\bar{\chi}(z)$ describes the line-of-sight comoving distance (1.41) and construct the evolution of the Hubble rate via [384]

$$H(z) = H_0 \exp\left[\int_0^z \left[\frac{1 + q(u)}{1 + u}\right] du\right] \tag{1.106}$$

and then, substituting the derived formula to the luminosity distance (1.44). Interestingly, in Ref. [383] this procedure is followed and using SnIa data the derived results indicate that the tilted cosmological models may perform similar to the standard ΛCDM paradigm.

In the present thesis, we focus on deviations from the standard ΛCDM paradigm. We study different cosmological data and perform appropriate statistical tests that have the ability to discriminate between the standard concordance model and alternatives theories. In particular:

- In Chapter 2, we focus on the growth tension and use up to date RSD data in order to construct an extensive compilation of 63 datapoints. Utilizing this compilation, we study a phenomenological parametrization for $G_{\rm eff}/G_{\rm N}$ and extract useful information regarding its best fit parameters, indicating a $4\sigma - 5\sigma$ deviation from the ΛCDM case as well as a decreasing form of $G_{\rm eff}/G_{\rm N}$ at low redshifts z. Furthermore, we study viable modified theories, such as the $f(R)$ and scalar tensor theories and show that such a decreasing form can not be realized in the context of a ΛCDM background. Finally, we impose strong constraints for the phenomenological parametrization $G_{\rm eff}/G_{\rm N}$ using the Planck15/ΛCDM CMB low l data.

- In Chapter 3, we determine the constraining power of a wide range of cosmological observables on cosmological parameters, showing that is not monotonically increasing but is a varying function of the redshift instead that exhibits degeneracy points (redshift blind spots) and maxima (optimum redshift ranges). As a result, we consider the up to date compilation of RSD data of the previous Chapter, an up to date compilation of BAO points, as well as recent SnIa and standard gravitational wave sirens data in order to identify the corresponding redshift blind spots and the optimum redshift ranges for specific relevant observables and parameters.

- In Chapter 4, we perform a tomographic analysis of the Pantheon SnIa focusing on the best fit value of the absolute magnitude M and/or Hubble constant H_0 in the context of a ΛCDM background. Considering only the statistical uncertainties, we show that in the low redshift regime ($z \lesssim 0.2$) a local variation at the 2σ level with respect to the best fit value indicated by the full dataset is observed that can be either due to a local matter underdensity with $\delta\rho_0/\rho_0 \simeq -0.10 \pm 0.04$, or due to a modified gravity theory scenario with an evolving Newton's constant or due to some unknown statistical fluctuations. In the context of a local void scenario, a degree of anisotropy is expected in the best fit value of H_0, so we utilize two different methods that are widely used in the literature to search for anisotropic signals, such as the Hemisphere Comparison (HC) and Dipole Fit (DF) methods. In the context of the modified gravity scenario, we use the same phenomenological parametrization of $G_{\rm eff}/G_{\rm N}$ that is used in Chapter 2 and find the best fit values of the relevant parameters supported by the Pantheon compilation. Finally, in the context of statistical fluctuations we construct random Monte Carlo simulated data, including the systematic uncertainties as well. Comparing the real with the simulated data, we find that only $4 - 5\%$ of the Monte Carlo simulations show the same local variations at low z, a percentage that approaches the 2σ threshold.

- In Chapter 5, we consider two recently proposed dark energy models that have the potential to address both the Hubble and the growth tensions simultaneously. In particular, the first one includes a late time abrupt transition of the absolute magnitude M, while the second one includes not only a transition on M but also on the equation of state parameter w_{DE}. We compare the quality of fit of the transition models with three well known smooth deformation models, such as the wCDM, the CPL and the Phenomenological Emergent Dark Energy model along with the standard ΛCDM. Using appropriate statistical criteria such as the Akaike Information Criterion and the Bayes factor we find that the transition models have significant advantages over the smooth deformation models in question. Finally, we shortly discuss possible theoretical models that can produce

the behavior of the transition model, such as some quintessence or phantom fields as well as a very recent false vacuum decay model.

- In Chapter 6, we focus on the sub-millimeter scales and consider two novel parametrizations for the effective potential $V_{\rm eff}$, that deviate from the standard Newtonian gravity. Using the torque residual data of the Washington experiment we find the provided quality of fit and utilizing Monte Carlo simulations we show that the relevant χ^2 differences are not statistically important.

- Finally, in Chapter 7 we summarize our results and discuss possible future prospects.

Chapter 2

Evolving Newton's Constant and the Growth Tension. Implications for Modified Gravity Theories

As we discussed in the Introduction, prominent among the dynamical probes are the Redshift Space Distortion (RSD) measurements. RSD is a phenomenon that occurs in the redshift space and describes the observed distribution of galaxies due to galaxies peculiar motion. At large scales, object such as galaxies, tend to infall into overdense regions. In an overdense region, the galaxies that are closest to us move towards the center of the overdensensity creating the illusion that the galaxies are closer to center than they really are. On the contrary, the galaxies of the "other side" of the region are moving towards us creating an illusion that they are much closer to us than they really are. As a result this overdense region seems squashed in redshift space (top panel of Fig. 2.1) [385–387]. At small scales, where astrophysical objects (such as clusters) move more arbitrary, they have random motions causing as the result to have somewhat different redshifts. Therefore, the overdensity region is elongated along the line of sight (bottom panel of Fig. 2.1). This phenomenon is referred to the bibliography as Finger of God effect [386–388]. This distortion phenomenon due to the peculiar velocities of galaxies affects the two point correlation function leading to an anisotropic power spectrum.

However, at large scales a part of the observed anisotropy of the power spectrum is also due to the use of an incorrect fiducial cosmology $H(z)$ assumed in converting the measured angles and redshifts into comoving coordinates in order to construct the correlation function and the corresponding power spectrum [66, 389, 390]. In particular, the comoving distance between a pair of galaxies separated by an angle $d\theta$ in the context of a FLRW metric is calculated to be [387, 391, 392]

$$d\ell_\perp = (1+z)\, d_A(z)\, d\theta\,, \tag{2.1}$$

where $d_A(z)$ corresponds to the angular diameter distance at the redshift of the pair discussed in the previous section. Moreover, the corresponding separation along the line of sight is

$$d\ell_\parallel = \frac{c\, dz}{H(z)}\,, \tag{2.2}$$

where in this case, $H(z)$ corresponds to the true Hubble expansion rate of the true underlying cosmology. Suppose now that instead of the true underlying cosmology, a different one with a

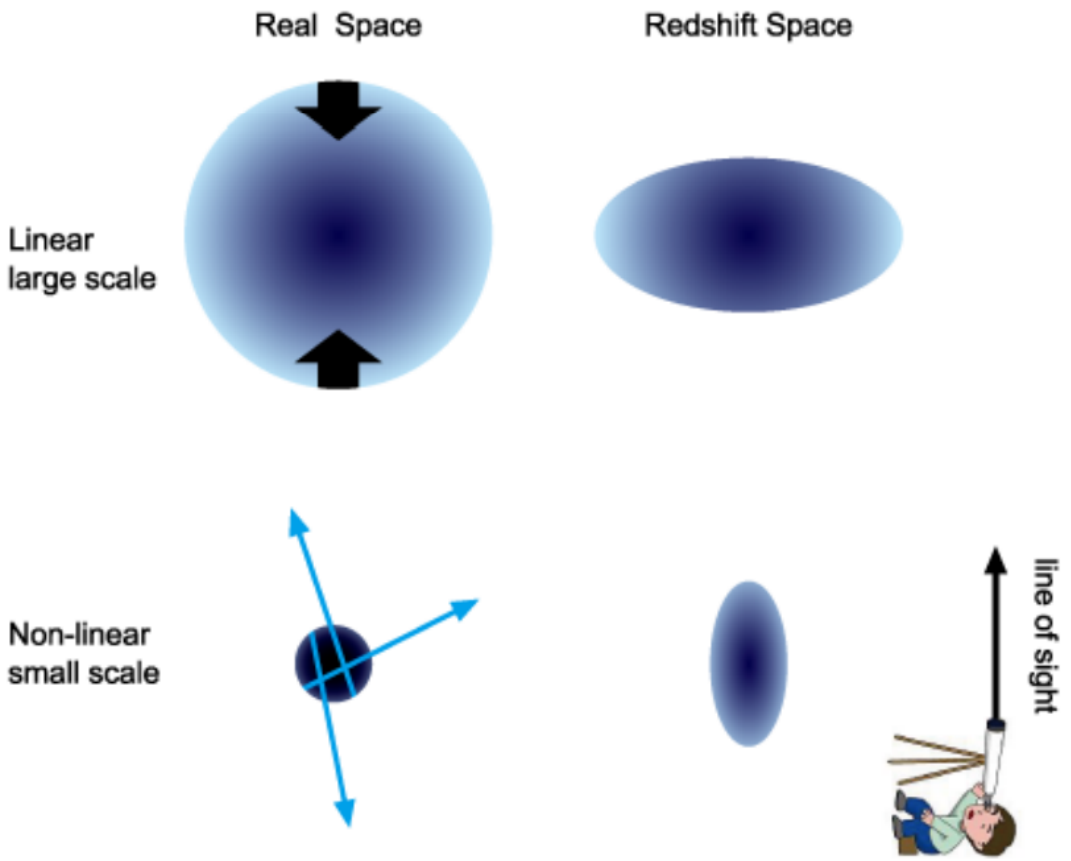

Figure 2.1: A schematic illustration of the redshift space distortion effect. The arrows represent the magnitude and direction of different velocities. From Ref. [387].

background $H'(z)$ is assumed (the prime here should not confused with the differentiation with respect to a quantity as in the previous Chapter). Then, the corresponding separations (2.1) and (2.2) take the form

$$d\ell'_{\perp} = (1+z)\, d'_A(z) d\theta = \left[\frac{d'_A(z)}{d_A(z)}\right] d\ell_{\perp} = \frac{d\ell_{\perp}}{f_{\perp}}, \tag{2.3}$$

$$d\ell'_{\parallel} = \frac{c\, dz}{H'(z)} = \left[\frac{H(z)}{H'(z)}\right] d\ell_{\parallel} = \frac{d\ell_{\parallel}}{f_{\parallel}}\,, \tag{2.4}$$

with $F \equiv f_{\parallel}/f_{\perp}$ corresponding to the induced anisotropy due to the use of incorrect fiducial cosmology and has a magnitude [390]

$$F = \frac{f_{\parallel}}{f_{\perp}} = \left[\frac{H'(z)}{H(z)}\right] \left[\frac{d'_A(z)}{d_A(z)}\right] . \tag{2.5}$$

This anisotropy that is produced by the incorrect fiducial cosmology is the Alcock-Paczynski (AP) effect [393] and is degenerate with the RSD anisotropy caused by the peculiar velocities.

The distortion of the distribution of galaxies at redshift space on large scales has been detected by various redshift surveys throughout the years, constraining the growth rate of cosmological perturbations $f(a)$. However, since about 2006, the majority of the surveys report the combination (1.54) instead as a probe of the growth of matter density perturbations. Taking

into account the AP effect, if an $f\sigma_8'$ measurement has been obtained assuming an incorrect fiducial cosmology $H'(z)$, the true $f\sigma_8$ measurement obtained assuming the true underlying cosmology $H(z)$, is given as [66]

$$f\sigma_8(z) \simeq \frac{H(z)\, d_A(z)}{H'(z)\, d_A'(z)} f\sigma_8'(z) \equiv q(z, \Omega_{\mathrm{m},0}, \Omega_{\mathrm{m},0}')\, f\sigma_8'(z)\,. \tag{2.6}$$

It is important to note here that (2.6) should be taken as a rough order of magnitude of the AP effect, since many alternative forms have been studied in the literature. For example, in Ref. [392] the used RSD data $f\sigma_8$, are converted from the WMAP [39] to the Planck best fit cosmology [394]. Therefore, assuming a ΛCDM background for both missions and considering the WMAP7 ΛCDM cosmology to be the fiducial one, the three dimensional correlation functions in the context of the AP effect take the form [392]

$$\xi_{Planck}(d\ell_\parallel, d\ell_\perp) = \xi_{fid.}(f_\parallel\, d\ell_\parallel, f_\perp\, d\ell_\perp)\,, \tag{2.7}$$

where $f_\parallel = H_{fid.}/H_{Planck}$ and $f_\perp = d_A^{Planck}/d_A^{fid}$. Using these definitions under specific approximations (*e.g.* the bias b is assumed proportional to σ_8), then the correction factor (2.6) takes the form

$$q(z, \Omega_{\mathrm{m},0}, \Omega_{\mathrm{m},0}') = C \left[\frac{H'(z)\, d_A'(z)^2}{H(z)\, d_A(z)^2}\right]^{3/2} \left(\frac{\sigma_8}{\sigma_8'}\right)^2\,. \tag{2.8}$$

Another alternative form for the correction factor is discussed in Ref. [391] that is written as

$$f\sigma_8' = \left\{\beta + \frac{n}{2}\left[1 - \frac{H'(z)\, d_A'}{H(z)\, d_A}\right]\right\} b\,\sigma_8\,, \tag{2.9}$$

where n is the logarithmic derivative of the power spectrum.

In this Chapter, we construct a compilation of 63 $f\sigma_8$ measurements that has been reported by a large variety of surveys from 2004 to 2018. Utilizing this compilation, we adopt the simple correction factor (2.6) and apply the maximum likelihood method in the context of a non trivial evolution of the effective Newton's constant and a ΛCDM background. Moreover, we study a theoretical parametrization of $f\sigma_8(z)$ and study its potential to fit the solution of the growth equation for both the GR and the modified gravity case. Finally, we impose strong constraints from the CMB data utilizing the `MGCAMB` numerical package.

2.1 Theoretical Predictions of $f\sigma_8(z)$

Throughout the years, a vast variety of different missions have published RSD growth data in the form of the $f\sigma_8$ product (1.54), including the Sloan Digital Sky Survey (SDSS), the 2 degree Field Galaxy Redshift Survey (2dFGRS), the VIMOS-VLT Deep Survey (VVDS), the 2MASS Redshift Survey (2MRS), the WiggleZ survey, the VIMOS Public Extra-galactic Redshift Survey (VIPERS), the Galaxy and Mass Assembly (GAMA) survey, the Baryon Oscillation Spectroscopic Survey (BOSS), the Subaru Fiber Multi-Object Spectrograph galaxy redshift survey (FastSound) and the 2MASS Tully-Fisher Survey (2MTF). A compilation of 63 measurements published by these surveys from 2004 to 2016 is presented in Table 2.1, including the corresponding fiducial cosmology for each case.

Index	Survey	z	$f\sigma_8$	Refs.	Year	Fiducial Cosmology
1	2dFGRS	0.17	0.51 ± 0.06	[395, 396]	23/06/2004	$(\Omega_{m,0}, \sigma_8) = (0.3, 0.79)$
2	SDSS-LRG	0.35	0.44 ± 0.05	[396, 397]	30/10/2006	$(\Omega_{m,0}, \sigma_8) = (0.25, 0.76)$
3	VVDS	0.77	0.49 ± 0.18	[396, 398]	13/02/2008	$(\Omega_{m,0}, \sigma_8) = (0.25, 0.78)$
4	2MRS	0.02	0.314 ± 0.048	[399, 400]	13/11/2010	$(\Omega_{m,0}, \sigma_8) = (0.266, 0.65)$
5	SnIa+IRAS	0.02	0.398 ± 0.065	[400, 401]	07/11/2011	$(\Omega_{m,0}, \sigma_8) = (0.3, 0.814)$
6	SDSS-LRG-200	0.25	0.351 ± 0.058	[402]	09/12/2011	$(\Omega_{m,0}, \sigma_8) = (0.276, 0.8)$
7	SDSS-LRG-200	0.37	0.4602 ± 0.0378	[402]	09/12/2011	
8	SDSS-LRG-60	0.25	0.3665 ± 0.0601	[402]	09/12/2011	$(\Omega_{m,0}, \sigma_8) = (0.276, 0.8)$
9	SDSS-LRG-60	0.37	0.4031 ± 0.0586	[402]	09/12/2011	
10	6dFGS	0.067	0.423 ± 0.055	[403]	20/04/2012	$(\Omega_{m,0}, \sigma_8) = (0.27, 0.76)$
11	WiggleZ	0.44	0.413 ± 0.080	[404]	12/06/2012	$(\Omega_{m,0}, h, \sigma_8) = (0.27, 0.71, 0.8)$
12	WiggleZ	0.60	0.390 ± 0.063	[404]	12/06/2012	
13	WiggleZ	0.73	0.437 ± 0.072	[404]	12/06/2012	
14	SDSS-BOSS	0.30	0.407 ± 0.055	[405]	22/06/2012	$(\Omega_{m,0}, \sigma_8) = (0.25, 0.804)$
15	SDSS-BOSS	0.40	0.419 ± 0.041	[405]	22/06/2012	
16	SDSS-BOSS	0.50	0.427 ± 0.043	[405]	22/06/2012	
17	SDSS-BOSS	0.60	0.433 ± 0.067	[405]	22/06/2012	
18	Vipers	0.80	0.47 ± 0.08	[406]	09/07/2013	$(\Omega_{m,0}, \sigma_8) = (0.25, 0.82)$
19	SDSS-DR7-LRG	0.35	0.429 ± 0.089	[407]	13/08/2013	$(\Omega_{m,0}, \sigma_8) = (0.25, 0.809)$
20	GAMA	0.18	0.36 ± 0.09	[408]	22/09/2013	$(\Omega_{m,0}, \sigma_8) = (0.27, 0.8)$
21	GAMA	0.38	0.44 ± 0.06	[408]	22/09/2013	
22	BOSS-LOWZ	0.32	0.384 ± 0.095	[409]	17/12/2013	$(\Omega_{m,0}, \sigma_8) = (0.274, 0.8)$
23	SDSS DR10/11	0.32	0.48 ± 0.10	[409]	17/12/2013	
24	SDSS DR10/11	0.57	0.417 ± 0.045	[409]	17/12/2013	
25	SDSS-MGS	0.15	$0.49^{+0.15}_{-0.14}$	[410]	30/01/2015	$(\Omega_{m,0}, h, \sigma_8) = (0.31, 0.67, 0.83)$
26	SDSS-veloc	0.10	0.37 ± 0.13	[411]	16/06/2015	$(\Omega_{m,0}, \sigma_8) = (0.3, 0.89)$
27	FastSound	1.40	0.482 ± 0.116	[412]	25/10/2015	$(\Omega_{m,0}, \sigma_8) = (0.27, 0.82)$
28	SDSS-CMASS	0.59	0.488 ± 0.060	[413]	02/05/2016	$(\Omega_{m,0}, h, \sigma_8) = (0.307115, 0.6777, 0.8288)$
29	BOSS DR12	0.38	0.497 ± 0.045	[45]	11/07/2016	$(\Omega_{m,0}, \sigma_8) = (0.31, 0, 0.8)$
30	BOSS DR12	0.51	0.458 ± 0.038	[45]	11/07/2016	
31	BOSS DR12	0.61	0.436 ± 0.034	[45]	11/07/2016	
32	BOSS DR12	0.38	0.477 ± 0.051	[414]	11/07/2016	$(\Omega_{m,0}, h, \sigma_8) = (0.31, 0.676, 0.8)$
33	BOSS DR12	0.51	0.453 ± 0.050	[414]	11/07/2016	
34	BOSS DR12	0.61	0.410 ± 0.044	[414]	11/07/2016	
35	Vipers v7	0.76	0.440 ± 0.040	[391]	26/10/2016	$(\Omega_{m,0}, \sigma_8) = (0.308, 0.8149)$
36	Vipers v7	1.05	0.280 ± 0.080	[391]	26/10/2016	
37	BOSS LOWZ	0.32	0.427 ± 0.056	[415]	26/10/2016	$(\Omega_{m,0}, \sigma_8) = (0.31, 0.8475)$
38	BOSS CMASS	0.57	0.426 ± 0.029	[415]	26/10/2016	
39	Vipers	0.727	$0.296^{+0.075}_{-0.078}$	[416]	21/11/2016	$(\Omega_{m,0}, \sigma_8) = (0.31, 0, 0.7)$
40	6dFGS+SnIa	0.02	$0.428^{+0.048}_{-0.045}$	[417]	29/11/2016	$(\Omega_{m,0}, h, \sigma_8) = (0.3, 0.683, 0.8)$
41	Vipers	0.6	0.48 ± 0.12	[418]	16/12/2016	$(\Omega_{m,0}, \Omega_{b,0}, n_s, \sigma_8) = (0.3, 0.045, 0.96, 0.831)$
42	Vipers	0.86	0.48 ± 0.10	[418]	16/12/2016	
43	Vipers PDR-2	0.60	0.550 ± 0.120	[419]	16/12/2016	$(\Omega_{m,0}, \Omega_{b,0}, \sigma_8) = (0.3, 0.045, 0.823)$
44	Vipers PDR-2	0.86	0.400 ± 0.110	[419]	16/12/2016	
45	SDSS DR13	0.1	0.48 ± 0.16	[420]	22/12/2016	$(\Omega_{m,0}, \sigma_8) = (0.25, 0.89)$
46	2MTF	0.001	$0.51^{+0.09}_{-0.08}$	[421]	16/06/2017	$(\Omega_{m,0}, \sigma_8) = (0.3121, 0.815)$
47	Vipers PDR-2	0.85	0.45 ± 0.11	[422]	31/07/2017	$(\Omega_{b,0}, \Omega_{m,0}, h) = (0.045, 0.30, 0.8)$
48	BOSS DR12	0.31	0.469 ± 0.098	[423]	15/09/2017	$(\Omega_{m,0}, h, \sigma_8) = (0.307, 0.6777, 0.8288)$
49	BOSS DR12	0.36	0.474 ± 0.097	[423]	15/09/2017	
50	BOSS DR12	0.40	0.473 ± 0.086	[423]	15/09/2017	
51	BOSS DR12	0.44	0.481 ± 0.076	[423]	15/09/2017	
52	BOSS DR12	0.48	0.482 ± 0.067	[423]	15/09/2017	
53	BOSS DR12	0.52	0.488 ± 0.065	[423]	15/09/2017	
54	BOSS DR12	0.56	0.482 ± 0.067	[423]	15/09/2017	
55	BOSS DR12	0.59	0.481 ± 0.066	[423]	15/09/2017	
56	BOSS DR12	0.64	0.486 ± 0.070	[423]	15/09/2017	
57	SDSS DR7	0.1	0.376 ± 0.038	[424]	12/12/2017	$(\Omega_{m,0}, \Omega_{b,0}, \sigma_8) = (0.282, 0.046, 0.817)$
58	SDSS-IV	1.52	0.420 ± 0.076	[425]	08/01/2018	$(\Omega_{m,0}, \Omega_{b,0}\, h^2, \sigma_8) = (0.26479, 0.02258, 0.8)$
59	SDSS-IV	1.52	0.396 ± 0.079	[426]	08/01/2018	$(\Omega_{m,0}, \Omega_{b,0}\, h^2, \sigma_8) = (0.31, 0.022, 0.8225)$
60	SDSS-IV	0.978	0.379 ± 0.176	[427]	09/01/2018	$(\Omega_{m,0}, \sigma_8) = (0.31, 0.8)$
61	SDSS-IV	1.23	0.385 ± 0.099	[427]	09/01/2018	
62	SDSS-IV	1.526	0.342 ± 0.070	[427]	09/01/2018	
63	SDSS-IV	1.944	0.364 ± 0.106	[427]	09/01/2018	

Table 2.1: The compilation of 63 RSD data that were published from 2004 to 2018, first presented in Ref. [70].

Obviously, many of the presented datapoints suffer from correlations due to the overlap in

the galaxy samples used for their derivation. Therefore, instead of the extended sample, many analyses [47,68,69,392,428–437] choose to select a small subsample of about 20 datapoints based on subjective criteria that favor more recent data or a qualitative minimization of correlations between the datapoints[1]. However, the use of ad hoc subsamples from the full $f\sigma_8$ may lead to a waste of useful information. So, we choose to utilize the full dataset to perform a more detailed analysis to identify hidden trends of the best fit parameters appearing in different cosmological models in the context of different subsamples, as well as to study the effects of fiducial cosmology or correlation among datapoints, even though the extended covariance matrix needed for their combined analysis is not available in the literature.

For the theoretical form of the $f\sigma_8(z)$, as discussed in the previous Chapter, it is essential to solve (1.50) in the range $a \in [0,1]$ with initial conditions assuming GR and matter domination (we set initially $\delta(a) \simeq a$) and substitute the solution to (1.54). Regarding the parametrization for $G_{\rm eff}/G_{\rm N}$ we choose a phenomenological parametrization which may be viewed as an extended Taylor expansion around $a = 1$ of the following form[2] [68]

$$G_{\rm eff} = G_{\rm N}\left[1 + g_a(1-a)^n - g_a(1-a)^{n+m}\right] = G_{\rm N}\left[1 + g_a\left(\frac{z}{1+z}\right)^n - g_a\left(\frac{z}{1+z}\right)^{n+m}\right], \tag{2.10}$$

where g_a is a phenomenological parameter and n, m correspond to integer parameters with $n \geq 2$ and $m > 0$. The values for n, m are essential assumptions since solar system tests [150] and nucleosynthesis constraints at the 1σ level [439] imply

$$\left|\frac{1}{G_{\rm N}}\frac{dG_{\rm eff}(z)}{dz}\Big|_{z=0}\right| < 10^{-3}h^{-1}\,, \tag{2.11}$$

$$\left|\frac{G_{\rm eff}}{G_{\rm N}} - 1\right| \leq 0.2\,. \tag{2.12}$$

In what follows we choose to set $n = m = 2$.

Therefore, using (2.10) and taking into account the correction factor (2.6) we solve numerically (1.50) in the context of a Planck15/ΛCDM background. The constructed solution for $f\sigma_8(z)$, is compared with the $f\sigma_8(z)$ solutions obtained for a pure Planck15/ΛCDM [17] background cosmology ($g_a = 0$), a pure WMAP7/ΛCDM [440] background cosmology ($g_a = 0$), as well as for the best fit ΛCDM case. The different solutions are illustrated in Fig. 2.2 superimposed with the RSD data of Table 2.1. Clearly, the pure WMAP7/ΛCDM background cosmology is more consistent with the full RSD data compilation than the pure Planck15/ΛCDM background cosmology since the corresponding Planck15/ΛCDM curve is higher than the majority of the RSD data. Hence, the Planck15/ΛCDM background cosmology predicts a larger $f\sigma_8$ than the one favored by the data.

However, Eq. (1.50) can also be solved analytically. In the context of ΛCDM, there are some complex analytical solutions of Eq. (1.50), expressed in terms of the Hypergeometric functions [303,441–443]. A way to disregard the complex process of finding analytical solutions is to use approximated parametrizations such as the "γ parametrization". In the context of

[1]For a robust compilation of 22 RSD datapoints that was constructed using the so called "Internal Robustness" method [438], see Ref. [71].

[2]Similar to $G_{\rm eff}$ the effective Newton constant for lensing $G_{\rm L}$ can defined. $G_{\rm L}$ changes the lensing of light through the sum of the Bardeen potentials $\phi + \psi$. In the context of GR, $G_{\rm L} = G_{\rm eff} = G_{\rm N}$. Throughout this Chapter $G_{\rm L}$ is ignored, since only $G_{\rm eff}$ appears in (1.50).

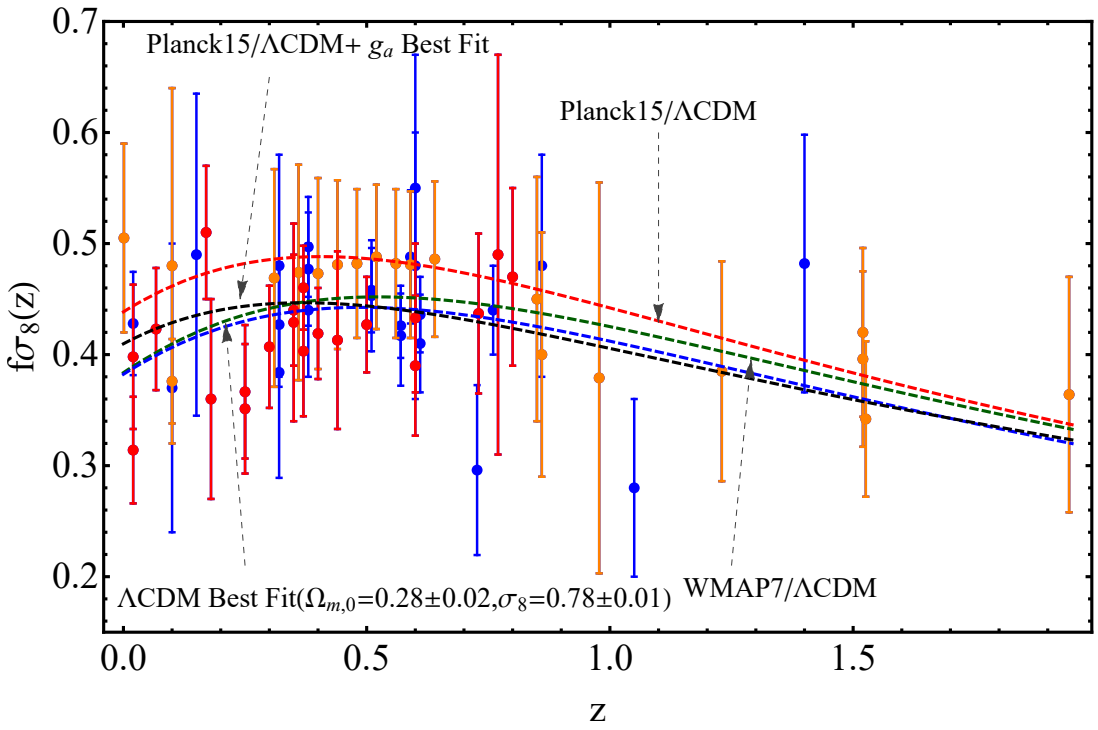

Figure 2.2: Plot of the $f\sigma_8(z)$ solutions for various cases, including the full RSD dataset of Table 2.1. The red dashed line corresponds to a pure Planck15/ΛCDM [17] background cosmology ($g_a = 0$), while the green dashed line corresponds to a pure WMAP7/ΛCDM [440] background cosmology ($g_a = 0$). The blue dashed line describes the best fit ΛCDM ($\Omega_{\rm m,0} = 0.28 \pm 0.02, \sigma_8 = 0.78 \pm 0.01$) for the full RSD dataset. The red points correspond to the 20 earliest published points, whereas the orange ones to the 20 latest published points. From Ref. [70] (see also Ref. [73] for an updated version for the Planck18/ΛCDM case).

ΛCDM, it is well known [303, 444–448] that the growth rate $f(z)$ is well approximated by a parametrization of the form

$$f(a) = \Omega_{\rm m}(a)^{\gamma(a)}\,, \tag{2.13}$$

$$\Omega_{\rm m}(a) \equiv \frac{\Omega_{\rm m,0}\; a^{-3}}{H^2(a)/H_0^2}\,, \tag{2.14}$$

$$\gamma(a) = \frac{\ln f(a)}{\ln \Omega_{\rm m}(a)} \simeq 0.55\,. \tag{2.15}$$

In Ref. [70], a specific parametrization for $f\sigma_8(z)$ in analogy with the parametrization (2.13) is discussed. In view of the fact that $\sigma_8(a) \sim \delta(a) \sim a$, in the context of a flat matter dominated Universe it is natural to anticipate a parametrization of the form [70]

$$f\sigma_8(z) = \lambda\, \sigma_8 \frac{\Omega_{\rm m}(z)^{\gamma}}{(1+z)^{\beta}}\,, \tag{2.16}$$

where

$$\Omega_{\rm m}(z) = \frac{\Omega_{\rm m,0}\,(1+z)^3}{\Omega_{\rm m,0}\,(1+z)^3 + 1 - \Omega_{\rm m,0}} \tag{2.17}$$

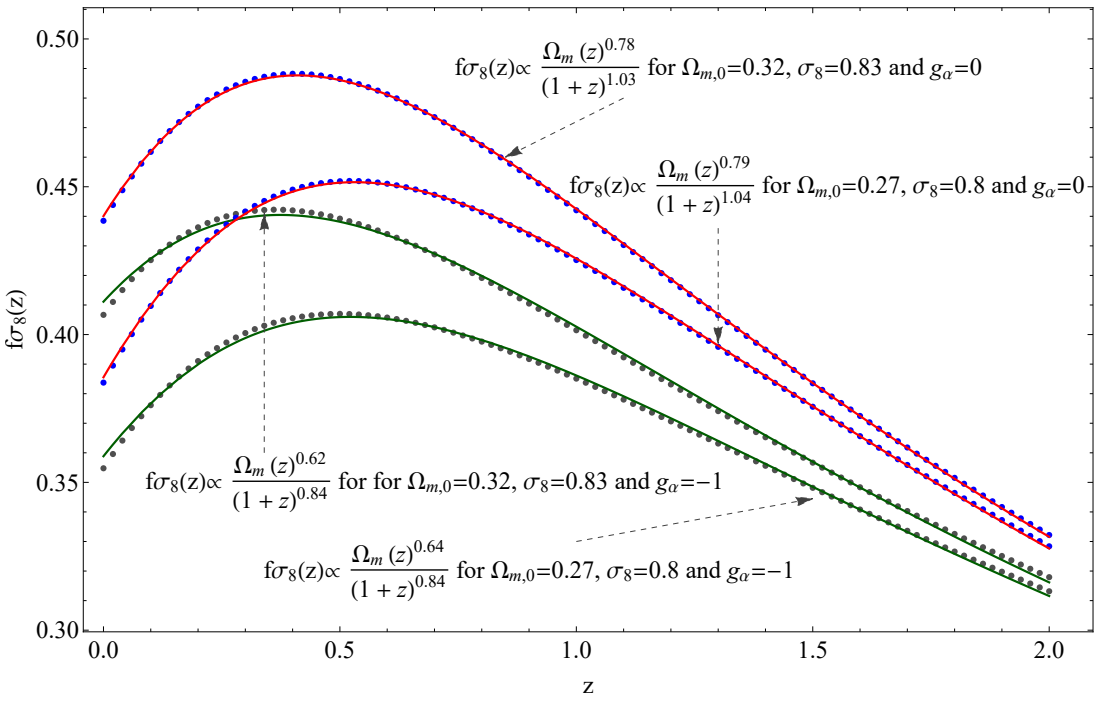

Figure 2.3: The parametrization (2.16) for Planck15/ΛCDM [17] and WMAP7/ΛCDM [440]. The thick blue dots of the upper (lower) curve correspond to the numerical solution of $f\sigma_8(z)$ for Planck15/ΛCDM (WMAP7/ΛCDM) superimposed with the analytic form (2.16) (red lines) assuming GR, whereas the gray ones of the upper (lower) curve represent the numerical solution of $f\sigma_8(z)$ for Planck15/ΛCDM (WMAP7/ΛCDM) superposed with the analytic form (2.16) (green lines) for modified gravity, *i.e.* $g_a = -1$. From Ref. [70].

and λ, β, γ correspond to parameters determined for a given cosmological model. Eq. (2.16) provides an excellent fit to the numerical solution $f\sigma_8(z)$ as it is illustrated in Fig. 2.3, where the numerical solution for $f\sigma_8(z)$ is shown (dotted lines) for Planck15/ΛCDM and WMAP7/ΛCDM backgrounds, superimposed with the analytic form of (2.17) (continous red lines) for $\gamma \simeq 0.78$ and $\beta \simeq 1$ (see the caption for the exact parameter values of each case). Similarly, under the assumption of modified gravity ($g_a = -1$)[3], the numerical solution (dotted lines) is shown in the same figure for the same backgrounds $H(z)$ superimposed with the corresponding analytic parametrization (continuous green lines). The parametrization (2.16) continues to provide still an excellent fit but for somewhat lower values of the parameters ($\beta \simeq 0.84$, $\gamma \simeq 0.63$).

Furthermore, we show the dependence of the parameters λ, β γ on $\Omega_{\rm m,0}$ for both the GR and modified gravity case where $g_a = 0$ and $g_a = -1$ respectively, in Fig. 2.4. The dots correspond to the numerically obtained values and the continuous lines are power laws that describe the dependence of the parameters on $\Omega_{\rm m,0}$. In the range $\Omega_{\rm m,0} \in [0.25, 0.35]$ and assuming GR ($g_a = 0$) we have $\gamma = 0.78 \pm 0.01$, $\lambda = 1.3 \pm 0.1$ and $\beta = 1.03 \pm 0.01$.

[3]This particular value for g_a is chosen since it is indicated that it can reduce the growth tension [68].

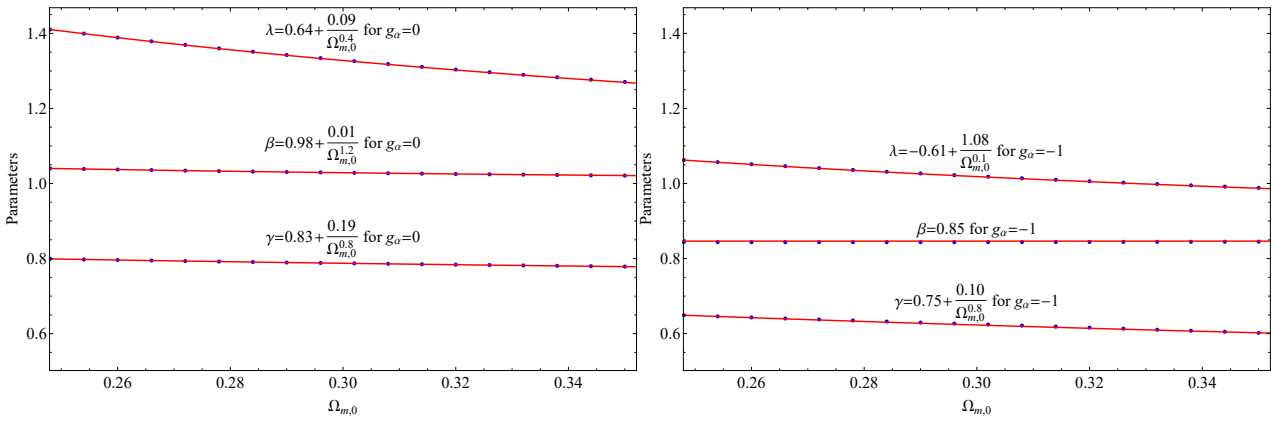

Figure 2.4: The dependence of the parameters λ (upper curve), β (middle curve) and γ (lower curve) on $\Omega_{\rm m,0}$. The blue dots are the numerically obtained values while the continuous (red) lines correspond to the best fit power laws for GR (left figure) where $g_a = 0$ and modified gravity (right figure) where $g_a = -1$. From Ref. [70].

2.2 General Trends in the $f\sigma_8$ Dataset

The full compilation of RSD data of Table 2.1 could be used to directly identify the best fit form of the background cosmology $H(z)$ as well as the best fit form of $G_{\rm eff}(z)$ performing a fit to the data as usually, *i.e.* applying the well known maximum likelihood method and constructing a χ^2 function [449, 450]. However, as we have already mentioned the derived results of such a brute force approach should be interpreted with care, since they are affected by the following factors that could possibly lead to incorrect results

- Correlations Among Datapoints: The fact that a complete covariance matrix for the full RSD compilation of Table 2.1 is unknown creates an obvious uncertainty, even if someone considers a subset from the full compilation.

- Fiducial Model Correction: The different fiducial cosmologies assumed for the RSD compilation (see the last column of Table 2.1) may lead to misleading results and it should be taken into account. A proper account of this effect would require a full reconstruction of the correlation function under a Planck15/ΛCDM fiducial cosmology for all datapoints of Table 2.1. An approximate solution (which is followed in our analysis) is to include an AP correction such as the one of Eq. (2.6).

- Survey Systematics: Systematics of surveys that may vary with time of publication and may lead to data inhomogeneities. It is only natural to assume that the more recent published datapoints have reduced possible systematics that affect the measurements.

After applying the maximum likelihood method, we estimate the magnitude of these effects in the derived best fit results.

In the context of the maximum likelihood method, the theoretical prediction of $f\sigma_8$ can be compared with the corresponding observations constructing the following χ^2 function [449, 450]

$$\chi^2(\Omega_{\rm m,0}, g_a, \sigma_8) = V^i C_{ij}^{-1} V^j \,, \tag{2.18}$$

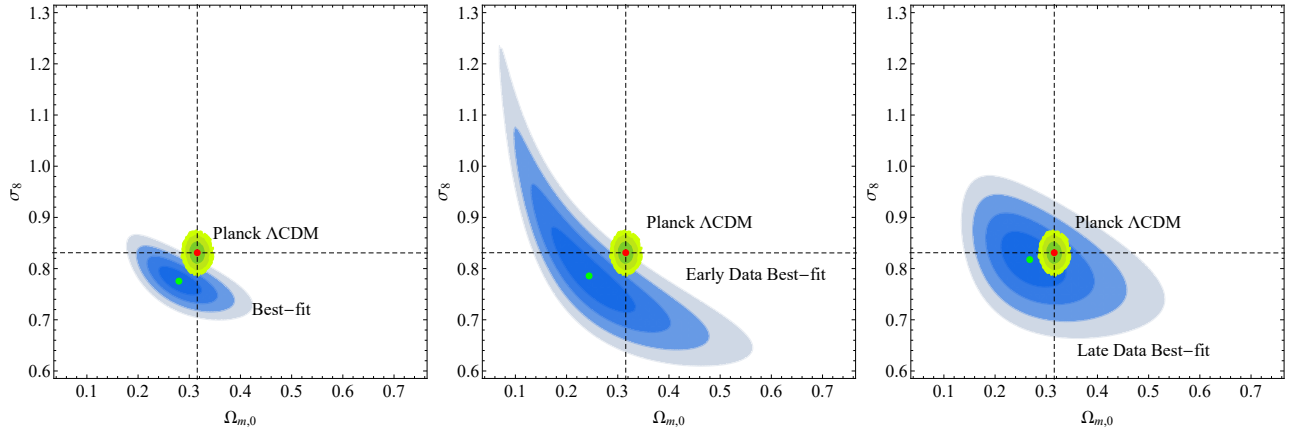

Figure 2.5: The $1\sigma - 4\sigma$ confidence contours in the parametric space $(\Omega_{\rm m,0} - \sigma_8)$ for $g_a = 0$. The blue contours correspond to the best fit of the 63 compilation data (left panel), the 20 early data (middle panel) and the 20 late data (right panel). The light green contours correspond to the Planck15/ΛCDM, while the red (green) dot describes the Planck15/ΛCDM (growth) best fit, applying the maximum likelihood method. From Ref. [70].

where the vector V^i is given by the following formula

$$V^i(z_i, \Omega_{\rm m,0}, g_a, \sigma_8) \equiv f\sigma_{8,i} - \frac{f\sigma_8(z_i, \Omega_{\rm m,0}, g_a, \sigma_8, g_a)}{q\left(z, \Omega_{\rm m,0}, \Omega_{\rm m,0}^{fid_i}\right)} \tag{2.19}$$

and C_{ij}^{-1} is the inverse covariance matrix. It is important to note here that for the construction of the vector, we have divided the theoretical prediction $f\sigma_8(z_i, \Omega_{\rm m,0}, g_a, \sigma_8)$ by the correction factor (2.6). The denominator is obtained from the fiducial ΛCDM model of each survey and the numerator involves the $\Omega_{\rm m,0}$ parameter to be fit by the data. We expect that this factor does not differ from unity more than $2-3\%$ and thus it leaves our best fit estimations practically unaffected. Regarding the total covariance matrix, we assume that it is diagonal except of the WiggleZ subset of the data (three datapoints) and has the following form

$$C_{ij}^{\rm growth,total} = \begin{pmatrix} \sigma_1^2 & 0 & 0 & \cdots \\ 0 & C_{ij}^{WiggleZ} & 0 & \cdots \\ 0 & 0 & \cdots & \sigma_N^2 \end{pmatrix}, \tag{2.20}$$

where the WiggleZ covariance matrix is given as

$$C_{ij}^{\rm WiggleZ} = 10^{-3} \begin{pmatrix} 6.400 & 2.570 & 0.000 \\ 2.570 & 3.969 & 2.540 \\ 0.000 & 2.540 & 5.184 \end{pmatrix} \tag{2.21}$$

and its non-diagonal elements can be approximated as $C_{ij} \simeq 0.5\sqrt{C_{ii}C_{jj}}$. The form of Eq. (2.20) is obviously an oversestimation as it ignores the existing correlations among different datapoints.

Minimizing Eq. (2.18), as usual, we derive the best fit values of the parameters and construct the relevant $1\sigma - 4\sigma$ confidence contours in the parametric space $(\Omega_{\rm m,0} - \sigma_8)$ using the full dataset of Table 2.1 and setting $g_a = 0$. This is illustrated in the left panel of Fig. 2.5 along

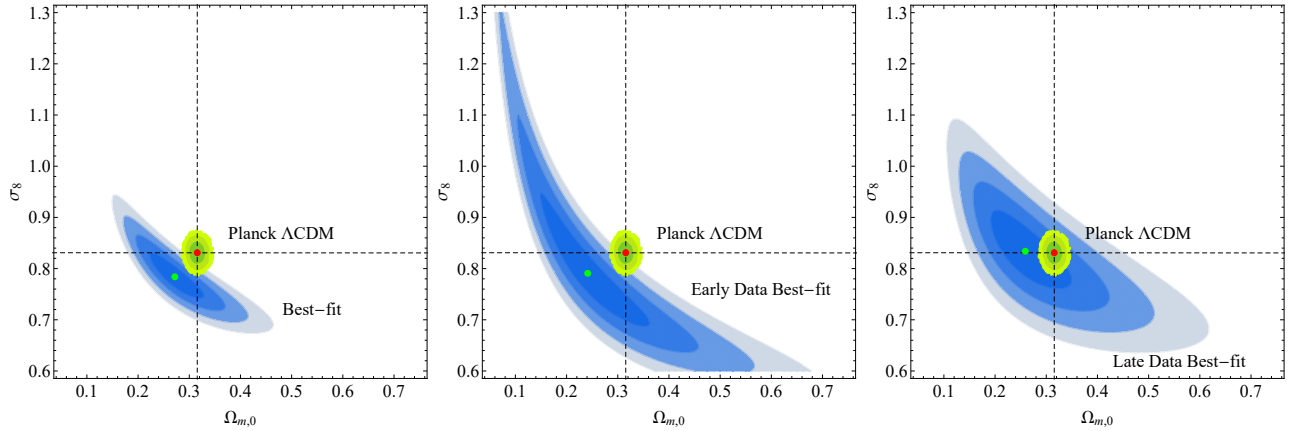

Figure 2.6: The $1\sigma - 4\sigma$ confidence contours in the parametric space $(\Omega_{\rm m,0} - \sigma_8)$ for $q \equiv 1$ and $g_a = 0$. The blue and light green contours correspond to the same as in Fig. 2.5. Clearly, the qualitative behaviour that was previously observed for the tension level remains the same. From Ref. [70].

with the corresponding Planck15/ΛCDM contours, where we can clearly identify a 5σ tension between the relevant $(\Omega_{\rm m,0} - \sigma_8)$ best fits. The growth data favor lower values for both the $\Omega_{\rm m,0}$ and σ_8 parameters, indicating weaker clustering than the one indicated by Planck15/ΛCDM. This behaviour can be achieved either by decreasing the value of $\Omega_{\rm m,0}$ or by decreasing the value of σ_8 or by considering a decreasing $G_{\rm eff}$ at low redshifts [68, 70]. Since the observed tension is at quite a high level, we perform a comparison of the tension level of the earliest and latest published RSD datapoints with Planck15/ΛCDM. This method can also work as a consistency check of the full compilation of Table 2.1. In the middle panel of Fig. 2.5, we show the $1\sigma - 4\sigma$ confidence contours in the parametric space $(\Omega_{\rm m,0} - \sigma_8)$ using the 20 earliest published datapoints (top 20 points of Table 2.1) as well as the $1\sigma - 4\sigma$ confidence contours in the parametric space $(\Omega_{\rm m,0} - \sigma_8)$ using the 20 latest published datapoints (bottom 20 points of Table 2.1) in the right panel of Fig. 2.5. Even though the size of the confidence contours increases due to the smaller number of datapoints, the tension level remains at about 4σ when the early data are considered. On the contrary, the tension level decreases drastically when the latest datapoints are considered (the tension drops below the 1σ threshold).

This general trend is quite an interesting feature and needs to be further investigated. This dramatic decrease of the tension level can be attributed to the following:

- The considered fiducial cosmologies of the early datapoints that is different from the fiducial cosmology (Planck15/ΛCDM) assumed in more recent studies. In order to estimate this effect, we reconstruct the $1\sigma - 4\sigma$ confidence contours of Fig. 2.5 setting the correction factor $q \equiv 1$. The new contours are shown in Fig. 2.6 for the full compilation (left panel), the 20 earliest RSD datapoints (middle panel) and the 20 latest (right panel) RSD datapoints. Obviously, the tension level remains practically unaffected. The same conclusion can be extracted if the correction factor $q(z, \Omega_{\rm m,0}^{Planck15}, \Omega'_{\rm m,0})$ as a function of the redshift z for different fiducial cosmologies is plotted (see Fig. 2.7). The difference of q from unity is less the 3% for $z < 1$. This difference is significantly smaller than the typical level of the errorbars of the RSD compilation and explains as a result the reduced role of the fiducial model correction in the deduction of the tension level.

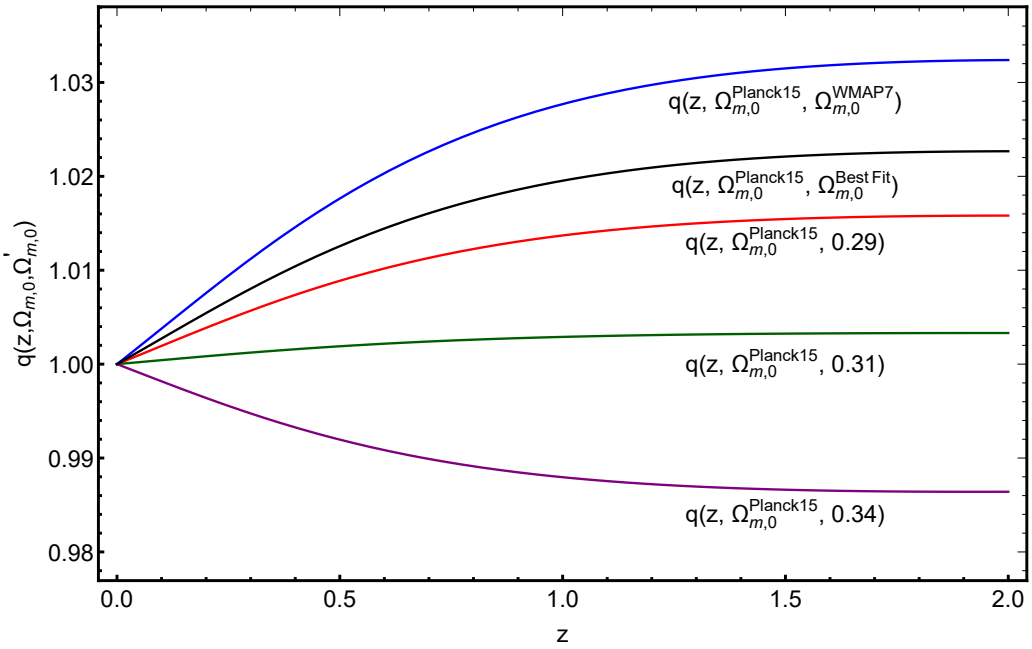

Figure 2.7: The correction factor $q(z, \Omega_{\rm m,0}^{Planck15}, \Omega'_{\rm m,0})$ as a function of redshift z, for different fiducial cosmologies $\Omega'_{\rm m,0}$. Its difference from unity is less than 3% for $z < 1$. From Ref. [70].

- The almost diagonal considered form of the covariance matrix (2.20) that assumes almost all the datapoints to be uncorrelated. The effect of any possible correlation among datapoints can be determined, introducing a number of randomly selected non-diagonal elements in the covariance matrix while keeping it symmetric. In this method, we randomly select 12 pairs of datapoints (approximately 20% of the full data). The position of the non-diagonal elements are randomly selected and the magnitude of the randomly selected covariance matrix element C_{ij} is set to be

$$C_{ij} = \frac{1}{2}\,\sigma_i\,\sigma_j\,, \tag{2.22}$$

  where $\sigma_i\,\sigma_j$ correspond to the published 1σ errors of the datapoints i, j. The coefficient $1/2$ is chosen in analogy with the magnitude of the approximated formula of the WiggleZ survey discussed above. Using this form for the covariance matrix, we construct the $1\sigma - 4\sigma$ confidence contours in the parametric space $(\Omega_{\rm m,0} - \sigma_8)$ in Fig. 2.8. Clearly, the previous qualititative feature, *i.e.* a significant reduction of the level of the tension for more recent RSD data, remains similar. It is interesting to note that in this case, even though the tension level remains the same (at the 5σ level) for both the full and early data, for the 20 most recently publiched datapoints the tension completely disappears (is below the 0.5σ level). The sigma differences for all the contour cases are summarized in Table 2.2.

- The increased redshifts of more recent datapoints that probe redshift regions where the different ΛCDM models make similar predictions. This is shown in Fig. 2.9 (right panel) where we plot the 20 point moving average (see definition below) of RSD redshifts depending on time of publication as well as the 20 pont moving average of the errorbars as a function of the publication time (left panel). The degeneracy in the redshifts is partially

Corresponding Contours	Full Dataset	Early Data	Late Data
Fig. 2.5 Contours	4.97σ	3.89σ	0.94σ
Fig. 2.6 Contours	5.44σ	4.36σ	0.97σ
Fig. 2.8 Contours	4.76σ	4.77σ	0.37σ

Table 2.2: The exact sigma differences from the Planck15/ΛCDM for Figs. 2.5, 2.6 and 2.8. From Ref. [70].

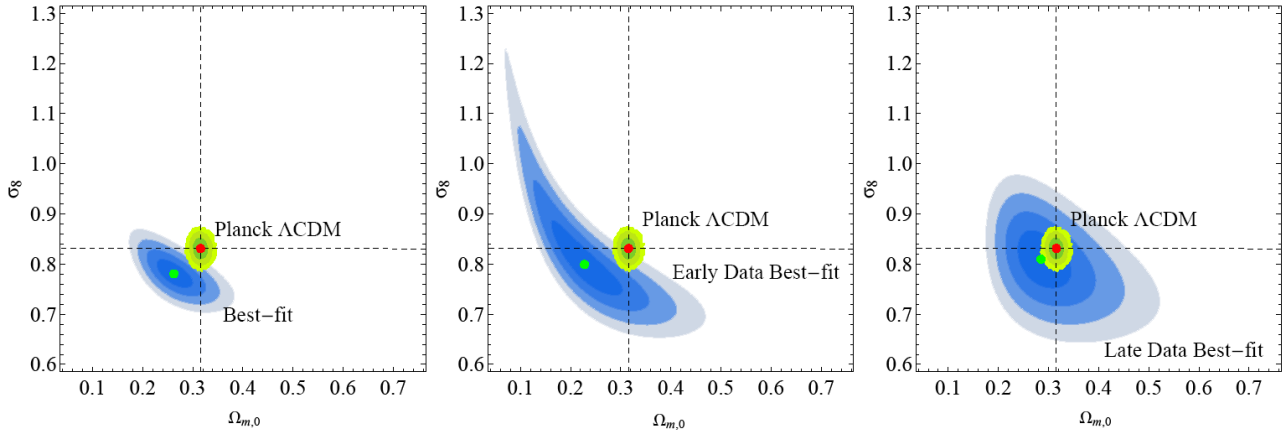

Figure 2.8: The $1\sigma-4\sigma$ confidence contours in the parametric space ($\Omega_{\rm m,0}-\sigma_8$) with a random covariance among 25% of the datapoints (assumed to be correlated in pairs). The tension level in all three panels remains approximately the same as in the previous figures. From Ref. [70].

due to matter domination that appears in all viable models at early times. Since more recent survey move to higher redshifts and have larger errorbars the more recent data are less powerful in distinguishing among different models. Although the increase of the average redshift is to be expected due to the improvement of the sensitivity of the surveys, the increased errorbars is an unexpected feature and deserves further investigation, since there are claims that the RSD errorbars may be overestimated [66].

- The improved methods and reduced systematics may lead to stronger evidence in favor of the concordance Planck15/ΛCDM model.

The trend for reduced tension of the growth data with Planck15/ΛCDM may also be seen taking into consideration the residuals of the datapoints of Fig. 2.2 with respect to the Planck15/ΛCDM RSD prediction. These residuals are defined as [70]

$$\delta f\sigma_8(z_i) \equiv \frac{f\sigma_8(z_i)^{data} - f\sigma_8(z_i)^{Planck15}}{\sigma_i} \tag{2.23}$$

and are plotted in the left panel of Fig. 2.10 ordered with respect to time of publication, assuming Planck15/ΛCDM fiducial model corrections. We also illustrate the 20 point moving average of these residuals in the right panel of Fig. 2.10 which is defined as [70]

$$\overline{f\sigma_{8j}} \equiv \sum_{i=j-20}^{j} \frac{\delta f\sigma_8(z_i)}{20}\,. \tag{2.24}$$

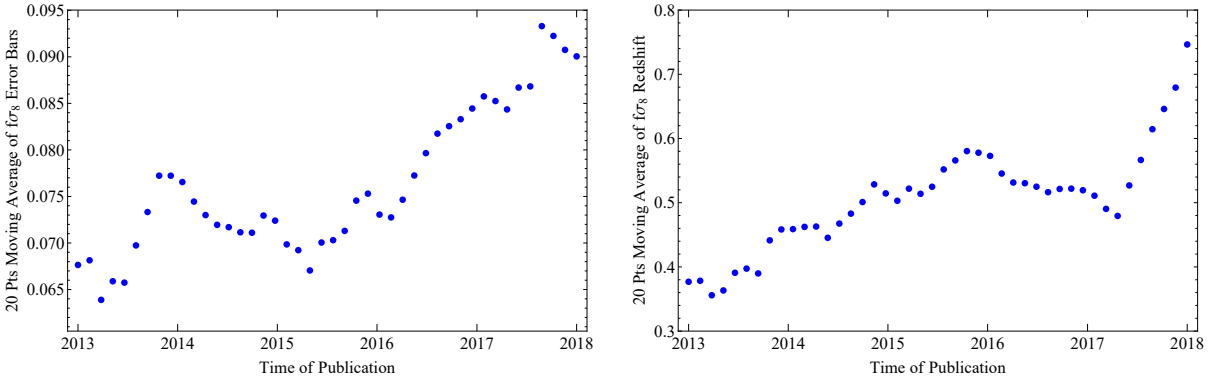

Figure 2.9: *Left Panel:* The 20 point moving average of RSD errorbars depending on time of publication. *Right Panel:* The 20 point moving average of RSD redshifts depending on time of publication. From Ref. [70].

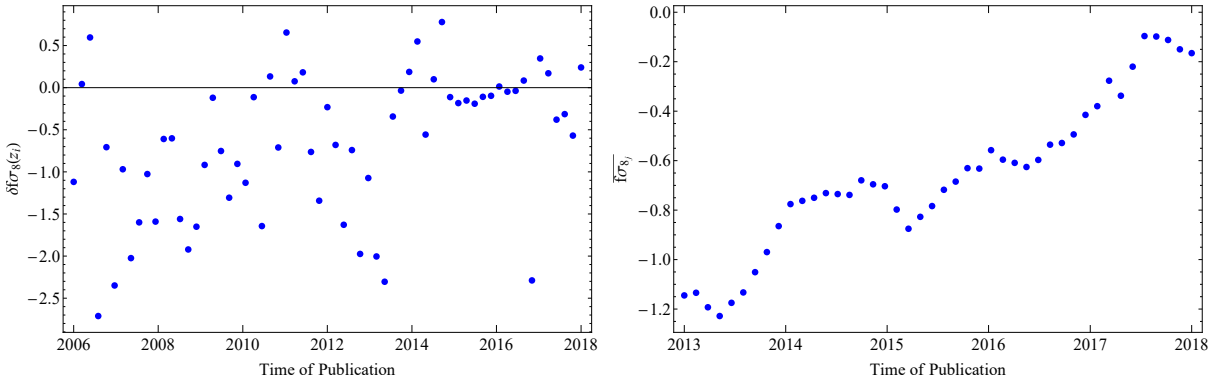

Figure 2.10: *Left Panel:* The residual of the data points assuming a Planck15/ΛCDM fiducial model correction based on Eq. (2.23). *Right Panel:* The 20 points moving average defined by Eq. (2.24) as a function of the time of publication. From Ref. [70].

Clearly, the consistency of the growth data with Planck15/ΛCDM significantly improves with the time of publication.

Let us now return to the possible overestimation of the errorbars of the growth data. If the errorbars of the growth data are indeed overestimated, then we expect the variance of the real data to be significantly smaller than the variance of random (Monte Carlo) data. Therefore, we construct 100 Monte Carlo realizations of the corresponding residual data, by assuming a gaussian distribution with zero mean value and a standard deviation equal to the errorbar of the real datapoint, for each Monte Carlo realization. The variance of the Monte Carlo data are illustrated in Fig. 2.11 as red dots along with the corresponding variance of the real data which is presented as a continues dashed line. The variance of the 100 Monte Carlo residual datasets is $\sigma^2_{MC} = 0.0079 \pm 0.0015$ while the variance of the real data residuals is $\sigma^2_{RealData} = 0.0030 \pm 0.055$. Clearly, the variance of the real data is significantly smaller than the variance of the Monte Carlo simulations. This reduced variance however is also affected by the possible correlations/double counting among these data. In order to estimate such effects, we artificially introduce double counting in the Monte Carlo data by enforcing 25% of the datapoints to have an identical corresponding datapoint in the Monte Carlo dataset. The corresponding results of this method are also illustrated in Fig. 2.11 as blue points. In this case, the variance of the Monte Carlo data

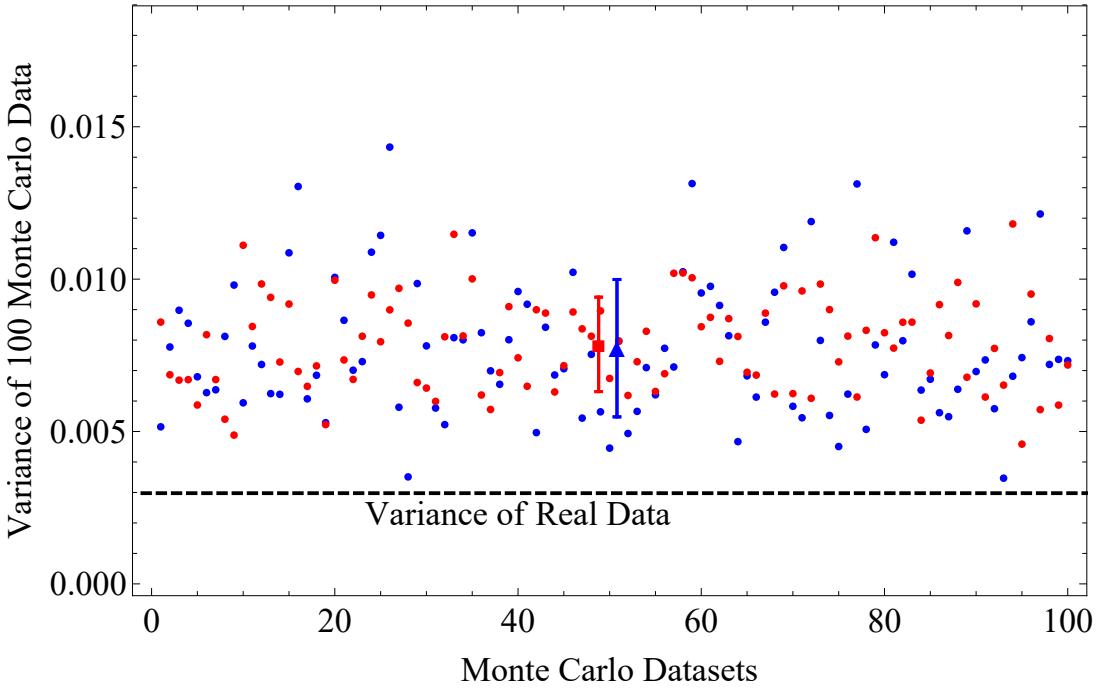

Figure 2.11: The variances of 100 Monte Carlo datasets. The red dots correspond to the variance of a Monte Carlo residual dataset with uncorrelated data, while each blue dot provides the variance of a residual dataset with 25% double counted datapoints (12 identical pairs of datapoints). The red square point describes the mean value of the uncorrelated data variances with the standard deviation, whereas the blue triangular point is the mean value of the correlated data variances with one standard deviation. From Ref. [70].

is $\sigma^2_{MC} = 0.0077 \pm 0.0023$, a value that is still significantly larger than the real data variance. As a result, we conclude that a moderate level of double counting is not enough to explain the reduced spread of the real data. This implies that either the errorbars of the growth data are truly overestimated or there are possible systematic effects the prevent data from having the anticipated spread from the errorbars.

2.3 Implications for the Phenomenological Parametrization (2.10)

2.3.1 Implication for the Phenomenological Parameter g_a

In the previous section we saw that more recent growth data are much more consistent with the Planck15/ΛCDM parameter values, since the level of tension drops significantly. This trend of reduced tension for the growth data would also affect the effective Newton's constant $G_{\rm eff}$ which we consider to have the form of the paremetrization (2.10). This trend can be well quantified by the parameter g_a, due to the fact that for $g_a = 0$ we reduce to the standard GR case. Assuming a Planck15/ΛCDM background, we fit the theoretically predicted $f\sigma_8(z, \Omega_{\rm m,0}^{Planck15}, \sigma_8^{Planck15}, g_a)$ obtained from Eqs. (1.50) and (1.54) to the full compilation (red square point in Fig. 2.12) presented in Table 2.1 as well as to the 20 earliest and recent subsets in order to identify the corresponding value of the parameter g_a starting starting from the

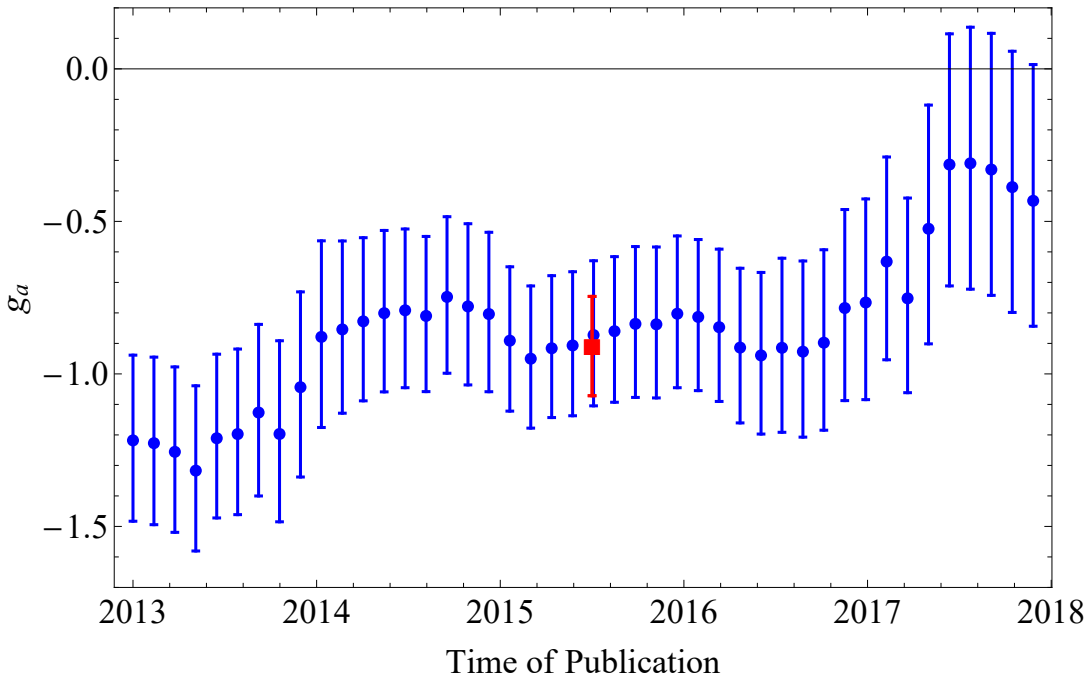

Figure 2.12: The evolution of the best fit of the parameter g_a with time of publication, superimposed with the 1σ range using the full RSD compilation presented in Table (2.1). Every blue point corresponds to the best fit of g_a obtained from a 20 point RSD subsample, starting from the earliest (first blue point on the left) to the latest (last blue point on the right) subsample. The red square point describes the best fit of g_a obtained from the full dataset along with its 1σ errorbar. From Ref. [70].

earliest to the latest subsample (blue points).

The 1σ range for g_a for the full compilation is $g_a = -0.91 \pm 0.17$. The 20 point subsamples best fit for g_a, begin from $g_a = -1.28^{+0.28}_{-0.26}$ (the earliest subsample) which is more than 4σ away than the GR predicted value ($g_a = 0$) and ends with the subsample of the 20 most recent datapoints which gives $g_a = -0.43^{+0.46}_{-0.41}$, a value consistent with the GR prediction since the difference is approximately at the 1σ level. It is important to note here that for all the subsamples, the growth data hint towards a negative value for g_a. Therefore, from the form of (2.10) we see that at high redshifts where the third term dominates $G_{\rm eff} > G_{\rm N}$, while at low (and intermediate) redshifts the second term dominates leading to $G_{\rm eff} < G_{\rm N}$. Hence we deduce that in order to optimize the fit to the growth data we either need to modify the background $H(z)$ [*e.g.* lowering the $\Omega_{\rm m,0}$ and/or the σ_8 parameter value) or by lowering the strength of gravity at low z [*e.g.* considering a modified gravity theory in the context of which $G_{\rm eff} < G_{\rm N}$ at low z, such as the phenomenological form of (2.10)].

2.3.2 Implications for the Growth Index γ

A decreasing $G_{\rm eff}$ at low z, exhibits also a characteristic behavior in the growth index γ. In the context of ΛCDM, the growth index is nearly constant as it is indicated by (2.15). For modified gravity theories however, γ departs from this quasi-constant behaviour [451] and can be written at low z as [452]

$$\gamma(z) = \gamma(0) + \gamma'(0)\, z = \gamma_0 + \gamma_0'\, z\,. \tag{2.25}$$

A similar differential equation as (1.50) can be constructed for the growth rate $f(a)$. Using its definition, Eq. (1.50) takes the form [444, 446, 448, 452, 453]

$$\frac{df}{d\ln a} + f^2 + \frac{1}{2}\left(1 - \frac{d\ln\Omega_m}{d\ln a}\right) f = \frac{3}{2}\frac{G_{\rm eff}}{G_{\rm N}}\Omega_m\,, \tag{2.26}$$

where Ω_m is given by Eq. (2.14). Substituting (2.15), Eq. (2.26) takes the form

$$2\ln\Omega_m\,\frac{d\gamma}{d\ln a} + (2\gamma - 1)\,\frac{d\ln\Omega_m}{d\ln a} + 1 + 2\Omega_m^{\gamma} - 3\frac{G_{\rm eff}}{G_{\rm N}}\Omega_m^{1-\gamma} = 0\,. \tag{2.27}$$

Hence, knowing the background expansion and the $\Omega_{\rm m,0}$ value we can calculate γ for a specific form of $G_{\rm eff}$, since we are left with a simple first order differential equation [446, 452, 453].

In order to solve the differential equation, we need to fix the initial condition in the past in order to find $\gamma(z)$. We choose to set $\gamma_0 \equiv \gamma(0)$ and $\gamma_0' \equiv \gamma'(0)$, for each (g_a, n) pair. It is important to note here that the initial conditions (in the past) are essentially irrelevant at the present time because of the presence of an attractor, so we get the same behavior at late time. At $z = 0$, Eq. (2.27) in the context of a Planck15/ΛCDM background is written as

$$\gamma_0' = \frac{1}{2\ln\Omega_{\rm m,0}}\left[3(2\gamma_0 - 1)(\Omega_{\rm m,0} - 1) + 1 + 2\Omega_{\rm m,0}^{\gamma_0} - 3\,\frac{G_{\rm eff}(0)}{G_{\rm N}}\Omega_{\rm m,0}^{1-\gamma_0}\right]\,. \tag{2.28}$$

In our case, by definition, we have $G_{\rm eff}(0) = G_{\rm N}$ thus irrespective of the value of g_a we obtain a linear relation between γ_0' and γ_0 (in consistency with the results of Ref. [446]), that is illustrated in Fig. 2.13.

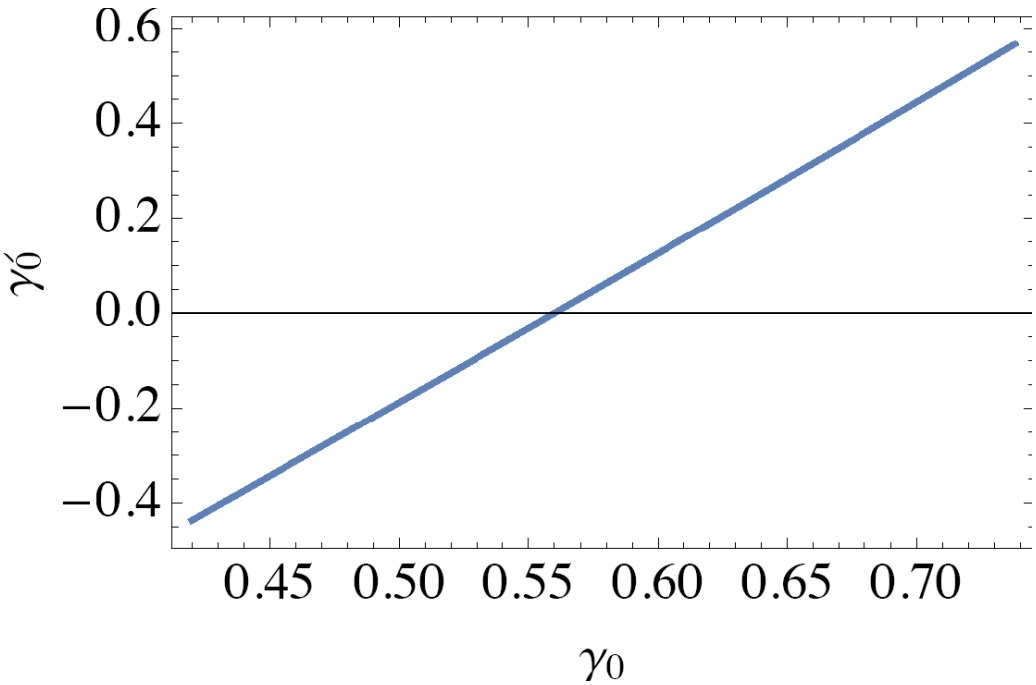

Figure 2.13: The linear relation that connects γ_0' and γ_0 irrespectively of the values of g_a and n and a fixed background to Planck15/ΛCDM. From Ref. [452]. For the reproduction of this figure visit the following dropbox link.

For completeness, we also provide the values of the pair (γ_0, γ_0') corresponding to the parameters (g_a, n) with $n \leq 6$ that are favored by the "Gold-2017" RSD data compilation presented in

n	g_a	γ_0	γ_0'
0.343	-1.200	0.686	0.398
2	-1.156	0.629	0.219
3	-1.534	0.620	0.189
4	-2.006	0.615	0.174
5	-2.542	0.612	0.165
6	-3.110	0.611	0.160

Table 2.3: The corresponding values of (γ_0, γ_0') for various best fit (n, g_a) pairs favored by the RSD compilation presented in Ref. [68].

Ref. [68]. For each value of n, the best fit value of g_a is shown in Table 2.3. Hence for each best fit of g_a we can identify the corresponding best fit form of $G_{\rm eff}$.

2.4 Implications for Specific Modified Gravity Models

The trend of growth data that seem to favor weaker gravity at low z is a unique feature that shows significant promise for a discrimination between different cosmological models and needs further investigation. It would be interesting to see if any of the most well known modified gravity models such as the ones discussed in Chapter 1 can support such a behavior. A naive approach would be to assume that any modified theory of gravity can lead to $G_{\rm eff} < G_{\rm N}$ at low z for specific parameter values. However, as we argue in the following subsections this is not the case for at least two prominent and intensively studied examples of modified gravity theories such as the $f(R)$ [448, 452] and scalar tensor theories [452].

2.4.1 $f(R)$ Gravities

In the context of $f(R)$ gravity theories, we recall Eq. (1.90) from Chapter 1 which gives the predicted form for $G_{\rm eff}$ as [300]

$$G_{\rm eff}(k,z) = G_{\rm N}\left\{\left(\frac{df}{dR}\right)^{-1}\left[\frac{1+4\left(\frac{d^2f}{dR^2}/\frac{df}{dR}\right)\cdot k^2\,(1+z)^2}{1+3\left(\frac{d^2f}{dR^2}/\frac{df}{dR}\right)\cdot k^2\,(1+z)^2}\right]\right\}.$$

In the literature, another alternative form for $G_{\rm eff}$ has been proposed including λ_c, *i.e.* the Compton wavelength of the scalaron [169]

$$G_{\rm eff}(k,z) = G_{\rm N}\left\{\left(\frac{df}{dR}\right)^{-1}\left[1+\frac{\left(\frac{\lambda_c}{\lambda}\right)^2}{3\left(1+\left(\frac{\lambda_c}{\lambda}\right)^2\right)}\right]\right\}, \tag{2.29}$$

where $\lambda = a(t)/k$ and $\lambda_c \equiv 3\frac{d^2f}{dR^2}/\frac{df}{dR}$ for consistency with (1.90). In viable $f(R)$ models, all relevant cosmic scales satisfy $\lambda \gg \lambda_c$, with $\frac{df}{dR} = 1$ to high accuracy, deep in the matter era regaining as a result the usual growth of perturbations during that era.

As we discussed in the Introduction, in order to ensure the stability of scalar perturbations in order to avoid ghost instabilities the $\frac{d^2 f}{dR^2}/\frac{df}{dR}$ should be positive. Therefore, the factor in front of the brackets increases when R decreases with the expansion, and thus it is always larger than unity. Moreover, the bracket expression is obviously always larger than one too. At low redshifts, as the critical length λ_c increases significantly with the decrease of matter density and of the Ricci scalar R, the expression inside the brackets can become as large as $\frac{4}{3}$ in the present era on scales $\lambda \ll \lambda_c$. Hence, the growth of matter perturbations on these scales will be enhanced compared to the standard growth. Note that this does not exclude the possibility for $G_{\rm eff}$ to evolve non monotonically as a function of z. Indeed, $G_{\rm eff}$ can, and generically does, increase with z on some interval in the present era, however always satisfying $G_{\rm eff} > G_{\rm N}$. Therefore, the $f(R)$ modified gravity theories support stronger gravity at low z than GR, hence unable they are unable to resolver the growth tension, independently of the form of the background $H(z)$ [452].

2.4.2 Scalar Tensor Theories

On the contrary, this is not the case if we consider standard scalar tensor theories as described in Chapter 1. In the context of scalar tensor theories, starting from an action of the form of Eq. (1.80), we derive the effective Newton's constant to be [146, 147]

$$G_{\rm eff}(z) = G_{\rm N}\left[\frac{1}{F(z)}\frac{F(z)+2\left(\frac{dF}{d\phi}\right)^2}{F(z)+\frac{3}{2}\left(\frac{dF}{d\phi}\right)^2}\right],$$

i.e. Eq. (1.85). Defining the rescaled square Hubble parameter as [68, 148]

$$q(z) = \frac{H^2(z)}{H_0}, \tag{2.30}$$

it is straightforward to show that Eq. (1.84) takes the form [68, 72, 148, 295]

$$F''(z) + \left[\frac{q'(z)}{2q(z)} - \frac{2}{1+z}\right]F'(z) - \frac{1}{(1+z)}\frac{q'(z)}{q(z)}F(z) + 3\frac{1+z}{q(z)}\Omega_{\rm m,0} = -\phi'(z)^2, \tag{2.31}$$

where in this case the primes denote differentiation with respect to the redshift z.

In the present analysis, we mainly focus on the low redshift regime, so we can Taylor expand the evolving Newton's constant (keeping terms up to second order) as

$$G_{\rm eff}(z) \approx G_{\rm eff}(0) + G'_{\rm eff}(0)\, z + G''_{\rm eff}(0)\,\frac{z^2}{2} + \dots \quad . \tag{2.32}$$

Taking into account the inequality for the first derivative of the effective Newton's constant induced by solar system test, *i.e.* Eq. (2.11), the calculations are massively simplified, since (2.32) reduces to

$$G_{\rm eff}(z) \approx G_{\rm eff}(0) + G''_{\rm eff}(0)\,\frac{z^2}{2} + \dots \quad . \tag{2.33}$$

Therefore, setting $G_{\rm N} = F(0) = 1$, $F'(0) \approx 0$ and differentiating (1.85) with respect to the redshift z, we deduce

$$G''_{\rm eff}(0) = F''(0)\left(-1 + \frac{F''(0)}{\phi'(0)^2}\right). \tag{2.34}$$

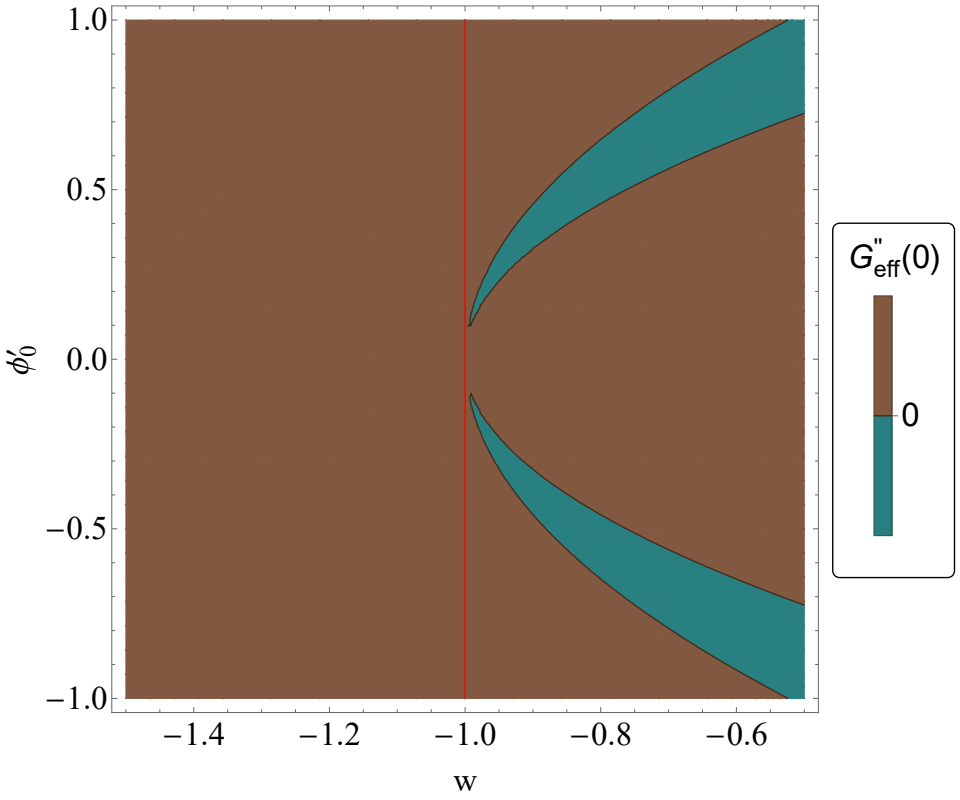

Figure 2.14: The second derivative of $G_{\rm eff}(0)$ in the parametric space of $\phi'(0)$ and w for $\Omega_{\rm m,0} = 0.3$. The brown (blue) regions correspond to the parameter values for $G''_{\rm eff}(0) > 0$ ($G''_{\rm eff}(0) < 0$), while the red straight line describe the ΛCDM case, where $w_\Lambda = -1$. From Ref. [452]. For the reproduction of this figure visit the following dropbox link.

In the context of wCDM background the rescaled square Hubble parameter based on (1.69), is written as

$$q(z) = \Omega_{\rm m,0}(1+z)^3 + (1-\Omega_{\rm m,0})\,(1+z)^{3(1+w)}\,. \tag{2.35}$$

Therefore, the second derivative of $G_{\rm eff}$ takes the following form [72, 452]

$$G''_{\rm eff}(0) = 9(1+w)(-1+\Omega_{\rm m,0}) + \frac{9(1+w)^2(-1+\Omega_{\rm m,0})^2}{\phi'(0)^2} + 2\,\phi'(0)^2\,. \tag{2.36}$$

Eq. (2.36) is quite interesting since it is considerably simplified in the context of a ΛCDM background, *i.e.* for a value $w_\Lambda = -1$, yielding [72, 452]

$$G_{\rm eff}(z) \approx G_{\rm eff}(0) + \frac{1}{2}G''_{\rm eff}(0)\,z^2 + \ldots = G_{\rm N} + \frac{1}{2}G''_{\rm eff}(0)\,z^2 + \ldots = 1 + \phi'^2(0)\,z^2 + \ldots \quad . \tag{2.37}$$

Clearly, $G_{\rm eff}(z)$ will increase rather than decrease in the past on low redshifts assuming that the kinetic term of $\phi'(z)$ is always positive, a crucial requirement for a self consistent theory. It is possible however to get a decreasing $G_{\rm eff}(z)$ if one moves away from a ΛCDM background towards higher values of w for either a positive or a negative value of $\phi'(0)$. This is shown in Fig. 2.14, where $G''_{\rm eff}(0) < 0$ (blue regions) can only be achieved for $w > -1$ for a fixed value $\Omega_{\rm m,0} = 0.3$ (this behavior however remains valid for different values of $\Omega_{\rm m,0}$). The presented results assume that $G'_{\rm eff}(0) \simeq 0$ due to solar system constraints. In the presence of screening

this assumption may not be necessary as in that case the cosmological behavior of $G_{\rm eff}$ gets decoupled from the corresponding behavior in the solar system where the mean curvature and density are significantly larger than in cosmological scales. However, as we have seen with $f(R)$ models, this does not necessarily imply that a decreasing $G_{\rm eff}(z)$ is allowed and actually in these models, it is not allowed.

2.5 Constraints of the Evolving Newton's Constant from Low l CMB and the Integrated Sachs Wolfe Effect

If the Newton's constant is indeed evolving with redshift, resolving as a result the growth tension, then we would expect to find similar hints to other geometrical and/or dynamical probes. For example, such an evolution would lead to an evolution of the degenerate combination $\mathcal{M} \equiv M - 5\,log_{10}(h) + 42.38$ of SnIa, where M corresponds to the absolute magnitude and $h \equiv H_0/100\ km\,s^{-1}\,Mpc^{-1}$ [73, 454–458][4]. Also, a possible evolution of $G_{\rm eff}(z)$ would affect [68, 459] the low l CMB angular power spectrum due to the Integrated Sachs Wolfe (ISW) effect [460, 461]. The ISW effect is created when the CMB photons escape from time varying gravitational potential which would be modified due to the evolving $G_{\rm eff}(z)$.

The construction of the CMB power spectrum analytically is a quite tedious process, since we need to take into account all particle species and calculate how the perturbations affect particle distributions by solving the Boltzmann equations, calculate the $\Delta T/T$ anisotropies and expand in spherical harmonics. The unintegrated Boltzmann equation has the following general form [298]

$$\frac{df}{dt} = C[f]\,, \tag{2.38}$$

where f corresponds to the distribution function. The right hand side contains all possible collision terms (*e.g.* the Compton scattering) and should be evaluated up to the first order for the line element (1.52). Fortunately, over the years, some numerical codes have been developed that perform such a task and numerically calculate the CMB and large scale structure observables, such as the `Code for Anisotropies in the Microwave Background (CAMB)` [462] and the `Cosmic Linear Anisotropy Solving System (CLASS)` [463, 464] codes. As we mentioned earlier, many modified gravity theories have been proposed in the literature as ΛCDM alternatives, leading as a result to the development of appropriate patches [such as the `Modified Growth with CAMB (MGCAMB)` [465–467] and the `hi_class` [468, 469] patches] in the aforementioned codes[5]. Utilizing the 2019 version of the `MGCAMB` numerical package [467] we fix the background $H(z)$ to the best fit Planck15/ΛCDM [17], use the parametrization (2.10) as the effective Newton's constant and construct the corresponding CMB angular power spectrum for various values of g_a as it is illustrated in Fig 2.15 superimposed with the Planck15 datapoints (blue points). Clearly, the low l Planck data show that even though modified gravity with an effective Newton's constant of the form of Eq. (2.10) is not excluded, they do not allow for significant variations of g_a entailing strong constraints in it.

In order to fully constrain the values of the predicted observables, `CAMB` works in tandem with the MCMC sampler `Cosmological MonteCarlo (COSMOMC)` [470, 471]. A similar patch as the `MGCAMB` is developed for `COSMOMC` called `MGCOSMOMC` [465–467] that sets constraints on

[4] See Chapter 4 for an extensive discussion on this subject.

[5] For more details about recent Boltzmann codes, see Appendix B.

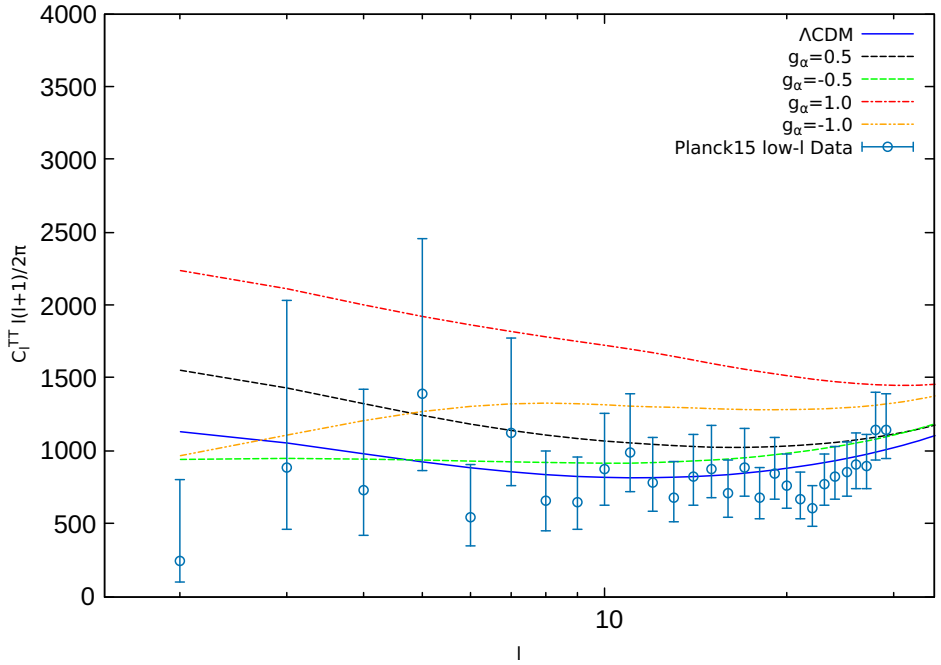

Figure 2.15: The CMB Planck 2015 power spectrum for different values of g_a using `MGCAMB` [467]. The low l data show that a modified gravity with an effective Newton's constant of the form of Eq. (2.10) is possible. From Ref. [73].

modified growth along with dark energy parameters using various cosmological data. Utilizing its 2019 version [467] we derive the constraints for the g_a parameter. In particular, fixing the majority of the parameters to the corresponding Planck15/ΛCDM values [17] except from the $(\Omega_{\rm m,0}, \sigma_8, H_0)$ that are free to vary we obtain the $1\sigma - 2\sigma$ confidence contours shown in Fig. 2.16.

Even though negative values of g_a are mildly favored, this parameter is significantly constrained by the CMB data [68] to be larger than -0.1 at a 3σ level. This range is at odds with the findings of the RSD compilation discussed above indicating that tension of the growth data with Planck15/ΛCDM can only be partially physical [452]. At least part of this tension is probably due to systematic effects of the growth data.

2.6 In Brief

In this Chapter we have constructed an updated compilation (63 datapoints) of distinct RSD data that have been published by several redshift surveys and are presented in Table 2.1. Even though this dataset is plagued by correlations among datapoints and possible double counting it is still useful in identifying general trends of the data as well as the sensitivity of the best fit parameters to the fiducial model corrections and to correlations among the datapoints. Considering various subsamples from the full dataset, we have demonstrated that the consistency of the growth data with Planck15/ΛCDM improves significantly with time. In particular, for the growth data that are published in the last couple of years, the tension with Planck15/ΛCDM reduces even below the 1σ threshold, in contrast to data before 2016 for which the tension ranges from $3\sigma - 5\sigma$ (depending on the selected subset).

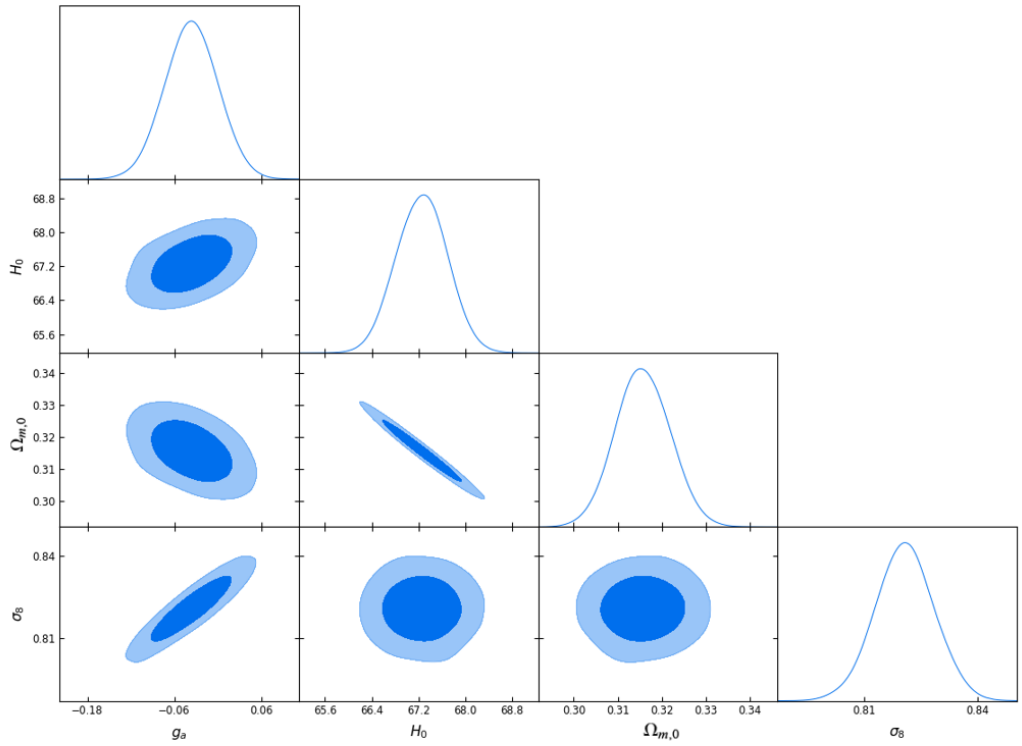

Figure 2.16: The $1\sigma-2\sigma$ confidence contours constructed using the `MGCOSMOMC` [467] package for the Planck15/ΛCDM CMB data [17], in the context of the parametrization (2.10) and setting $n = m = 2$. From Ref. [73].

This trend for reduced tension of the growth data with Planck15/ΛCDM is quite an interesting feature. If this trend is not due to some unknown systematic effect, it naturally leads to hints for an evolving effective Newton's constant $G_{\rm eff}(z)$. Even though a partial cause for this reduced tension is obviously due to the fact that more recent data tend to probe higher redshifts (with higher errorbars) where there is degeneracy among different models due to matter domination, all the considered RSD subsamples seem to prefer a $g_a < 0$ value, implying a decreasing function of $G_{\rm eff}(z)$ with respect to the redshift z. Furthermore, we have demonstrated that a parametrization such as (2.16) provides an excellent fit to the product $f\sigma_8(z)$ in both GR ($g_a = 0$) and in modified gravity theories ($g_a \neq 0$).

Moreover, we have studied the consequences of a decreasing $G_{\rm eff}$ with redshift to the growth index γ. The required behavior for $G_{\rm eff}$ assuming a ΛCDM background exhibits a characteristic signature in the corresponding growth index γ. In particular, for the parametrization (2.10) with $n \leq 6$ a growth index parametrization (2.25) gives $0.61 \leq \gamma_0 \leq 0.69$ and $0.16 \leq \gamma_0' \leq 0.4$ according to Table 2.3. We have further studied the implications of a decreasing function of $G_{\rm eff}(z)$ with respect to the redshift z for two of the most prominent and intensively studied modified gravity models, such as the $f(R)$ and scalar tensor theories. In the context of $f(R)$ modified gravity theories the effective Newton's constant is given by Eq. (1.90) and it is clear from its form that in order to ensure the absence of ghost instabilities $G_{\rm eff} > G_{\rm N}$ irrespective of the background expansion $H(z)$. On the contrary, for the scalar tensor theories a decreasing $G_{\rm eff}$ at low redshifts is only possible if $w > -1$ and can not be realized in the context of a ΛCDM background.

Finally, we have discussed the consequences of a decreasing $G_{\rm eff}$ with redshift to other

geometrical and/or dynamical probes. Such a behaviour affects the low l CMB angular power spectrum due to the ISW effect. Utilizing the `MGCAMB` and `MGCOSMOMC` numerical codes for the parametrization (2.10), we derived strong constraints regarding the phenomelogical parameter g_a, showing that the Planck data mildly favor a Newton's constant that is weaker at low z compared to GR.

Chapter 3

Constraining Power of Cosmological Observables: Blind Redshift Spots and Optimal Ranges

ΛCDM is currently under intense investigation in the last twenty years using a wide variety of cosmological surveys in an attempt to identify any hidden unexpected features and signatures of theories beyond the concordance model. A general trend of the ongoing and future cosmological surveys is to focus in redshift ranges that are larger than the redshift ranges of the earlier surveys. In theory, this trend seems to be in the right direction for the identification of any possible hidden signals of a modified theory of gravity. However, it entails an assumption of an increasing constraining power of observables on cosmological parameters with redshift, which is not true in all cases.

Previous works [472, 473] considering older growth compilations, have identified interesting degeneracies of the $f\sigma_8(z)$ observable with respect to the equation of state parameter w_{DE} at $z \approx 1.7$ and that the optimal range is in the redshift range $z \in [0.1, 1.5]$. Furthermore, in Fig. 2.2 we saw that for $z > 1.5$ the different models make similar predictions due to matter domination, so it is only natural to wonder if a similar behavior is apparent to other cosmological parameters. In this Chapter we extend the results of the previous works [472, 473] to a more broad range of cosmological observables.

At first, we consider the sensitivity of the $f\sigma_8(z)$ observable on the cosmological parameters $\Omega_{\mathrm{m},0}, w$ and the extra parameter g_a that appears in the phenomenological parametrization (2.10), using the extensive compilation presented in Table 2.1 of Chapter 2. The parameter w corresponds to a wCDM background, *i.e.* to a model with a constant equation of state $w_{DE} \equiv w$. Next after carefully scanning the literature for BAO data and constructing a similar compilation, we identify the sensitivity of the relevant BAO observables on the same cosmological parameters as before. Finally, we focus on SnIa and their luminosity distance modulus as well as on the gravitational wave distance modulus and repeat the same analysis.

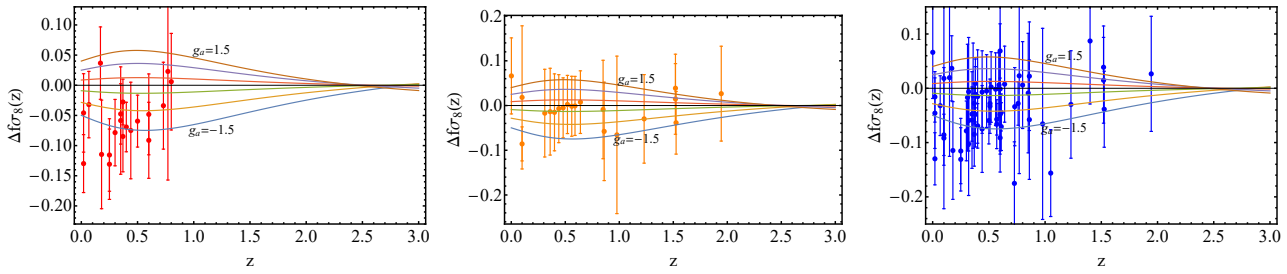

Figure 3.1: The variation (3.1) for $O = f\sigma_8$ as a function of redshift z, for g_a values $g_a \in [1.5, -1.5]$. Also, we include the compilation of Table 2.1 showing the 20 earliest growth data of the compilation (left panel), the 20 latest growth data of the compilation (middle panel) as well as the full compilation (right panel). From Ref. [474].

3.1 Growth of Density Perturbations: The Observables $f\sigma_8(z)$ and $f(z)$

Based on the analysis presented in Chapter 1 and in particular based on Eq. (1.54), it is easy to derive the evolution of the $f\sigma_8(z)$ and $f(z)$ observables for the parameters $\Omega_{\rm m,0}, w$ and g_a around the corresponding Planck15/ΛCDM parameters $\left(\Omega^{PL}_{\rm m,0} = 0.31, w = -1 \text{ and } g_a = 0\right)$. For each observable O, we construct the following variations

$$\Delta O_{g_a} \equiv O(\Omega^{PL}_{\rm m,0}, -1, g_a) - O(\Omega^{PL}_{\rm m,0}, -1, 0)\,, \tag{3.1}$$

$$\Delta O_{w} \equiv O(\Omega^{PL}_{\rm m,0}, w, 0) - O(\Omega^{PL}_{\rm m,0}, -1, 0)\,, \tag{3.2}$$

$$\Delta O_{\Omega_{\rm m,0}} \equiv O(\Omega_{\rm m,0}, -1, 0) - O(\Omega^{PL}_{\rm m,0}, -1, 0) \tag{3.3}$$

and as observables for the case of the growth data we consider either $O \equiv f\sigma_8(z)$ or $O \equiv f(z)$.

In Fig. 3.1 we consider the variation (3.1) for the parameter values $g_a \in [-1.5, 1.5]$ for the $f\sigma_8(z)$ observable. Moreover, we include the growth compilation presented in Table 2.1 applying no fiducial model correction and following the methods of the previous Chapter, we colour-code the data (data published before 2015 as red, data published after 2016 as orange and the full compilation as blue). As we can see from the left panel, the early growth data (red points) favor weaker gravity, *i.e.* negative values for g_a, around $z \simeq 0.5$ in consistency with the results of Fig. 2.12. Furthermore, we clearly see from all panels that the observable $f\sigma_8(z)$ presents a blind spot with respect to the parameter g_a at $z \simeq 2.7$, a value close to the one repored by previous studies [472] for a similar gravitational strength parameter. On the contrary, the optimum redshift region is around $z \simeq 0.5$ for the parameter g_a, indicating that more recent probes that measure $f\sigma_8(z)$ at larger redshifts, in reality approach the blind spot region. As a result, the newest datapoints have reduced sensitivity in identifying any deviations from $G_{\rm eff}$. In Figs. 3.2 and 3.3 we consider the variations (3.2) and (3.3) for the observable $f\sigma_8(z)$ for $w \in [-1.5, 0.5]$ and $\Omega_{\rm m,0} \in [0.25, 0.35]$. From these figures we find similar conclusions as before. More recent data approach the blind spot for both the parameters w and $\Omega_{\rm m,0}$, in contrast to earlier data.

However, the identification of an optimal redshift range in which the constraining power is maximum or minimum can not be solely addressed by pinpointing where the blind spots and optimal redshift ranges are. The constraining power depends also on the number of modes that are sampled by the survey, *i.e.* on the effective survey volume $V_{\rm eff}(k, z)$. The effects of the

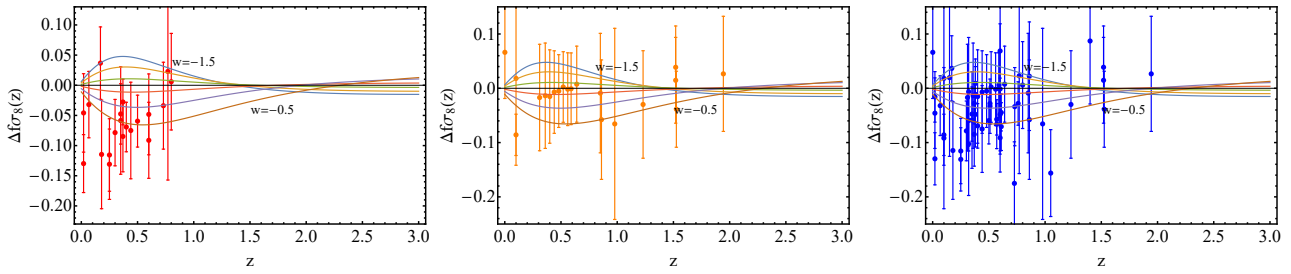

Figure 3.2: Same as Fig. 3.1 for the w values $w \in [-1.5, -0.5]$. From Ref. [474].

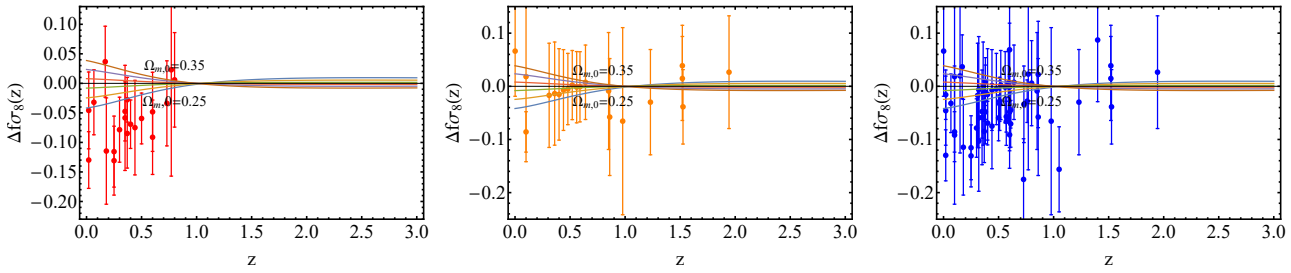

Figure 3.3: Same as Fig. 3.1 for the $\Omega_{\rm m,0}$ values $\Omega_{\rm m,0} \in [0.25, 0.35]$. From Ref. [474].

survey volume can be quantified through the "sensitivity" measure [474]. For a specific k mode of the power spectrum $P(k,z)$ the effective survey volume probed for this particular k mode is given by

$$V_{\rm eff}(k,z) = \Delta\Omega \int_0^z \left[\frac{n(z')\,P(k,z')}{1+n(z')\,P(k,z')}\right]^2 \frac{dV}{dz'\,d\Omega} dz'\,, \tag{3.4}$$

where z in the upper limit of the integral corresponds to the maximum redshift of the effective survey volume $V_{\rm eff}(k,z)$ and $\Delta\Omega$ is the sky area of the survey. The ratio

$$\frac{dV}{dz\,d\Omega} = \frac{\chi^2(z)}{H(z)} \tag{3.5}$$

describes the infinitesimal comoving volume element for a FLRW Universe and χ is given by (1.41), while the number density $n(z)$ of the detected galaxies is calculated as

$$n(z) = \int_{M_{lim}(z)}^{\infty} \frac{dN}{dV\,dM} dM \tag{3.6}$$

and the function $M_{lim}(z)$ is the limiting mass threshold which is detected for the given survey.

The typical error σ_P of the measurement of the power spectrum $P(k,z)$ for a given mode k is [475–478]

$$\left(\frac{\sigma_P}{P(k,z)}\right)^2 = \frac{2}{4\,\pi\,k^3 \Delta(\ln\,k)} \frac{(2\pi)^3}{V_{\rm eff}(k,z)} \left[\frac{1+n(z)\,P(k,z)}{n(z)\,P(k,z)}\right]^2\,, \tag{3.7}$$

demonstrating that the error σ_P increases as the effective survey volume $V_{\rm eff}(k,z)$ decreases. Therefore, since the typical error σ_P is inversely proportional to $\sqrt{V_{\rm eff}(k,z)}$, the "sensitivity" measure for an observable O is defined as [474]

$$S_p^O \equiv \frac{\Delta O(p)}{\Delta p} \sqrt{V_{\rm eff}(k,z)}\,, \tag{3.8}$$

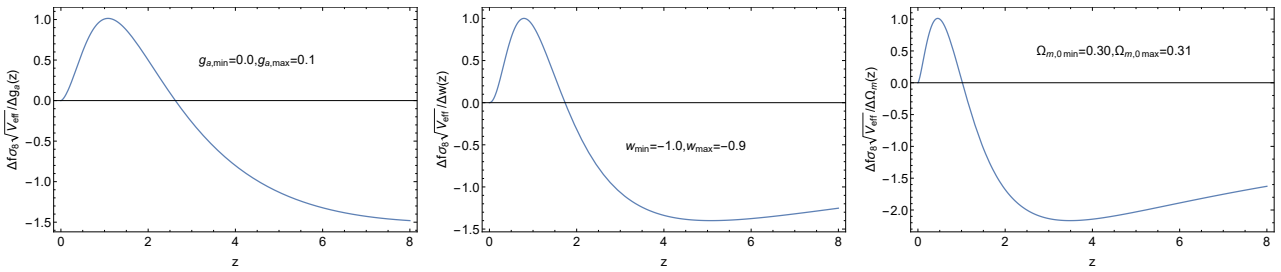

Figure 3.4: The "sensitivity" measure (3.8) for the parameters $p = g_a$, $p = w$ and $p = \Omega_{\rm m,0}$. From Ref. [474].

where ΔO is the deviation of the observable O for a given parameter p that varies in a fixed small range $\Delta p = p_{max} - p_{min}$ around a fiducial model value (*e.g.* Planck15/ΛCDM). Fixing k in such a way that $np = 3$ assuming sufficient signal to noise per pixel [478] and rescaling the "sensitivity" S so that is unity at its maximum absolute value, we construct the plot of the "sensitivity" measure S for the $f\sigma_8(z)$ observable with respect to g_a, w and $\Omega_{\rm m,0}$. This plot is demonstrated in Fig. 3.4 and the corresponding blind spots are illustrated as the points were $S = 0$, *i.e.* the roots of the sensitivity measure whereas the corresponding optimum redshift region is illustrated as the extrema (maximum or minimum values) of S.

Obviously, all three panels present both blind spots and optimum redshift regions. According to Fig. 3.4, for the parameter g_a the blind spot is at $z \simeq 2.6$, while the optimum redshift region is at $z \simeq 1.2$. For the parameter w the blind spot is detected close to $z \simeq 2$, while the optimum redshift region is at $z \simeq 0.8$. For the parameter $\Omega_{\rm m,0}$ the blind spot is pinpointed close to $z \simeq 1$, while the optimum redshift region is close to $z \simeq 0.5$[1]. It is important to note here that when incorporating the effects of the effective survey volume, the optimum redshift region shift to somewhat higher redshifts while the blind spots remain unchanged.

A similar study can be implemented for the growth rate $f(z)$ observable [see Eq. (1.54)] using the mock data of the Euclid survey that have been presented in Ref. [479]. The Euclid mission, that aims to study the nature of dark matter dark energy and gravity measuring galaxy clusters up to redshifts $z \simeq 2$, indicated that the large number of galaxy clusters and its depth will allow a reliable simultaneous estimate of the bias b and of the growth rate $f(z)$ through the redshift distortion β that is defined as

$$\beta(z) = \frac{f(z)}{b(z)}\,. \tag{3.9}$$

Therefore, the mission has the ability to directly probe the bias free combination $f\sigma_8(z)$ and the growth observable $f(z)$. Of course, what is actually observed is the redshift distortion β parameter which is obtained through the ratio between the monopoles of the correlation functions in real and in redshift space, so the identification of the blind spots and the optimum redshift regions remain valid assuming that the bias $b(z)$ has a weak dependence on the redshift z.

The deviation of the observable $f(z)$ [recall Eqs. (3.1)-(3.3)] for the parameters $p = g_a$ (left panel), $p = w$ (middle panel) and $p = \Omega_{\rm m,0}$ (right panel) superimposed with the mock Euclid data assuming a Planck15/ΛCDM fiducial model and their 1σ errors [479] are illustrated in

[1]Even though the redshift region $z > 2$ seems an area with better sensitivity for all the parameters, there are currently almost no RSD data available in this redshift range.

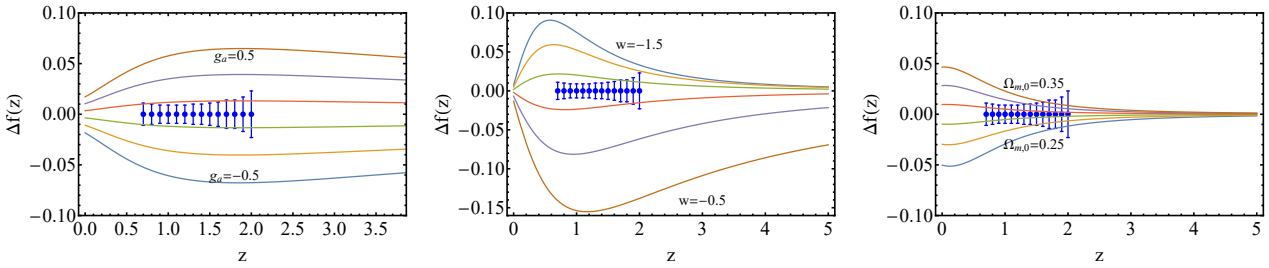

Figure 3.5: The variations (3.1)-(3.3) for $O = f$ as a function of redshift z for the same parameters limits as before. We also include the mock data of the Euclid survey as presented in Ref. [479]. From Ref. [474].

Fig. 3.5. Clearly, the predicted redshift range of the Euclid data is ideal for the parameter g_a, in contrast for the matter density parameter $\Omega_{\rm m,0}$ or for w especially if $w < -1$.

3.2 Baryon Acoustic Oscillations: The $D_V(z) \times \frac{r_s^{fid}}{r_s}$, $H \times \frac{r_s}{r_s^{fid}}$ and $D_A \times \frac{r_s^{fid}}{r_s}$ Observables

3.2.1 BAO Observables and their Variation with Cosmological Parameters

At the beginning of cosmological time, the Universe was in a very hot and dense state where the dark matter, baryons, photons and neutrinos were all coupled constituting a thermal plasma. In this state photons were tightly coupled to the electrons via Compton scattering while the neutrinos moved very fast and did not interact at all. As the time passed, the baryons were drawn in high density regions due to gravity while at the same time the photons tried to free streaming out of these high density regions. However, since they were coupled in a baryonic-photon fluid a shock was induced that formed spherical shells of a baryonic-photon fluid that oscillated as spherical sound waves. At recombination, *i.e.* when the redshift is $z \approx 1300$, the Universe cooled down enough so that the protons and electrons combined, forming the first hydrogen atoms through the following reaction

$$e^- + p^+ \leftrightarrow H + \gamma \tag{3.10}$$

and the photons free streamed leaving the shells of baryons "frozen" in spacetime. Dark matter did not follow the same process and was just attracted and eventually fell in the high density regions. Therefore after recombination we are left with high densities of dark matter at the centre of the overdense regions which are surrounded by shells of baryons. This is illustrated in Fig. 3.6.

This procedure, that was first reported in Refs. [481,482], inflicts a characteristic BAO scale that appears either as a peak in the galaxy correlation function or equivalently as damped oscillations in the large scale structure power spectrum. The angular scale of the sound horizon θ_s at the drag epoch, *i.e.* at cosmological times shortly after recombination when photons decouple from baryons, is a measurable quantity that can be adopted to probe the Hubble

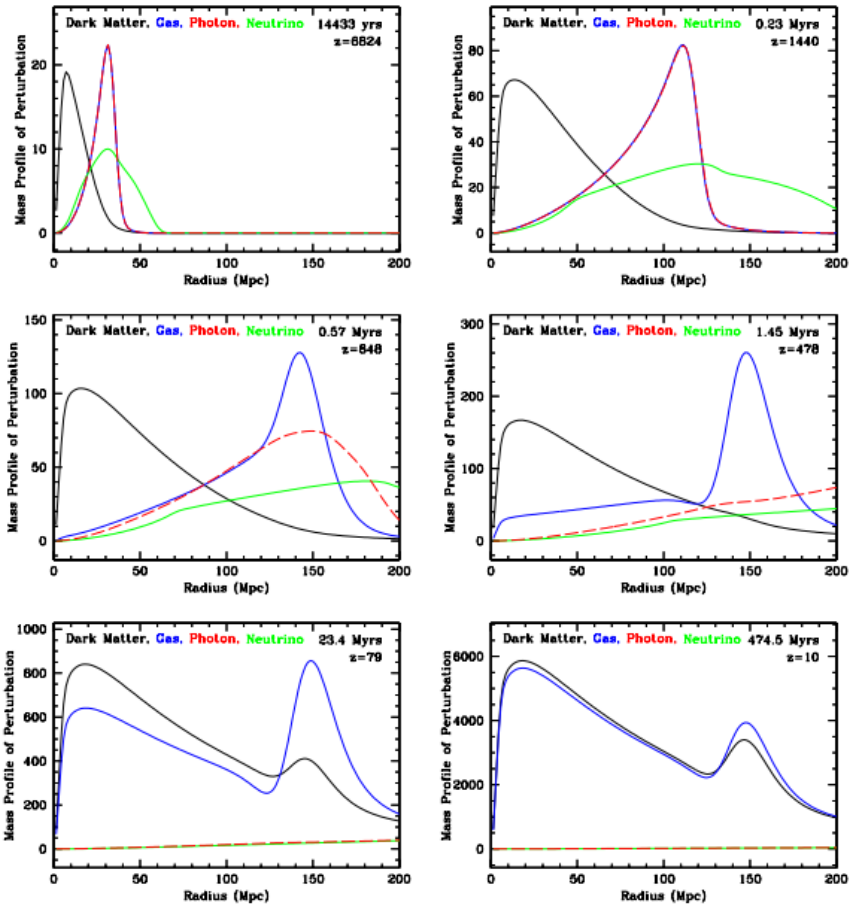

Figure 3.6: An illustration of the radial mass profile of perturbation as a function of the comoving radius of an initially point like overdensity located at the origin for various redshift values. The top subfigures correspond to early cosmological times before recombination, the middle subfigures correspond to redshifts a little bit after recombination, while the bottom subfigures correspond to cosmological times long after recombination. The black, blue, red and green lines correspond to the dark matter, baryons, photons, and neutrinos respectively From Ref. [480].

expansion rate through the standard ruler equation that yields [483]

$$\theta_s = \frac{r_s}{(1+z)\, d_A}\,, \tag{3.11}$$

where d_A is the angular diameter distance defined in (1.46) and r_s corresponds to the radius of sound horizon at last scattering that is defined as [46]

$$r_s = \int_{z_d}^{\infty} \frac{c_s(z)}{H(z)} dz\,. \tag{3.12}$$

The lower limit of (3.12) corresponds to the drag redshift z_d that can either be calculated through a numerical package, *e.g.* `CAMB` or using the approximate formula provided by [484]

$$z_d = \frac{1291(\Omega_m h^2)^{0.251}}{1+0.659(\Omega_m h^2)^{0.828}} \left[1 + b_1 (\Omega_b\, h^2)^{b_2}\right]\,, \tag{3.13}$$

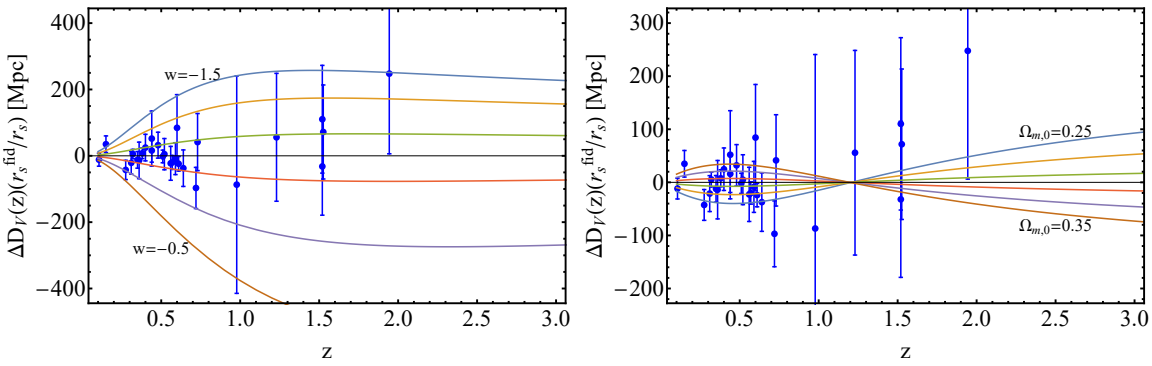

Figure 3.7: The variations (3.2) (left panel) and (3.3) (right panel) for $O = D_V \times \left(r_s^{fid}/r_s\right)$ as a function of redshift z. We also include the BAO data $D_V(z) \times \left(r_s^{fid}/r_s\right)$ presented in Table D.1 in the Appendix D. From Ref. [474].

with

$$b_1 = 0.313(\Omega_m h^2)^{-0.419}\left[1 + 0.607(\Omega_m h^2)^{0.674}\right], \tag{3.14}$$

$$b_2 = 0.238(\Omega_m h^2)^{0.223}. \tag{3.15}$$

The numerator of (3.12), *i.e.* $c_s(z)$, is the sound speed of the baryonic-photon fluid

$$c_s(z) = \frac{c}{\sqrt{3\left(1 + \frac{3\Omega_b}{4\Omega_\gamma}\frac{1}{1+z}\right)}}. \tag{3.16}$$

So, substituting (3.16) in (3.12), it is straightforward to show that the radius of the sound horizon is written as

$$r_s(z) = \frac{c}{\sqrt{3}}\int_{z_d}^{\infty}\frac{dz}{H(z)\sqrt{1 + \frac{3\Omega_b}{4\Omega_\gamma}\frac{1}{1+z}}}. \tag{3.17}$$

It is important to note here that Eq. (3.17) should be multiplied by a correction factor of 154.66/150.82 in order to achieve consistency with the more accurate numerical estimate [485]. Deviation of cosmological parameters can change the sound horizon r_s, hence BAO measurements in reality constrain specific combinations. In particular, they constrain the combinations $D_A(z) \times \frac{r_s^{fid}}{r_s}$ and $H(z) \times \frac{r_s}{r_s^{fid}}$, where $D_A(z) = d_A(z)$ is the angular diameter distance and r_s^{fid} corresponds to the fiducial cosmology assumed in the construction of the large scale structure correlation function. Another BAO measurement that is commonly published in the literature, is the following combination

$$D_V(z) \times \frac{r_s^{fid}}{r_s} = \left[c\, z\, D_M^2(z)/H(z)\right]^{1/3} \times \frac{r_s^{fid}}{r_s}, \tag{3.18}$$

where $D_M(z) = (1+z)D_A(z)$ [486]. Using (3.17) and assuming a Planck15/ΛCDM fiducial cosmology ($k = 0, h = 0.676$ and $r_s^{fid} = 147.49\, Mpc$) it is easy to construct the theoretically predicted redshift dependence of the BAO observables for various values of $\Omega_{\rm m,0}$ and w and compare with the corresponding BAO data compilation that is illustrated in Appendix D.

Using the theoretically predicted redshift dependence of the BAO observables we construct the deviations (3.2) and (3.3) for various values of w and $\Omega_{\rm m,0}$ respectively. In Fig. 3.7 we show

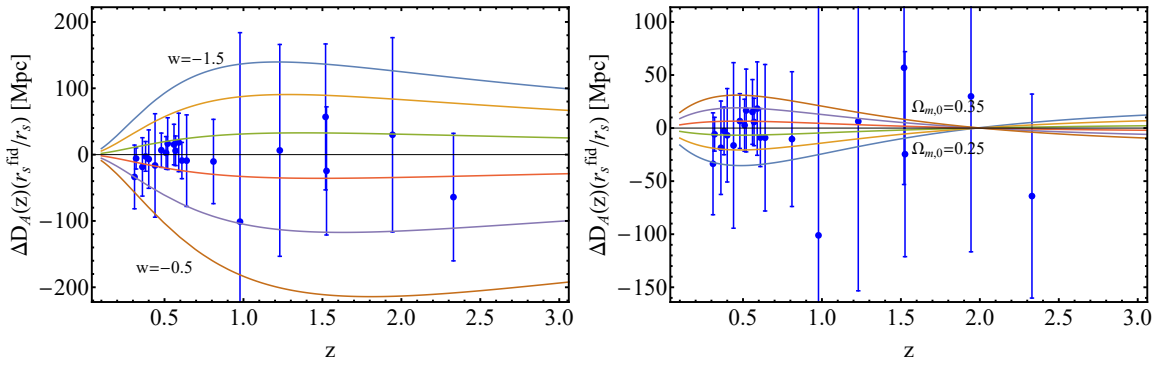

Figure 3.8: The variations (3.2) (left panel) and (3.3) (right panel) for $O = D_A \times \left(r_s^{fid}/r_s\right)$ as a function of redshift z. We also include the BAO data $D_A(z) \times \left(r_s^{fid}/r_s\right)$ presented in Table D.1 in the Appendix D. From Ref. [474].

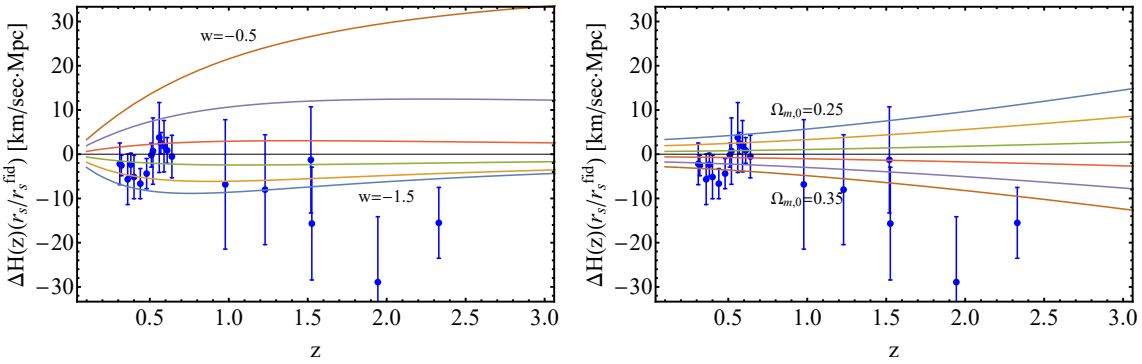

Figure 3.9: The variations (3.2) (left panel) and (3.3) (right panel) for $O = H \times \left(r_s/r_s^{fid}\right)$ as a function of redshift z. We also include the BAO data $H(z) \times \left(r_s/r_s^{fid}\right)$ presented in Table D.1 in the Appendix D. From Ref. [474].

the deviations of the observable $D_V(z) \times \frac{r_s^{fid}}{r_s}$ for $w \in [-1.5, -0.5]$ around $w = -1$ (left panel) and for $\Omega_{\rm m,0} \in [0.25, 0.35]$ around $\Omega_{\rm m,0} = 0.3$ (right panel). Notice the existence of a blind spot for the parameter $\Omega_{\rm m,0}$ at $z \simeq 1.2$, whereas the optimum redshift region is at $z \simeq 0.6$[2]. On the contrary, for the parameter w there is no blind redshift spot, while the optimum redshift region is at $z > 1.2$. Similarly, for the observable $D_A \times \frac{r_s^{fid}}{r_s}$ we construct Fig. 3.8. As we can see, a similar behavior with $D_V(z) \times \frac{r_s^{fid}}{r_s}$ is detected despite the fact that the blind spot for the parameter $\Omega_{\rm m,0}$ appears in a higher redshift ($z \simeq 2$). It is also interesting to note that the redshift region $z > 2$ produces significantly reduced sensitivity for the parameter $\Omega_{\rm m,0}$ in comparison to the $D_V(z) \times \frac{r_s^{fid}}{r_s}$ observable.

In Fig. 3.9 we construct the theoretically predicted deviations (3.2) (left panel) and (3.3) (right panel) for various values of w and $\Omega_{\rm m,0}$ respectively for the BAO observable $H(z) \times \frac{r_s}{r_s^{fid}}$. Obviously, the sensitivity increases monotically with redshifts for both the parameters w and $\Omega_{\rm m,0}$ and there are no blind redshift spots. Notice the asymmetry obtained for the equation of state parameter which is due to the fact that for $w < -1$ at early times the effects of dark energy are negligible for all values of w, leading to a degeneracy for this range of parameters

[2]Even though the redshift region $z > 2$ seems an area with better sensitivity for all the parameters, there are currently almost no BAO data available in this redshift range.

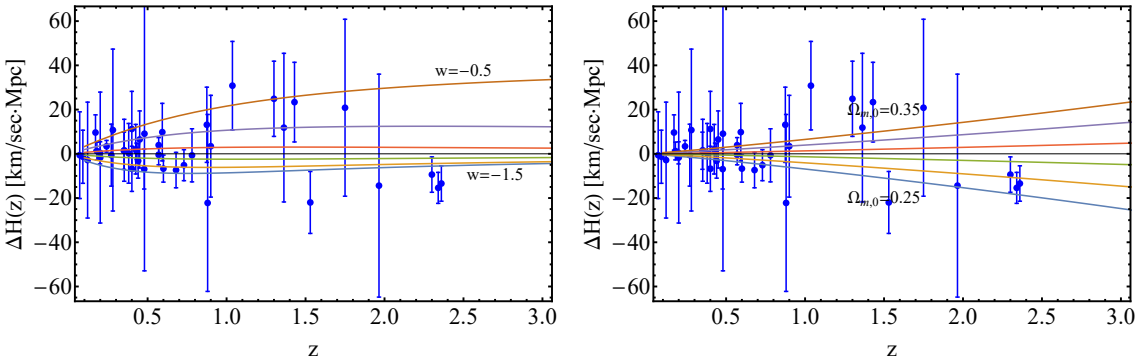

Figure 3.10: The variations (3.2) (left panel) and (3.3) (right panel) for the observable $O = H$ as a function of redshift z, superimposed with the full compilation of cosmic chronometer data presented in Table D.2 in the Appendix D. From Ref. [474].

at high z. However, the Hubble rate $H(z)$ is also directly probed by the cosmic chronometer data for specific redshift values. The cosmic chronometer data approach is based on the simple fact that the definition of the Hubble paramet itself can be expressed as

$$H(a) \equiv \frac{\dot{a}}{a} \Rightarrow H(z) = -\frac{1}{1+z}\frac{dz}{dt}\,. \tag{3.19}$$

A basic advantage of these kind of data is that, in contrast to BAO or SnIa (that we will discuss shortly), there is no dependence on a complex integration. Nevertheless, the calculation of the ratio dz/dt is a rather complicated task (see Refs. [43, 487, 488] for more details). So it would be interesting to use the cosmic chronometer data instead of the $H(z) \times \frac{r_s}{r_s^{fid}}$ BAO data to see if the results coincide. In Fig. 3.10 we show the deviation of the Hubble expansion rate $H(z)$ for various values of w (left panel) and $\Omega_{\rm m,0}$ (right panel), superimposed with the cosmic chronometer data presented in Table D.2 in Appendix D. Comparing Figs. 3.9 with 3.10 it is clear that despite the similarity of the two figures, the BAO data are significantly more constraining compared to the cosmic chronometer data for both w and $\Omega_{\rm m,0}$, especially at low redshfits.

3.2.2 Contour Shapes and Redshift Ranges

It is only natural to expect that the presence of blind redshift spots and optimum redshift regions for specific cosmological parameters also affect the forms of the corresponding confidence contours, since the Figure of Merit, *i.e.* the mutual area of the confidence contours in parametric space, increases (decreases) for compilations close to the optimum redshift region (blind redhsift spot). Therefore, in order to demonstrate this effect, we need to construct the confidence contours for the parameters w and $\Omega_{\rm m,0}$ using the BAO observables described in the previous subsection at different redshift regions.

For the construction of the confidence contours we apply the maximum likelihood as described in Chapter 2. More specifically, for the BAO data we construct a relevant χ^2 function that is then minimized. The corresponding vector $V^i_{BAO}(z_i, \Omega_{\rm m,0}, w)$ is written as

$$V^i_{BAO}(z_i, \Omega_{\rm m,0}, w) \equiv BAO^m_i - BAO^m_{theoretical}\,, \tag{3.20}$$

where the integer m takes one of the values $m \in [1,3]$ representing the different BAO data of Table D.1 presented in Appendix D, while the theoretical expressions correspond to the formulas of the previous subsection. Therefore, the relevant χ^2 functions [similar to Eq. (2.18)] are given as

$$\chi^2(\Omega_{\rm m,0}, w) = V^i_{BAO} C^{-1}_{ij} V^j_{BAO}\,. \tag{3.21}$$

Regarding the forms of the covariance matrices C_{ij}, for the parameter $D_V(z) \times \frac{r_s^{fid}}{r_s}$ we have

$$C^{\rm BAO,total}_{ij,D_V\times\left(r_s^{fid.}/r_s\right)} = \begin{pmatrix} \sigma_1^2 & 0 & 0 & \cdots \\ 0 & C_{ij}^{WiggleZ} & 0 & \cdots \\ 0 & 0 & \cdots & \sigma_N^2 \end{pmatrix}, \tag{3.22}$$

where $N = 28$ and the submatrix of the WiggleZ survey is [489]

$$C_{ij}^{WiggleZ} = 10^4 \begin{pmatrix} 2.18 & -1.12 & 0.47 \\ -1.12 & 1.71 & -0.72 \\ 0.47 & -0.72 & 1.65 \end{pmatrix}^{-1}. \tag{3.23}$$

For the $D_A \times \frac{r_s^{fid}}{r_s}$ and $H \times \frac{r_s}{r_s^{fid}}$ we consider a diagonal form

$$C^{\rm BAO,total}_{ij} = \begin{pmatrix} \sigma_1^2 & 0 & 0 & \cdots \\ 0 & \sigma_2^2 & 0 & \cdots \\ 0 & 0 & \cdots & \sigma_N^2 \end{pmatrix}, \tag{3.24}$$

where in this case N corresponds to the relevant number of BAO datapoints. Of course, the forms of the considered covariance matrices (3.23) and (3.24) are an overestimation as they ignore possible correlations between the relevant BAO data, but to the best of our knowledge, the non-diagonal terms for both the $D_A \times \frac{r_s^{fid}}{r_s}$ and $H \times \frac{r_s}{r_s^{fid}}$ observables are not publicly available.

For the estimation of this effect, we follow the same procedure of the previous Chapter performing Monte Carlo simulations including random non-diagonal terms to the covariance matrices for the $D_A \times \frac{r_s^{fid}}{r_s}$ and $H \times \frac{r_s}{r_s^{fid}}$ observables of magnitude similar to the non-diagonal terms of the non-diagonal terms corresponding to $D_V \times \frac{r_s^{fid}}{r_s}$. Thus we set the magnitude of the matrix to be [70]

$$C_{ij} = \frac{1}{2}\sigma_i \cdot \sigma_j\,, \tag{3.25}$$

where σ_i corresponds to the errors of the i published datapoints and σ_j corresponds to the errors of the j published datapoints. The simulations suggest that including the non-diagonal terms the best fit parameters do not change more than 10%. Hence we anticipate a possible reasonable correlation among datapoints to not significantly alter the results of our analysis.

Minimizing Eq. (3.21) we derive the best fit values of the parameters and construct the relevant $1\sigma - 3\sigma$ confidence contours in the parametric space $(\Omega_{\rm m,0} - w)$. In the left panel of Fig. 3.11, we show the corresponding contours for the full $D_V \times r_s^{fid.}/r_s$ compilation presented in Table D.1 in the Appendix D. The best fit parameters of the BAO data (green point) are differ approximately 1σ from the corresponding Planck15/ΛCDM best fit values (red point). Moreover, we split the data into two distinct compilations. In the first one we include the BAO with $z < 0.55$ (14 datapoints) that we denote as low redshift $D_V \times r_s^{fid.}/r_s$ data, while

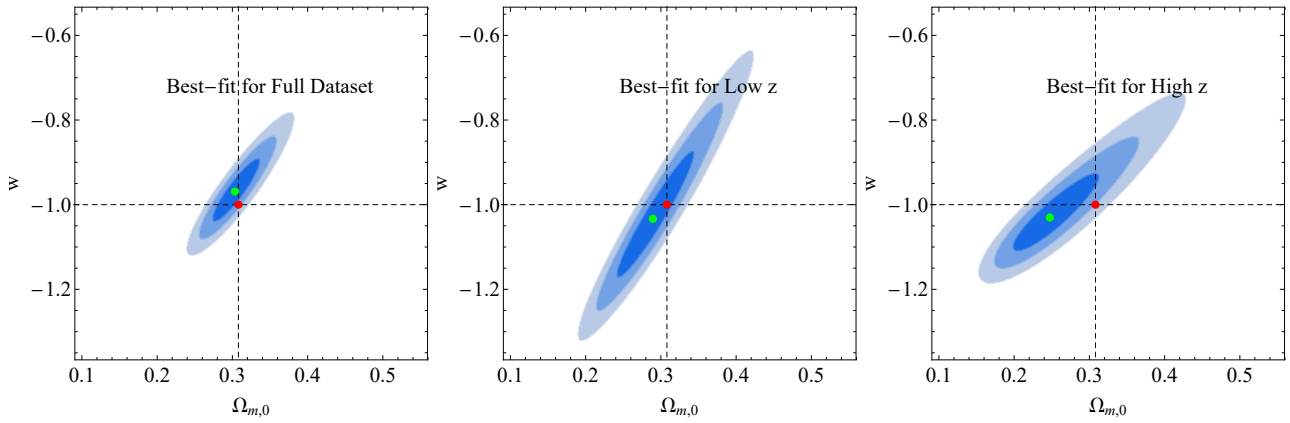

Figure 3.11: The $1\sigma - 3\sigma$ confidence contours in the parametric space $(\Omega_{\rm m,0} - w)$ for the full BAO $D_V \times r_s^{fid.}/r_s$ compilation (left panel), the low redshift data (middle panel) and the high redshift data (right panel). The red dot corresponds to the Planck15/ΛCDM best fit, while the green dot to the corresponding BAO best fit. From Ref. [474].

in the second one we incorporate the BAO with $z > 0.55$ (14 datapoints) that we denote as high redshift $D_V \times r_s^{fid.}/r_s$ data. Using these two compilations we construct the corresponding $1\sigma - 3\sigma$ confidence contours for the low z (middle panel) and the high z data (right panel). As expected, the low redshift data that correspond to the optimum redshift region make the confidence contour thinner in the $\Omega_{\rm m,0}$ axis and longer in the w axis. On the contrary, the high redshift data that are close to the to the blind spot, make the contours thicker in the $\Omega_{\rm m,0}$ axis and shorter in the w axis. Similar confidence contours can also be constructed for the low and high redshift data of the $D_A \times \frac{r_s^{fid}}{r_s}$ and $H \times \frac{r_s}{r_s^{fid}}$ observables, deriving akin results.

3.3 Distance Modulus from SnIa and from Gravitational Waves

A prominent example among the geometrical probes that is extensively considered in the literature is the luminosity distance (1.44). The luminosity distance d_L is measured using astrophysical objects known as standard candles. As a standard candle we define an astrophysical object with an absolute luminosity that is unrelated to the distance. Characteristic examples of standard candles are the SnIa or the standard gravitational wave sirens.

In general, supernovae are very powerful and bright stellar explosions that release a tremendous amount of energy. Supernovae can be categorised depending on their light curves and their absorption line of different chemical elements in their spectrum [450]. In particular, if the observed spectrum contains spectral lines of hydrogen, it is identified as Type II, otherwise is identified as Type I. Furthermore, if a single ionized silicon at $615nm$ appears in the spectrum, then the supernovae is further classified as Type Ia. The basic mechanism for the appearance of SnIa includes a binary system of stars in which one of them is a white dwarf. When the other one (companion star) reaches its red giant phase, the white dwarf collects material from the companion star due to gravity creating the very well known accretion disc. At a certain point the white dwarf will reach a critical mass that is known as the Chandrasekhar mass $m_{ch} \simeq 1.4\, M_\odot$ where the symbol $M_\odot$ corresponds to the solar mass [490]. As the white dwarf

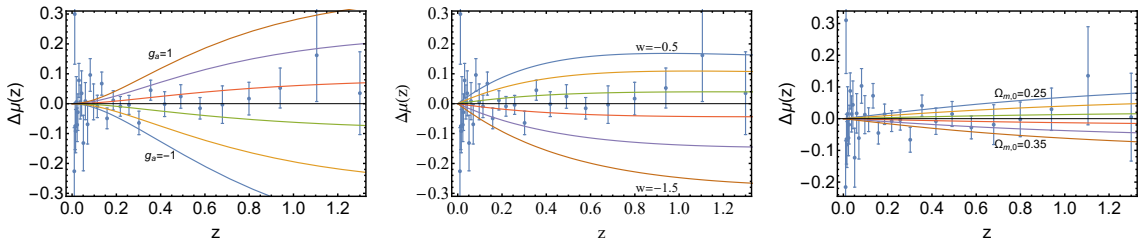

Figure 3.12: The variations (3.1)-(3.3) for $O = \mu$ as a function of redshift for various values of the parameters g_a, w and $\Omega_{\rm m,0}$, superimposed with the binned JLA data of Table D.3 in the Appendix D. From Ref. [474].

is progressively compressed the temperature rises leading to the carbon fusion, triggering a "cataclysmic" outburst (see Ref. [94] for more details). The standard gravitational wave sirens provide an independent way to measure the luminosity distance as long as the detected gravitational wave, that can be created by a binary neutron star merger, has an electromagnetic counterpart (this is what we call as standard siren) [491–494].

In the context of a wCDM model, the luminosity distance $d_L(z)$ of a SnIa is given as

$$d_L(z) = \frac{c}{1+z}\int_0^z \frac{dz'}{H_0\sqrt{\Omega_{\rm m,0}(1+z')^3 + (1-\Omega_{\rm m,0})\,(1+z')^{3(1+w)}}}\,, \tag{3.26}$$

where we have used (1.69) setting $\Omega_{\rm r,0} = 0$. Based on Eq. (3.26) it is straightforward to construct the distance modulus $\mu(z)$ that is defined as the difference between the apparent magnitude $m_{th}(z)$ and the absolute magnitude M and is connected with the luminosity distance through

$$\mu(z) \equiv m_{th}(z) - M = 5\,\log_{10}[d_L(z)] + 25\,. \tag{3.27}$$

For an evolving Newton's constant $G_{\rm eff}(z)$, such as the form of (2.10), the absolute magnitude of SnIa varies as [455, 456, 495]

$$M - M_0 = \frac{15}{4}\,\log_{10}\left(\frac{G_{\rm eff}}{G_{\rm N}}\right)\,, \tag{3.28}$$

with M_0 corresponds to the reference local value of the absolute magnitude (see also the following Chapter for an extensive discussion regarding the ratio 15/4 that appears in this equation). Therefore, the distance modulus of SnIa also depends on the evolving Newton's constant $G_{\rm eff}(z)$ via

$$\mu(z) = 5\,\log_{10}[d_L(z)] + \frac{15}{4}\,\log_{10}\left(\frac{G_{\rm eff}}{G_{\rm N}}\right) + 25\,. \tag{3.29}$$

Similarly, in the case of the gravitational wave luminosity distance the relevant gravitational wave distance modulus is of the following form [496]

$$\mu_{gw}(z) = 5\,\log_{10}\left[d_L(z)\sqrt{\frac{G_{\rm eff}}{G_{\rm N}}}\right] + 25\,. \tag{3.30}$$

In Fig. 3.12 we construct the theoretically predicted deviations (3.1) (left panel), (3.2) (middle panel) and (3.3) for various values of the parameters g_a, w and $\Omega_{\rm m,0}$ for the distance

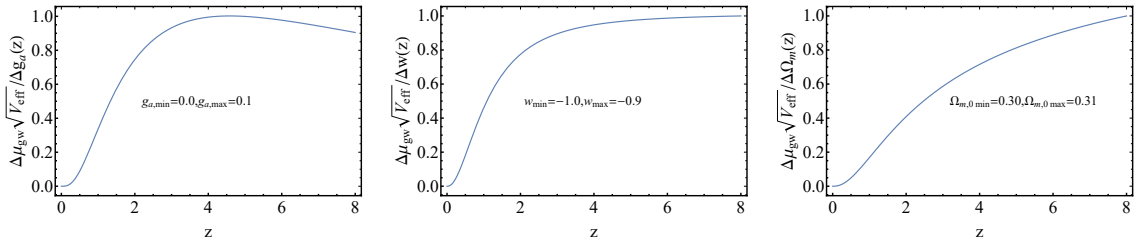

Figure 3.13: The sensitivity measure (3.8) for μ_{gw} for the parameters g_a, w and $\Omega_{\rm m,0}$. From Ref. [474].

modulus (3.29). We also show the binned Joint Light-curve Analysis (JLA) SnIa data [40] presented in Table D.3 in the Appendix D. Furthermore, in Fig. 3.13 we construct the sensitivity measure of the gravitational wave distance modulus μ_{gw}, using (3.8) for the parameters g_a (left panel), w (middle panel) and $\Omega_{\rm m,0}$ (right panel). Notice that even though the deviation $\Delta\mu_{gw}$ appears to be increasing with redshift for all the parameters considered, the absolute value of the sensitivity measure with respect to the parameter g_a has a maximum for redshifts in the range $z \in [4, 5]$, indicating the presence of an optimal redshift range. For the parameters w and $\Omega_{\rm m,0}$ Eqs. (3.29) and (3.30) are equal so, in Fig. 3.14 we only show the deviation $\Delta\mu_{gw}(z)$ for the parameter g_a superimposed with the single available datapoint [326]. As we can see the standard sirens need drastic improvement in order to identify the blind spots and the optimum redshift range and to constrain $G_{\rm eff}$ in general.

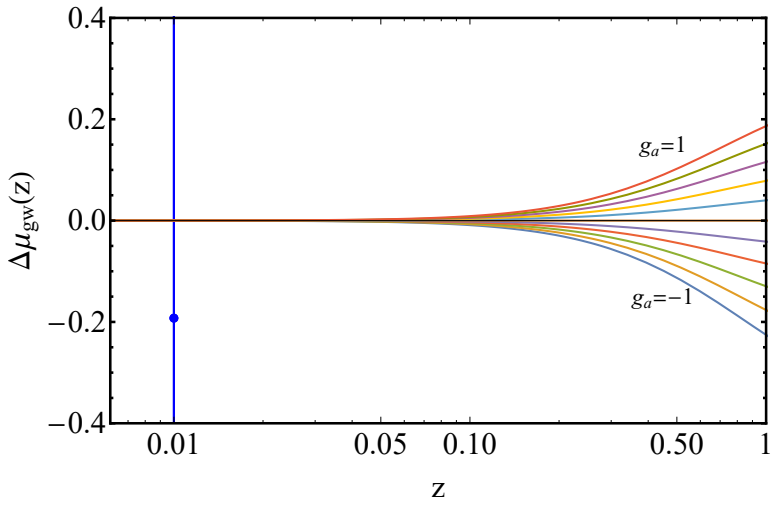

Figure 3.14: The variations (3.1) for $O = \mu_{gw}$ as a function of redshift for various values of the parameter g_a, superimposed with the single available datapoint. From Ref. [474].

3.4 In Brief

In this Chapter we have determined the blind spots and optimum redhsift regions of basic cosmological observables with respect to the matter density parameter $\Omega_{\rm m,0}$, the equation of state parameter w assumed constant and g_a, a phenomelogical parameter of a modified gravity parametrization for $G_{\rm eff}$ [Eq. (2.10)]. In particular, we have considered the growth rate of

matter density perturbations expressed through $f\sigma_8(z)$ and $f(z)$, the distance modulus $\mu(z)$ from SnIa, the gravitational wave distance modulus $\mu_{gw}(z)$ as well as BAO observables expressed through $D_V \times \left(r_s^{fid}/r_s\right)$, $D_A \times \left(r_s^{fid}/r_s\right)$ and $H(z) \times \left(r_s/r_s^{fid}\right)$ and showed that in many cases the constraining power does not vary monotonically with redshift. Furthermore, we have introduced a new statistic which we called "sensitivity" [Eq. (3.8)] that includes the effective survey volume $V_{\rm eff}$ as a measure of the constraining power for each observable.

The results of our analysis revealed that many of the recent growth data surveys that tend to increase the redshift of the measurement actually approach the blind spot of $f\sigma_8(z)$ for all three cosmological parameters in consistency with the result of the previous Chapter. A similar trend was also identified for the $D_A \times \left(r_s^{fid}/r_s\right)$ observable with respect to $\Omega_{\rm m,0}$. Concluding, a strategy that may prove more helpful in the design of future surveys is that they should improve the measurements at lower redhsift (close to the optimum redshift region for each observable) instead of focusing on higher redhsifts.

Chapter 4

Hints of a Local Matter Underdensity or Modified Gravity in the Low z Pantheon data

As we discussed in Chapter 2, a possible decrease of the effective Newton's constant at low redshifts z would leave a characteristic signature in SnIa data [73, 455–458, 497]. In particular, if the effective Newton's constant is indeed a decreasing function at low z, then this would lead to an evolving Chandrasekhar mass m_{ch} and therefore to the detection of lower values for the absolute magnitude M at recent cosmological times with respect to the best fit value of M in the context of ΛCDM. As a result, such an evolution of M, conveys to low $\mathcal{M}$ values at low z, since $\mathcal{M}$ is given as [285, 497]

$$\mathcal{M} \equiv M + 5\,\log_{10}\left(\frac{c/H_0}{1\mathrm{Mpc}}\right) + 25 = M - 5\,\log_{10}(h) + 42.38\,, \tag{4.1}$$

where we recall that $h \equiv H_0/100\ \mathrm{km\,s^{-1}\,Mpc^{-1}}$. However, as we can clearly see from Eq. (4.1), if $\mathcal{M}$ is indeed evolving, then this evolution could also be produced by higher local values of H_0 in the context of *e.g.* a local matter underdensity scenario. The scenario that we live in a local underdence region that fades away at large scales is not new and can in principle explain the H_0 tension. In fact, it has been proposed as an alternative theory to explain the accelerated expansion of the Universe without the presence of a cosmological constant [260–267]. However, in order to explain simultaneously the accelerated expansion of the Universe and the H_0 problem the Gpc scale and depth of the underdensity region required is inconsistent with current observations [268–275]. Nevertheless, there are some works in the literature that study different survey galaxies arguing that a local underdensity should not be completely omitted [276–286].

SnIa have been widely used as standard candles to probe the expansion rate $H(z)$ of the late Universe, *i.e.* for $z < 2$. The theoretically predicted apparent magnitude $m_{th}(z)$ of the SnIa can also be expressed as [148, 287, 340]

$$m_{th}(z) = M + 5\,\log_{10}\left[D_L(z)\right] + 5\,log_{10}\left(\frac{c/H_0}{1\mathrm{Mpc}}\right) + 25 = \mathcal{M} + 5\,\log_{10}\left[D_L(z)\right]\,. \tag{4.2}$$

Here $D_L(z)$ is the Hubble free luminosity distance that is connected with the luminosity distance d_L [calculated by Eq. (1.44)] through

$$D_L(z) = H_0\,\frac{d_L(z)}{c}\,. \tag{4.3}$$

Usually, when the parameters of the studied $H(z)$ are pinpointed, the degenerate parameters M, H_0 (or equivalently $\mathcal{M}$) are marginalized as nuisance parameters [40,41,498]. For instance, in the context of the standard ΛCDM, where the expansion rate is given as

$$H^2(z) = H_0^2 \left[\Omega_{\rm m,0}(1+z)^3 + (1-\Omega_{\rm m,0})\right] . \tag{4.4}$$

Eq. (4.2) is used for the construction of a marginalized $\tilde{\chi}^2$ function of the form

$$\tilde{\chi}^2(\Omega_{\rm m,0}) \equiv -2\,\ln\left[\int d\mathcal{M}\,\exp\left(-\frac{\chi^2(\mathcal{M},\Omega_{\rm m,0})}{2}\right)\right] , \tag{4.5}$$

which is then minimized. Such a procedure however can lead to valuable physical information loss connected to possible M and/or H_0 variations. So, in the analysis of this Chapter we choose to keep the degenerate parameter $\mathcal{M}$ and perform a tomographic analysis in the latest publicly available SnIa data, *i.e.* the Pantheon dataset [41], systematically searching for any redshift dependence of the parameter $\mathcal{M}$.

4.1 Searching for a redshift dependence of $\mathcal{M}$

For the search of any possible redshift dependence of the parameter $\mathcal{M}$, we use the Pantheon dataset [41]. This dataset is the largest publicly available compilation today, consisting of six independent probes that cover the redshift range $0.01 < z < 2.3$, giving a total of 1048 SnIa. The corresponding data, that can be found in this github repository, report the name of each SnIa, the CMB and heliocentric redshifts, the observed colour and stretch corrected apparent magnitudes m_{obs} with its corresponding error $\sigma_{m_{obs}}$. In the context of a maximum likelihood analysis, we need to construct a χ^2 function [similar to Eqs. (2.18) and (3.21)] for the Pantheon dataset, using Eq. (4.2) as a function of the parameters $\mathcal{M}$ and $\Omega_{\rm m,0}$. The χ^2 function for the Pantheon dataset is written as [285,497]

$$\chi^2(\mathcal{M},\Omega_{\rm m,0}) = V^i_{Panth.}\, C^{-1}_{ij}\, V^j_{Panth.} , \tag{4.6}$$

where $V^i_{Panth.} \equiv m_{obs}(z_i) - m_{th}(z)$ and C_{ij} is the total covariance matrix [41].

The total covariance matrix C_{ij} is constructed as the sum of a diagonal covariance matrix of the statistical uncertainties which we call $\bar{D}_{ij}$ and a non-diagonal matrix associated with the systematic uncertainties that emerges from the bias correction method. The non-diagonal matrix is called $\bar{C}_{sys}$ (see Ref. [41] for more details). The corresponding files for each matrix in the github repository are the `lcparam_full_long_zhel.txt`[1] and `sys_full_long.txt` respectively. In this section (as well as in the following two) we consider only the statistical uncertainties. This procedure makes the analysis much simpler due to the diagonal nature of the covariance matrix $\bar{D}_{ij}$ but leads to somewhat lower uncertainties of the derived best fit parameters. In Section 4.4 however, we will include the systematic uncertainties and repeat the analysis of searching for a possible redshift dependence of $\mathcal{M}$ in order to estimate the statistical significance of the observed effects discussed below.

Applying the maximum likelihood method while fixing a ΛCDM background, we minimize the χ^2 function (4.6) to find the parameters best fit values for the full dataset to be $\Omega_{\rm m,0} =$

[1] Approximately eight months after the official Pantheon data release the authors did an update in the heliocentric redshifts of the SnIa including this file in the github repository. The heliocentric redshifts provide a slight correction to the form of the luminosity distance that emerges due to peculiar motions [499].

0.285 ± 0.012 and $\mathcal{M} = 23.803 \pm 0.007$ in consistency with previous studies [41, 500]. If $\mathcal{M}$ is redshift independent, we anticipate that any subset of the Pantheon dataset should give a best fit value consistent (within the 1σ threshold) with the corresponding best fit values of the full dataset. In order to test this hypothesis, at first, we fix $\Omega_{\rm m,0}$ to its best fit value of the full dataset and consider cumulative subsets of the full data compilation. The first subsets' redshift range corresponds to $z \in [0.02, 0.03]$ while for the construction of the rest of the subsets we keep the lower value $z_{min} = 0.02$ fixed and increase the maximum value z_{max} (cutoff) of the redshift range in steps of $\Delta z_{max} = 0.01$ in order to have large enough subsamples for an acceptable statistics of the results. The first subsample is obviously the smaller one and includes only 46 datapoints. For each subsample, we apply the maximum likelihood method and find the best fit $\mathcal{M}$ values along with their corresponding 1σ errors as illustrated in the left panel of Fig. 4.1.

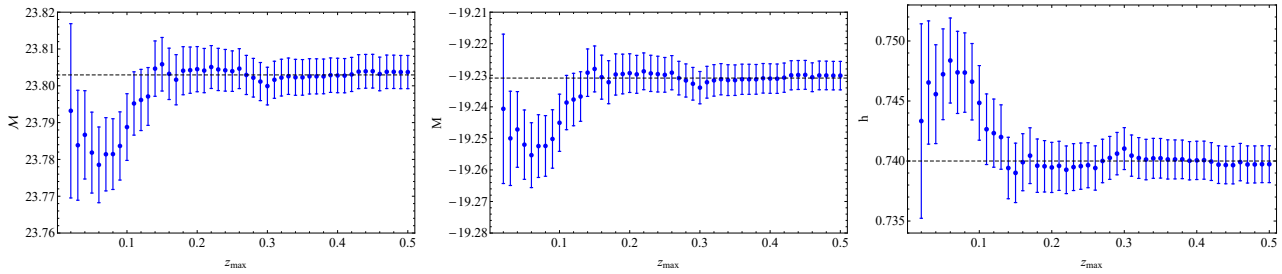

Figure 4.1: The evolution of the best fit values (blue dots) of $\mathcal{M}$ (left panel), M (middle panel) and h (right panel) along with their 1σ error for various cutoff values of z_{max}. The dashed lines correspond to the best fit values indicated by the full dataset. From Ref. [285].

We repeat this procedure to calculate the best fit values of M for the same SnIa subsamples (middle panel of Fig. 4.1) using the definition (4.1) and fixing $h = 0.74$ [501]. Similarly, we calculate the best fit values of h for the same SnIa subsamples (right panel of Fig. 4.1) fixing $M = -19.23$ (a value indicated by the best fit value of $\mathcal{M}$ for the full dataset). Clearly, at low reshifts and in particular in the resdhift range $z_{max} \in [0.02, 0.15]$ the data seem to prefer lower values of $\mathcal{M}$ from the best fit value indicated by the full dataset (continuous dashed line). This difference is at a level of about 2σ and drops drastically for $z_{max} > 0.15$ leading to values of $\mathcal{M}$ for each subsample consistent (well within the 1σ threshold) with the relevant best fit value indicated by the full dataset. The observed difference in the resdhift range $z_{max} \in [0.02, 0.15]$, corresponds to lower values of M (middle panel of Fig. 4.1) or equivalently higher values of h (right panel of Fig. 4.1) in the same redshift range.

A similar behavior is detected if instead of considering cumulative bins, we rank the Pantheon data from lower to higher redshifts. Initially, we consider the lowest redshift subsample consisting of 100 datapoints and find its best fit value of $\mathcal{M}$ along with the corresponding 1σ error assuming a ΛCDM background, as well as the mean value of the 100 point subsample z_{mean}. Then, after shifting the 100 point subsample by one datapoint towards a higher redshift, we construct the next point and continue until we cover the entire Pantheon dataset. The results of the procedure are illustrated in the left panel of the following Fig. 4.2. Similarly to Fig. 4.1, the middle/right panel of Fig. 4.2 corresponds to the best value of M/h instead of $\mathcal{M}$. We observe that for $z_{mean} < 0.3$ the best fit value of $\mathcal{M}$ oscillates around the best fit value of the full dataset at a level of about $1\sigma - 2\sigma$ implying a similar behavior for M (middle panel) and h (right panel) in the same redshift range. The redshift range of the oscillation in this case is larger than the detected redshift range of the variation in Fig. 4.1 since as the cutoff redshift

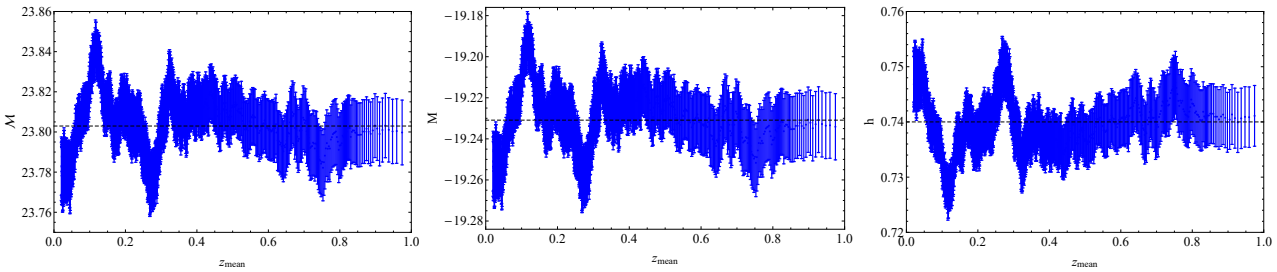

Figure 4.2: The evolution of the best fit values (blue dots) of $\mathcal{M}$ (left panel), M (middle panel) and h (right panel) along with their 1σ error for 100 point subsamples as a function of the mean redshift z_{mean}. The dashed lines correspond to the best fit values indicated by the full dataset. From Ref. [285].

increases, so does the size of the corresponding subsample canceling as a result the oscillating effect.

Furthermore, in order to increase the low z subsample and improve the statistics, we sort once more the Pantheon data from lowest to highest redshifts and split the entire dataset in foul equal bins containing 262 uncorrelated datapoints. Applying the maximum likelihood method in each bin separately in the context of a ΛCDM background and minimizing Eq. (4.6) we obtain the best fit values of $\Omega_{\rm m,0}$ and $\mathcal{M}$ and their corresponding 1σ error for each bin as it is shown in Fig. 4.3.

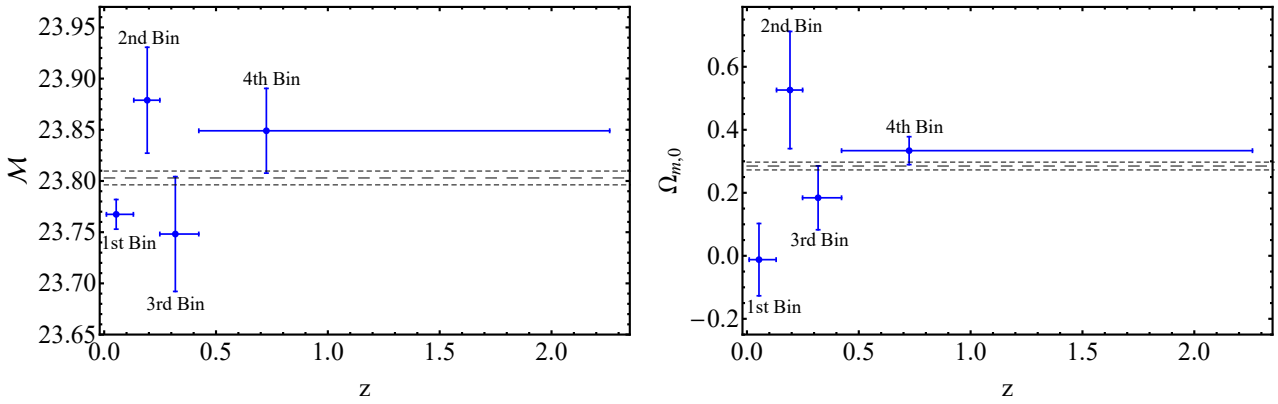

Figure 4.3: The best fit values of $\mathcal{M}$ (left panel) and $\Omega_{\rm m,0}$ (right panel) with the 1σ errors for the four uncorrelated bins. The horizontal axis corresponds to the redshift range of each bin. The continuous dashed line describes the best fit value of the full dataset while the dot dashed lines the 1σ error region. From Ref. [285].

An oscillating behavior such as the one observed in Fig. 4.2 is evident at low redshifts z. Moreover, we notice that the best fit values of $\mathcal{M}$ and $\Omega_{\rm m,0}$ for the lowest z bin ($0.01 < z < 0.13$) are more than 2σ lower than the corresponding best fit values of the full dataset, in consistency with Figs. 4.1 and 4.2. This trend is also apparent in Fig. 4.4 where we plot the $1\sigma - 3\sigma$ confidence contours of the four uncorrelated redshift bins in the parametric space $(\Omega_{m,0} - \mathcal{M})$.

The probability that such low values of $\mathcal{M}$ and $\Omega_{m,0}$ can occur in the context of the standard ΛCDM model can be estimated utilizing Monte Carlo simulations of Pantheon like datasets assuming a ΛCDM background. Specifically, we construct 500 simulated Pantheon datasets with redshifts $0.01 < z < 0.13$, *i.e.* the corresponding redshifts of the first bin, and replace

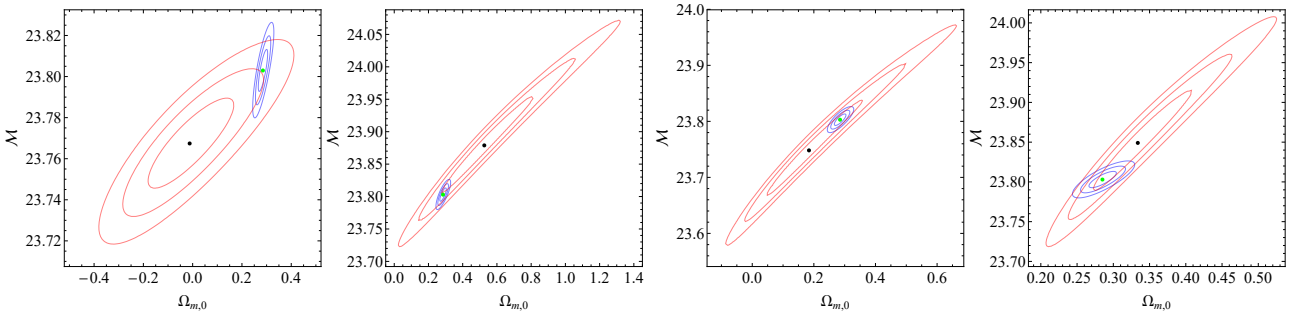

Figure 4.4: The $1\sigma - 3\sigma$ confidence contours in the parametric space $(\Omega_{m,0} - \mathcal{M})$ for the four uncorrelated redshift bins. The blue confidence contours correspond to the $1\sigma - 3\sigma$ full Pantheon dataset best fit, while the red contours describe the $1\sigma - 3\sigma$ confidence contours of the four bins (from left to right). The black points represent the best fit of each bin, while the green dot represents the best fit value indicated by the full Pantheon dataset. From Ref. [285].

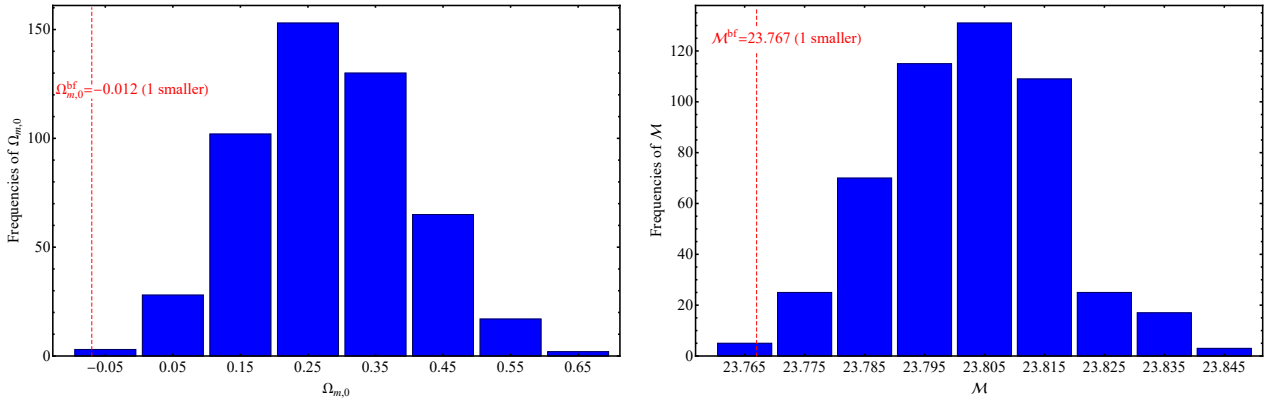

Figure 4.5: The distributions of $\Omega_{m,0}$ (left panel) and $\mathcal{M}$ (right panel) using 500 Monte Carlo simulations of Pantheon like datasets under the assumption of an underlying ΛCDM model, in the redshift region of the first bin $(0.01 < z < 0.13)$. The red dashed lines correspond to the best fit values of the first bin indicated by the real data. From Ref. [285].

the relevant apparent magnitude of the real data $[m_{obs}(z_i)]$ with simulated datapoints $m_{sim}(z_i)$ created under a random normal (gaussian) distribution with a mean value obtained from the best fit ΛCDM value of the apparent magnitude m_{th}. As the standard deviation of the gaussian distribution we select the $\sigma_{m_{obs}}$ of each datapoint respectively [502]. After constructing the 500 Monte Carlo simulation, we apply the maximum likelihood method and see how many of the simulated data give lower values for $\mathcal{M}$ and $\Omega_{m,0}$ than the best fit values indicated by the real data of the first bin. The results of this procedure that are demonstrated in Fig. 4.5, show that less than 1% (0.2% for either $\Omega_{m,0}$ or $\mathcal{M}$) of the Monte Carlo simulations give smaller best fit values for $\mathcal{M}$ or $\Omega_{m,0}$ than the actual best fit values of the first bin. Therefore, we confirm that the reduced value of $\mathcal{M}$ is a rather unlikely event in the context of an underlying physical ΛCDM model.

The $2\sigma - 3\sigma$ detected signal regarding both the $\Omega_{m,0}$ and $\mathcal{M}$ has also been identified by previous studies [283, 503]. This variation of $\mathcal{M}$ at low redshifts can be attributed to the following:

- A local underdensity, *i.e.* a "Local Void" that vanishes at large scales. As we showed in

Figs. 4.1 and 4.2 a lower $\mathcal{M}$ than the best fit value indicated by the full dataset in the low redshift regime, leads to a higher value of h [see Eq. (4.1)] than the indicated best fit value of the full dataset in the same redshift region. A generic way to explain this larger h value, would be if our local Universe is more underdense compared to the mean density of the Universe affecting as a result the measured h value. In the context of a "Local Void" model, the value of h increases by $2-3\%$ (see Fig. 4.2 - right panel) and such a scenario would also predict an anisotropy for the best fit value of $\mathcal{M}$ in the sky. This case is studied in the following Section 4.2.

- A modified theory of gravity. Another possible explanation for the $\mathcal{M}$ variation at low z is a redshift depence of the absolute magnitude M, due to *e.g.* a time variation of Newton's constant in the context of a modified theory scenario. This case will be studied in Section 4.3.

- Statistical and/or systematic fluctuations of the data around the true ΛCDM model. The probability of this case can be estimated creating a large number of simulated Pantheon like datasets in the context of a ΛCDM background (as we did previously) with a multivariate gaussian distribution that takes into account the full covariance matrix C_{ij} instead of just the statistical uncertainties. This probability (that is less than 1%) is expected to increase in the context of the full covariance matrix and if the "look elsewhere effect" is taken into account. This case is extensively discussed in Section 4.4.

4.2 Local Matter Underdensity Scenario

If the scenario that we live in an underdense region is realized in Nature, then the locally measured value of H_0 would be larger than the true global value of H_0, leading to a lower value of $\mathcal{M}$ at local scales, justifying the results of the previous section. If the observer is located exactly (or really close) at the center of the underdense region, then no evidence of anisotropy would be detected. However, a slightly off-center observer of the underdense region would experience a preferred cosmological direction and an overall anisotropy that could be detected in the context of the Pantheon dataset. Hence, in what follows, we use two different methods that are widely used in the literature in order to search for possible anisotropies. These are the Hemisphere Comparison [285, 502, 504–507] and the Dipole Fit [285, 506–509] methods.

4.2.1 Hemisphere Comparison Method

The Hemisphere Comparison (HC) method was first presented in Ref. [504] and applied in the context of the Union2 dataset in Ref. [502]. The main steps of the HC method are summarized below [502]:

- Initially, a random direction is considered that has the following form

$$\hat{r}_{rndm} = \left(\cos\phi\sqrt{1-\cos^2\theta},\, \sin\phi\sqrt{1-\cos^2\theta},\, \cos\theta\right) , \tag{4.7}$$

where $\phi \in [0, 2\pi]$ and $\cos\theta \in [-1, 1]$. These variables are randomly selected in these intervals with a uniform probability distribution.

- Two different hemispheres are considered that are called "up hemisphere" and "down hemisphere". The "up hemisphere" corresponds to the subset where $\hat{r}_{rndm} \cdot \hat{r}_{data} > 0$, whereas the "down hemisphere" corresponds to the subset $\hat{r}_{rndm} \cdot \hat{r}_{data} < 0$. The unit vector $\hat{r}_{data}$ describes the direction of each SnIa in galactic coordinates.

- Identify the best fit value of $\mathcal{M}$ in the up (down) hemisphere $\mathcal{M}_{up}$ ($\mathcal{M}_{down}$) applying the maximum likelihood method for the best fit value of $\Omega_{m,0}$ indicated by the full dataset. Using these quantities, define the Anisotropy Level (AL) as [502]

$$\frac{\Delta\mathcal{M}}{\bar{\mathcal{M}}} \equiv 2\frac{\mathcal{M}_{up} - \mathcal{M}_{down}}{\mathcal{M}_{up} + \mathcal{M}_{down}} \tag{4.8}$$

  and its corresponding 1σ error as [502]

$$\sigma_{\Delta\mathcal{M}/\bar{\mathcal{M}}} = \frac{\sqrt{\sigma^2_{\mathcal{M}_{up}} + \sigma^2_{\mathcal{M}_{down}}}}{\mathcal{M}_{up} + \mathcal{M}_{down}} \,. \tag{4.9}$$

- Repeat this procedure for N random directions $\hat{r}_{rndm}$ and find the maximum AL and the related direction. The number of random directions needs to be well above the number of datapoints in each hemisphere, so for the Pantheon data we set $N = 3000$.

Implementing the HC method in the Pantheon dataset, we construct the AL colour map for $\mathcal{M}$ in Fig. 4.6.

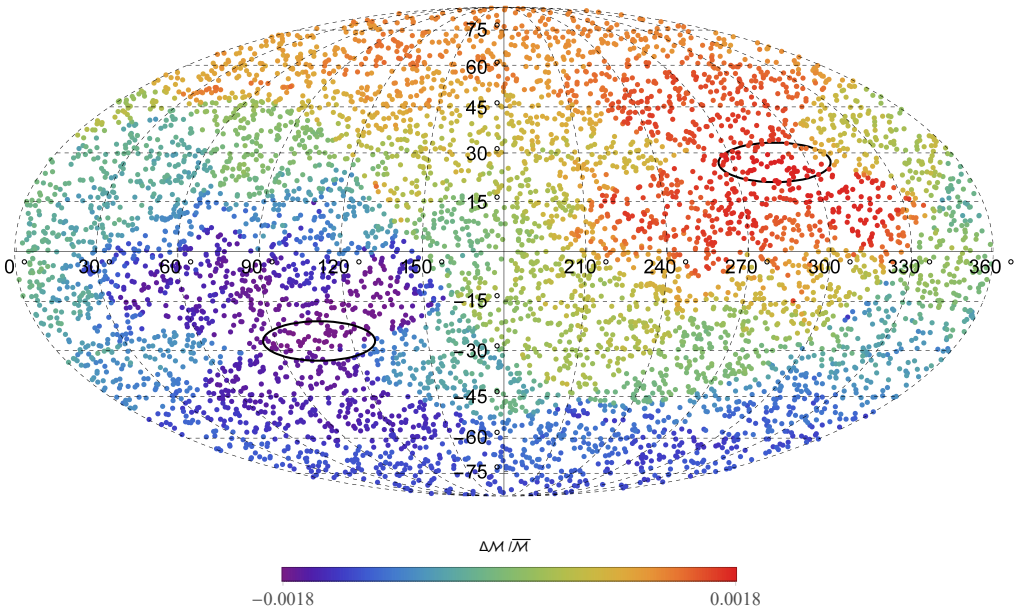

Figure 4.6: The AL colour map constructed using HC method for 3000 random directions. The red dots correspond to the pair of coordinates where the ratio $\Delta\mathcal{M}/\bar{\mathcal{M}}$ is maximum, while the purple dots correspond to the pair of coordinates where $\Delta\mathcal{M}/\bar{\mathcal{M}}$ is minimum as it is indicated by the relevant bar below the AL map. The black ellipses denote the 1σ error region of the maximum and minimum AL. From Ref. [285].

The magnitude of the maximum AL that is detected using the Pantheon data is

$$\left(\Delta\mathcal{M}/\bar{\mathcal{M}}\right)_{max} = 0.0018 \pm 0.0002 \tag{4.10}$$

and the direction of the maximum anisotropy is $(l, b) = (286.93° \pm 18.52°, 27.02° \pm 6.50°)$.

In order to check the consistency of the Pantheon SnIa with statistical isotropy, we compare the extrema of the real data with the corresponding derived using simulated Pantheon like datasets. For the simulated Pantheon data, we assume a statistical isotropy in the context of a ΛCDM background keeping fixed the direction of each datapoint in the sky while randomly selecting the Pantheon apparent magnitudes from a gaussian distribution with the best fit ΛCDM mean and standard deviation equal to the corresponding Pantheon datapoint 1σ error. We thus construct 30 isotropic simulated "Pantheon" datasets and for each dataset we use 3000 random directions to split it in two hemispheres and identify the corresponding extrema of AL using $\Delta\mathcal{M}/\bar{\mathcal{M}}$. These 30 axes of extrema of AL are shown in Fig. 4.7 using galactic coordinates and showing two opposite points for each maximum AL direction (left panel) along with the corresponding real Pantheon data sky directions (right panel).

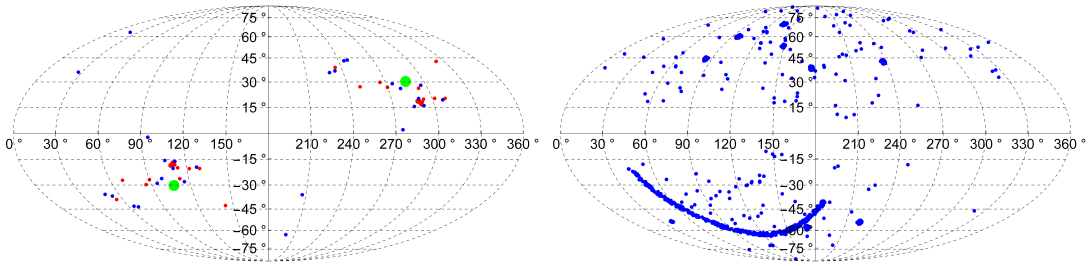

Figure 4.7: *Left Panel:* The 30 axes of extrema of AL constructed from the isotropic simulated Pantheon datasets axes using 3000 random hemisphere directions in each dataset. Notice that only two of the thirty maxima AL directions are in the upper left quadrisphere (southern hemisphere in the longitude range of $[0°, 180°]$), inducing an artificial region of preferred directions in the observed anisotropy in the lower left/upper right quadrisphere. The green dot corresponds to the maximum anisotropy of the real data, while the blue (red) dots describe the simulated datasets which have smaller (larger) magnitudes of $\Delta\mathcal{M}/\bar{\mathcal{M}}$ than the real data. *Right Panel:* The distribution of the full Pantheon data in galactic coordinates. Notice that the data are not uniformly distributed with strong preference of datapoint locations in the southern hemisphere in the longitude range $[0°, 180°]$ (lower left hemisphere). From Ref. [285].

The maximum AL of $\Delta\mathcal{M}/\bar{\mathcal{M}}$ magnitude of 16 (red dots in the left panel of Fig. 4.7) out of the 30 simulated datasets was larger than the corresponding magnitude of the real Pantheon data. This indicates that there is no statistically significant $\Delta\mathcal{M}/\bar{\mathcal{M}}$ AL in the Pantheon data.

It is important to note that from the 30 extrema AL directions, only two of them are in the upper left quadrisphere, *i.e.* in the longitude range of $[0°, 180°]$. This is because as we can clearly see from the right panel of Fig. 4.7 the Pantheon SnIa are not isotropically distributed in the sky and the majority of them are concentrated in the southern left quadrisphere, while the southern (lower) right quadrisphere is almost empty of SnIa. A possible solution to this problem could be the smooth residual method that is discussed extensively in Refs. [375, 510–512] that seem to be advantageous (on some occasions) when dealing with anisotropically distributed data. This method attempts to ameliorate any anisotropy of the data using a 2D smoothing

interpolation of the data on the surface of a unit sphere. An alternative approach to this smoothing method is to construct a more isotropic subset of the full dataset, that will be less biased in the selection of the maximum AL direction. Therefore, we randomly choose a subsample containing 375 scattered more isotropically data in the four quadrispheres (100 in the first three quadispheres and 75 in the down right quadrisphere) and construct a new reduced dataset as it is shown in the right panel of Fig. 4.8. Utilizing this isotropic distributed dataset, we generate 100 simulated Pantheon isotropic subsamples reducing the random direction to 1500[2]. Then, we split it in two hemispheres and identify the corresponding maximum $\Delta\mathcal{M}/\bar{\mathcal{M}}$ AL magnitude. This is illustrated in the left panel of Fig. 4.8 where we show two opposite points for each maximum AL direction. Clearly, the preferred range of directions vanishes for

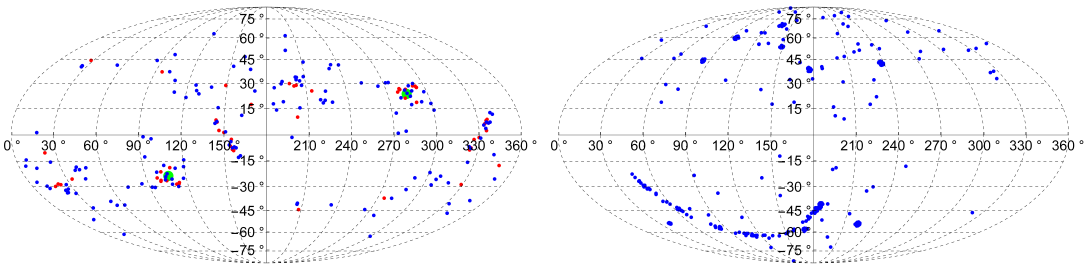

Figure 4.8: *Left Panel:* The 100 axes of extrema of AL using 1500 random directions for each isotropically distributed Pantheon subsample. The preferred direction disappears completely for the more isotropic distributed subset. The green dot corresponds to the maximum anisotropy of the real data, while the blue (red) dots describe the simulated datasets which have smaller (larger) magnitudes of $\Delta\mathcal{M}/\bar{\mathcal{M}}$ than the real data. *Right Panel:* The distribution of the reduced isotropic subset in galactic coordinates. From Ref. [285].

the case of the more isotropically distributed dataset. Even in this case however, no signal of anisotropy is found since 33 (red dots in the left panel of Fig. 4.8) out of the 100 simulated datasets have larger maximum AL magnitudes of $\Delta\mathcal{M}/\bar{\mathcal{M}}$ than the corresponding magnitude of the real Pantheon data.

The lack of any anisotropy signal continues even when we split the Pantheon data in four redshift uncorrelated bins. Using the same method as before, we construct for each bin 30 isotropic simulated Pantheon-like datasets and for each dataset, we use 1000 random directions and identify the corresponding maximum $\Delta\mathcal{M}/\bar{\mathcal{M}}$ magnitudes. Then, we compare the maximum magnitudes $\Delta\mathcal{M}/\bar{\mathcal{M}}$ of the simulated Pantheon like datasets with the corresponding maximum magnitude $\Delta\mathcal{M}/\bar{\mathcal{M}}$ of the real data for each bin. The results are summarized in the following Table 4.1.
Interestingly, the strongest evidence for anisotropy are found in the highest bin with $0.42 < z < 2.3$ and not in the lowest bin. From the thirty simulated datasets only three have larger $\Delta\mathcal{M}/\bar{\mathcal{M}}$ magnitudes than the corresponding magnitude of the real data. Nevertheless, this effect remains mild and not statistically significant since it remains below the 2σ threshold.

Although no evidence for anisotropy regarding $\Delta\mathcal{M}/\bar{\mathcal{M}}$ have been found in the Pantheon data, the scenario that we live in a local underdensity can not be excluded yet especially if we are located very close to the center of the undredensity. In order to quantify the local expansion

[2]The number of the random directions considered for the identification of the direction of the maximum AL is smaller in this case, since the new dataset is significantly smaller than the original.

Bin	Redshift Range	Number of Simulated Datasets with $\left\vert\frac{\Delta\mathcal{M}}{\bar{\mathcal{M}}}\right\vert_{sim} > \left\vert\frac{\Delta\mathcal{M}}{\bar{\mathcal{M}}}\right\vert_{real}$
$1st$	$0.01 < z < 0.13$	21/30
$2nd$	$0.13 < z < 0.25$	8/30
$3rd$	$0.25 < z < 0.42$	14/30
$4th$	$0.42 < z < 2.26$	3/30

Table 4.1: The results of the HC method for each bin as described above.

rate $\delta H_0/H_0$ of the possible local underdensity, we need to quantify how much lower the $\mathcal{M}$ value of the low z bin is with respect to the value indicated by the full dataset. Returning to Fig. 4.3 we find the corresponing difference to be

$$\Delta\mathcal{M} \equiv \mathcal{M}_{bf} - \mathcal{M}_{bin1} \approx 23.80 - 23.76 \approx 0.04 \pm 0.02\,, \tag{4.11}$$

where $\mathcal{M}_{bf}$ corresponds to the best fit value of $\mathcal{M}$ indicated by the full dataset and $\mathcal{M}_{bin1}$ corresponds to the relevant best fit value of the lowest z bin. Obviously, in the context of a local matter underdensity scenario, $\mathcal{M}_{bin1}$ corresponds to the $\mathcal{M}$ value that is measured inside the local underdensity, while $\mathcal{M}_{bf}$ corresponds to the true global $\mathcal{M}$ value. The difference on $\mathcal{M}$ leads to a variation of the local expansion rate $\delta H_0/H_0$ through [283]

$$\left(\frac{\delta H_0}{H_0}\right) \approx 0.2\,\ln(10)\,\Delta\mathcal{M} = 0.019 \pm 0.007\,. \tag{4.12}$$

From Eq. (4.12), we can also constrain the density contrast $\delta\rho_0/\rho_0$ as well as the dimensionless mater density contrast $\delta\Omega_0/\Omega_0$ in the context of a LTB model with a cosmological constant assuming a top hat density profile for the void, using the following coupled system of equations that are described in the appendix of Ref. [283]

$$\frac{\delta H_0}{H_0} = \frac{\delta\rho_0}{\rho_0}\left[-0.171 - 0.322\,(\Omega_{m,0} - 0.3) + 0.249\,(\Omega_{m,0} - 0.3)^2\right] + \left(\frac{\delta\rho_0}{\rho_0}\right)^2 [0.031+$$
$$+0.063\,(\Omega_{m,0} - 0.3)] - 0.022\left(\frac{\delta\rho_0}{\rho_0}\right)^3\,, \tag{4.13}$$
$$\frac{\delta\Omega_0}{\Omega_0} = \frac{\delta\rho_0}{\rho_0}\left[1.342 + 0.643\,(\Omega_{m,0} - 0.3) - 0.499\,(\Omega_{m,0} - 0.3)^2\right] + \left(\frac{\delta\rho_0}{\rho_0}\right)^2 [0.367+$$
$$+0.847\,(\Omega_{m,0} - 0.3)] + 0.056\left(\frac{\delta\rho_0}{\rho_0}\right)^3\,. \tag{4.14}$$

Substituting $\Omega_{m,0} = 0.3153$, *i.e.* the CMB value indicated by the Planck mission [18] and $\delta H_0/H_0 \approx 0.02$ as indicated by Eq. (4.12) in Eq. (4.13), we obtain $\delta\rho_0/\rho_0 = -0.10 \pm 0.04$. Setting this value to (4.14) we calculate $\delta\Omega_0/\Omega_0 = -0.12 \pm 0.02$, in consistency with previous studies [283].

4.2.2 Dipole Fit Method

Another method that is extensively used in the literature to search for possible anisotropies is the Dipole Fit (DF) method [285, 506–509]. In most physical mechanisms the predicted

Quantity	Best Fit Value $\pm 1\sigma$ Error
c_1	$(-1.41 \pm 3.76) \times 10^{-4}$
c_2	$(-0.82 \pm 4.54) \times 10^{-4}$
c_3	$(5.28 \pm 7.14) \times 10^{-4}$
A	$(5.53 \pm 6.04) \times 10^{-4}$
B	$(-0.59 \pm 3.01) \times 10^{-4}$
l	$210.254^\circ \pm 136.564^\circ$
b	$72.852^\circ \pm 60.631^\circ$

Table 4.2: The best fit values with the 1σ error of the c_is', of the monopole and dipole terms obtained using the DF method.

cosmological anisotropy can be described by a dipole proportional to $cos\theta$. The DF method is more sensitive to the detection of such an anisotropy, so we define the deviation of the apparent magnitude from its best fit ΛCDM values $\bar{m}(z)$ as

$$\left(\frac{\Delta m(z)}{\bar{m}(z)}\right)_{obs} \equiv \frac{\bar{m}(z) - m(z)}{\bar{m}(z)}\,. \tag{4.15}$$

The main steps of the DF method are summarized below [508]:

- Transform the SnIa coordinates from equatorial to galactic, defining the unit vector $\hat{n}_i$ as

$$\hat{n}_i = \cos(b_i)\,\cos(l_i)\,\hat{x} + \cos(b_i)\,\sin(l_i)\,\hat{y} + \sin(b_i)\,\hat{z}\,. \tag{4.16}$$

- Define the dipole axis $\vec{D}$ in terms of the parameters c_1, c_2 and c_3 in cartesian coordinates as

$$\vec{D} = c_1\,\hat{x} + c_2\,\hat{y} + c_3\,\hat{z}\,. \tag{4.17}$$

- The monopole+dipole angular distribution model for the apparent magnitude is given as

$$(\Delta m/m)_{th} = A\,\cos\theta + B\,, \tag{4.18}$$

  where A and B describe the dipole and monopole terms of the anisotropy respectively and θ is the angle between the datapoint direction of the SnIa with the vector $\vec{D}$ such as that

$$\hat{n}_i\,\vec{D} = A\,\cos\theta_i\,. \tag{4.19}$$

- Fitting the Pantheon data to a dipole anisotropy model of the form of Eq. (4.18) and applying the maximum likelihood method, we minimize the following χ^2 function

$$\chi^2 = V^i\,C_{ij}^{-1}\,V^j\,, \tag{4.20}$$

  where $V^i \equiv (\Delta m/m)_{obs} - (\Delta m/m)_{th} = [\bar{m}(z_i) - m(z_i)]\,/\bar{m}(z_i) - A\,\cos\theta_i - B$ and C_{ij} is the covariance matrix neglecting the systematic uncertainties. From the minimization process the best fit values of the monopole and dipole terms are derived, using the fact that $A = \sqrt{\sum_{j=1}^{3} c_j^2}$. We also calculate the corresponding 1σ errors using the covariance matrix approach.

Implementing the DF method in the Pantheon dataset, we derive the following results that are presented in Table 4.2. Clearly, both the dipole and monopole terms are consistent with zero at the 1σ level. For this particular best fit values of the parameters A and B the anisotropy direction is $(l, b) = (210.254^\circ \pm 136.564, 72.852^\circ \pm 60.631^\circ)$. Notice that the errors of the (l, b) coordinates are quite large, covering almost the entire sky area in consistency with the results of previous studies [500, 507, 513].

Similarly to what we did in the HC method, we check the consistency of the derived dipole and monopole terms with statistical isotropy using isotropic simulated Pantheon datasets. In particular, we construct 30 simulated Pantheon datasets as described in Subsection 4.2.1 and identify the corresponding dipole anisotropy directions and the best fit values of the dipole and monopole parameters as illustrated in Fig. 4.9.

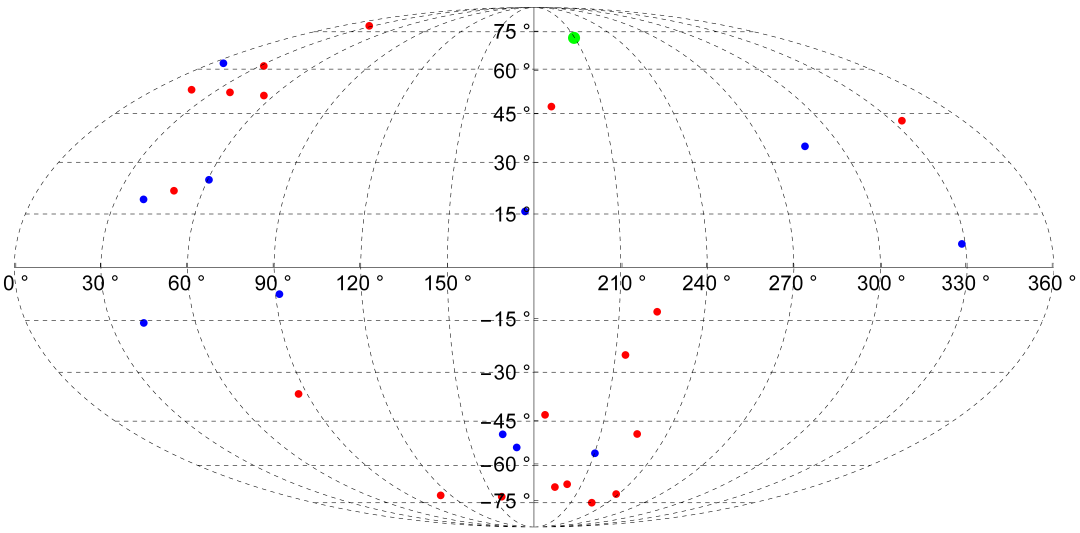

Figure 4.9: The different maximum AL directions corresponding to the 30 random simulated datasets. The green dot corresponds to dipole of the real data, while the blue (red) dots describe the dipole direction of simulated datasets which have smaller (larger) magnitudes of A than the real data. The 1σ errors of the (l, b) galactic coordinates are quite large covering almost the entire sky area. From Ref. [285].

Obviously, no preferred direction is identified in the context of the DF method, since 19 (red points in Fig. 4.9) of the 30 isotropic simulated Pantheon datasets have larger dipole magnitudes than the real data. Hence, we conclude that no statistically significant anisotropy is found using the DF method, in agreement with the corresponding result of the HC method.

4.2.3 Comparison of the Hemisphere Comparison and Dipole Fit Methods

From the implementation of the two methods, the following useful conclusions can be extracted:

- The HC method can identify more general anisotropies, since the DF is sensitive to an anisotropy that has a dipole form such as the one in Eq. (4.18).

- The obtained 1σ errors of the DF method are quite large and include almost the entire sky area. This indicates that a dipole anisotropy seems to be significantly disfavored by the Pantheon data. On the contrary, the HC method that is tuned to identify much broader range of signals gives significantly smaller 1σ errors. Therefore, the HC method seems to be more appropriate in order to identify any anisotropy signals hidden in the Pantheon data.

To summarize, no evidence of anisotropy have been identified in the Pantheon data in agreement with previous studies [500, 507, 513–516]. This lack of anisotropy does not favor (but also does not exclude) the local underdensity scenario as a possible explanation of the observed reduced value of $\mathcal{M}$ at low z indicated in the previous Section 4.1.

4.3 Modified Theory of Gravity Scenario

If the scenario of a modified gravity theory is realized in Nature, then a possible explanation for the abnormal variation of $\mathcal{M}$ at low z can be explained in the context of a redshift dependence of the absolute magnitude M. This evolution of M could be used as a probe of the evolution of fundamental constants like the evolving Newton's constant $G_{\rm eff}$. Previous studies [455, 495] assume the absolute luminosity L is proportional to the amount of ^{56}Ni produced in a SnIa which in turn is a fixed fraction of the Chandrasekhar mass m_{ch} that depends on $G_{\rm eff}$, *i.e.* L obeys the following equation

$$L \sim M_{Ni} \sim m_{ch} \sim G_{\rm eff}^{-3/2} \,. \tag{4.21}$$

This equation, implies that as L increases $G_{\rm eff}$ decreases. However, a recent study [457] using a semi-analytical model to obtain SnIa light curves in the context of modified gravity, indicates that as L increases $G_{\rm eff}$ also increases. Specifically, in the used semi analytical model, extra parameters such as the initial nickel mass in the ejecta, the initial radius of shock breakout, the scale velocity, the effective opacity as well as total ejecta mass were included. Then, the generated light curves were standardised by rescaling the shape to match a template width and the numerical dependence of the standardised intrinsic absolute luminosity L on $G_{\rm eff}$ was identified leading to a positive power instead of the power $-3/2$. In any case, assuming a general power law dependence of the form

$$L \sim G_{\rm eff}^{b} \,, \tag{4.22}$$

any detected redshift dependence of the SnIa absolute luminosity (or equivalently of the SnIa absolute magnitude) can be transformed into a redshift dependence of $G_{\rm eff}$ for a fixed value of b. For the general case of (4.22) the following simple power law relation between the absolute magnitude M and $G_{\rm eff}$ is obtained [285]

$$M - M_0 = -\frac{5\,b}{2}\,\log_{10}\left(\frac{G_{\rm eff}}{G_{\rm N}}\right) \,, \tag{4.23}$$

which for the standard value $b = -3/2$ reduces to Eq. (3.28). Substituting M in (4.2) the theoretically predicted apparent magnitude is modified as

$$m_{th}(z) = \mathcal{M} + 5\,\log_{10}\left[D_L(z)\right] - \frac{5\,b}{2}\,\log_{10}\left(\frac{G_{\rm eff}}{G_{\rm N}}\right) \tag{4.24}$$

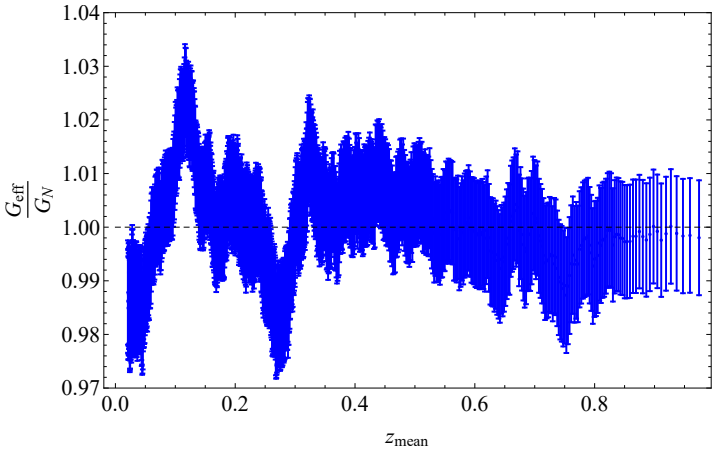

Figure 4.10: The evolution of the ratio $G_{\rm eff}/G_{\rm N}$ along with its 1σ error as a function of the mean redshift z_{mean} of each 100 datapoints subsample. In the context a modified theory, we detect a $2-3\%$ deviation from the GR predicted value $G_{\rm eff}/G_{\rm N}=1$ (dashed line) at a level of approximately 2σ. From Ref. [285].

where $\mathcal{M}$ is given by Eq. (4.1) with M replaced by M_0.

In order to identify any possible evolution of the ratio $G_{\rm eff}/G_{\rm N}$, we use Eq. (4.24) and the 100 point moving subsample method described in Section 4.1, fixing b to the standard value $b=-3/2$. Following the method, we find the best fit value of M, setting M_0 equal to the best fit value of the absolute magnitude M indicated by the full dataset with $h=0.74$. From the best fit values of M, we identify the corresponding best fit values of the ratio $G_{\rm eff}/G_{\rm N}$, appointing any redshift dependence of M into the ratio $G_{\rm eff}/G_{\rm N}$. The achieved best fit values for each subsample superimposed with their 1σ errors are illustrated in Fig 4.10. Obviously, the same oscillating behaviour observed for M at low redshift z that is shown in the middle panel of Fig. 4.2, is also evident for the ratio $G_{\rm eff}/G_{\rm N}$ in the same low z region with $G_{\rm eff}/G_{\rm N}(z=0)<1$.

Next, we consider the parametrization (2.10) and substitute it to (4.24) in order to construct a modified χ^2 function. In this case, the modified χ^2 depends not only on the same parameters as before, *i.e.* $(\mathcal{M},\Omega_{m,0})$ but also on the extra parameters g_a and b. Then we apply the maximum likelihood method, by minimizing the modified χ^2 function allowing the extra parameter b to take various values in the range $b\in[-2,2]$ and interpolate the best fits of the extra parameter g_a as a function of b. This is illustrated in Fig. 4.11. For $b<0$ we derive negative best fit values for g_a implying that the ratio $G_{\rm eff}/G_{\rm N}<1$, in consistency with the results of the previous Chapter.

Considering $b=-3/2$, *i.e.* the value considered by most previous studies [455, 495], it is straightforward to construct the $1\sigma-4\sigma$ confidence contours in the parametric space $(\mathcal{M},\Omega_{m,0},g_a)$. The best fit values obtained are $\mathcal{M}=23.793\pm0.009$, $\Omega_{m,0}=0.179\pm0.078$ and $g_a=-0.47\pm0.36$. The 2D projections of the confidence contours are shown in Fig. 4.12 and the results should be interpreted with care. The projections go through the best fit point in the 3D parameter space. Notice that the GR point ($g_a=0$) appears to be more than 4σ away from the best fit which corresponds to weaker gravity ($g_a<0$) in accordance with weak lensing and growth cosmological data. However, this is a projection effect since in the context of the full 3D parameter space we have $g_a=-0.47\pm0.36$, a value that is approximately 1.5σ away from the GR predicted one.

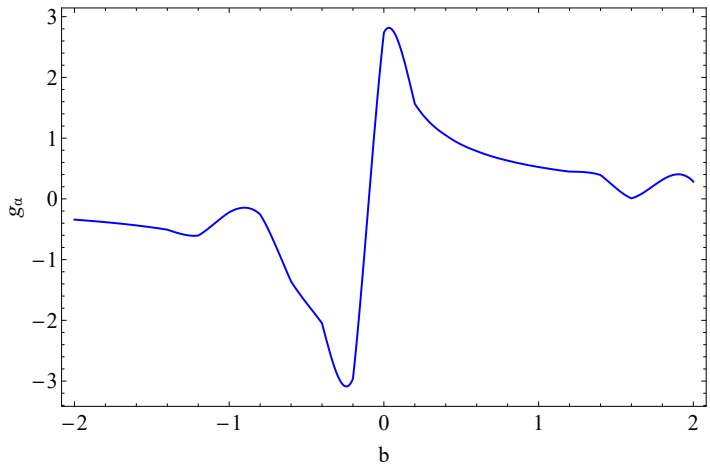

Figure 4.11: The parameter g_a as a function of b. For $b > 0$ we obtain $g_a > 0$, while for $b < 0$ we find $g_a < 0$. From Ref. [285].

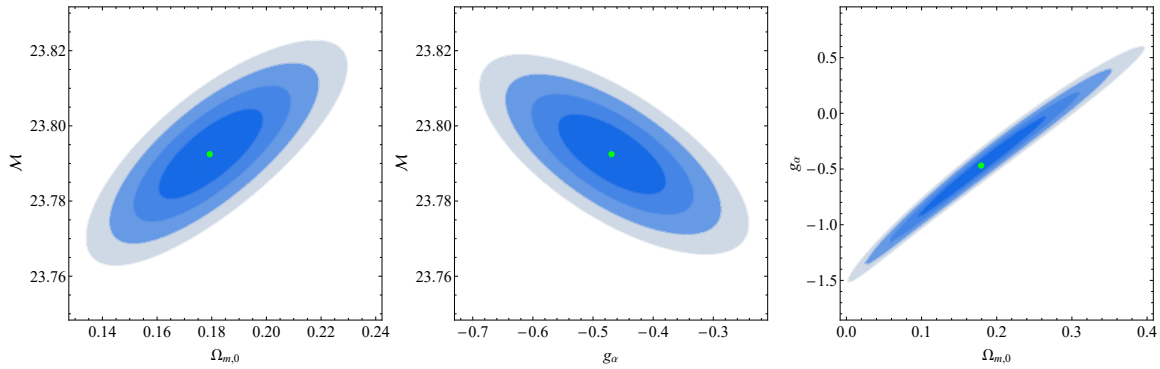

Figure 4.12: The $1\sigma - 4\sigma$ confidence contours in the parametric space $(\mathcal{M}, \Omega_{m,0}, g_a)$. The projections go through the best fit point (green point) in the 3D parameter space. Notice that the GR point corresponding to $g_a = 0$ appears to be more than 4σ away from the best fit which is a projection effect since in the context of the full 3D parameter space we have $g_a = -0.47 \pm 0.36$. From Ref. [285].

4.4 Statistical Fluctuations Scenario

Another possible explanation for the observed variation of $\mathcal{M}$ at low redshifts z is the existence of statistical fluctuations, since any realization of the data based on a given model have its own specific characteristics that might look bizarre but in reality they appear due to random fluctuations. Hence, the standard method that is followed in order to estimate if the observed effect is real, is the comparison between real data with a large number of Monte Carlo simulations. If the variation that we see in the real data appears simultaneously to the majority of Monte Carlo simulations, then the variation is due to statistical fluctuations. A key part for such an analysis is to consider the full covariance matrix which includes both the statistical and systematic errors. Doing so, we find that $\mathcal{M} = 23.81 \pm 0.01$ and $\Omega_{m,0} = 0.29 \pm 0.02$ for the full dataset in agreement with the results of Ref. [41].

Next, following the same procedure as in Section 4.1, we sort the Pantheon compilation from the lowest to the highest redshift and split the entire dataset in four equal uncorrelated bins

consisting of 262 datapoints. Applying the maximum likelihood method in each bin separately for the full covariance matrix in the context of a ΛCDM background, we obtain the best fit values for $\Omega_{m,0}$ and $\mathcal{M}$ along with their corresponding 1σ errors and construct Fig. 4.13 (which is similar to Fig. 4.3 including the systematic uncertainties in this case).

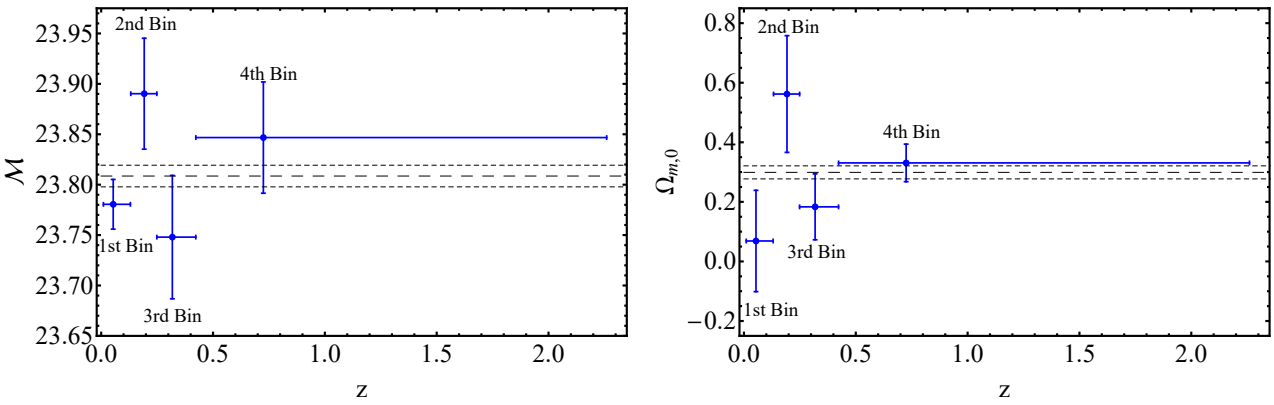

Figure 4.13: The 1σ best fit values (blue dots) of $\mathcal{M}$ and $\Omega_{m,0}$ of the real data for each bin. The dashed line corresponds to the best fit value of the full dataset, while the dot dashed line to the 1σ error region. This plot is similar to Fig. 4.3 including the full covariance matrix and not only the statistical uncertainties as in Fig. 4.3. From Ref. [497]. For the reproduction of this figure visit the following dropbox link.

The exact results of the minimization process for each bin, considering the full covariance matrix can be seen in Table 4.3.

Bin	z Range	$\mathcal{M} \pm 1\sigma$ error	$\Delta\sigma_{\mathcal{M}}$	$\Omega_{m,0} \pm 1\sigma$ error	$\Delta\sigma_{\Omega_{m,0}}$
1st	$0.01 < z < 0.13$	23.78 ± 0.03	1.14	0.07 ± 0.17	1.35
2nd	$0.13 < z < 0.25$	23.89 ± 0.06	1.48	0.56 ± 0.19	1.34
3rd	$0.25 < z < 0.42$	23.75 ± 0.06	0.99	0.18 ± 0.11	1.05
4th	$0.42 < z < 2.26$	23.85 ± 0.06	0.69	0.33 ± 0.06	0.50

Table 4.3: The best fit values with the 1σ error of $\mathcal{M}$ and $\Omega_{m,0}$ for the four uncorrelated redshift bins for the real data, using the full covariance matrix. Notice that for the first three redshift bins the σ distance ($\Delta\sigma$) of the best fit from the full dataset best fit is at least 1σ and on the average it is larger than 1.2σ.

Clearly, all first three bins of the real data best fits of $\mathcal{M}$ and $\Omega_{m,0}$ differ by at least 1σ from the relevant full dataset best fits. It is important to note here that the number of bins is a crucial parameter of the current analysis that could affect the results. Too many bins may lead to overfitting of the data[3] while a small number of bins may lead to loss of any hidden signals. In our study, we choose four bins consisting of equal number of datapoints in consistency with the previous subsections. Obviously this choice is not unique. For example, bins could have been chosen so that each bin has the same redshift interval, while it is not appropriate for the

[3]See for example Fig. 5 of Ref. [458] where there is an abrupt decrease of the χ^2 value when the number of bins is five.

present analysis since most of SnIa in Pantheon are concentrated in the lower part of their redshift range, or have the same cumulative signal to noise (including downweighting from systematics, which correlate points within the same bin).

In order to estimate the likelihood of such a σ deviation of best fit values in the first three bins, we construct 1000 Monte Carlo simulations of Pantheon like datasets and split the random data in four uncorrelated bins. For the construction of the simulated data, we consider random apparent magnitudes m created assuming a multivariate normal distribution with a mean value equal to the best fit ΛCDM value of the real data using the full covariance matrix of the real data. The corresponding probability distribution is of the form [517]

$$f_{\boldsymbol{m}}\left(m_1,\ldots,m_k\right)=\frac{\exp\left[-\frac{1}{2}\left(\boldsymbol{m}-\bar{\boldsymbol{m}}\right)^T\boldsymbol{C}^{-1}\left(\boldsymbol{m}-\bar{\boldsymbol{m}}\right)\right]}{\sqrt{(2\pi)^k\left|\boldsymbol{C}\right|}}\,, \tag{4.25}$$

where $\boldsymbol{C}$ is the full non-diagonal covariance matrix including both statistical and systematic errors, $|\boldsymbol{C}|$ corresponds to the determinant of the full covariance matrix, $\boldsymbol{m}$ is the vector $\{m_1, m_2, \ldots m_k\}$ and $\bar{\boldsymbol{m}}$ corresponds to the mean value of the apparent magnitude vector. Adopting (4.25), we generate the simulated datasets and find the percent fraction of them where the first three redshfift bins have simultaneously best fit ΛCDM parameter values $\mathcal{M}$ and $\Omega_{m,0}$ that differ from the real data best fit more than $k\ \sigma \equiv \sigma_k\ \sigma$ times. The results for the parameters $\mathcal{M}$ ($\sigma_k = \sigma_{k\mathcal{M}}$) and $\Omega_{m,0}$ ($\sigma_k = \sigma_{k\Omega}$) are illustrated in Fig. 4.14.

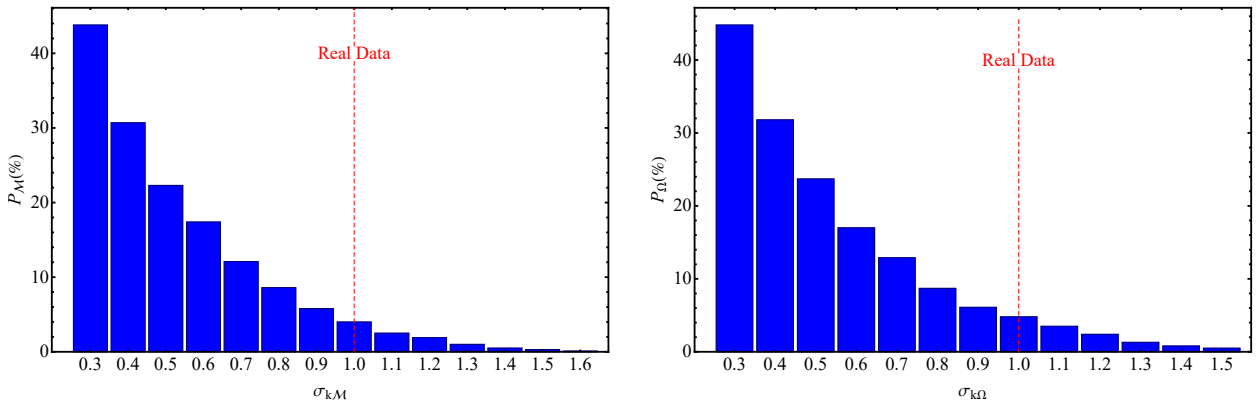

Figure 4.14: *Left Panel:* Percent of simulated Pantheon dataset (including systematics) where the first three out of four bins all differ simultaneously more than $\sigma_{k\mathcal{M}}\ \sigma$ from the best fit of the full dataset. The red dotted line corresponds to the real data that differ more than 1σ ($1.14, 1.48$ and 0.99σ for the first three bins respectively according to Table 4.3) from the full dataset best fits. *Right Panel:* Same as the left panel but for the parameter $\Omega_{m,0}$ instead of $\mathcal{M}$. From Ref. [497]. For the reproduction of this figure visit the following dropbox link.

Clearly, the probability that all three first bins differ simultaneously more than 1σ from the best fit of each simulated full dataset in the context of ΛCDM is less than 5%. This is an effect approximately at the 2σ level. Actually, the probability is even smaller if we consider the exact σ differences that are shown in Table 4.3 and calculate the fraction of the simulated datasets with simultaneous σ differences larger that the exact corresponding σ differences of the real data. In particular, the probability to have simultaneously 1.14σ difference (or larger) in the first bin, 1.48σ difference (or larger) in the second bin and 0.99σ difference (or larger) in the third bin for $\mathcal{M}$, is $1.3 \pm 0.7\%$, while the relevant probability for $\Omega_{m,0}$ is $1.4 \pm 2\%$. However this

result should be interpreted with care since the exact differences are based on the fine tuned σ deviations of the real data bins from the full data best fits (1.14σ, 1.48σ and 0.99σ) and not a generic feature as the 1σ choice. Therefore, this is an aposteriori statistic constructed after looking at the data. Notice that a similar oscillating effect was also observed in Refs. [285, 458] even though its statistical significance was not quantified using simulated data.

Furthermore, it is interesting to check if this behavior is also evident for any three out of the four bins. Constructing 1000 Monte Carlo realizations, we find that the probability that the derived $\Omega_{m,0}$ in any three bins differ more than 1σ from the relevant $\Omega_{m,0}$ best fit to the whole random dataset is $10.4 \pm 2.2\%$, whereas the corresponding probability for $\mathcal{M}$ is $11.1 \pm 2.4\%$, as demonstrated in Fig. 4.15.

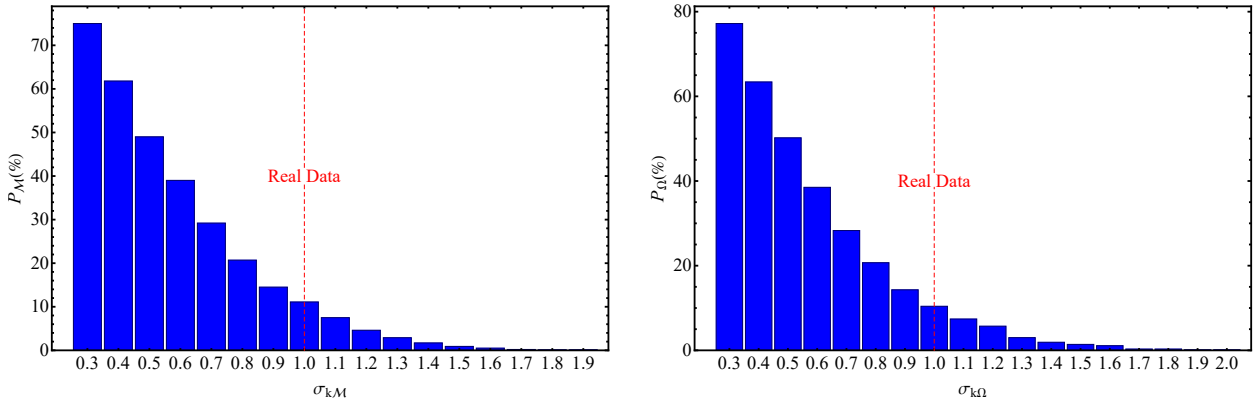

Figure 4.15: *Left Panel:* Percent of simulated Pantheon dataset (including systematics) where any three out of four bins all differ simultaneously more than $\sigma_{k\mathcal{M}}$ σ from the best fit of the full dataset. *Right Panel:* Same as the left panel but for the parameter $\Omega_{m,0}$ instead of $\mathcal{M}$. From Ref. [497]. For the reproduction of this figure visit the following dropbox link.

Similarly to the previous results considering the first three bins the probabilities reduce if we consider the exact σ difference of Table 4.3. In particular, the number of cases where the derived $\Omega_{m,0}$ in any 3 bins is more than $\sigma^{real}_{\Omega_{m,0}}$ away from the best fit $\Omega_{m,0}$ to the whole (random) data sample is $7.5 \pm 1.5\%$, while the relevant number of cases for $\mathcal{M}$ is $7.4 \pm 1.5\%$. A summary of the results can be seen in Table 4.4. These results indicate that the aforementioned oscillating effect is much more prominent at low $z \lesssim 0.5$ where the dark energy density is more prominent than in the fourth bin, which involves higher z. This fact favors the possibility that the effect has a physical origin since a systematic effect would probably affect equally all four redshift bins.

4.5 In Brief

In this Chapter we have performed a tomographic analysis of the latest publicly available SnIa data (Pantheon) in the context of a ΛCDM scenario. In particular, we applied the maximum likelihood method and fitted at the same time the parameters $\Omega_{\rm m,0}$ and the degenerate parameter $\mathcal{M}$, that is given by Eq. (4.1) as a combination of the absolute magnitude M and the Hubble parameter H_0. At first, we neglected the systematic uncertainties and found a $2\sigma - 3\sigma$ tension between the best fit value of $\mathcal{M}$ for SnIa with $0.01 < z < 0.2$ and the $\mathcal{M}$ value derived for the full Pantheon dataset. This tension at low redshifts can be interpreted either as a local

Number of cases	Probability
$\Omega_{m,0}$ in the first 3 bins $> 1\sigma$ away from the best fit $\Omega_{m,0}$ to the full dataset	$4.8 \pm 2\,\%$
$\mathcal{M}$ in the first 3 bins $> 1\sigma$ away from the best fit $\mathcal{M}$ to the full dataset	$4 \pm 2.5\,\%$
$\Omega_{m,0}$ in any 3 bins $> 1\sigma$ away from the best fit $\Omega_{m,0}$ to the full dataset	$10.4 \pm 2.2\,\%$
$\mathcal{M}$ in any 3 bins $> 1\sigma$ away from the best fit $\mathcal{M}$ to the full dataset	$11.1 \pm 2.4\,\%$
$\Omega_{m,0}$ in the first 3 bins $> \sigma^{real}$ away from the best fit $\Omega_{m,0}$ to the full dataset	$1.4 \pm 2\,\%$
$\mathcal{M}$ in the first 3 bins $> \sigma^{real}$ away from the best fit $\mathcal{M}$ to the full dataset	$1.3 \pm 0.7\,\%$
$\Omega_{m,0}$ in any 3 bins $> \sigma^{real}$ away from the best fit $\Omega_{m,0}$ to the full dataset	$7.5 \pm 1.5\,\%$
$\mathcal{M}$ in any 3 bins $> \sigma^{real}$ away from the best fit $\mathcal{M}$ to the full dataset	$7.4 \pm 1.5\,\%$

Table 4.4: Summary of the Monte Carlo deviations from the simulated and real data. The obtained results considering the exact σ_{real} differences should be treated with care, since this decrease of the probabilities is not generic and it is based on a fine tuned σ value.

matter underdensity with $\delta\Omega_0/\Omega_0 = -0.12 \pm 0.02$ or a modified theory scenario or this tension can due to statistical fluctuations.

In the context of the local underdensity scenario, a lower value of $\mathcal{M}$ leads to a higher value of h than the one indicated by the full dataset at low z, according to Eq. (4.1). If this scenario is truly realized in Nature, then we would naturally expect a signal of anisotropy in the parameter $\mathcal{M}$. Therefore, we utilized and compared two methods that search for such anisotropies: The Hemisphere Comparison (HC) method and the Dipole Fit (DF) method. In spite of the absence of any statistically significant anisotropic signal, a number of interesting conclusions have been unveiled. Using simulated Pantheon like data that were generated assuming a ΛCDM model, we showed that an anisotropy in the direction $b \in [-15°, -45°]$, $l \in [60°, 150°]$ (or in the opposite direction $b \in [15°, 45°]$, $l \in [240°, 330°]$) is favored generically by the data. This preference disappeared when we constructed a more isotropically distributed subset of the Pantheon data but this dataset less powerful in detecting overall anisotropy due to reduced number of SnIa. Furthermore, we showed that the HC method seems to be more appropriate in detecting general anisotropies in contrast to the DF method due to the sensitiveness of this particular method to an anisotropy that has a dipole form. The absence of any statistical anisotropy does not favor (but neither excludes) the local underdensity scenario as a possible explanation for the reduced value of $\mathcal{M}$ at low z.

In the context of a modified gravity theory, a lower value of $\mathcal{M}$ leads to a lower value of the absolute magnitude M in the low redshift regime which can be realized in the context of a modified theory of gravity with an evolving Newton's constant. In this scenario, using the general form of Eq. (4.22), we found a 2σ deviation of $\sim 2 - 3\%$ from the relevant ΛCDM value for $b = -3/2$. Assuming the phenomenological parametrization (2.10) and applying the maximum likelihood method, the best fit value of the extra parameter g_a was derived to be $g_a = -0.47 \pm 0.36$, *i.e.* approximately 1.5σ away from the relevant ΛCDM value ($g_a = 0$), favoring a reduced Newton's constant compared to GR, in consistency with the finding of Chapter 2.

Finally, we studied the possibility that the observed lower value of $\mathcal{M}$ is due to statistical fluctuations of the data. In particular, if the observed effect is real, then the same behavior should be present to a large number Monte Carlo simulations. So, including the systematic uncertainties this time, we sorted the Pantheon data from the lowest to the highest bin, divided

the entire dataset in four equal uncorrelated bins consisting of 262 datapoints and applied the maximum likelihood method finding the same abnormal variation of $\mathcal{M}$ in the low redshift regime in a somewhat lowered level. Then, we generated simulated Pantheon like data and found that the percent of the simulated Pantheon dataset with a similar behavior is $\simeq 5\%$, *i.e.* approaching the 2σ threshold. Even though this statistical significant further increases if instead of the first three bins we consider any three out of the four bins leaving the statistical fluctuation scenario a viable explanation, we stress that the first three bins correspond to SnIa with $z < 0.42$, *i.e.* where dark energy is dominant, hinting towards the existence of some hidden physics beyond the standard ΛCDM concordance model.

Chapter 5

Late-transition vs smooth $H(z)$ deformation models for the resolution of the Hubble crisis

One of the major observational problems that the standard ΛCDM model faces is the H_0 tension. This tension is currently at a 5σ level and refers to the mismatch in the measurement of the H_0 as estimated by indirect measurements from the CMB, BAO and uncalibrated SnIa using the inverse distance ladder method that report $H_0 = 67.36 \pm 0.54$ km s^{-1} Mpc^{-1} [18] with the direct measurement from the Pantheon+ SnIa sample using the standard distance ladder method that reports $H_0 = 73.04 \pm 1.04$ km s^{-1} Mpc^{-1} [518][1]. Nevertheless, there are more than one way to obtain the Hubble constant value and the majority of the early indirect estimates agree with Planck data, while most of the late time measurements agree with SH0ES even if different methods or geometric calibrators are used [317,318,519–521]. In particular, H_0 measurements coming from a calibration of the Tip of the Red Giant Branch method (instead of the usual Cepheid calibration one) on SnIa data [322,323], HII galaxy measurements [324] as well as various low redshift data combinations [325] report a value that lies in the intermediate area of these two (recall Fig. 1.7).

Motivated by the disagreement, a wide range of theoretical models have been proposed as possible solutions [73,88,90–93] and can be categorized in three broad classes

- "Early Time" Solutions: These kind of models, recalibrate the scale of the sound horizon at recombination by modifying physics during the pre-recombination era. In particular, these models deform the Hubble expansion rate before recombination at $z > 1200$ including additional components in the standard ΛCDM scenario increasing this way, the CMB derived value of H_0 [522–524]. These solutions include (but not limited to) early dark energy [217–223], extra neutrinos or relativistic species at recombination [212,224,525–530], evaporating primordial black holes [228] *etc.* Even though these models have the potential to alleviate the Hubble tension they predict stronger growth of perturbations being at odds with the reduced growth predicted by RSD and WL data, worsen as a result the growth tension [531].

- "Late Time" Deformation Solutions: These kind of models preserve the $H(z)$ consistent with the observed CMB anisotropy spectrum at high z but increase $H(z)$ at low z using a

[1] During the writing of the present thesis the data are not yet publicly available, so we focus on the Pantheon compilation.

late time smooth deformation, reaching the locally measured value of the Hubble constant at $z = 0$. These solution include (but not limited to) running vacuum models [106–114], interacting dark matter with dark energy models [204–211], exotic dark energy models [229–243] *etc.* However, they can not fully resolve the Hubble problem, since they face difficulties in fitting low z cosmological data (such as BAO and SnIa) [532] and tend to predict a lower value of SnIa absolute magnitude M than the value implied by Cepheid calibrators [533].

- "Late Time" Solutions with a Redshift Dependent SnIa Absolute Magnitude: This class of models have been recently proposed as a possible solution to the Hubble tension [534–536]. These models adopt an abrupt reduction of the SnIa absolute magnitude M by $\Delta M \simeq -0.2$ mag at a transition redshift z_t that can be caused by an abrupt change of fundamental physics, such as a transition of the evolving Newton's constant $G_{\rm eff}$. This type of transition may be possibly coupled with a transition on the dark energy equation of state w_{DE} from the standard ΛCDM value $w_\Lambda = -1$ at $z > z_t$ to a lower value at $z < z_t$. This class of models also have the potential to address the growth tension, since they reduce the growth rate of cosmological perturbation due to a lower value of $G_{\rm eff}$ at $z > z_t$ [535] and have been challenged by different cosmological data [537, 538].

Let us now be a little more thorough with the standard distance ladder methodology that is used by the SH0ES team to obtain the H_0 value. This methodology works by calibrating the Cepheid variable stars applying parallax methods and then using the calculated distances to "move further" towards galaxies that include mostly SnIa. Next, utilizing Eq. (4.2) in the redshift range $0.023 < z < 0.15$, the parameter $\mathcal{M}$ is measured under the assumption of a constant M and the Hubble free luminosity distance $D_L(z)$ is Taylor expanded as [539]

$$D_L(z) = z\left[1 + \frac{1}{2}(1 - q_0)\, z - \frac{1}{6}(1 - q_0 - 3\, q_0^2 + j_0)\, z^2 + \ldots\right], \tag{5.1}$$

where q_0 and j_0 are the deceleration and jerk parameters [540] that are assumed to be $q_0 = -0.55$ and $j_0 = 1$, *i.e.* they are fixed to their corresponding ΛCDM values. As a result, the value of H_0 is inferred using an extrapolation method. This methodology however, is oblivious to any possible transitions of M that could have happened at very low redshifts, *i.e.* for $z < 0.023$. If for example, such a transition had occurred at $z_t = 0.01$ (or lower), then the M that was derived using the Cepheids for z up to ≈ 0.01 should not be considered to be the same for the nearby SnIa. So, recent works argue that the designation "*M tension/crisis*" might be more suitable to describe the problem [541, 542]. Instead of focusing on the different H_0 values published by the Planck mission [18] and the SH0ES collaboration [518], these works propose to focus on the different absolute magnitudes M values, which for the Planck mission is $M = -19.401 \pm 0.027$ mag [543] while for the SH0ES collaboration corresponds to $M_c = -19.244 \pm 0.037$ mag [544].

In this Chapter we focus on the third class of possible solutions, *i.e.* on late time M transition models (LMT) that possibly include a transition in the dark energy equation of state parameter w_{DE} ($LwMT$) and estimate their best fit parameter values. Then, we consider different $H(z)$ deformation models and compare their quality of fit with the transition models LMT and $LwMT$. Previous works using the CMB effective parameters as well as different cosmological data indicated that transition models improve the quality of fit to cosmological data [533–535]. In this Chapter, we implement a more complete and accurate approach using the full Planck18 CMB data in the context of the Boltzmann code `CLASS` [463, 464] and a Monte

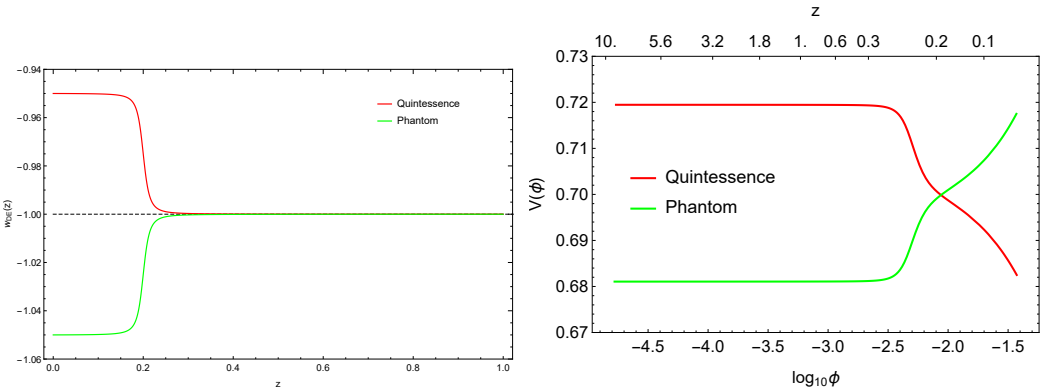

Figure 5.1: *Left Panel:* An example of how a transition in the equation of state $w_{DE}(z)$ looks. *Right Panel:* An example of how the transition of the left panel can be achieved in the context of a sharp transition in a quintessence (red line) or phantom (green line) potential (right panel), with the scalar field running down/up the potential respectively. For this plot we assume $\Omega_{m,0} = 0.3$, $z_t = 0.2$ and $\Delta w = \pm 0.05$ for quintessence/phantom fields and reconstructed the potentials following the procedure of Ref. [105]. From Ref. [536]

Carlo Markov Chain analysis using the `MontePython` code [545, 546]. Both of these numerical packages are similar to the `MGCAMB` and `MGCOSMOMC` codes that we used in Chapter 2.

5.1 Fitting the Transition Models to Cosmological Data

The transition models that we will confront with up to date cosmological data are the LMT and $LwMT$ models. In particular, the LMT model involves an abrupt transition of the absolute magnitude M of the following form [534, 536]

$$M(z) = M_< + \Delta M\, \Theta(z - z_t)\,, \tag{5.2}$$

where z_t corresponds to the transition redshift, $M_< \equiv M_c = -19.24$ mag is the Cepheid value of the absolute magnitude as calibrated by the SH0ES teams reconstructed in Refs. [541, 544], ΔM is the parameter that quantifies the shift from the M_c value and Θ corresponds to the Heaviside step function. The LMT model is a special case of the $LwMT$ model that has been initially discussed in Ref. [534] and has a simultaneous transition on the same redshift z_t of the dark energy equation of state w_{DE} of the form [534, 536]

$$w_{DE}(z) = -1 + \Delta w\, \Theta(z_t - z)\,, \tag{5.3}$$

where Δw describes the shift from the ΛCDM value ($w_\Lambda = -1$) for $z < z_t$. Such transitions in the equation of state $w_{DE}(z)$ can happen in the context of a minimally coupled scalar field in GR, either of the quintessence or phantom type, as it is demonstrated in Fig. 5.1 where we show how a transition of w_{DE} in the left panel can be achieved by a quintessence (red line) or phantom (green line) potential with the scalar field running down (up) the potential for the quintessence (phantom) case. For Fig. 5.1 we reconstruct the potential using the procedure of Ref. [105] setting $\Omega_{m,0} = 0.3$, $z_t = 0.2$ and $\Delta w = \pm 0.05$ where the positive (negative) sign corresponds to the quintessence (phantom) field. Obviously, altering the aforementioned parameters the steepness as well as the transition redshift can be tuned.

For the estimation of the best fit parameters of the transition models LMT and $LwMT$, we utilize the `CLASS/MontePython` numerical codes. Of course, the codes do not include the transition models by default, so we need to modify them accordingly (see Appendix B for more details regarding the performed modifications). In the context of the MCMC analysis performed by the modified `MontePython` code, we consider the following datasets:

- The Planck18 CMB data and in particular, the TTTEEE likelihoods for high-l ($l > 30$), the temperature data TT and EE power spectra data for low-l ($2 < l < 30$), as well as the CMB lensing likelihood [18].
- The BAO data discussed in Refs. [45, 547, 548] as well as the Lyα BAO [549, 550].
- The Pantheon SnIa compilation [41].
- A robust compilation of RSD data discussed in Ref. [71], using the likelihood presented in Ref. [551].

The main advantage of the transition models, is that they provide a great amount of flexibility in fitting the observational data, since they can closely reproduce ΛCDM for $z > z_t$, while being fully consistent with local measurements of the absolute magnitude M due to the extra parameter ΔM. Therefore, if we set the transition at a rather low value, then we expect to have a quality of fit similar to ΛCDM. Obviously, if the transition occurs at ultra low redshifts where no data (from the selected datasets) are available, an even better quality of fit to that of ΛCDM is expected due to the extra number of parameters of the transition models. In this case however, there would be no H_0 tension, since the local measurement of H_0 should coincide with the measurement of Planck if the M transition is taken into account. Hence, we impose the prior $\Delta w \in [-0.7, 0.7]$ as well as $z_t \geq 0.01$ for the $LwMT$ model that corresponds to $a_t \leq 0.99$, since any lower value of z_t can not be probed due to the Hubble flow. The best fit values of the $LwMT$ model with $z_t \geq 0.01$ are shown in Table 5.1, while the $1\sigma - 2\sigma$ confidence contours are shown in Fig. 5.2.

Parameter	best-fit	mean$\pm\sigma$	95.5% lower	95.5% upper
$\Omega_{m,0}$	0.3018	$0.3066^{+0.0064}_{-0.0065}$	0.2939	0.3196
n_s	0.9708	$0.9685^{+0.0038}_{-0.0037}$	0.9608	0.9759
H_0	68.56	$68.03^{+0.55}_{-0.58}$	66.94	69.15
σ_8	0.8141	0.8089 ± 0.0065	0.7957	0.8219
ΔM	-0.1676	-0.1698 ± 0.012	-0.1933	-0.1467
Δw	unconstrained	unconstrained	unconstrained	unconstrained
a_t	0.9856	> 0.985	> 0.984	> 0.984
$M_> \equiv M_c + \Delta M$	-19.408	-19.410 ± 0.012	-19.433	-19.387
$-\ln \mathcal{L}_{\rm min}$	1917.02			
$\chi^2_{\rm min}$	3834			

Table 5.1: The best fit values and the $1\sigma-2\sigma$ constraints of the parameters for the $LwMT$ model with $z_t \geq 0.01$ (or equivalently $a_t \leq 0.99$) using the CMB+BAO+Pantheon+RSD likelihoods described above.

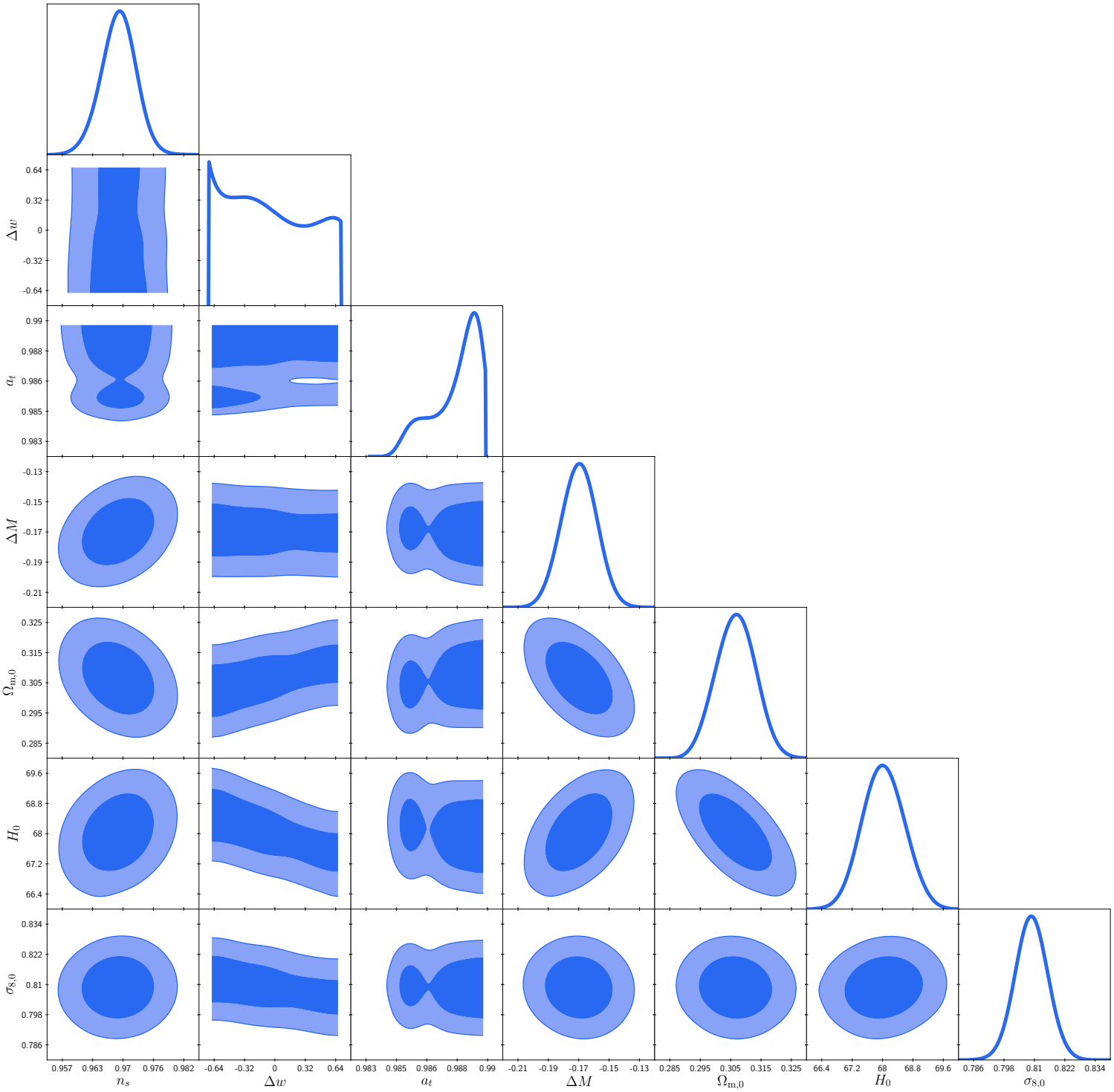

Figure 5.2: The $1\sigma - 2\sigma$ confidence contours for the $LwMT$ model with $z_t \geq 0.01$, using the CMB+BAO+Pantheon+RSD likelihoods. In this plot $\sigma_{8,0} \equiv \sigma_8$. From Ref. [536].

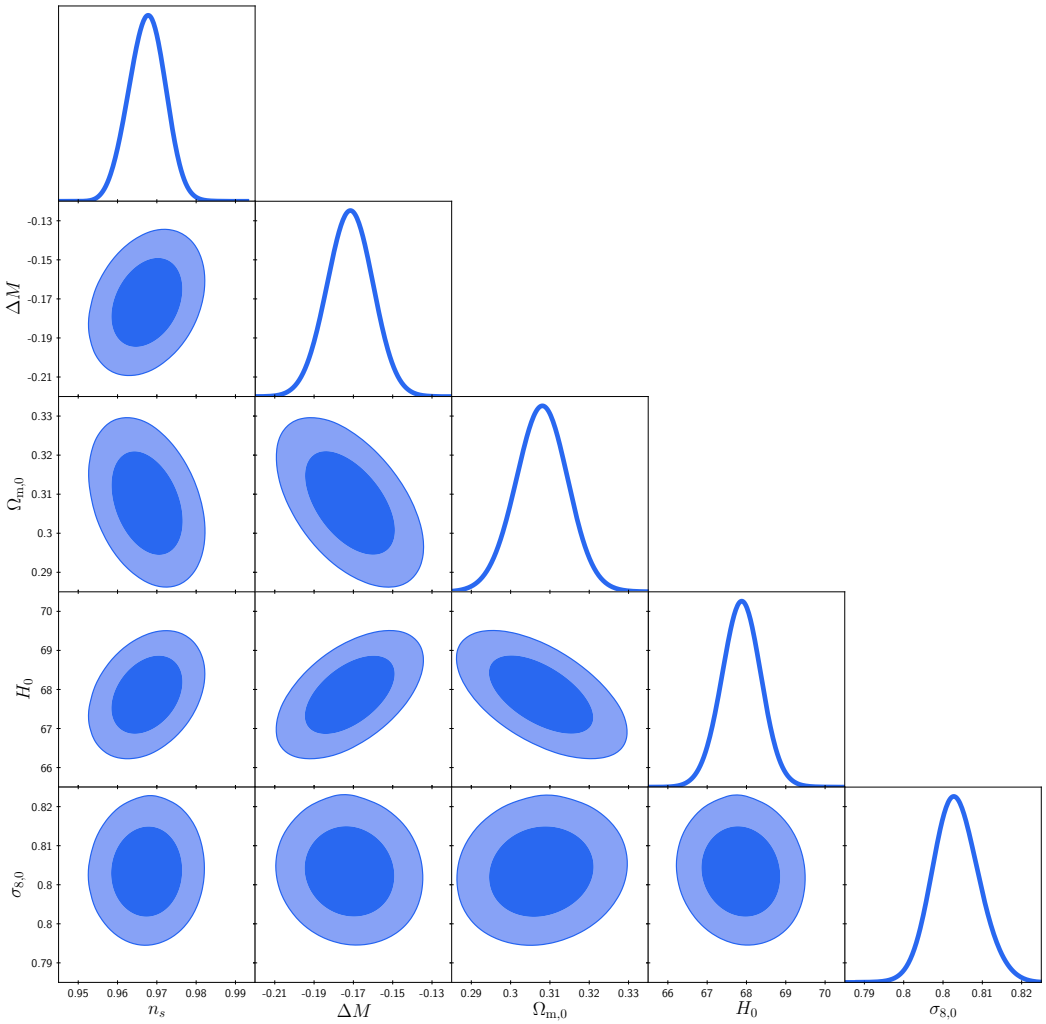

Figure 5.3: The $1\sigma-2\sigma$ confidence contours for the LMT model with $z_t = 0.01$ (or equivalently $a_t = 0.99$), using the CMB+BAO+Pantheon+RSD likelihoods. In this plot $\sigma_{8,0} \equiv \sigma_8$. From Ref. [536].

In Table 5.1, we also present the corresponding value of the parameter $M_> \equiv M_c + \Delta M$ that arises for $z > z_t$.

Clearly, the parameter a_t (or equivalently z_t) reaches the highest (lowest) eligible value imposed by the prior in order to achieve the best possible quality of fit, favoring an ultra low redshift transition. One could argue that the timing of the transition is fined tuned, however since the dark energy has started dominating at low redshifts, we naturally expect that new physics could emerge in that area. Most importantly we observe, that despite allowing for an extra degree of freedom through the parameter Δw, the data seem to neglect it. Since $z_t \approx 0.01$ is favored by the data, the parameter Δw becomes irrelevant due to the fact that for $z_t = 0.01$, Δw would modify $H(z)$ only in a non existing data area ($z < 0.01$). Therefore, we repeat the analysis considering only a transition on M ("Late M Transition" - LMT) setting $\Delta w = 0$ and $a_t = 0.99$ (or equivalently $z_t = 0.01$), *i.e.* the maximum of the posterior of a_t for the $LwMT$ model. The best fit values of the LMT model with $z_t = 0.01$ are shown in Table 5.2, while the corresponding $1\sigma - 2\sigma$ confidence contours are showing in Fig. 5.3.

Parameter	best-fit	mean$\pm\sigma$	95.5% lower	95.5% upper
$\Omega_{\rm m,0}$	0.3088	$0.3082^{+0.0052}_{-0.0058}$	0.2976	0.3193
n_s	0.9697	$0.968^{+0.0038}_{-0.0037}$	0.9606	0.9754
H_0	67.88	$67.89^{+0.42}_{-0.40}$	67.06	68.71
σ_8	0.8085	$0.8084^{+0.0058}_{-0.0061}$	0.7963	0.8205
ΔM	-0.170	-0.172 ± 0.012	-0.195	-0.149
$M_> \equiv M_c + \Delta M$	-19.410	-19.412 ± 0.012	-19.435	-19.389
$-\ln \mathcal{L}_{\rm min}$	1917.52			
$\chi^2_{\rm min}$	3835			

Table 5.2: The best fit values and the $1\sigma-2\sigma$ constraints of the parameters for the LMT model and $z_t = 0.01$ (or equivalently $a_t = 0.99$) using the CMB+BAO+Pantheon+RSD likelihoods described above.

Comparing Table 5.1 with Table 5.2 and Fig. 5.2 with Fig. 5.3, we confirm that the introduction of Δw has basically no effect in the quality of fit, *i.e.* on the χ^2 value. It is interesting to note that the inferred value of $M_> = -19.41$ mag fully agrees with the CMB constraint of the absolute magnitude $M = -19.40$ mag [543], indicating the mismatch between the local calibration of the SnIa absolute magnitude and the value inferred from the other probes is very significant, suggesting that the designation M tension/crisis is truly more suitable to describe the H_0 crisis [541, 542]. So, it is only natural to wonder if some other popular dark energy models in the literature that attempt to explain the Hubble crisis are consistent with the Cepheid measurement M_c and how can their quality of fit compare with the transition models presented above. This case will be discussed extensively in the following section, where we perform a comparison between the transition models $LwMT$ and LMT with some popular smooth deformation dark energy models.

5.2 Comparison of Different Dark Energy Models

In order to truly resolve the Hubble crisis, the selected dark energy model should not only provide a consistent measurement for M with M_c at the 1σ level, but also a χ^2 value similar (or even better) to ΛCDM. In this section, we compare the transition models $LwMT$ and LMT with some popular smooth deformation dark energy models following three different methods:

- Impose a flat prior on the absolute magnitude $M \in [-19.28, -19.2]$ mag, forcing all models (both the transitions and the smooth deformations ones) to be consistent with the Cepheid absolute magnitude M_c measurement [541,544] at the 1σ level. This analysis is studied in Subsection 5.2.1.

- Impose the local Cepheid calibrated gaussian prior by SH0ES on the absolute magnitude $M_c = -19.24 \pm 0.04$ mag [541]. This case will be discussed in Subsection 5.2.2.

- Follow the usual method that is adopted in the literature, by imposing the SH0ES value of H_0 [518], allowing at the same time the absolute magnitude M to vary freely. This is illustrated in Appendix E as a complementary analysis.

Regrading the considered smooth deformation models, we select the wCDM model with a Hubble parameter (1.69) neglecting radiation and neutrinos at late times and the CPL model with a Hubble parameter (1.71), assuming $\Omega_{\rm r,0} = 0$ and setting $w_1 = w_a$. Furthermore, we consider the phenomenologically emergent dark energy (PEDE) model which shows significant promise in resolving the H_0 problem. This model, was first discussed in Ref. [234] with an equation of state of the form

$$w_{DE}(z) = -\frac{1}{3\ln(10)}(1 + \mathrm{Tanh}[\log_{10}(1+z)]) - 1\,, \tag{5.4}$$

with a corresponding Hubble parameter

$$H(z) = H_0\sqrt{\Omega_{\rm m,0}(1+z)^3 + (1-\Omega_{\rm m,0})\cdot[1 - \mathrm{Tanh}\left(\log_{10}(1+z)\right)]}\,. \tag{5.5}$$

The basic advantage of PEDE, is that it has the same degrees of freedom as ΛCDM. Hence, taking into consideration the transition models $LwMT$ with $z_t > 0.01$ and LMT with $z_t = 0.01$ along with the ΛCDM model itself we have a total of six different models.

5.2.1 Dark Energy Models Comparison using a Flat Prior on M

In the current subsection we perform a Monte Carlo Markov Chain (MCMC) analysis using the likelihoods described above and adopting the flat prior on the SnIa absolute magnitude $M \in [-19.28, -19.2]$ mag, forcing all the considered models to be consistent with the Cepheid calibrated measurement M_c at the 1σ level. For the transition model $LwMT$ we use Eq. (5.2) as the SnIa absolute magnitude and Eq. (5.3) as the equation of state, leaving ΔM as a free parameter, while for the transition model LMT we use only Eq. (5.2) as the SnIa absolute magnitude. Clearly, the transition models are the only models that can by construction escape from the imposed flat prior on M. The best fit values of the cosmological parameters as well as the $1\sigma - 2\sigma$ confidence contours are illustrated in Table 5.3 and Fig. 5.4 respectively.

Parameters	ΛCDM	wCDM	CPL	$LwMT$ ($z_t \geq 0.01$)	PEDE	LMT ($z_t = 0.01$)
$\Omega_{\rm m,0}$	$0.2564^{+0.0018}_{-0.0019}$	$0.2571^{+0.0019}_{-0.0020}$	$0.2719^{+0.0041}_{-0.0044}$	0.3066 ± 0.0063	0.2582 ± 0.0020	0.3082 ± 0.0053
n_s	0.992 ± 0.003	0.972 ± 0.004	0.967 ± 0.004	0.968 ± 0.004	0.971 ± 0.003	0.968 ± 0.004
H_0	72.40 ± 0.16	$73.99^{+0.26}_{-0.27}$	72.38 ± 0.48	68.03 ± 0.55	$73.90^{+0.17}_{-0.19}$	67.89 ± 0.40
σ_8	$0.8045^{+0.0072}_{-0.0081}$	$0.8507^{+0.0084}_{-0.0083}$	$0.8511^{+0.0084}_{-0.0081}$	0.8088 ± 0.0063	0.8517 ± 0.0059	0.8084 ± 0.0059
S_8	0.7437 ± 0.0077	0.7876 ± 0.0084	0.8103 ± 0.0100	$0.8177^{+0.0101}_{-0.0103}$	0.7901 ± 0.0065	0.8194 ± 0.0100
M	~ -19.28	~ -19.28	~ -19.28	$-19.24\,(M_<)$	~ -19.28	$-19.24\,(M_<)$
ΔM	-	-	-	-0.170 ± 0.011	-	-0.172 ± 0.011
$M_> \equiv M_c + \Delta M$	-	-	-	-19.410 ± 0.011	-	-19.412 ± 0.011
Δw	-	-	-	unconstrained	-	-
a_t	-	-	-	> 0.987	-	-
w_0	-	$-1.162^{+0.021}_{-0.019}$	$-0.844^{+0.077}_{-0.089}$	-	-	-
w_a	-	-	$-1.27^{+0.38}_{-0.31}$	-	-	-
$\chi^2_{\rm min}$	3964	3889	3875	3834	3886	3835
$\Delta\chi^2_M$	-	-75	-89	-130	-78	-129

Table 5.3: The 1σ constraints of the parameters for all the dark energy models explored in this Chapter when the flat prior $M \in [-19.28, -19.2]$ mag is imposed, using the CMB+BAO+Pantheon+RSD likelihoods described above.

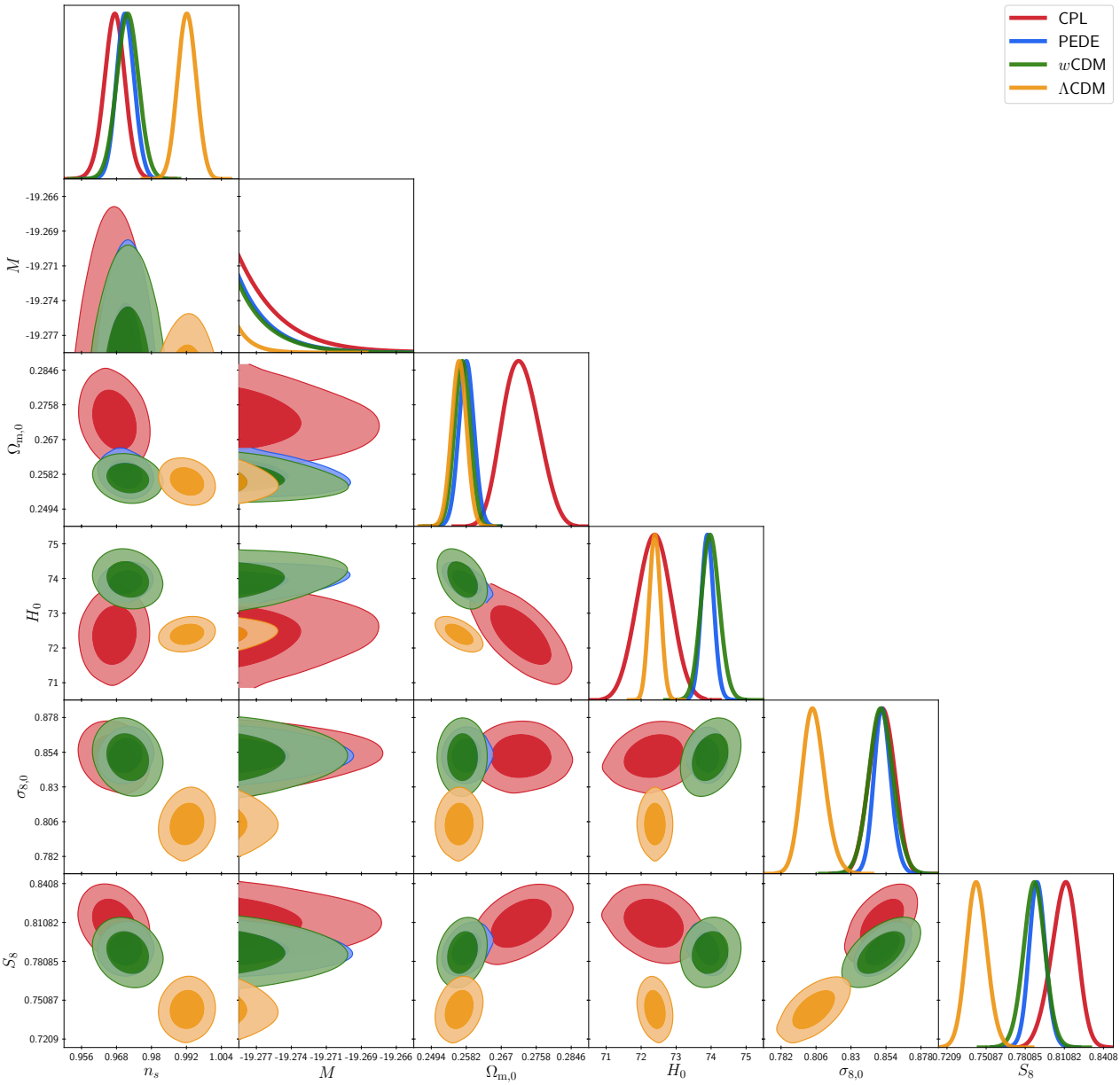

Figure 5.4: The $1\sigma - 2\sigma$ confidence contours for the common parameters of the ΛCDM, CPL, wCDM and PEDE dark energy models corresponding to the constraints of Table 5.3 imposing the flat prior $M \in [-19.28, -19.2]$ mag. For the contours, we used the CMB+BAO+Pantheon+RSD likelihoods. The M prior severely constrains the best fit of M to the lowest possible value, displaying the tendency of the models to provide a significantly lower value for M. In this plot $\sigma_{8,0} \equiv \sigma_8$. From Ref. [536].

Obviously, this prior is an artificial one, since the correct prior is the gaussian one. However the use of the flat prior helps estimating the impact of the local calibration on the quality of fit of the various models.

According to Table 5.3 all models, except the transition ones, provide a H_0 value that is consistent with the local measurement of H_0 by the SH0ES collaboration [518] and $M \sim -19.28$ mag, *i.e.* the lowest eligible value of the imposed prior. This behavior displays the tendency

of the models to give a significantly lower value of M. On the contrary, the transition models provide a H_0 value within the 1σ level to the typical ΛCDM value reported by the Planck mission [18], providing at the same time $M \approx -19.4$ mag as expected. Notice, that ΛCDM has the worse overall fit due to the fixed value of M to the local M_c value. In this case the SnIa data constrain the luminosity distance of ΛCDM to values inconsistent with CMB and BAO showing that ΛCDM is unable to resolve the M crisis [541, 542]. On the contrary, the more flexible wCDM, CPL and PEDE models provide significantly better fit but still much worse than the transition models $LwMT$ and LMT as shown in Table 5.4.

Datasets	ΛCDM	wCDM	CPL	$LwMT$ ($z_t \geq 0.01$)	PEDE	LMT ($z_t = 0.01$)
$\chi^2_{\rm min}$ CMB	2858	2786	2779	2783	2784	2781
$\chi^2_{\rm min}$ BAO	46	33	42	10	30	11
$\chi^2_{\rm min}$ Pantheon	1049	1051	1034	1024	1052	1027
$\chi^2_{\rm min}$ RSD	12	19	20	17	20	16
Total $\chi^2_{\rm min}$	3964	3889	3875	3834	3886	3835

Table 5.4: The individual $\chi^2_{\rm min}$ of each likelihood for all the dark energy models studied in the present Chapter using the flat prior $M \in [-19.28, -19.2]$ mag.

5.2.2 Dark Energy Models Comparison using a Local Prior on M

In the current subsection we perform a MCMC analysis using the likelihoods described above and adopting the gaussian prior on the SnIa absolute magnitude $M_c = -19.24 \pm 0.04$ mag. The best fit values of the cosmological parameters as well as the $1\sigma - 2\sigma$ confidence contours are shown in Table 5.5 and Fig. 5.5 respectively.

Parameters	ΛCDM	wCDM	CPL	$LwMT$ ($z_t \geq 0.01$)	PEDE	LMT ($z_t = 0.01$)
$\Omega_{\rm m,0}$	$0.3022^{+0.0051}_{-0.0052}$	0.2943 ± 0.0065	$0.2974^{+0.0067}_{-0.0068}$	$0.3073^{+0.0063}_{-0.0062}$	0.2789 ± 0.0049	0.3082 ± 0.0053
n_s	0.9704 ± 0.004	0.968 ± 0.004	0.967 ± 0.004	0.968 ± 0.004	0.963 ± 0.003	0.968 ± 0.004
H_0	68.36 ± 0.4	69.47 ± 0.72	69.25 ± 0.73	67.96 ± 0.55	71.85 ± 0.45	67.89 ± 0.40
σ_8	$0.8076^{+0.0058}_{-0.0062}$	$0.8215^{+0.0095}_{-0.0097}$	$0.8248^{+0.0096}_{-0.0097}$	$0.8084^{+0.0064}_{-0.0065}$	0.8531 ± 0.0059	0.8085 ± 0.0057
S_8	$0.8105^{+0.0097}_{-0.01}$	0.8135 ± 0.0098	$0.8210^{+0.0107}_{-0.0106}$	0.8181 ± 0.0100	0.8226 ± 0.0095	0.8194 ± 0.0099
M	-19.40 ± 0.01	-19.38 ± 0.02	-19.37 ± 0.02	-19.26 ± 0.04	-19.33 ± 0.01	-19.24 ± 0.04
ΔM	-	-	-	$-0.145^{+0.038}_{-0.035}$	-	-0.168 ± 0.039
$M_>$	-	-	-	-19.410 ± 0.011	-	-19.411 ± 0.011
Δw	-	-	-	unconstrained	-	-
a_t	-	-	-	> 0.986	-	-
w_0	-	-1.050 ± 0.027	-0.917 ± 0.078	-	-	-
w_a	-	-	$-0.53^{+0.33}_{-0.28}$	-	-	-
$\chi^2_{\rm min}$	3854	3851	3848	3833	3867	3835
$\Delta\chi^2$	-	-3	-6	-21	$+13$	-19

Table 5.5: The 1σ constraints of the parameters for all the dark energy models explored in the present Chapter when a gaussian prior $M_c = -19.24 \pm 0.04$ mag is imposed, using the CMB+BAO+Pantheon+RSD likelihoods described above.

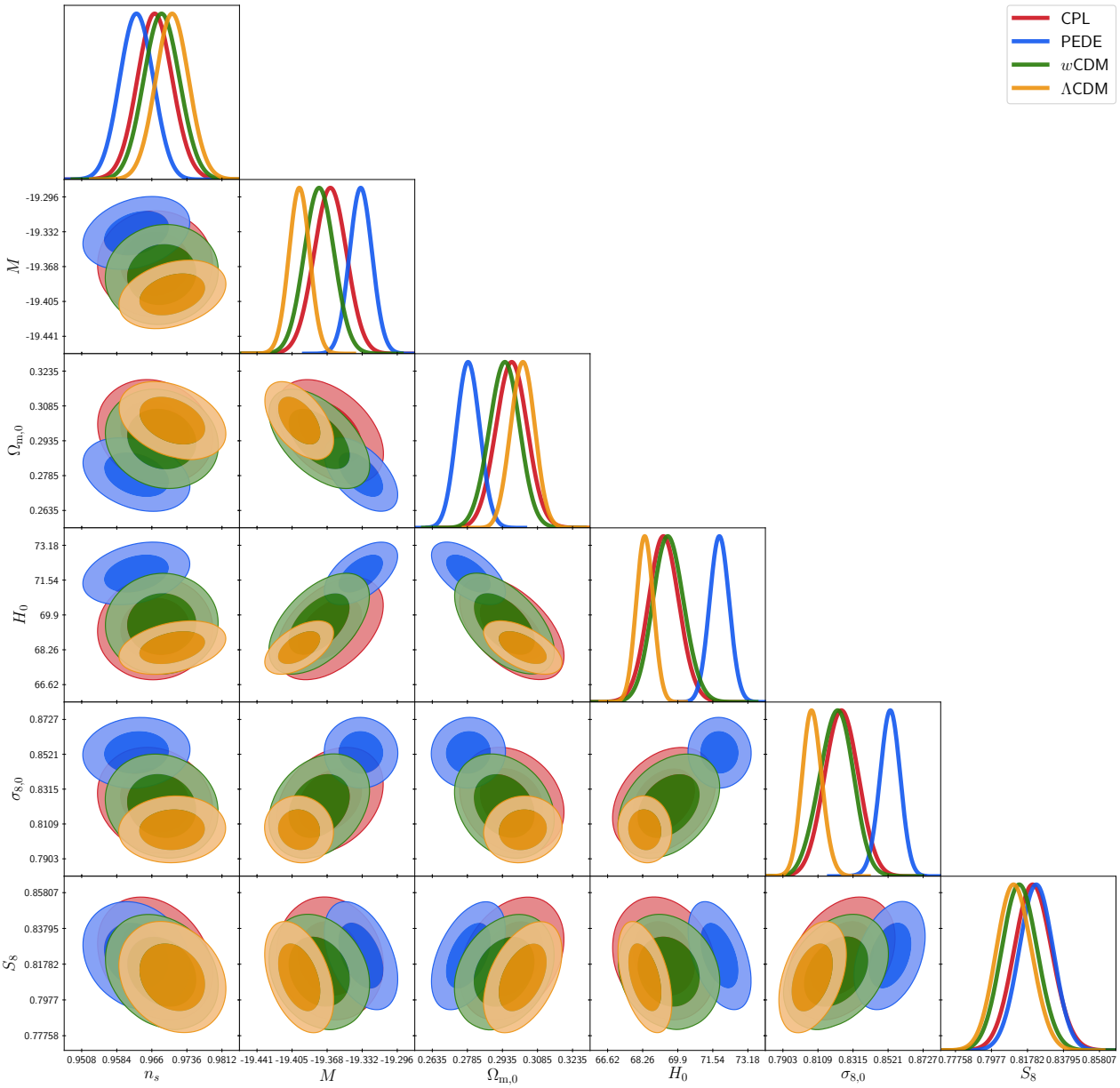

Figure 5.5: The $1\sigma - 2\sigma$ confidence contours for the common parameters of the ΛCDM, CPL, wCDM and PEDE dark energy models corresponding to the constraints of Table 5.5 imposing the gaussian prior $M_c = -19.24 \pm 0.04$ mag. For the contours, we used the CMB+BAO+Pantheon+RSD likelihoods. In this plot $\sigma_{8,0} \equiv \sigma_8$. From Ref. [536].

The transition $LwMT$ and LMT models perform better than the rest of the models, providing not only an absolute magnitude value consistent with the Cepheid calibrated value M_c (the only ones) but also a better quality of fit with respect to ΛCDM. Regarding the quality of fit, the wCDM and CPL models achieve a slightly better fit to data compared to ΛCDM, while the PEDE model has a significantly worse fit to data, in agreement with previous studies [236].

5.2.3 Model Selection

For the proper identification of the optimal model, we also need to compare the statistical significance of the considered models taking into account the number of parameters and not only the χ^2 value. In this subsection we focus only on the gaussian prior case as it uses the actual Cepheid prior from the SH0ES collaboration. Therefore, we consider the Akaike Information Criterion (AIC) [552, 553] which is defined as

$$AIC \equiv -2\,ln\,\mathcal{L}_{\rm max} + 2\,N_{\rm tot} = \chi^2_{\rm min} + 2\,N_{\rm tot}\,, \tag{5.6}$$

where $N_{\rm tot}$ corresponds to the total number of free parameters of the considered model and $\mathcal{L}_{\rm max}$ corresponds to the maximum likelihood. This criterion penalizes the considered models for any extra parameter in such a way that the model with the lowest value is supported the most. In particular, using Eq. (5.6) we calculate the AIC values for all the models of Table 5.5 and generate the corresponding differences $\Delta AIC \equiv AIC_{\rm model} - AIC_{\Lambda\rm CDM}$. The specific differences of all the considered DE models are shown in Table 5.6. If $|\Delta AIC| \leq 2$, then the compared models can be interpreted as consistent with each other, while if $|\Delta AIC| \geq 4$ it is an indication that the model with the larger AIC value is disfavored [553].

Gaussian M Prior Case	$\Delta\chi^2$	ΔAIC	$\ln B$
ΛCDM	–	–	–
$LMT(z_t = 0.01)$	-19	-17	$+9.1$
$LwMT(z_t \geq 0.01)$	-21	-15	$+6.2$
wCDM	-3	-1	$+2.2$
CPL	-6	-2	-2.4
PEDE	$+13$	$+13$	-6.5

Table 5.6: $\Delta\chi^2$ and corresponding ΔAIC and lnB values for all models of Table 5.5 with respect to ΛCDM. Negative values of $\Delta\chi^2$ and ΔAIC and positive values of lnB show that a model is favored over ΛCDM.

According to the third column of Table 5.6, the transition models are strongly favored over ΛCDM, while the PEDE model is strongly disfavored.

Furthermore, we consider the MCEvidence package [554] which computes Bayesian evidences, *i.e.* the marginal likelihoods, of each model of Table 5.5 taking into account the relevant MCMC chains. MCEvidence, uses the k nearest neighbour of the Mahalanobis distances [555] in the parametric space which corresponds to the $k = 1$ case that minimizes any inaccuracies (see Ref. [555] for more details). Using the revised Jeffreys' scale [556], we can compare the $|\ln B|$ value of two different models (B corresponds to the Bayes factor) and see which one of the two models is favored by the data. In particular, if $|\ln B| < 1$ the two considered models can be interpreted as consistent with each other, if $1 < |\ln B| < 2.5$ then the model with the larger $|\ln B|$ is weakly favored, if $2.5 < |\ln B| < 5$ then the model with the larger $|\ln B|$ is moderate favored, while if $|\ln B| > 5$ the model with the larger $|\ln B|$ value is strongly favored. In the last column of Table 5.6, we show the $\ln B$ difference with respect to ΛCDM for the M prior case, so the positive (negative) values indicate that the model is favored (disfavored) over ΛCDM. Clearly, the wCDM and CPL are weakly favored and disfavored respectively, the PEDE model is strongly disfavored whereas the transition models $LwMT$ and LMT are strongly favored over ΛCDM in consistency with the results of the AIC.

5.3 In Brief

In this Chapter we have considered two recently proposed dark energy models with a transition at a recent redshift z_t that have been proposed as possible solutions of the Hubble tension and compared their quality of fit with up to date cosmological data. The first one that we call LMT includes a transition on the absolute magnitude M of the form of Eq. (5.2), while the second one also includes a transition in the equation of state parameter w_{DE} of the form of Eq. (5.3) on top of the transition on M. Furthermore, we compared the transition models $LwMT$ and LMT with three well known smooth $H(z)$ deformation dark energy models that attempt to resolve the Hubble crisis (wCDM, CPL and PEDE) as well the standard ΛCDM model. Using appropriate statistical criteria such as the Akaike Information Criterion and the Bayes factor, we found that the transition models are strongly favored over ΛCDM, wCDM is weakly favored, CPL is weakly disfavored while PEDE is strongly disfavored by the data. The transition models LMT and $LwMT$ are not only strongly favored by the data, giving a quality of fit similar to ΛCDM, but they have the additional advantage that can, by construction, be consistent with the SnIa absolute magnitude M_c measured by Cepheid calibrators in contrast with the smooth smooth $H(z)$ deformation dark energy models.

If these transition models are truly realized in Nature, then they would lead naturally to a similar transition of the ratio $G_{\rm eff}/G_{\rm N}$ to values lower than unity, addressing as a result simultaneously the growth tension [535]. In particular, for the transition models LMT and $LwMT$ we have

$$\left\{ \begin{array}{l} \frac{G_{\rm eff}}{G_{\rm N}} = 1 + \frac{\Delta G_{\rm eff}}{G_{\rm N}}, \ \text{for} \ z > z_t \\ \frac{G_{\rm eff}}{G_{\rm N}} = 1, \ \text{for} \ z < z_t \end{array} \right\} . \tag{5.7}$$

But, without loss of generality we can assume that

$$\ln\left(1 + \frac{\Delta G_{\rm eff}}{G_{\rm N}}\right) \simeq \frac{\Delta G_{\rm eff}}{G_{\rm N}} , \tag{5.8}$$

since $\Delta G_{\rm eff}/G_{\rm N} \ll 1$. So, Eq. (4.23) takes the form [536]

$$\Delta M = -\frac{5\,b}{2}\frac{\ln\left(\frac{G_{\rm eff}}{G_{\rm N}}\right)}{\ln(10)} . \tag{5.9}$$

Using Eq. (5.7) for $z > z_t$, it is straightforward to show that

$$\ln\left(\frac{G_{\rm eff}}{G_{\rm N}}\right) \simeq \frac{\Delta G_{\rm eff}}{G_{\rm N}} . \tag{5.10}$$

Therefore, substituting Eq. (5.10) in (5.9) and solving with respect to b, we derive [536]

$$b = -\frac{2\ln(10)}{5}\frac{\Delta M}{\frac{\Delta G_{\rm eff}}{G_{\rm N}}} . \tag{5.11}$$

So, based on Eq. (5.11) we can constrain the value of b taking into account that b should also obey the general bounds $|b| \in [b_{\rm min}, +\infty)$, where the $+\infty$ is the ΛCDM value. Various works in the literature have reported constrains on the ratio $\Delta G_{\rm eff}/G_{\rm N}$, hence using these values as well as the values indicated in Table 5.2 we can constrain the allowed values of b.

In particular, measurement from up to date primitive element abundances, cosmic microwave background as well as nuclear and weak reaction rates report $|\Delta G_{\rm eff}/G_{\rm N}|_{\rm min} = 0.05$ [557]. Substituting this value in Eq. (5.11) and setting the 2σ upper bound from Table 5.2, *i.e.* setting $|\Delta M|_{\rm min} = -0.172 + 2 \times 0.012 = -0.148$ mag we derive

$$b_{\rm min,0.05} = (-\infty, -2.7] \cup [2.7, +\infty)\,. \tag{5.12}$$

Similarly measurements from the Hubble diagram SnIa [558] as well as from Paleontology [559] report $|\Delta G_{\rm eff}/G_{\rm N}|_{\rm min} = 0.1$ that corresponds to

$$b_{\rm min,0.1} = (-\infty, -1.4] \cup [1.4, +\infty)\,. \tag{5.13}$$

This range includes the $b = -3/2$ value considered by most previous studies [455, 495].

It is important to note here that these transition models are not without a physical theoretical basis. As we discussed in Subsection 5.1, such transitions could occur in the context of a minimally coupled scalar field in GR either of the quintessence or of the phantom type with the scalar field rolling down or up the potential respectively. Another quite interesting physical mechanism in the context of scalar tensor theories that could in principle reproduce the behavior of the transition models includes a very recent false vacuum decay [560, 561]. This model would in principle induce a transition on $G_{\rm eff}/G_{\rm N}$ leading to the required transition of the absolute magnitude M. Specifically, for a bubble with an energy scale similar to the cosmological constant, the scale of the bubbles would be $R_b = \delta/H_0$ where δ is a coefficient that is given as [538, 560, 561]

$$\delta = 4\,B_1\,\ln\left(\frac{M_{pl}}{T_c}\right)^{-1}\,, \tag{5.14}$$

where B_1 is a constant and T_c is the transition temperature energy scale. Plugging $H_0 = 70\,{\rm km\,s^{-1}\,Mpc^{-1}}$ and $T_c = 2.7\,{\rm K}$ we derive $R_b \simeq 20\,{\rm Mpc}$. Even though this scale is significantly lower than the transition redshift value $z_t = 0.01$ value that is considered in this Chapter and can not be studied using the above likelihoods, recent studies using Cepheid [538] and Tully Fisher data [537] have pointed out towards this direction.

Chapter 6

Hints of Modified Gravity in Sub-Millimeter Scales

If ΛCDM is truly the correct scenario that describes our Universe, then it is only natural to expect that its predictions would be consistent with observations on all scales. In the previous Chapters we mainly focused on the inconsistencies that ΛCDM faces on cosmological scales. Interestingly, however, there are some predictions on small scales, *i.e.* on scales of a few kpc and below, that seem to disagree with the predictions of the concordance model [562–565]. A quite appealing scale that we choose to focus throughout this Chapter and is directly connected with the existence of dark energy corresponds the sub-millimeter (sub-mm) scales.

Actually, in the context of a ΛCDM scenario we expect the dark energy scale λ that corresponds to the cosmological constant to be

$$\lambda_\Lambda \equiv \sqrt[4]{\frac{\hbar\, c}{\rho_\Lambda}} \xRightarrow{(1.67)} \lambda_\Lambda \approx 0.085\,\mathrm{mm}\,, \tag{6.1}$$

where we used $\Omega_{\mathrm{m},0} = 0.3$ and $H_0 = 70\ \mathrm{km\,s^{-1}\,Mpc^{-1}}$, *i.e.* a value that lies in the intermediate are of the Planck [18] and the SnIa measurements [518]. Therefore, it is only natural to expect to find observational signals in the form of new forces on the sub-mm scales, that either confirm or contradict the standard ΛCDM scenario. In fact, recent analyses [566, 567] that used data from short range gravity experiments [568–570] discovered a 2σ deviation from Newtonian gravity assuming an oscillating parametrization for the potential.

In the literature, the parametrizations of the potential that are most commonly used in order to quantify deviations from the Newtonian gravity, include a Yukawa type [568, 569, 571] or a power law type [571] correction in the gravitational potential. In particular, for the Yukawa correction we have a potential of the form [568, 569, 571]

$$V_{\mathrm{eff}} = -\frac{G_{\mathrm{N}}\, M}{r}(1 + \alpha\, e^{-mr})\,, \tag{6.2}$$

while for the power law correction we have [571]

$$V_{\mathrm{eff}} = -\frac{G_{\mathrm{N}}\, M}{r}\left[1 + \beta_k \left(\frac{1\mathrm{mm}}{r}\right)^{k-1}\right]\,. \tag{6.3}$$

However, recent analyses argue that an oscillating form of the potential [566, 567]

$$V_{\rm eff} = -\frac{G_{\rm N}\, M}{r}\left[1 + \alpha \cos(mr + \theta)\right] , \tag{6.4}$$

provides a better quality of fit compared to the popular Yukawa correction (6.2)[1]. The three aforementioned parametrizations not only seem to be consistent with short range gravity experiments but also are well motivated theoretically in the context of a large variety of modified gravity theories such as massive Brans Dicke and scalar tensor theories [572–574], $f(R)$ gravities [575–577], some braneworld models [578–581], compactified extra dimension models [192, 193, 582–585] as well as nonlocal gravity theories [566, 586–588].

One short range gravity experiment that is constructed to identify deviations from Newtonian gravity and has received a lot of attention lately is the Washington experiment [568, 569]. In this Chapter, we review the experiment (its structure, measurements *etc.*) and using the available data, we apply the maximum likelihood method considering two additional novel potential forms that deviate from Newtonian gravity and Eqs. (6.2)-(6.4) in an attempt to identify any hidden signals of a modified gravity theory on sub-mm scales.

6.1 Review of the Washington Experiment

The Washington experiment is a torsion based experiment with an apparatus that is illustrated in the following figure

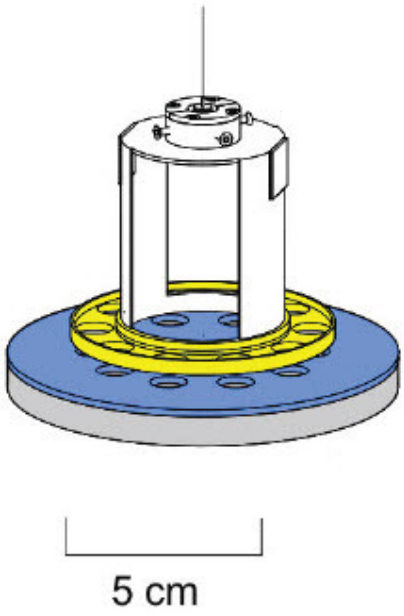

Figure 6.1: The Washington experiment setup (see the text for details). From Ref. [568].

It includes a fiber pendulum of 82 cm long that is connected to a slim ring with 10 equally distant cylindrical holes of 9.5mm diameter (yellow plate in Fig. 6.1). The slim ring is placed above a circular attractor with 10 equally distant identical holes that rotates (blue plate in in

[1] In Eqs. (6.2)-(6.4), a, β, k and θ correspond to parameters that are constrained by the data.

Fig. 6.1). The test-bodies that measured the gravitational interaction were the holes that lead the attractor to be twisted by a torque given by

$$N(\phi) = -\frac{\partial V(\phi)}{\partial \phi}\,, \tag{6.5}$$

where $V(\phi)$ corresponds the potential energy of the ring and ϕ is the angle with respect to the pendulum.

The data reported by the experiment were constructed by taking the differences between the measured torques τ and their corresponding Newtonian values (τ_N), *i.e.* constructing the torque residuals as $\delta\tau \equiv \tau - \tau_N$. The data acquisition process was repeated for two additional setups using the same detector but changing the thickness of the attractor disk reducing the systematic errors and were called Experiments II and III respectively, while the apparatus of Fig. 6.1 was called Experiment I, giving a total of 87 datapoints. The compilation of the torque residuals are shown in Table F.1 in Appendix F. The measured torques residuals were fitted in Refs. [568, 569] adopting both a Yukawa (6.2) and a power law (6.3) potential form. A later reanalysis [566] of the torque residuals of the Washington experiment, showed that an oscillating potential of the form (6.4) (blue line) provides a significantly better cosmological fit compared with a Yukawa potential (6.2) (pink line) as demonstrated in Fig. 6.2.

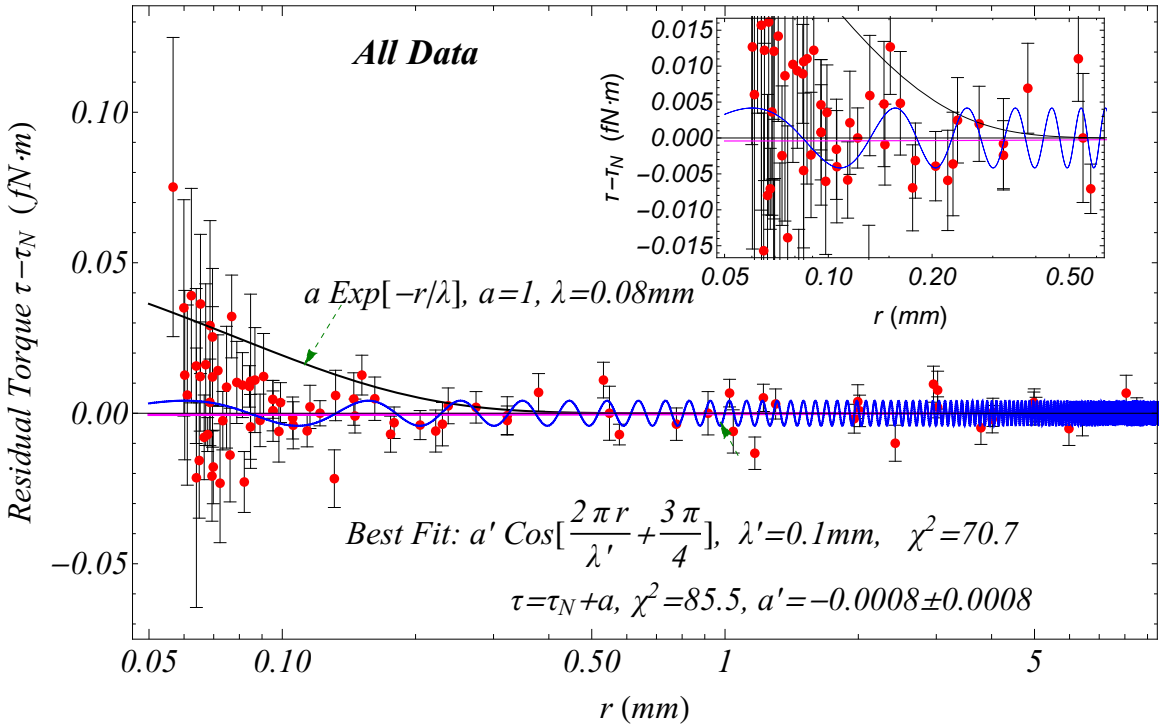

Figure 6.2: Residual torque data (red points) from the Washington experiment along with the best fit parameterizations (6.2)-(6.4). From Ref. [566].

These results (if not due to systematic effects) clearly indicate that similar signals of more general parametrizations may be hidden in the data of the Washington experiment. These hidden signals can be associated with specific modified theories of gravity.

6.2 Fit of Different Parametrizations on the Washington Experiment Data

In order to search for any hints of a modified theory of gravity hidden on short range experiments, we consider a generalized potential parametrization of (6.3) of the form

$$V_{\rm eff} = -\frac{G_{\rm N}\, M}{r}\left[1+\beta^k\left(\frac{1{\rm mm}}{c\, r}\right)^{k-1}\right], \tag{6.6}$$

as well as a potential parametrization that is given by

$$V_{\rm eff} = -\frac{G_{\rm N}\, M}{r}\left[1+\alpha\,\frac{\cos(mr)}{r}\right], \tag{6.7}$$

which is similar to (6.4). Furthermore, in the data comparison we present the parametrizations (6.2), (6.4) as well as a parametrization with a constant correction term, *i.e.* an offset Newtonian, that have already been demonstrated in Ref. [566]. Utilizing once more the maximum likelihood method, we construct the relevant χ^2 function as [566]

$$\chi^2(\alpha', m', \beta', c') = \sum_{i=1}^{N}\frac{\left[\delta\tau(i)-\delta\tau_j(\alpha', m', r_i, \beta', c')\right]^2}{\sigma_i^2}, \tag{6.8}$$

where the index i refers to the i^{th} residual of the Washington experiment, the index j describes the selected theoretical parametrization ($j \in [1,5]$), N corresponds to the total number of datapoints, *i.e.* $N = 87$ and α', m', β', c' are parameters to be fit by the data. The primes are used in order to avoid confusion with the fundamental parameters of each parametrization discussed above, since in order to directly connect the unprimed with the primed parameters specific details of the apparatus of the experiment are needed [566].

The results of the maximum likelihood method for the different parametrizations are illustrated in the following Table 6.1.

Parametrization	χ^2
$\delta\tau = \alpha'$	85.5
$\delta\tau = \alpha' e^{-m'r}$	85.4
$\delta\tau = \alpha'\cos(m'r + 3\pi/4)$	70.7
$\delta\tau = \beta'_k\left[1{\rm mm}/\left(c'\, r\right)\right]^{k'-1}$	82.1
$\delta\tau = \alpha'\,\cos(m'r)/r$	85.1

Table 6.1: The best fit value of χ^2 for each parametrization using the Washington experiment torque residual data.

As we can see from the above table, despite the two alternative parametrizations, the oscillating one discussed in Ref. [566] provides the best quality of fit to the data. It is important to note here that in the parametrization (6.4), the parameter $\theta' = 3\pi/4$ is fixed to the value that achieves the optimum fit to the data [566].

The statistical significance of the results for the two additional parametrizations, can also be estimated following the method of Monte Carlo simulation described in Chapter 4. In particular,

Parametrization	**Number of Simulated Datasets with Lower Values for the Parameters than the Real Data**
$\delta\tau = \beta'_k \left[1\text{mm}/\left(c'\, r\right)\right]^{k'-1}$	290/500
$\delta\tau = \alpha' \cos(m'r)/r$	170/500

Table 6.2: The results of the Monte Carlo simulations as described in the text.

we consider 500 simulated datasets with redshifts corresponding to the redshift of the actual data and replace the real torque residuals with simulated datapoints created under a random normal (gaussian) distribution with a mean value equal to zero and a standard deviation equal to the 1σ errors of the real data. After constructing the simulated data, we apply the maximum likelihood method and see how many of the simulated data give lower values for the relevant parameters of each parametrization than the best fit values indicated by the real data. The results for the two additional parametrizations are illustrated in Table 6.2. Unfortunately, the results are not statically significant indicating that the two parametrizations do not improve the quality of fit to the Washington data.

Nevertheless, the oscillating parametrization (6.4) proposed in Ref. [566] not only provides the best overall fit but may also have a physical origin. In particular, this parametrization can be realized in the context of a class of theories including infinite derivatives in the Lagrangian, *i.e.* the well known nonlocal theories of gravity. The corresponding Lagrangian of these theories is given as [589]

$$L_{IDG} = \frac{1}{8\,\pi\,G_{\rm N}}\sqrt{-g}\left[R + \alpha\left(RF_1(\Box)R + R^{\mu\nu}F_2(\Box)R_{\mu\nu} + R^{\mu\nu\rho\sigma}F_3(\Box)R_{\mu\nu\rho\sigma}\right)\right], \tag{6.9}$$

with

$$F_i(\Box) = \sum_{n=0}^{\infty} f_{i,n}\left(\frac{\Box}{M^2}\right)^n \qquad \Box = g^{\mu\nu}\nabla_\mu\nabla_\nu \tag{6.10}$$

and $\Box$ corresponds to the d' Alembertian operator. In the context of nonlocal theories of gravity, the corresponding modified potential is [587]

$$V_{\rm eff}(r) = -\frac{G_{\rm N}\,M}{r} f(r,m) \tag{6.11}$$

and the function $f(r,m)$ is given as

$$f(r,m) = \frac{1}{\pi}\int_{-\infty}^{+\infty} dk\,\frac{sin(k\,r)e^{-\tau(k,m)}}{k}\,. \tag{6.12}$$

A common form for the function $\tau(k,m)$ is

$$\tau(k,m) = \frac{k^{2n}}{m^{2n}}\,. \tag{6.13}$$

So, based on the value of the parameter n the exact form of the function $f(r,m)$ is derived solving Eq. (6.12). For $n=1$, Eq. (6.12) gives

$$f(r,m) = \text{Erf}\left(\frac{m\,r}{2}\right), \tag{6.14}$$

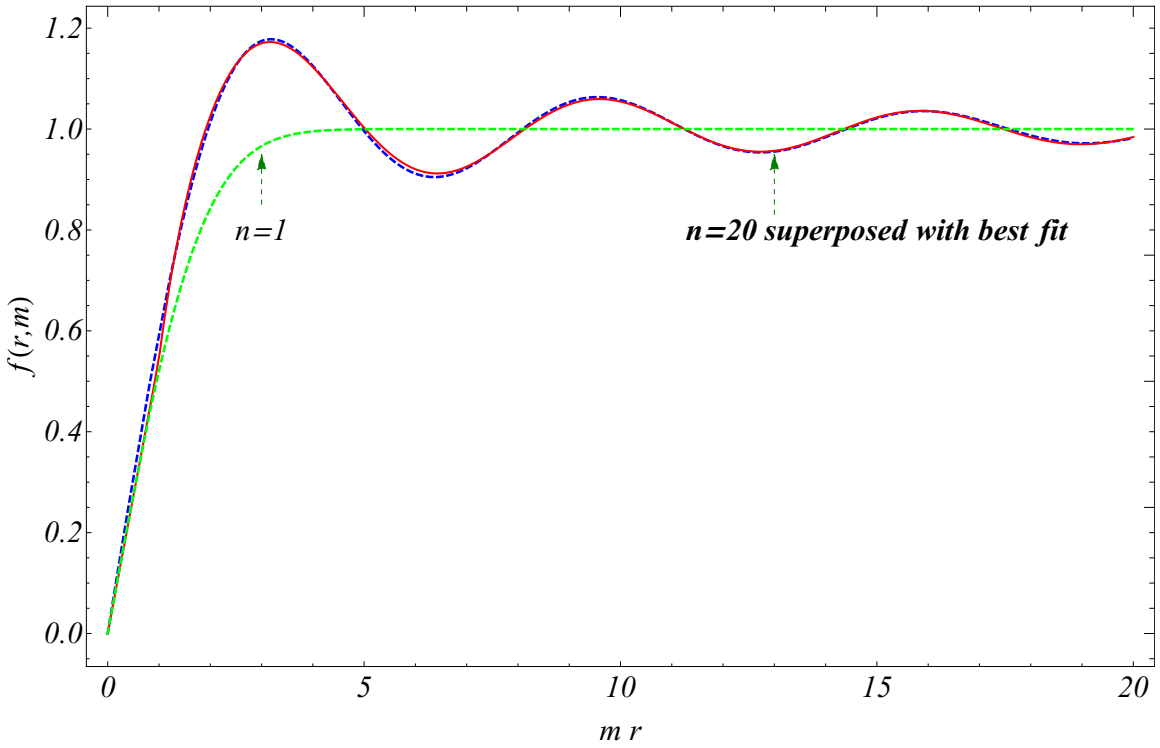

Figure 6.3: The function $f(r, m)$ as a function of $m\,r$ for different n values. The green dashed line corresponds to the $n = 1$ value, while the blue dashed line correspond to the $n = 20$ value. We also show the approximating function (6.15) for $\alpha_1 = 0.544$, $\alpha_2 = 0.572$ and $\theta = 0.885\pi$ as a red continuous line. The linear behavior close to the origin dissolves the divergence of the Newtonian potential. From Ref. [566].

that for $m\,r \ll 1$, Eq. (6.14) is linear and for $m\,r \gg 1$ approaches unity (see green line of Fig. 6.3). However, for a significantly larger value of n (*e.g.* $n = 20$), Eq. (6.12) starts as a linear function and takes the form of a damped oscillation as illustrated in Fig. 6.3 (blue dashed line), which reproduces the needed behavior of the oscillating parametrizations discussed above. The produced form of $f(r, m)$ for large values of n, can be mimicked by the following function

$$f(r,m) = \begin{cases} \alpha_1\, m\, r, & \text{for } 0 < m\,r < 1, \\ 1 + \alpha_2 \frac{\cos(m\,r+\theta)}{m\,r}, & \text{for } 1 < m\,r, \end{cases} \tag{6.15}$$

where $\alpha_1 = 0.544$, $\alpha_2 = 0.572$ and $\theta = 0.885\pi$. This is also demonstrated in Fig. 6.3 as a red continuous line.

The nonlocal gravity theories are quite interesting, since they can also provide some theoretical advantages over GR. More specifically, in the context of GR unrenormalisable ultraviolet divergences emerge [590] which in the context of nonlocal gravities are relaxed [589, 591, 592]. Furthermore, nonlocal gravity theories are free of singularities (such as the Big Bang singularity [589]) and they naturally emerge from quantum gravity [593]. Finally, a quite appealing advantage of this class of theories is their ability to reproduce the observed accelerated expansion of the Universe without the existence of a cosmological constant [594–597].

6.3 In Brief

In this Chapter we have considered two novel potential parametrizations that deviate from the Newtonian gravity and using the torque residual data of the Washington experiment we searched if they could provide a better quality of fit than the ones already discussed in the literature. In particular motivated by previous results, we studied the parametrizations (6.6) and (6.7) on top of the usual (6.2)-(6.4) parametrizations and applied the maximum likelihood method, minimizing Eq. (6.8). From the statistical analysis we showed that the two additional parametrizations (6.6) and (6.7) do not improve the overall quality of fit and the relevant χ^2 differences are not statistically significant.

However, the oscillating parametrization (6.4) provides the best quality of fit to the data, with a statistical significance of 2σ. If the existence of this signal is not due to some unknown systematic effect it may provide early evidence for a short distance modification of GR through a modified theory of gravity (*e.g.* a nonlocal gravity theory). It is therefore important to purse this line of research further using additional datasets, improved data analysis methods and search for further theoretical support of the favored best fit parameterizations.

Chapter 7

Summary and Future Prospects

7.1 Summary

Undoubtedly, we live in an exciting cosmological era. Since 1998 and the confirmation of the existence of the cosmological constant, a plethora of alternative cosmological data in the last years hint towards the conclusion that the concordance model ΛCDM is not the end of the road and a new more complete theory of gravity is needed. In the present PhD thesis we presented the basic theoretical and observational challenges of the concordance model and investigated viable alternative theories that address the challenges in a more fundamental manner.

In Chapter 1, we revised the basic principles of standard cosmology. In particular, we discussed the concept of the cosmological principle and presented Einstein's Field Equations. Moreover, we discussed in detail the idea of the cosmological constant and the concordance model ΛCDM. Furthermore, we reviewed the main cosmological observables and presented the basic differences of the geometrical and the dynamical probes, as well as, the basic cosmological models that can be categorized in two classes: The Friedmann models, *i.e.* those with $\Omega_{\Lambda,0} = 0$ and the Lemaitre models, *i.e.* with $\Omega_{\Lambda,0} \neq 0$. Finally, we examined the basic triumphs and challenges of the concordance model ΛCDM, as well as viable alternative theories that have been proposed in an attempt to address the challenges in a more fundamental manner including (but not limited to) $f(R)$ gravity theories, scalar tensor theories, dynamical dark energy models *etc.*

In Chapter 2 we constructed an extended compilation of 63 growth data that have been published from 2006 to 2018 and using this dataset with care, we deduced useful trends for the probed growth datapoints. After fiducial model correction, we obtained the best fit $\Omega_{\rm m,0} - \sigma_8$ ΛCDM parameters and showed that they are at a $3\sigma - 5\sigma$ tension with the corresponding Planck15/ΛCDM values, depending on the selected dataset. However, this tension seems to be reduced either considering only more recently published datapoints (the growth data published in the last couple of years) which seem to be significantly more consistent with Planck15/ΛCDM or by considering a non trivial evolution of the effective Newton's constant, which can be parametrized as $G_{\rm eff}(z)/G_{\rm N} = 1 + g_a \left(\frac{z}{1+z}\right)^2 - g_a \left(\frac{z}{1+z}\right)^4$, where g_a is a parameter and z is the redshift.

Although a partial cause for this reduced tension is the fact that more recent data tend to probe higher redshifts (with higher errorbars) where there is degeneracy among different models due to matter domination, all the considered growth subsamples seem to prefer negative values

for g_a, implying that $G_{\rm eff}$ is a decreasing function at low z. Moreover, we showed that the required behavior for $G_{\rm eff}$ can not be realized in the context of $f(R)$ and scalar tensor modified gravity theories assuming a ΛCDM background. In the context of $f(R)$ gravities the effective Newton's constant is always $G_{\rm eff} > G_{\rm N}$ irrespective of the background expansion in order to ensure the absence of ghost instabilities. On the contrary, for the scalar tensor theories a decreasing $G_{\rm eff}$ at low redshifts is only possible if $w > -1$ and can not be realized in the context of a ΛCDM background.

A decreasing form of $G_{\rm eff}$ at low redshifts would also leave a characteristic signature in other geometrical and/or dynamical probes. Such a behavior affects the low l CMB angular power spectrum due to the ISW effect. Hence, we utilize the `MGCAMB` and `MGCOSMOMC` numerical codes that solve the Boltzmann equations for a given set of cosmological parameters that appear in various modified gravity theories and construct the predicted CMB and large scale structure observables in the context of various backgrounds. Adopting the aforementioned phenomenological parametrization for the effective Newton's constant $G_{\rm eff}$, we showed that the CMB data strongly constrain the parameter g_a, mildly favoring a negative value for g_a.

In Chapter 3 we studied the constraining of a wide range of cosmological observables and showed that is not monotonically increasing but presents blind redshift spots and optimum redshift regions with respect to the parameters $\Omega_{\rm m,0}$, the constant equation of state under the assumption that it is constant and the phenomenological parameter g_a that was introduced in the previous Chapter. At first, we considered the growth rate of matter density perturbations expressed through the observables $f\sigma_8(z)$ and $f(z)$ and using the compilation of 63 growth data of the previous Chapter revealed the existence of a blind spot at $z \simeq 2.7$ for g_a, at $z \simeq 2$ for w and at $z \simeq 1$ for $\Omega_{\rm m,0}$. The corresponding optimum redshift regions are at $z \simeq 0.5$, at $z \simeq 2$ and $z \simeq 1$ respectively. These results clearly indicated that the more recent surveys that tend to increase the redshift of the measurement approaches the blind spot and not the optimum redshift region. We also studied the $f(z)$ observable since the Euclid mission published some mock data, showing that the redshift range of the Euclid mission is optimal.

Furthermore, we constructed an updated compilation for the three BAO observables $D_V \times \left(r_s^{fid}/r_s\right)$, $D_A \times \left(r_s^{fid}/r_s\right)$ and $H(z) \times \left(r_s/r_s^{fid}\right)$ published from 2009 to 2018 and used it to find the blind spots and optimum redshift regions for the $\Omega_{\rm m,0}$ and w cosmological parameters. For the observable $D_V \times \left(r_s^{fid}/r_s\right)$ we showed the existence of a blind spot at $z \simeq 1.2$, while the optimum redshift region is at $z \simeq 0.6$ for the parameter $\Omega_{\rm m,0}$. On the contrary, for the same observable with respect to the parameter w there is no blind redshift spot while the optimum redshift region is at $z > 1.2$. For the $D_A \times \left(r_s^{fid}/r_s\right)$ we find a similar behavior even though the blind redhsift spot with respect to $\Omega_{\rm m,0}$ appears to a somewhat higher redshift $z \simeq 2$ and the sensitivity of this observable is significantly reduced compared to the sensitivity of $D_V \times \left(r_s^{fid}/r_s\right)$. Regarding the $H(z) \times \left(r_s/r_s^{fid}\right)$ observable we found that there is no blind redshift spot, while the sensitivity appears to increase monotonically with redshift for both the $\Omega_{\rm m,0}$ and w parameters. Similar conclusions were observed using cosmic chronometer data that also measure the $H(z)$, but the BAO are much more constraining compared to the cosmic chronometers.

Moreover, we used the binned JLA SnIa as well as the standard gravitational wave sirens expressed through the distance modulus μ and μ_{gw} respectively and discovered that the constraining power is monotonically increasing for the distance modulus. In addition, we introduced a new statistic of the form $S_p^O(z) \equiv \frac{\Delta O}{\Delta p}(z) \cdot V_{\rm eff}^{1/2}$ including the effective survey volume $V_{\rm eff}$, as a measure of the constraining power of a given observable O with respect to a cosmological

parameter p as a function of redshift z. For this new statistic, the blind spots are illustrated as roots, while the optimum redshift region appears as maxima of S. Finally, using the only available datapoint from the standard siren GW170817, we showed that a drastic improvement is needed in order to successfully constrain $G_{\rm eff}$ in general.

In Chapter 4 we focused on the Pantheon SnIa dataset and performed a tomographic analysis. In the context of ΛCDM, we obtained the best fit values of the absolute magnitude M and/or Hubble constant H_0 and presented weak evidence of a local variation of $\mathcal{M} \equiv M + 5\,log_{10}\left[\frac{c/H_0}{1\rm Mpc}\right] + 25$ at low redshifts ($z \lesssim 0.2$), with respect to the best fit of the full dataset. This variation reaches the 2σ level if the systematic uncertainties are ignored and falls approximately at the 1σ level if the systematic uncertainties are included. This interesting trend was confirmed for the case of the ignored systematic uncertainties not only by fixing $\Omega_{\rm m,0}$ to its best fit value indicated by the full dataset and considering cumulative subsets of the full Pantheon compilation but also by ranking the Pantheon data from lower to higher redshifts and selecting the first 100 datapoints under the assumption of a best fit ΛCDM background. Then, we shifted the subsample by one point towards higher redshifts covering the entire Pantheon dataset. This signal, if physical, can be attributed to a local matter underdensity that vanishes at large scales or a modified theory of gravity due to a variation of Newton's constant. Otherwise, this signal can be due to the existence of statistical and/or systematic fluctuations of the data.

A lower value of $\mathcal{M}$ naturally leads to a local matter underdensity scenario, with $\delta\rho_0/\rho_0 \simeq -0.10 \pm 0.04$ due to a higher value of h. In this case, a signal of anisotropy is expected in the parameter $\mathcal{M}$. Therefore, we used and compared two methods that are widely used for searching anisotropies. The first one was the Hemisphere Comparison (HC) method and the second one was the Dipole Fit (DF) method. From the HC method, we found an anisotropy level that is consistent with simulated isotropic Pantheon like datasets. However, the anisotropic sky distribution of the Pantheon SnIa data induces a preferred range of directions even in simulated Pantheon data obtained in the context of isotropic ΛCDM. Constructing a more isotropically distributed subset of the Pantheon SnIa we showed that the preferred range of directions disappears. Utilizing this more isotropically distributed subset we found no evidence for statistically significant anisotropy using either the HC or the DF method.

For a modified gravity scenario, a lower value of $\mathcal{M}$ can also be due to a lower value of the absolute magnitude M in the low redshift regime. This behavior can be explained in the context of a modified theory of gravity with an evolving Newton's constant. Adopting the parametrization presented in Chapter 2 for $G_{\rm eff}$, we found the best fit values of the phenomenological parameter g_a to be $g_a = -0.47 \pm 0.36$, *i.e.* approximately 1.5σ away from the corresponding ΛCDM value, further supporting a reduced Newton's constant compared to GR at low z.

Finally, we considered the possibility that the lower value of $\mathcal{M}$ is due to the statistical fluctuation of the data. If the observed effect is real, then the same behavior should also appear in a large number of Monte Carlo simulations. Therefore, including the systematic uncertainties, we sorted the Pantheon data from the lowest to the highest bin and divided the entire dataset in four equal uncorrelated bins consisting of 262 datapoints. Generating 1000 Pantheon like data and applying the maximum likelihood method we found that the percent of the simulated Pantheon dataset with a similar behavior (for the first three bins) corresponds to approximately 5%, reaching the 2σ threshold. This percentage further increases if instead of the first three bins we consider any three out of the four bins leaving the statistical fluctuation scenario as a viable explanation. However it is important to note that the first three bins

correspond to SnIa with $z < 0.42$, *i.e.* where dark energy is dominant, hinting towards the existence of some hidden physics beyond the standard ΛCDM concordance model.

In Chapter 5, we considered two recently proposed dark energy models that have the potential to address both the Hubble and the growth tensions simultaneously. In particular, the first one included a late time abrupt transition of the absolute magnitude M, of the form $M(z) = M_< + \Delta M\,\Theta(z - z_t)$, where z_t is the redhsift where the transition occurs, $M_< \equiv M_c$ corresponds to the Cepheid value of the absolute magnitude as calibrated by the SH0ES team and Θ is the Heaviside step function. This model is called LMT. The second dark energy models discussed is a dark energy model including a transition on the equation of state parameter w_{DE} on top of the transition on M, of the form $w_{DE}(z) = -1 + \Delta w\,\Theta(z_t - z)$. This model is called $LwMT$.

Modifying the numerical packages `CLASS` and `MontePython` (which are similar to `MGCAMB` and `MGCOSMOMC`) accordingly in order to include the transition models LMT and $LwMT$, we used up to date CMB, BAO, growth and SnIa compilations, in order to find the corresponding quality of fit as well as the corresponding best fit values of the parameters. The MCMC analysis showed that both the transition models give an absolute magnitude consistent with the Cepheid value of the absolute magnitude M_c. Moreover, despite the extra degree of freedom, the extra parameter Δw seems to be ignored by the data.

Next we compared the quality of the transition models LMT and $LwMT$ with three well known smooth deformation models, such as the wCDM, the CPL and the Phenomenological Emergent Dark Energy model along with the standard ΛCDM scenario following two methods. In the first one, we imposed a flat prior on the absolute magnitude $M \in [-19.28, -19.2]$ mag, forcing all models (both the transitions and the smooth deformations ones) to be consistent with the Cepheid absolute magnitude M_c. In the second one we imposed the local Cepheid calibrated gaussian prior by SH0ES on the absolute magnitude $M_c = -19.24 \pm 0.04$ mag. The results of the flat prior method showed that even though all the discussed models performed significantly better than ΛCDM, the smooth deformation models give an H_0 value consistent to the SH0ES measurement and $M \sim -19.28$ mag, *i.e.* the lowest eligible value of the imposed prior. In contrast, the transition models provide a H_0 value within the 1σ level to the typical ΛCDM value reported by the Planck mission, providing at the same time $M \approx -19.4$ mag as expected. The results of the analysis adopting the gaussian prior on the SnIa absolute magnitude $M_c = -19.24 \pm 0.04$ mag revealed that the transition models not only perform better than the concordance ΛCDM model and the rest of the models in question, but were also the only ones consistent with the Cepheid calibrated value M_c.

Nevertheless, for the proper identification of the optimal model, we need to take into account the number of parameters that give the corresponding χ^2 value. Focusing on the gaussian prior case, we applied appropriate statistical criteria such as the Akaike Information Criterion and the Bayes factor and found that the transition models have significant advantages over the smooth deformation models in question. Finally, we shortly discussed possible theoretical models that can produce the behavior of the transition model, such as some quintessence or phantom fields as well as a very recent false vacuum decay model.

Finally in Chapter 6, we focused on the sub-millimeter scales in order to search for deviations from the Newtonian gravity. Considering two novel parametrizations for the effective potential $V_{\rm eff}$ of an oscillating and a power law form that are motivated by modified theories of gravity we applied the maximum likelihood method in order to derive the quality of fit. The data that are used in the statistical analysis correspond to the data of the Washington experiment. The

results showed that these particular parametrizations do not improve the quality of fit and the relevant χ^2 differences are not statistically significant.

However, in a previous analysis, an oscillating parametrization for the effective potential of the form $V_{\rm eff} = -\frac{G_{\rm N}\,M}{r}\left[1+\alpha\cos(mr+\theta)\right]$ provides the best quality of fit to the data with a statistical significance of 2σ. So, if this effect is not due to some unknown systematic effect it may provide evidence for a short distance modification of GR through a modified theory of gravity.

7.2 Future Prospects

In this PhD thesis we focused on intriguing open questions of standard cosmology. Motivated by the basic problems of the concordance model ΛCDM, we presented various phenomenological parametrizations as well as extended up to date data compilations in an attempt to address these issues in a more fundamental manner. With that in mind, a number of interesting extensions can be performed in the near future both at the theoretical level (*e.g.* providing theoretical models that explain the observed signatures) and the observational level (*e.g.* using even more recent data compilation from the upcoming surveys).

Regarding the theoretical extensions, it would be interesting to see if the results of Chapter 2 that indicate $G_{\rm eff} < G_{\rm N}$ (weaker gravity) at low redshifts can be realized in other more general modified theories of gravity. This trend may prove a key tool for discriminating between different modified gravity models. Interestingly, recent works indicate that the weaker gravity may be possible in the context of teleparallel theories of gravity [598,599] or more general scalar tensor theories, such as the Horndeski [600–602] and beyond Horndeski theories [603] providing specific constraints among the terms of the Lagrangian. Moreover, regarding the tomographic analysis on SnIa performed in Chapter 4 it would interesting to see if this abnormal variation of $\mathcal{M}$ persists in an extended SnIa dataset with a more uniform distribution in the sky (*e.g.* using the Pantheon+ dataset that is not yet publicly available). Another interesting extension to the results of this Chapter would be to apply alternative datasets that are used as standard candles probes (*e.g.* γ ray bursts) as well as different statistical tests probing for cosmological anisotropies in an attempt to identify similar hints of variations in H_0 and/or $G_{\rm eff}$.

In addition, the consideration of alternative background expansion cosmologies may also affect the results of Chapter 4, thus it would be interesting to see how the general trends and results alter in the context of different backgrounds $H(z)$. Regarding the transition models discussed in Chapter 5 it would interesting to include the investigation of whether this gravitational transition is also apparent in other geological, solar system and astrophysical data [604,605] as well as the identification for any possible systematic effects in the Cepheid data and parameters that could mimic such a transition on the absolute magnitude M. Finally, concerning the results of Chapter 6 interesting extensions involve the further investigation of viable theoretical models that support appropriate parametrizations that provide good fit to small scale gravitational experiment data in general, as well as to repeat the performed analysis in the context of other datasets in an effort to identify similar hidden signatures.

We expect that the issues discussed in the present thesis will be further clarified in the next decades, when new improved observational data from upcoming missions will be published. An incomplete list of these missions that are going to be launched in the next few years are the following (see Ref. [538] for a more complete list)

- Euclid Mission: The Euclid mission [606] will launch in March 2023 and aims at mapping the geometry of the Universe providing a better knowledge to the nature of the dark matter and dark energy. This mission will use WL and Galaxy Clustering measurements to estimate the BAO up to $z \simeq 2$.

- LSST: The Large Synoptic Survey Telescope (LSST) [607] is a ground telescope that will start its observations on late 2022. This mission aims to map and catalogue galaxies, in order to study their impact on the distortion of spacetime.

- CMB-S4: The fourth generation of the ground based CMB experiment (CMB-S4) [608] aims at testing GR at large scales, probing the B-mode polarization signature of primordial gravitational waves, the number and masses of the neutrinos as well as searching for evidence of new light relics and constraining the nature of dark energy. It is anticipated to start its observations on 2027.

- JWST: The James Webb Space Telescope (JWST) [609] is the new generation experiment that replaces the Hubble Space Telescope and will broaden its discoveries probing galaxies at $z \leq 15$. The JWST launched on 25 December of 2021.

Appendices

Appendix A

Analytical Calculations of Standard Cosmology

A.1 Cosmological Perturbation Theory

As we discussed in Chapter 1 our Universe at large scales is homogeneous and isotropic. However, if we move to smaller scales we will see that the Universe contains structures like clusters and galaxies. Therefore in order to accurately describe it we need to introduce inhomogeneities and study their evolution. Naturally, we expect that these inhomogeneities are quite small, so we can consider a metric that slightly deviates from the FLRW one (1.2) and can be written as a sum of an unperturbed FLRW part plus some extra terms that we encompass in the "perturbed" metric.

When we deal with small perturbations, the basic tool that is used is the linear perturbation theory. In this context, any quantity is given as the sum of its background value that corresponds to the homogeneous and isotropic model, and a perturbation that deviates from its background value. With the term linear we refer to the fact that the perturbations are important up to the first order and that a product of two or more perturbations should be ignored.

Considering small perturbations $\delta g_{\mu\nu}$ around the FLRW metric $\bar{g}_{\mu\nu}$, we can write that

$$g_{\mu\nu} = \bar{g}_{\mu\nu} + \delta g_{\mu\nu} \,. \tag{A.1}$$

Let us start by rewriting the FLRW metric (1.2) as follows

$$\begin{aligned} ds^2 = c^2\,dt^2 - a^2(t)\left[\frac{dr^2}{1-k\,r^2} + r^2(d\theta^2 + \sin^2\theta\,d\phi^2)\right] = c^2\,dt^2 - a^2(t)\left[\frac{dr^2(1-k\,r^2) + k\,r^2\,dr^2}{1-k\,r^2}\right] \\ + r^2\,d\Omega^2 = c^2\,dt^2 - a^2(t)\left[dr^2 + k\frac{r^2\,dr^2}{1-k\,r^2} + r^2\,d\Omega^2\right] = c^2\,dt^2 - a^2(t)\left[d\vec{x}^2 + k\,\frac{(\vec{x}\cdot d\vec{x})^2}{1-k\,\vec{x}^2}\right] \Rightarrow \\ \Rightarrow ds^2 = c^2\,dt^2 - a^2(t)\,\gamma_{ij}\,dx^i\,dx^j \,, \end{aligned} \tag{A.2}$$

where $\gamma_{ij} \equiv \delta_{ij} + k\,\frac{x_i\,x_j}{1-k(x_p\,x^p)}$. Focusing on the flat case, where $k = 0$, Eq. (A.2) reduces to

$$ds^2 = c^2\,dt^2 - a^2(t)\,\delta_{ij}\,dx^i\,dx^j \,.$$

For convenience, instead of the cosmic time t we will use the conformal time τ, which is defined as

$$\tau \equiv \int \frac{1}{a}\,dt \Rightarrow d\tau = \frac{dt}{a(t)} \,. \tag{A.3}$$

Hence, setting $c = 1$, the flat FLRW background metric is written as

$$ds^2 = dt^2 - a^2(t)\,\delta_{ij}\,dx^i\,dx^j \Rightarrow ds^2 = a^2(\tau)\left[d\tau^2 - \delta_{ij}\,dx^i\,dx^j\right]\,. \tag{A.4}$$

Based on the previous equation, the general perturbed metric reads [610]

$$ds^2 = a^2(\tau)\left[(1+2A)d\tau^2 - 2\,B_i\,dx^i\,d\tau - (\delta_{ij}+h_{ij})dx^i\,dx^j\right]\,, \tag{A.5}$$

where A, B_i and h_{ij} are functions of space and time. At this point it is extremely useful to use the decomposition theorem which allows us to divide the perturbations in three independent types: scalar, vector and tensor perturbations. Each type evolves independently, so the functions B_i ad h_{ij} are given by [610]

$$\begin{aligned} B_i &= \partial_i\,B + \hat{B}_i\,,\\ h_{ij} &= 2\,C\,\delta_{ij} + 2\left(\partial_i\partial_j - \frac{1}{3}\delta_{ij}\nabla^2\right)E + \left(\partial_i\,\hat{E}_j + \partial_j\,\hat{E}_i\right) + 2\hat{E}_{ij}\,, \end{aligned} \tag{A.6}$$

where the hatted quantities are divergenceless. In order to avoid any problems arising from the fact that the metric perturbations are not uniquely defined, we further define specific quantities that are combinations of metric perturbations and do not transform under a change of coordinates. These are the Bardeen variables defined as [610]

$$\begin{aligned} \psi &\equiv A + \mathcal{H}(B - E') + (B - E')'\,,\\ \phi &\equiv -C - \mathcal{H}(B - E') + \frac{1}{3}\nabla^2 E\,,\\ \hat{\phi}_i &\equiv \hat{E}_i' - \hat{B}_i\,, \end{aligned}$$

with $\mathcal{H} = a'/a$, *i.e.* the Hubble parameter in conformal time. Notice that in this section the prime corresponds to derivation with respect to the conformal time (and not with respect to the scale factor or redshift as in the one that follows). In order to further simplify the calculations, we choose the so called "Newtonian gauge" where $B = E = 0$. In this case the Bardeen variables ψ and ϕ reduce to

$$\psi \equiv A + \cancelto{0}{\mathcal{H}(B - E')} + \cancelto{0}{(B - E')'} \Rightarrow \psi = A\,, \tag{A.7}$$

$$\phi \equiv -C - \cancelto{0}{\mathcal{H}(B - E')} + \frac{1}{3}\nabla^2\cancelto{0}{E} \Rightarrow \phi = -C\,, \tag{A.8}$$

while, the tensor h_{ij} reduces to

$$h_{ij} = 2\,C\,\delta_{ij} + 2\left(\partial_i\partial_j - \frac{1}{3}\delta_{ij}\nabla^2\right)E + \left(\partial_i\,\hat{E}_j + \partial_j\,\hat{E}_i\right) + 2\hat{E}_{ij} \Rightarrow h_{ij} = 2\,C\,\delta_{ij}\,, \tag{A.9}$$

since we keep only the scalar terms. Substituting Eqs. (A.7)-(A.9) in (A.5), the perturbed metric takes the form

$$\begin{aligned} ds^2 = a^2(\tau)\left[(1+2A)d\tau^2 - (\delta_{ij}+2C\,\delta_{ij})dx^i\,dx^j\right] &= a^2(\tau)\left[(1+2A)d\tau^2 - (1+2C)\delta_{ij}\,dx^i\,dx^j\right]\\ \Rightarrow ds^2 = a^2(\tau)\left[(1+2\psi)d\tau^2 - (1-2\phi)\delta_{ij}\,dx^i\,dx^j\right]\,, \end{aligned} \tag{A.10}$$

i.e. conformal time version of Eq. (1.52).

From the perturbed metric (A.10), it is straightforward to obtain the perturbed Einstein's Field Equations $\delta G_{\mu\nu} = 8\pi G_{\rm N}\,\delta T_{\mu\nu}$, following the standard procedure discussed in Chapter 1. Hence, using the definition (1.6) we calculate the following non-zero Christoffel symbols

$$\therefore \Gamma^0_{00} = \frac{1}{2}g^{0\lambda}\left(\partial_0 g_{\lambda 0} + \partial_0 g_{\lambda 0} - \partial_\lambda g_{00}\right) = \frac{1}{2}g^{0\lambda}\left(2\partial_0 g_{\lambda 0} - \partial_\lambda g_{00}\right) \overset{\lambda=0}{\Longrightarrow} \Gamma^0_{00} = \frac{1}{2}g^{00}\partial_0 g_{00} \Rightarrow$$

$$\Gamma^0_{00} = \frac{1}{2a^2}(1-2\psi)\frac{d}{d\tau}\left[a^2(1+2\psi)\right] \Rightarrow \boxed{\Gamma^0_{00} = \mathcal{H} + \psi'}\,, \tag{A.11}$$

$$\therefore \Gamma^0_{0i} = \frac{1}{2}g^{0\lambda}\left(\partial_0 g_{\lambda i} + \partial_i g_{\lambda 0} - \partial_\lambda g_{0i}\right) \overset{\lambda=0}{\Longrightarrow} \Gamma^0_{0i} = \frac{1}{2}g^{00}\left(\partial_0 g_{0i} + \partial_i g_{00} - \partial_0 g_{0i}\right) = \frac{1}{2}g^{00}\partial_i g_{00}$$

$$\Rightarrow \Gamma^0_{0i} = \frac{1}{2\cancel{a^2}}(1-2\psi)\partial_i[\cancel{a^2}(1+2\psi)] = \partial_i\psi + \cancelto{0}{O(2)} \Rightarrow \boxed{\Gamma^0_{0i} = \partial_i\psi}\,, \tag{A.12}$$

$$\therefore \Gamma^i_{00} = \frac{1}{2}g^{i\lambda}\left(\partial_0 g_{\lambda 0} + \partial_0 g_{\lambda 0} - \partial_\lambda g_{00}\right) \overset{\lambda=j}{\Longrightarrow} \Gamma^i_{00} = -\frac{1}{2}g^{ij}\partial_j g_{00} = -\frac{1+2\phi}{2\cancel{a^2}}\delta^{ij}[-\partial_j(\cancel{a^2}(1+2\psi)]$$

$$\Rightarrow \Gamma^i_{00} = \frac{1+2\phi}{\cancel{2}}\cancel{2}\delta^{ij}\partial_j\psi = \delta^{ij}\partial_j\psi + \cancelto{0}{O(2)} \Rightarrow \boxed{\Gamma^i_{00} = \delta^{ij}\partial_j\psi}\,, \tag{A.13}$$

$$\therefore \Gamma^0_{ij} = \frac{1}{2}g^{0\lambda}\left(\partial_i g_{\lambda j} + \partial_j g_{\lambda i} - \partial_\lambda g_{ij}\right) \overset{\lambda=0}{\Longrightarrow} \Gamma^0_{ij} = -\frac{1}{2}g^{00}\partial_0 g_{ij} = -\frac{(1-2\psi)}{2a^2}\frac{d}{d\tau}[(-a^2)(1-2\phi)\delta_{ij}]$$

$$\Rightarrow \Gamma^0_{ij} = \frac{1}{\cancel{2}a^2}(1-2\psi)\left[\cancel{2}a\,a'(1-2\phi)\delta_{ij} + a^2(-\cancel{2}\phi')\delta_{ij}\right] = (1-2\psi)\left[\mathcal{H}(1-2\phi)\delta_{ij} - \phi'\delta_{ij}\right]$$

$$\Rightarrow \Gamma^0_{ij} = \mathcal{H}\delta_{ij} - 2\mathcal{H}\phi\delta_{ij} - 2\psi\mathcal{H}\delta_{ij} - \phi'\delta_{ij} + \cancelto{0}{O(2)} \Rightarrow \boxed{\Gamma^0_{ij} = \mathcal{H}\delta_{ij} - \left[\phi' + 2\mathcal{H}(\phi+\psi)\right]\delta_{ij}}\,, \tag{A.14}$$

$$\therefore \Gamma^i_{j0} = \frac{1}{2}g^{i\lambda}\left(\partial_j g_{\lambda 0} + \partial_0 g_{\lambda j} - \partial_\lambda g_{j0}\right) \overset{\lambda=k}{\Longrightarrow} \Gamma^i_{j0} = \frac{1}{2}g^{ik}\partial_0 g_{kj} = \frac{1+2\phi}{2a^2}\delta^{ik}\frac{d}{d\tau}\left[(a^2)(1-2\phi)\delta_{kj}\right]$$

$$\Rightarrow \Gamma^i_{j0} = \frac{1}{\cancel{2}a^2}(1+2\phi)\delta^{ik}[\cancel{2}a\,a'(1-2\phi)\delta_{kj} + a^2(-\cancel{2}\phi)\delta_{kj}] = \frac{a'}{a}\delta^{ik}\delta_{kj} - \phi'\delta^{ik}\delta_{kj} + \cancelto{0}{O(2)} \Rightarrow$$

$$\Rightarrow \boxed{\Gamma^i_{j0} = \mathcal{H}\delta^i_j - \phi'\delta^i_j}\,, \tag{A.15}$$

$$\therefore \Gamma^i_{jk} = \frac{1}{2}g^{i\lambda}\left(\partial_j g_{\lambda k} + \partial_k g_{\lambda j} - \partial_\lambda g_{jk}\right) \overset{\lambda=l}{\Longrightarrow} \Gamma^i_{jk} = \frac{1}{2}g^{il}\partial_j g_{lk} + \frac{1}{2}g^{il}\partial_k g_{lj} - \frac{1}{2}g^{il}\partial_l g_{jk} \Rightarrow$$

$$\Rightarrow \Gamma^i_{jk} = -\frac{1+2\phi}{2a^2}\delta^{il}\left\{\partial_j\left[(-a^2)(1-2\phi)\delta_{lk}\right] + \partial_k\left[(-a^2)(1-2\phi)\delta_{lj}\right] - \partial_l\left[(-a^2)(1-2\phi)\delta_{jk}\right]\right\}$$

$$\Rightarrow \Gamma^i_{jk} = -\frac{1+2\phi}{\cancel{2a^2}}\delta^{il}\left(\cancel{2a^2}\partial_j\phi\,\delta_{lk} + \cancel{2a^2}\partial_\kappa\phi\,\delta_{lj} - \cancel{2a^2}\partial_l\phi\,\delta_{jk}\right) = -\delta^{il}\delta_{lk}\partial_j\phi - \delta^{il}\delta_{lj}\partial_k\phi + \delta^{il}\delta_{jk}\partial_l\phi$$

$$+\cancelto{0}{O(2)} \Rightarrow \boxed{\Gamma^i_{jk} = -(\delta^i_k\partial_j\phi - \delta^i_j\partial_k\phi) + \delta_{jk}\delta^{il}\partial_l\phi}\,. \tag{A.16}$$

Thus, gathering the previous calculations the non-zero Christoffel symbols are

$$\Gamma^0_{00} = \mathcal{H} + \psi', \qquad \Gamma^0_{0i} = \partial_i\psi\,,$$
$$\Gamma^i_{00} = \delta^{ij}\partial_j\psi, \qquad \Gamma^0_{ij} = \mathcal{H}\delta_{ij} - \left[\phi' + 2\mathcal{H}(\phi+\psi)\right]\delta_{ij}\,,$$
$$\Gamma^i_{j0} = \mathcal{H}\delta^i_j - \phi'\delta^i_j, \qquad \Gamma^i_{jk} = -(\delta^i_k\partial_j\phi + \delta^i_j\partial_k\phi) + \delta_{jk}\delta^{il}\partial_l\phi\,.$$

In order to derive the Einstein's Field Equations it is crucial to calculate the perturbed Ricci tensor $R_{\mu\nu}$ as well as the perturbed Ricci scalar R. The perturbed Ricci tensor components can

be calculated using the definition (1.9) along with the derived Christoffel symbols (A.11)-(A.16). The (00)-component is calculated as follows

$$R_{00} = \partial_\lambda\Gamma^\lambda_{00} - \partial_0\Gamma^\lambda_{0\lambda} + \Gamma^\lambda_{\lambda\rho}\Gamma^\rho_{00} - \Gamma^\rho_{0\lambda}\Gamma^\lambda_{0\rho} = \cancel{\partial_0\Gamma^0_{00}} + \partial_i\Gamma^i_{00} - \cancel{\partial_0\Gamma^0_{00}} - \partial_0\Gamma^i_{0i} + \cancel{\Gamma^0_{0\rho}\Gamma^\rho_{00}} + \Gamma^i_{i\rho}\Gamma^\rho_{00} -$$
$$\cancel{-\Gamma^\rho_{00}\Gamma^0_{0\rho}} - \Gamma^\rho_{0i}\Gamma^i_{0\rho} = \partial_i\Gamma^i_{00} - \partial_0\Gamma^i_{0i} + \Gamma^i_{i0}\Gamma^0_{00} + \cancel{\Gamma^i_{ij}\Gamma^j_{00}}^{O(2)} - \cancel{\Gamma^0_{0i}\Gamma^i_{00}}^{O(2)} - \Gamma^j_{0i}\Gamma^i_{0j} = \partial_i(\delta^{ij}\partial_j\psi) -$$
$$-\delta^i_i\,\partial_0(\mathcal{H}-\phi') + \delta^i_i(\mathcal{H}-\phi')(H+\psi') - (\mathcal{H}\delta^j_i - \phi'\delta^j_i)(\mathcal{H}\delta^i_j - \phi'\delta^i_j) = \nabla^2\psi - 3\mathcal{H}' + 3\phi'' +$$
$$+\cancel{3\mathcal{H}^2} + 3\mathcal{H}\psi' - 3\mathcal{H}\phi' - \cancel{3\mathcal{H}^2} + 6\mathcal{H}\phi' + \cancel{O(2)}^{0} \Rightarrow \boxed{R_{00} = \nabla^2\psi - 3\mathcal{H}' + 3\mathcal{H}(\phi'+\psi') + 3\phi''}\,. \tag{A.17}$$

The (0i)-component is derived to be

$$R_{0i} = \partial_\lambda\Gamma^\lambda_{0i} - \partial_i\Gamma^\lambda_{0\lambda} + \Gamma^\lambda_{\lambda\rho}\Gamma^\rho_{0i} - \Gamma^\rho_{0\lambda}\Gamma^\lambda_{i\rho} = \partial_0\Gamma^0_{0i} + \partial_j\Gamma^j_{0i} - \partial_i\Gamma^0_{00} - \partial_i\Gamma^j_{0j} + \Gamma^0_{0\rho}\Gamma^\rho_{0i} + \Gamma^j_{j\rho}\Gamma^\rho_{0i} -$$
$$-\Gamma^\rho_{00}\Gamma^0_{i\rho} - \Gamma^\rho_{0j}\Gamma^j_{i\rho} = \partial_0\partial_i\psi + \partial_j\left(\mathcal{H}\delta^j_i - \phi'\delta^j_i\right) - \partial_i(\mathcal{H}+\psi') - \partial_i(\mathcal{H}\delta^j_j - \phi'\delta^j_j) + \Gamma^0_{0\rho}\Gamma^\rho_{0i} + \Gamma^j_{j\rho}\Gamma^\rho_{0i}$$
$$-\Gamma^\rho_{00}\Gamma^0_{i\rho} - \Gamma^\rho_{0j}\Gamma^j_{i\rho} = \cancel{\partial_0\partial_i\psi} + \cancel{\partial_i\mathcal{H}} - \partial_i\phi' - \cancel{\partial_i\mathcal{H}} - \cancel{\partial_i\partial_0\psi} - 3\partial_i(\mathcal{H}-\phi') + \cancel{\Gamma^0_{00}\Gamma^0_{0i}} + \cancel{\Gamma^0_{0j}\Gamma^j_{0i}} +$$
$$+\Gamma^j_{j0}\Gamma^0_{0i} + \Gamma^j_{jk}\Gamma^k_{0i} - \cancel{\Gamma^0_{00}\Gamma^0_{i0}} - \Gamma^k_{00}\Gamma^0_{ik} - \cancel{\Gamma^0_{0j}\Gamma^j_{i0}} - \Gamma^k_{0j}\Gamma^j_{ik} = -\partial_i\phi' + 3\partial_i\phi' + (\mathcal{H}\delta^j_j - \phi'\delta^j_j)\partial_i\psi +$$
$$+\left(-\delta^j_k\partial_j\phi - \delta^j_j\partial_k\phi + \delta_{jk}\delta^{jl}\partial_l\phi\right)(\mathcal{H}\delta^k_i - \phi'\delta^k_i) - (\delta^{kj}\partial_j\psi)\left[\mathcal{H}\delta_{ik} - \phi'\delta_{ik} - 2\mathcal{H}(\phi+\psi)\delta_{ik}\right] -$$
$$-(\mathcal{H}\delta^k_j - \phi'\delta^k_j)(-\delta^j_k\partial_i\phi - \delta^j_i\partial_k\phi + \delta_{ik}\delta^{jl}\partial_l\phi) = -\partial_i\phi' + 3\partial_i\phi' + 3\mathcal{H}\partial_i\psi + (\cancel{\delta^l_i\partial_l\phi} - \cancel{\partial_i\phi} - 3\partial_i\phi)\mathcal{H}$$
$$-\partial_j\psi\mathcal{H}\delta^{kj}\delta_{ik} + 3\mathcal{H}\partial_i\phi + \cancel{\partial_i\phi} - \cancel{\delta^l_i\partial_l\phi} + \cancel{O(2)}^{0} = 2\partial_i\phi' + 2\mathcal{H}\partial_i\psi - \cancel{3\partial_i\phi\mathcal{H}} + \cancel{3\mathcal{H}\partial_i\phi} \Rightarrow$$
$$\Rightarrow \boxed{R_{0i} = 2\partial_i\phi' + 2\mathcal{H}\partial_i\psi}\,. \tag{A.18}$$

Similarly, the (ij) component of the perturbed Ricci tensor is equal to [610]

$$R_{ij} = \left[\mathcal{H}' + 2\mathcal{H}^2 - \phi'' + \nabla^2\phi - 2\left(\mathcal{H}' + 2\mathcal{H}^2\right)(\phi+\psi) - \mathcal{H}\psi' - 5\mathcal{H}\phi'\right]\delta_{ij} + \partial_i\partial_j(\phi-\psi)\,. \tag{A.19}$$

Now we are ready to calculate the perturbed Ricci scalar R using (1.10) as follows

$$R = g^{\mu\nu}R_{\mu\nu} = g^{00}R_{00} + \cancel{g^{0i}R_{0i}}^{0} + \cancel{g^{i0}R_{i0}}^{0} + g^{ij}R_{ij} = g^{00}R_{00} + g^{ij}R_{ij} = \frac{1-2\psi}{a^2}\left[\nabla^2\psi - 3\mathcal{H}' +\right.$$
$$\left.+3\mathcal{H}(\phi'+\psi') + 3\phi''\right] + \left(-\frac{1}{a^2}\right)(1+2\phi)\delta^{ij}\left\{\left[\mathcal{H}' + 2\mathcal{H}^2 - \phi'' + \nabla^2\phi - 2\left(\mathcal{H}' + 2\mathcal{H}^2\right)(\phi+\psi) -\right.\right.$$
$$\left.\left.-\mathcal{H}\psi' - 5\mathcal{H}\phi'\right]\delta_{ij} + \partial_i\partial_j(\phi-\psi)\right\} \Rightarrow a^2R = (1-2\psi)\left[\nabla^2\psi - 3\mathcal{H}' + 3\mathcal{H}(\phi'+\psi') + 3\phi''\right] -$$
$$-(1+2\phi)\delta^{ij}\delta_{ij}\left[\mathcal{H}' + 2\mathcal{H}^2 - \phi'' + \nabla^2\phi - 2\left(\mathcal{H}' + 2\mathcal{H}^2\right)(\phi+\psi) - \mathcal{H}\psi' - 5\mathcal{H}\phi'\right] - (1+$$
$$+2\phi)\delta^{ij}\partial_i\partial_j(\phi-\psi) = \nabla^2\psi - 3\mathcal{H}' + 3\mathcal{H}(\phi'+\psi') + 3\phi'' + 6\mathcal{H}'\psi - 3(1+2\phi)\left[\mathcal{H}' + 2\mathcal{H}^2 - \phi'' +\right.$$
$$\left.+\nabla^2\phi - 2\left(\mathcal{H}' + 2\mathcal{H}^2\right)(\phi+\psi) - \mathcal{H}\psi' - 5\mathcal{H}\phi'\right] - (1+2\phi)\nabla^2(\phi-\psi) + \cancel{O(2)}^{0} = \nabla^2\psi - 3\mathcal{H}' +$$
$$+3\mathcal{H}(\phi'+\psi') + 3\phi'' + 6\mathcal{H}'\psi - 3\mathcal{H}' - 6\mathcal{H}^2 + 3\phi'' - 3\nabla^2\phi + 6(\mathcal{H}' + 2\mathcal{H}^2)(\phi+\psi) + 3\mathcal{H}\psi' +$$
$$+15\mathcal{H}\phi' - 6\mathcal{H}'\phi - 12\mathcal{H}^2\phi - \nabla^2(\phi-\psi) + \cancel{O(2)}^{0} \Rightarrow$$
$$\Rightarrow \boxed{R = \frac{1}{a^2}\left[-6(\mathcal{H}' + \mathcal{H}^2) + 2\nabla^2\psi - 4\nabla^2\phi + 12(\mathcal{H}' + \mathcal{H}^2)\psi + 6\phi'' + 6\mathcal{H}(\psi' + 3\phi')\right]}\,. \tag{A.20}$$

Next, we move on to the Einstein tensor using its definition (1.12) along with Eqs. (A.17) and (A.20). The (00)-component yields

$$G_{00} = R_{00} - \frac{1}{2}g_{00}R = \nabla^2\psi - 3\mathcal{H}' + 3\mathcal{H}(\phi' + \psi') + 3\phi'' - \frac{1}{2}\cancel{a^2}(1+2\psi)\frac{1}{\cancel{a^2}}[-6(\mathcal{H}' + \mathcal{H}^2) + 2\nabla^2\psi$$
$$-4\nabla^2\phi + 12(\mathcal{H}' + \mathcal{H}^2)\psi + 6\phi'' + 6\mathcal{H}(\psi' + 3\phi')] = \nabla^2\psi - 3\mathcal{H}' + 3\mathcal{H}(\phi' + \psi') + 3\phi'' - \frac{1}{2}[-6(\mathcal{H}'$$
$$+\mathcal{H}^2) + 2\nabla^2\psi - 4\nabla^2\phi + 12(\mathcal{H}' + \mathcal{H}^2)\psi + 6\phi'' + 6\mathcal{H}(\psi' + 3\phi')] - \psi(-6)(\mathcal{H}' + \mathcal{H}^2) + \cancelto{0}{O(2)} =$$
$$= -\cancel{3\mathcal{H}'} + \cancel{\nabla^2\psi} + 3\mathcal{H}\phi' + \cancel{3\mathcal{H}\psi'} + \cancel{3\mathcal{H}'} + 3\mathcal{H}^2 - \cancel{\nabla^2\psi} + 2\nabla^2\phi - \cancel{6\mathcal{H}'\psi} - \cancel{6\mathcal{H}^2\psi} - \cancel{3\mathcal{H}\psi'} - 9\mathcal{H}\phi'$$
$$+\cancel{6\psi\mathcal{H}'} + \cancel{6\psi\mathcal{H}^2} \Rightarrow \boxed{G_{00} = 3\mathcal{H}^2 - 6\mathcal{H}\phi' + 2\nabla^2\phi}\,. \tag{A.21}$$

The (0i) component is trivially calculated to be

$$G_{0i} = R_{0i} - \frac{1}{2}\cancelto{0}{g_{0i}R} = R_{0i} \Rightarrow \boxed{G_{0i} = 2\partial_i\phi' + 2\mathcal{H}\partial_i\psi}\,. \tag{A.22}$$

After some algebra one can derive the remaining components of the perturbed Einstein tensor to be [610]

$$G_{ij} = -(2\mathcal{H}' + \mathcal{H}^2)\delta_{ij} + \left[\nabla^2(\psi - \phi) + 2\phi'' + 2(2\mathcal{H}' + \mathcal{H}^2)(\phi + \psi) + 2\mathcal{H}\psi' + 4\mathcal{H}\phi'\right]\delta_{ij} +$$
$$+\partial_i\partial_j(\phi - \psi)\,. \tag{A.23}$$

As a final step for the derivation of the Einstein's Field Equations, we need to find the perturbations of the energy momentum tensor $T_{\mu\nu}$. In a homogeneous background the energy density ρ, the pressure p as well as the four-velocity u^μ are time dependent quantities. On the contrary in a perturbed Universe, these function may also depend on the position. So, the perturbation of the energy-momentum tensor is [610]

$$\delta T^\mu_\nu = (\delta\rho + \delta p)\bar{u}^\mu\bar{u}_\nu + (\bar{\rho} + \bar{p})\left[(\delta u^\mu)\bar{u}_\nu + \bar{u}^\mu(\delta u_\nu)\right] + \delta p\,\delta^\mu_\nu + \Pi^\mu_\nu\,, \tag{A.24}$$

where Π^μ_ν corresponds to the anisotropic stress tensor which vanishes for perfect fluids. In the context of Newtonian gauge (A.5), it is straightforward to show the non-zero components of the perturbed energy-momentum tensor δT^μ_ν are

$$\delta T^0_0 = \delta\rho, \qquad \delta T^i_0 = (\bar{\rho} + \bar{p})u^i\,,$$
$$\delta T^0_j = -(\bar{\rho} + \bar{p})(u_j + \cancelto{0}{B_j}) \equiv -q_j, \qquad \delta T^i_j = -\delta p\,\delta^i_j - \Pi^i_j\,,$$

with $\vec{q} = \vec{u}(\bar{\rho} + \bar{p})$ where $\vec{v}$ is the three velocity. Armed with the previous results we can compute

the linearized perturbed Einstein Field Equations

$$\therefore \text{For } \mu = i \text{ and } \nu = j \text{ with } i \neq j, \text{ we find}$$

$$G_{ij} = 8\pi\, G_{\rm N} T_{ij} \Rightarrow -(2\mathcal{H}' + \mathcal{H}^2)\delta_{ij} + \left[\nabla^2(\psi - \phi) + 2\phi'' + 2(2\mathcal{H}' + \mathcal{H}^2)(\phi + \psi) + 2\mathcal{H}\psi' + 4\mathcal{H}\phi'\right]\delta_{ij} + \partial_i\partial_j(\phi - \psi) = -8\pi\, G_{\rm N}\Pi_{ij} \Rightarrow \partial_i\partial_j(\phi - \psi) = 0 \Rightarrow \boxed{\phi = \psi}\,, \tag{A.25}$$

$$\therefore \text{For } \mu = \nu = 0 \text{ we derive}$$

$$G_{00} = 8\pi\, G_{\rm N} T_{00} = 8\pi\, G_{\rm N}\, g_{0p}\, T^p_0 = 8\pi\, G_{\rm N}\left(g_{00}\, T^0_0 + g_{0i}\, T^i_0\right) \Rightarrow G_{00} = 8\pi\, G_{\rm N}\, g_{00}\, T^0_0 \Rightarrow$$

$$\xRightarrow{(A.25)} 3\mathcal{H}^2 - 6\mathcal{H}\phi' + 2\nabla^2\phi = 8\pi\, G_{\rm N}\, a^2(1 + 2\phi)(\bar{\rho} + \delta\rho) = 8\pi\, G_{\rm N}\, a^2(1 + 2\phi)\bar{\rho}(1 + \delta + 2\phi) \Rightarrow$$

$$\Rightarrow 3\mathcal{H}^2 - 6\mathcal{H}\phi' + 2\nabla^2\phi = 8\pi G_{\rm N}\, a^2\bar{\rho}\,[1 + 2\phi + \delta + \cancelto{0}{O(2)}] = 8\pi G_{\rm N}\, a^2\bar{\rho}(1 + \delta + 2\phi) \Rightarrow$$

$$\Rightarrow \cancel{3\mathcal{H}^2} - 6\mathcal{H}\phi' + 2\nabla^2\phi = \cancel{8\pi G_{\rm N}\, a^2\bar{\rho}} + 8\pi G_{\rm N}\, a^2\bar{\rho}(\delta + 2\phi) \Rightarrow \nabla^2\phi = 4\pi G_{\rm N}\, a^2\bar{\rho}\,\delta +$$

$$+8\pi G_{\rm N}\, a^2\bar{\rho}\phi + 3\mathcal{H}\phi' \Rightarrow \boxed{\nabla^2\phi = 4\pi G_{\rm N}\, a^2\bar{\rho}\delta + 3\mathcal{H}(\phi' + \mathcal{H}\phi)}\,, \tag{A.26}$$

$$\therefore \text{For } \mu = 0 \text{ and } \nu = i \text{ we obtain}$$

$$G_{0i} = 8\pi\, G_{\rm N} T_{0i} \Rightarrow 2\,\partial_i\,(\phi' + \mathcal{H}\psi) = 8\pi\, G_{\rm N}\,(g_{0\mu}T^\mu_i) = 8\pi\, G_{\rm N}\left(g_{00}T^0_i\right) = 8\pi\, G_{\rm N}\bar{g}_{00}T^0_i + \cancelto{0}{O(2)} \Rightarrow$$

$$\Rightarrow 2\,\partial_i\,(\phi' + \mathcal{H}\psi) = -8\pi\, G_{\rm N}\, a^2\, q_i \Rightarrow \partial_i\,(\phi' + \mathcal{H}\psi) = -4\pi\, G_{\rm N}\, a^2\,(\bar{\rho} + \bar{p})u_i \Rightarrow \partial_i\,(\phi' + \mathcal{H}\psi) =$$

$$= -4\pi\, G_{\rm N}\, a^2\,(\bar{\rho} + \bar{p})\partial_i u \xRightarrow[\int]{(A.25)} \boxed{\phi' + \mathcal{H}\phi = -4\pi\, G_{\rm N}\, a^2\,(\bar{\rho} + \bar{p})u}\,, \tag{A.27}$$

where in (A.25) we dropped the anisotropic stress term (*i.e.* we considered $\Pi_{ij} \equiv 0$) and in (A.27) we assumed that the perturbation decay at infinity in order to perform the integration. Recall that δ corresponds to the linear matter growth factor. Similarly, the trace-part of the (ij) component is [610]

$$\phi'' + 3\mathcal{H}\phi' + (2\mathcal{H}' + \mathcal{H}^2)\phi = 4\pi\, G_{\rm N}\, a^2\,\delta p\,. \tag{A.28}$$

In some cases, it is useful to use the continuity and the Euler equations that are obtained from the conservation law for the energy momentum $\nabla^\mu T_{\mu\nu}$. For $\nu = 0$ it is straightforward to show that the continuity equation is written as [610]

$$\delta' + \left(1 + \frac{\bar{p}}{\bar{\rho}}\right)(\vec{\nabla}\,\vec{u} - 3\phi') + 3\mathcal{H}\left(\frac{\delta p}{\delta\rho} - \frac{\bar{p}}{\bar{\rho}}\right)\delta = 0\,, \tag{A.29}$$

while the Euler equation is derived for $\nu = i$ to be [610]

$$\vec{u}' + \mathcal{H}\vec{u} - 3\mathcal{H}\frac{\bar{p}'}{\bar{\rho}'}\vec{u} = -\frac{\vec{\nabla}\delta p}{\bar{\rho} + \bar{p}} - \vec{\nabla}\psi \tag{A.30}$$

A.2 Proof of Eq. (1.49)

We are mainly interested in the evolution of matter fluctuations both at early (*i.e.* when radiation dominates) and late times (*i.e.* when dark energy dominates). Moreover, we focus on the sub-horizon scales *i.e.* at scales deep inside the Hubble radius where $k \gg \mathcal{H}$. For matter

domination we derive the equations (A.29) and (A.30) in the context of a pressureless fluid ($w = 0$) with a very small sound speed defined as

$$c_s^2 \equiv \frac{\delta p}{\delta \rho} \ll 1 \,. \tag{A.31}$$

At early times, the continuity equation (A.29) for the matter density is written as

$$\delta_m' + (1+w)\left(\vec{\nabla}\,\vec{u}_m - 3\phi'\right) + 3\mathcal{H}\left(c_s^2 - w\right)\delta = 0 \Rightarrow \delta_m' + (\vec{\nabla}\,\vec{u}_m - 3\cancelto{0}{\phi'}) + 0 = 0 \Rightarrow \delta_m' = -\vec{\nabla}\,\vec{u}_m \,, \tag{A.32}$$

while the Euler equation (A.30) takes the form

$$\vec{u}_m' + \mathcal{H}\vec{u}_m - 3\mathcal{H}w\,\vec{u}_m = -\frac{\vec{\nabla}\delta p}{\bar{\rho}+\bar{p}} - \vec{\nabla}\psi \xrightarrow[w=0]{\text{(A.25)}} \vec{u}_m' + \mathcal{H}\vec{u}_m = -\vec{\nabla}\phi \Rightarrow \vec{u}_m' = -\mathcal{H}\vec{u}_m - \vec{\nabla}\phi \,. \tag{A.33}$$

Differentiating (A.32) and substituting (A.33) it is straightforward to see

$$\begin{aligned} \delta_m'' = -\vec{\nabla}\vec{u}_m' \xrightarrow{\text{(A.33)}} \delta_m'' = -\vec{\nabla}\left(-\mathcal{H}\vec{u}_m - \vec{\nabla}\phi\right) \Rightarrow \delta_m'' = \mathcal{H}\vec{\nabla}\vec{u}_m + \nabla^2\phi \Rightarrow \delta_m'' - \mathcal{H}\vec{\nabla}\vec{u}_m = \nabla^2\phi \\ \xrightarrow{\text{(A.32)}} \delta_m'' + \mathcal{H}\delta_m' = \nabla^2\phi \,. \end{aligned} \tag{A.34}$$

Since radiation oscillates quickly compared to the Hubble time on small scales, averaging over time the gravitational potential is only sourced by matter fluctuations, so the Poisson equation is only sensitive to matter leading (A.27) to take the form

$$\nabla^2\phi = 4\pi G_{\rm N}\, a^2 \bar{\rho}_m \delta \,. \tag{A.35}$$

Combining (A.34) with (A.35) we find

$$\delta_m'' + \mathcal{H}\delta_m' - 4\pi G_{\rm N}\, a^2 \bar{\rho}_m \delta = 0 \,. \tag{A.36}$$

At late times, our Universe is a mixture of pressureless matter and dark energy. Since dark energy does not have fluctuations, Eq. (A.35) is modified to

$$\nabla^2\phi = 4\pi G_{\rm N}\, a^2 \bar{\rho}_m \Delta \,, \tag{A.37}$$

where $\Delta \equiv \delta_m - 3\mathcal{H}u_m$ is the comoving density contrast. With similar calculations and taking into account (A.37), Eq. (A.36) generalizes to [610]

$$\Delta'' + \mathcal{H}\Delta' - 4\pi G_{\rm N}\, a^2 \bar{\rho}_m \Delta = 0 \,. \tag{A.38}$$

This is the conformal time equivalent version of (1.49) but now valid on all scales. In the context of a modified theory of gravity the standard Newton's constant $G_{\rm N}$ is promoted to the effective Newton's constant $G_{\rm eff}$.

A.3 Proof of Eq. (1.50)

In this section we will show how to rewrite Eq. (1.49) in terms of the redshift z and of the scale factor $a(t)$. For the redhsift case, it is easy to see that for a general function $q(t)$ we have

$$\frac{dq}{dt} = \frac{dq}{dz}\frac{dz}{dt} = \frac{dq}{dz}\left[-H(z)(1+z)\right] = -H(z)(1+z)q' \Rightarrow \frac{dq}{dt} = -H(z)(1+z)q' \tag{A.39}$$

$$\frac{d^2q}{dt^2} = \frac{d}{dt}\left(\frac{dq}{dt}\right) = \frac{dz}{dt}\frac{d}{dz}\left(\frac{dq}{dt}\right) = \frac{dz}{dt}\frac{d}{dz}\left(-H(z)(1+z)q'\right) = \left[-H(z)(1+z)\right]\left[-H'(z)(1+z)q'\right.$$
$$\left.-H(z)q' - H(z)(1+z)q''\right] \Rightarrow \frac{dq}{dt} = H(z)H'(z)(1+z)^2q' + H^2(z)(1+z)q' + H^2(z)(1+z)^2q'', \tag{A.40}$$

where we used the fact that

$$H = \frac{\dot{a}}{a} = (1+z)\frac{d}{dt}\left(\frac{1}{1+z}\right) = -\frac{dz/dt}{1+z} \Rightarrow \frac{dz}{dt} = -H(z)(1+z)\,. \tag{A.41}$$

In this case the prime stands for differentiation with respect to redshift z and the dot differentiation with respect to cosmic time t. Therefore, from Eqs. (A.39) and (A.40) it is easy to show that

$$\ddot{\delta} = HH'(z)(1+z)^2\delta' + H^2(1+z)\delta' + H^2(1+z)^2\delta'',$$
$$\dot{\delta} = -H(z)(1+z)\delta'.$$

Substituting these equations in Eq. (1.49) we derive

$$HH'(z)(1+z)^2\delta' + H^2(1+z)\delta' + H^2(1+z)^2\delta'' + 2H\left[-H(z)(1+z)\delta'\right] - 4\pi\,G_{\rm eff}\,\rho_m\,\delta = 0 \Rightarrow$$
$$\xrightarrow{:(1+z)^2} H^2\delta'' + HH'\delta' + \frac{H^2}{1+z}\delta' - \frac{2H^2}{1+z}\delta' - 4\pi\,G_{\rm eff}\,\rho_m\,\frac{\delta}{(1+z)^2} = 0 \Rightarrow H^2\delta'' + \left[\frac{(H^2)'}{2} - \right.$$
$$\left. - \frac{H^2}{1+z}\right]\delta' - 4\pi\,G_{\rm eff}\,\frac{\rho_{m,0}}{a^3}\,\frac{\delta}{(1+z)^2} = 0 \Rightarrow H^2\delta'' + \left[\frac{(H^2)'}{2} - \frac{H^2}{1+z}\right]\delta' -$$
$$-4\pi\,G_{\rm eff}\,\frac{\rho_{m,0}}{\rho_{crit,0}}\rho_{crit,0}(1+z)^3\,\frac{\delta}{(1+z)^2} = 0 \Rightarrow H^2\delta'' + \left[\frac{(H^2)'}{2} - \frac{H^2}{1+z}\right]\delta'$$
$$-4\pi G_{\rm eff}\,\Omega_{m,0}\,\frac{3H_0^2}{8\pi\,G_{\rm N}}(1+z) = 0 \Rightarrow \boxed{H^2\delta'' + \left[\frac{(H^2)'}{2} - \frac{H^2}{1+z}\right]\delta' = \frac{3}{2}(1+z)H_0^2\frac{G_{\rm eff}}{G_{\rm N}}\Omega_{\rm m,0}\,\delta}\,, \tag{A.42}$$

i.e. Eq. (1.49) in terms of the redshift z.

In order to rewrite this equation in terms of the scale factor a, we need the following useful derivations

$$1+z = \frac{1}{a} \Rightarrow dz = -\frac{1}{a^2}da \Rightarrow \frac{da}{dz} = -a^2\,,$$
$$\frac{d\delta}{dz} = \frac{d\delta}{da}\frac{da}{dz} = \delta'(-a^2) = -a^2\delta'\,,$$
$$\frac{d(H^2)}{dz} = 2H\frac{dH}{dz} = 2H\frac{dH}{da}\frac{da}{dz} = -2HH'a^2\,,$$
$$\frac{d^2\delta}{dz^2} = \frac{d}{dz}\frac{d\delta}{dz} = \frac{da}{dz}\frac{d}{da}\left(\frac{d\delta}{dz}\right) = \frac{da}{dz}\frac{d}{da}\left(-a^2\delta'\right) = \frac{da}{dz}\left[\delta''(-a^2) + \delta'(-2a)\right] = \delta''a^4 + 2\delta'a^3\,,$$

where in this case the prime denotes derivation with respect to the scale factor a. Substituting these derivations in Eq. (A.42) it is straightforward to show

$$H^2\delta'' + \left[\frac{(H^2)'}{2} - \frac{H^2}{1+z}\right]\delta' - 4\pi\, G_{\rm eff}\,\rho_m\,\frac{\delta}{(1+z)^2} = 0 \Rightarrow H^2\left(\delta'' a^4 + 2\delta' a^3\right) - \left(\frac{2HH'a^2}{2}\right.$$
$$\left. + H^2 a\right)\left(-a^2\delta'\right) = 4\pi\, G_{\rm eff}\,\rho_m\, a^2\delta \Rightarrow H^2\left(\delta'' a^4 + 2\delta' a^3\right) + \left(HH' a^4 + H^2 a^3\right)\delta' = 4\pi G_{\rm eff}\,\rho_m\, a^2\delta$$
$$\xrightarrow{\cdot\frac{1}{H^2a^4}} \delta'' + 2a^{-1}\delta' + \frac{H'}{H}\delta' + \frac{\delta'}{a} = \frac{4\pi\, G_{\rm eff}}{H^2(a)}\frac{\rho_{m,0}}{a^5}\delta \Rightarrow \delta''(a) + \left(\frac{3}{a} + \frac{H'(a)}{H(a)}\right)\delta'(a) =$$
$$= \frac{4\pi\, G_{\rm eff}}{H^2(a)a^5}\frac{\rho_{m,0}}{\rho_{crit,0}}\,\rho_{crit,0}\,\delta(a) \Rightarrow \boxed{\delta''(a) + \left(\frac{3}{a} + \frac{H'(a)}{H(a)}\right)\delta'(a) - \frac{3}{2}\frac{\Omega_{\rm m,0}\, G_{\rm eff}(a,k)/G_{\rm N}}{a^5 H(a)^2/H_0^2}\,\delta(a) = 0},$$

i.e. Eq. (1.50)

A.4 Proof of Eq. (1.54)

The derivation of (1.54) can be easily shown by rewriting the equation for the growth rate of perturbations as

$$f(a) \equiv \frac{dln\delta(a)}{dlna} = \frac{da}{dlna}\frac{dln\delta(a)}{da} \Rightarrow f(a) = \frac{\delta'(a)}{\delta(a)}\,a\,. \tag{A.43}$$

Hence the observation product $f\sigma_8(a)$ takes the form

$$f\sigma_8(a) \equiv f(a)\cdot\sigma(a) = \frac{\delta'(a)}{\cancel{\delta(a)}}\,a\,\sigma_8\,\frac{\cancel{\delta(a)}}{\delta(1)} \Rightarrow \boxed{f\sigma_8(a) = \frac{\sigma_8}{\delta(1)}\,a\,\delta'(a)},$$

i.e. Eq. (1.54).

Appendix B

Boltzmann Codes

As we shortly discussed in Section 2.5, in order to construct the CMB power spectrum, one should take into consideration all the particle species and calculate how the perturbations affect particle distributions by solving the Boltzmann equations, calculate the ratio $\Delta T/T$ and expand in spherical harmonics. Fortunately, throughout the years some numerical codes have been developed, such as the `CMBFAST` [611], the `Davis Anisotropy Shortcut (DASh)` [612], the `CMBEASY` (an updated version of `CMBFAST` written in C++) [613], the `Code for Anisotropies in the Microwave Background (CAMB)` [462] and the `Cosmic Linear Anisotropy Solving System (CLASS)` [463, 464] that have the ability to solve the Boltzmann equations for a given set of cosmological parameters and construct the predicted CMB and large scale structure observables in the context of ΛCDM, as well as some default dark energy models (*e.g.* the wCDM, the CPL *etc.*). Nowadays, the last two are kept up to date, with current cosmological data and are by far the most widely used numerical packages for the construction of the power spectrum.

Their increasing popularity over the years led to the development of appropriate patches [such as the `Modified Growth with CAMB (MGCAMB)` [465–467] and the `hi_class` [468, 469] patches] in the aforementioned codes that solve the Boltzmann equations for a given set of cosmological parameters and construct the predicted CMB and large scale structure observables for different modified gravity theories. In this appendix we will briefly discuss some of these packages and shortly elaborate their functionality.

B.1 `(MG)CAMB/(MG)COSMOMC`

The first numerical package that we discuss is `CAMB` [462]. Its latest version can be either downloaded from its official github repository or by simply using the `git clone` command in the terminal as indicated in the readme file. After the successful installation of the current version of `CAMB`, one of the `.ini` files (*e.g.* the `params.ini`) that are inside the `inifiles` folder can be used as the reference input file, in order to set specific values to the basic parameters of the cosmological model in question. Then, this file is executed following the instructions of the readme and the C_l's of the corresponding CMB power spectrum are obtained.

The `CAMB` package, works in tandem with `Cosmological MonteCarlo (COSMOMC)`, which is a Markov Chain Monte Carlo (MCMC) engine for exploring cosmological parameter space [462]. `COSMOMC` does accurate brute force theoretical matter power spectrum and C_l calculations

utilizing `CAMB`. In particular, the code calls `CAMB` for each sampled point of the parameter space and performs a simple Metropolis algorithm or an optimized fast-slow sampling method (ideal for likelihoods with many nuisance parameters, such as the Planck likelihoods) MCMC over user selected parameters. The latest version of `COSMOMC` may be downloaded either from the official github repository or by using the `git clone` command in the terminal. After successfully installing its current version, one needs to modify the `test.ini` file in order to include the needed likelihoods, as well as the `common.ini` and the relevant `.ini` files inside the `batch3` folder in order to set the priors of the parameter of the model in question.

The increasing popularity of this particular Boltzmann code, led to appropriate patches that solve the Boltzmann equations for specific modified gravity models. Regarding `CAMB`, the corresponding patch is the `Modified Growth with CAMB (MGCAMB)` [465–467]. Its latest version can be downloaded from the official github repository or by simply using the `git clone` command in the terminal, as indicated in the readme file. This patch works in the same way as `CAMB` code but introduces phenomenological modification of growth along with dynamical dark energy models. The corresponding parameters for the modified gravity models can be specified in the `params_MG.ini` file and this file is used along with the `params.ini` file to run the code. Concerning `COSMOMC`, the corresponding patch is the `MGCOSMOMC`. The latest version can downloaded either from the official github repository or by simply using the `git clone` command in the terminal as usual.

For the reproduction of Fig. 2.15 we use the numerical package `MGCAMB`. After successfully installing it, we modify the `mgcamb.f90` file by adding in the relevant `mu, gamma functions` the parametrization (2.10) as a separate case and then we generate different `params_CMB_MG.ini` and `params.ini` files for each pair of (g_a, n)[1]. For example for the pair $(g_a, n) = (0.5, 2)$, we have created the file `params_MG_ga05.ini` which has the following settings:

(∗ Part 1. Choose the Modified Growth flag ∗)
MG_flag **= 1**
(∗ Choose at which time to turn on MG ∗)
GRtrans **= 0.001*d*0**
(∗ Part 2.1 - Pure MG models ∗)
pure_MG_flag **= 1**
(∗ Part 2.2 - Alternative MG models ∗)
alt_MG_flag **= 1**
(∗ Part 2.3 - QSA models ∗)
QSA_flag **= 4**
(∗ Part 3.1.1. - mu, gamma functions ∗)
mugamma_par **= 3**
(∗ Effective Newton's Constant ∗)
ga **= 0.5**
nn **= 2**

[1] Actually, for this task we contacted the authors of the program and they created this separate branch for us.

(* Part 3.1.2. - mu, Sigma functions *)
musigma_par = 1
mu0 = −1
sigma0 = 0
(* Part 3.1.3. - Q,R functions *)
QR_par = 1
MGQfix = 1
MGRfix = 1
Qnot = 1.
Rnot = 1.
sss = 0
(* Part 3.2.1 - Linder Gamma *)
Linder_gamma = 0.545
(* Part 3.3.1 - QSA f(R) model *)
B0 = 1.d − 3
(* Part 3.3.2 - QSA Symmetron model *)
beta_star = 1.0d0
a_star = 0.5d0
xi_star = 0.001d0
(* Part 3.3.3 - QSA Dilaton model *)
beta0 = 1.d0
xi0 = 0.0001
DilS = 0.24d0
DilR = 1.d0
A2 = 1e3
(* Part 3.3.4 - QSA Hu-Sawicki f(R) *)
F_R0 = 0.0001d0
FRn = 1.d0
(* Part 4. Parameters for the DE model *)
DE_model = 0
w0DE = −1.d0
waDE = 0.d0

Obviously the majority of the parameters is set in the default values and are omitted by the code since we focus on the `mu, gamma functions` loop. Similarly, we construct the rest of the files for the corresponding (g_a, n) pairs. Then, these files are used by `params.ini` and utilizing the `gnuplot` program we construct Fig. 2.15.

B.2 CLASS/MontePython

Another Boltzmann code that is widely used in the literature is the CLASS [463,464] numerical package. A basic advantage of CLASS over other similar programs, is that it is written in C++ with a very modular documentation. Furthermore, CLASS is a compartmentalized program so it is relatively easy to modify. Its latest version can be installed from the official github repository of the numerical package. The reference input file for this program is the explanatory.ini file that contains all possible input parameters as well as detailed comments. The package (as well as CAMB) has by default implemented some basic dark energy models as well the standard ΛCDM scenario. More specifically, in the section "Dark energy contributions" three models are implemented by default. These are the following:

- ΛCDM corresponding to Omega_Lambda.
- CPL corresponding to Omega_fld.
- Scalar Field corresponding to Omega_scf that solves the Klein Gordon equation for a scalar field.

If the user needs to run the code for one of the aforementioned models, he needs to fix the values of the two out of the three parameters to zero and leave the third one undefined. For example, if the user wants to use the standard ΛCDM scenario, then he should set Omega_scf=0 (in order to avoid any contribution from the scalar field), Omega_fld=0 and leave the Omega_Lambda to be unspecified. Similarly, if one wants to study the CPL case, then, he should comment the Omega_fld and set the other two equal to zero.

The CLASS numerical package works in tandem with MontePython (similar to CAMB with COSMOMC) which is a MCMC engine used for parameter inference and includes various methods to explore parameter space, such as a Metropolis-Hastings sampling method, a Nested Sampling method *etc.* (see Ref. [546] for more details). The latest version of the program can be downloaded from the official github repository. After successfully installing it, the user needs to create a .param file following the example files inside the input folder. In the constructed .param file the likelihoods as well as the priors of the parameter of the cosmological model in question are specified.

In Chapter 5 we utilized the CLASS/MontePython programs for the transition models $LwMT$ and LMT. For this purpose, we modified the CPL case in CLASS and then run the programs as usual. Regarding the modifications, we firstly calculated the equation of state parameter $w(a)$, its derivative with respect to the scale factor a as well as the following integral

$$f_{DE} \equiv -3 \int_1^a \frac{1+w(a')}{a'} da'$$

and rewrote the derived forms in C format. Then, the calculated forms were substituted in the CPL case in the background.c file that is located inside the source folder. More specifically, the functions *w_fld, *dw_over_da_fld as well as the *integral_fld were modified and then, in the input.c file, the default values of the extra parameters of the transition models inside the /** - background structure */ were defined. Finally, we determined in the background.h file, that is located in the include folder, the type of the variables of the transition models inside the struct background loop[2].

[2]For more detailed instructions concerning the modifications visit our website page.

B.3 `emcee`

Another open source program that is widely used in the literature is the publicly available `emcee`. This is a Python implementation program that, in contrast to `COSMOMC` or `MontePython`, is not directly connected with applications to problems in cosmology. In essence, as all MCMC samplers, is aimed to simulate the posterior distribution of the given problem at hand, but now based on an affine-invariant ensemble scheme, first introduced in Ref. [614]. In this scheme, the user starts by defining the number of walkers, *i.e.* the numbers of the members of the ensemble, that scan the parametric space in the prior ranges that the user has chosen to vary over.

After defining the prior ranges for the parameters and the likelihood function of the cosmological model in question, each walker starts searching the parametric space and move to a candidate point based on his relation with the other walkers. If the new position provides a higher proposal probability function than the previous one, then the walker accepts the new proposal. If not, the new proposed point is rejected with a given probability. In the end, the ensemble of walkers will cover the parameter space of interest, and within it the optimum region where the model describes better the observations is identified. A more detailed analysis regarding the `emcee` program is beyond the scope of the current thesis but the reader, if interested, can see Ref. [615] for more details.

Appendix C

Chapter 2 Calculations

In this appendix we present the proof of Eq. (2.26) and shortly discuss the basic algorithms that were used for the statistical analysis and the construction of the figures of Chapter 2. For a more extensive analysis regarding the code, visit the "Growth-Tomography repository."

C.1 Proof of Eq. (2.26)

The derivation of (2.26) is straightforward. We calculate each term of (2.26) separately as follows

$$\frac{df}{dlna} = \delta'' \frac{a^2}{\delta(a)} + a\frac{\delta'(a)}{\delta(a)} - a^2\frac{[\delta'(a)]^2}{\delta^2(a)}\,, \tag{C.1}$$

$$f^2 = a^2\frac{[\delta'(a)]^2}{\delta^2(a)}\,, \tag{C.2}$$

$$\frac{dln\Omega_m}{dlna} = -3 - 2a\frac{H'(a)}{H(a)}\,, \tag{C.3}$$

$$\frac{1}{2}\left(1 - \frac{dln\Omega_m}{dlna}\right) f = \frac{f}{2} - \frac{f}{2}\frac{dln\Omega_m}{dlna} = a\frac{\delta'(a)}{2\delta(a)} + \frac{3}{2}a\frac{\delta'(a)}{\delta(a)} + a^2\frac{\delta'(a)\,H'(a)}{\delta(a)\,H(a)}\,, \tag{C.4}$$

$$\frac{3}{2}\frac{G_{\rm eff}}{G_{\rm N}}\Omega_m = \frac{3}{2}\frac{G_{\rm eff}}{G_{\rm N}}\frac{\Omega_{\rm m,0}\,a^{-3}\,H_0^2}{H^2(a)}\,. \tag{C.5}$$

Therefore, adding the terms (C.1)-(C.5), we easily obtain

$$\frac{df}{d\ln a} + f^2 + \frac{1}{2}\left(1 - \frac{d\ln\Omega_m}{d\ln a}\right) f = \frac{3}{2}\frac{G_{\rm eff}}{G_{\rm N}}\Omega_m \Rightarrow \delta''\frac{a^2}{\delta(a)} + a\frac{\delta'(a)}{\delta(a)} - \cancel{a^2\frac{[\delta'(a)]^2}{\delta^2(a)}} + \cancel{a^2\frac{[\delta'(a)]^2}{\delta^2(a)}} +$$
$$+a\frac{\delta'(a)}{2\delta(a)} + \frac{3}{2}a\frac{\delta'(a)}{\delta(a)} + a^2\frac{\delta'(a)\,H'(a)}{\delta(a)\,H(a)} = \frac{3}{2}\frac{G_{\rm eff}}{G_{\rm N}}\frac{\Omega_{\rm m,0}\,a^{-3}\,H_0^2}{H^2(a)} \Rightarrow \delta''\frac{a^2}{\delta(a)} + 3a\frac{\delta'(a)}{\delta(a)} + a^2\frac{\delta'(a)\,H'(a)}{\delta(a)\,H(a)}$$
$$= \frac{3}{2}\frac{G_{\rm eff}}{G_{\rm N}}\frac{\Omega_{\rm m,0}\,a^{-3}\,H_0^2}{H^2(a)} \xrightarrow{\times\delta(a)/a^2} \boxed{\delta''(a) + \left(\frac{3}{a} + \frac{H'(a)}{H(a)}\right)\delta'(a) - \frac{3}{2}\frac{\Omega_{\rm m,0}\,G_{\rm eff}(a,k)/G_{\rm N}}{a^5H^2(a)/H_0^2}\,\delta(a) = 0}\,,$$

i.e. Eq. (1.50).

C.2 Reproduction of Fig. 2.2

As a first step we need to import the growth compilation presented in Table 2.1 which we have in a txt file entitled `Growth_tableII`. Moreover we import the subcovariance matrix of the WiggleZ survey (2.21) which also in a txt file entitled `Cij_WiggleZ`. Furthermore, for the reproduction of Fig. 2.2, we need Eqs. (1.50), (2.10) in order to construct the theoretical forms of (1.54). This is demonstrated in the following Mathematica code:

```
datag = Import[".\\data\\Growth_tableII.txt", "Table"];
Cijwigglez = Import[".\\data\\Cij_WiggleZ.txt", "Table"];
δ[a_, w_, Ω_]:=aHypergeometric2F1[1/(-3w), 1/2 - 1/(2w), 1 - 5/(6w), a^(-3w)(1 - 1/Ω)]
fwCDM[a_, w_, Ω_]:=aD[Log[δ[aa, w, Ω]], aa]/.aa → a
fσ8wCDM[a_, w_, Ω_, σ8_]:=fwCDM[a, w, Ω]σ8 δ[a, w, Ω]/δ[1, w, Ω]
(* The wCDM Form of Background *)
H[a_, w_, om_]:=Sqrt[oma^(-3) + (1 - om)a^(-3(1+w))]

(* Analytic Form for the Luminosity Distance *)
dLh[a_, om_, w_]:=2/(a Sqrt[om]) (Hypergeometric2F1[1/2, -1/(6w), 1 - 1/(6w), 1 - 1/om] -
- Sqrt[a] Hypergeometric2F1[1/2, -1/(6w), 1 - 1/(6w), (1 - 1/om)a^(-3w)])
amin = 0.001;
(* The Phenomenological Parametrization (2.10) *)
Geff[a_, ga_, n_]:=1 + ga(1 - a)^n - ga(1 - a)^(2n);
dsol[om_?NumberQ, w_?NumberQ, ga_?NumberQ, n_?NumberQ]:=
(dsol[om, w, ga, n] = Module[{a}, NDSolve[{-(3om d[a]Geff[a, ga, n])/(2a^5 H[a, w, om]^2) + d'[a]
+ (3/a + D[H[a, w, om], a]/H[a, w, om]) + d''[a] == 0, d[amin]==amin, d'[amin] == 1}, d, {a, amin, 1}]
[[1]]])
(* The growth rate and fσ8 *)
Da[a_, om_, w_, ga_, n_]:=d[a]/.dsol[om, w, ga, n]
fa[aa_, om_, w_, ga_, n_]:=ad'[a]/d[a]/.a → aa/.dsol[om, w, ga, n]
fσ8geff[a_?NumberQ, om_?NumberQ, w_?NumberQ, ga_?NumberQ, n_?NumberQ, σ8_?NumberQ]:=
σ8Da[aa, om, w, ga, n]/Da[1, om, w, ga, n] fa[aa, om, w, ga, n]/.aa → a
fσ8z[z_?NumberQ, om_?NumberQ, w_?NumberQ, ga_?NumberQ, n_?NumberQ, σ8_?NumberQ]
```

```
:=σ8Da[aa, om, w, ga, n]/Da[1, om, w, ga, n] fa[aa, om, w, ga, n]/.aa → 1/(1 + z)
(* Full Dataset *)
datag1 = Table[{datag[[i, 1]], datag[[i, 2]], datag[[i, 3]]}, {i, 1, Length[datag]}];
pldatag = ErrorListPlot [datag1, Frame → True, FrameLabel → {z, "fσ8(z)",
BaseStyle → FontSize → 16, PlotRange → {0, 0.8}, PlotStyle → {PointSize → Large, Blue}] ;
(* 20 Early Data *)
datagearly = Take[datag, 20];
datag1early = Table[{datagearly[[i, 1]], datagearly[[i, 2]], datagearly[[i, 3]]},
{i, 1, Length[datagearly]}];
pldatagearly = ErrorListPlot [datag1early, Frame → True, FrameLabel → {z, "fσ8(z)"} ,
BaseStyle → FontSize → 16, PlotRange → {0, 0.8}, PlotStyle → {PointSize → Large, Red}] ;
(* 20 Late Data *)
dataglate = Take[datag, −20];
datag1late = Table[{dataglate[[i, 1]], dataglate[[i, 2]], dataglate[[i, 3]]}, {i, Length[dataglate]}];
pldataglate = ErrorListPlot [datag1late, Frame → True, FrameLabel → {z, "fσ8(z)"} ,
BaseStyle → FontSize → 16, PlotRange → {0, 0.8}, PlotStyle → {PointSize → Large, Orange}]
```

The commands `pldatag`, `pldatagearly` and `pldataglate` plot the full, the 20 earliest and the 20 latest RSD datapoints respectively. So, using the command `fσ8z` we can plot all the dashed lines of Fig. 2.2.

C.3 Maximum Likelihood Method for Growth Data

For the construction of (2.18) we need to define the vector V^i (2.19) as well as the correction factor $q\left(z, \Omega_{\mathrm{m},0}, \Omega_{\mathrm{m},0}^{fid_i}\right)$ denoted as `ratio`. Then, using the vector we construct the χ^2 function denoted as `chi2corr`

```
(* Support term for the Covariance Matrix of the WiggleZ Survey *)
Wigglez = {10, 11, 12};
Cijfs8 = DiagonalMatrix[datag[[All, 3]]^2];
Cijfs8[[Wigglez, Wigglez]] = Cijwigglez;
InvCijfs8 = Inverse[Cijfs8];

(* Corrections due to the Fiducial Cosmology *)
ratio1[z_, w_, om_, omfid_]:= (H[a, w, om]dLh[a, om, w]/H[a, −1, omfid]dLh[a, omfid, −1])^(−1)/.a → 1/(1 + z);

ratio2[z_, w_, om_, omfid_]:=1;
vecgr[data_, w_, om_, ga_, n_, σ8_]:=Table [data[[i, 2]] − ratio1[data[[i, 1]], w, om, data[[i, 4]]]
```

```
fσ8geff[1/(1+data[[i,1]]), om, w, ga, n, σ8], {i, 1, Length[data]}]
(* The χ^2 Function (2.18) *)
chi2corr[data_, w_, om_, ga_, n_, σ8_]:=vecgr[data, w, om, ga, n, σ8].InvCijfs8.vecgr[data, w, om,
ga,n,σ8]
```

Afterwards it is straightforward to apply the maximum likelihood method using the command `FindMinimum` and calculate the best fit values of the various parameters as follows

```
(* Minimization with respect to the Parameters Ω_{m,0} and σ_8 *)
mnoms8 = FindMinimum[chi2corr[datag, −1, om, 0, 1, σ8], {om, .3, .31}, {σ8, .8, .81}]
(* Minimization with respect to the Parameters w and Ω_{m,0} *)
mnomw = FindMinimum[chi2corr[datag, w, om, 0, 1, σ8pl], {w, −1, −1.1}, {om, .3, .31}]
(* Minimization with respect to the Parameters w and σ_8 *)
mnws8 = FindMinimum[chi2corr[datag, w, ompl, 0, 1, σ8], {w, −1, −1.1}, {σ8, .8, .81}]
```

C.4 Reproduction of Fig. 2.5

For the repoduction of the $1\sigma - 4\sigma$ confidence contours in the parametric space $(\Omega_{\mathrm{m},0} - \sigma_8)$ for $g_a = 0$, we need to use the command `ContourPlot` and construct the corresponding contours. For example, for the left panel of Fig. 2.5, we use the following Mathematica commands:

```
(* Convert the Δχ^2 in σ Differences *)
dchi[nsig_, M_]:=2InverseGammaRegularized[M/2, 1 − Erf[nsig/√2]]//N
cont1s4soms8full = ContourPlot[chi2corr[datag, −1, om, 0, 1, σ8], {om, 0.05, 0.7}, {σ8, 0.6, 1.3},
Contours → {mnoms8[[1]] + dchi[1, 2], mnoms8[[1]] + dchi[2, 2], mnoms8[[1]] + dchi[3, 2],
mnoms8[[1]] + dchi[4, 2]}, ContourShading → {Hue[0.6, .9, .9], Hue[0.6, .77, .9], Hue[0.6, .55, .9],
Hue[0.6, .1, .9], White}, ContourStyle → {Hue[0.6, .9, .9], Hue[0.6, .77, .9], Hue[0.6, .55, .9],
, Hue[0.6, .1, .9], White}]
```

Notice that we used the function `dchi` which converts the χ^2 functions in σ differences for the number of free parameters M. With similar commands one can construct the middle and right panel of Fig. 2.5, as well as Figs. 2.6 and 2.8.

C.5 Reproduction of Fig. 2.9

For the reproduction of Fig. 2.9 we need the `DateListPlot` command which plots points with values as sequence of dates. The use of this command is illustrated below:

```
(* Error Bar Evolution with Time *)
errortab = Table[datag[[i, 3]], {i, 1, Length[datag]}];
Mean[Take[errortab, 20]];
Mean[Take[errortab, -20]];
fig9a = DateListPlot [MovingAverage[errortab, 20], {{2013, 1, 1}, {2018, 1, 1}}, Frame → True,
FrameLabel → {"Time of Publication", "20 Pts Moving Average of fσ8 Error Bars"},
BaseStyle → {FontFamily → "Times", 18}, FrameStyle → Directive[Black], PlotRange → All,
PlotStyle → {PointSize → Large, Blue}, Joined → False, Axes → True, ImageSize → Large];
(* Redshift Evolution with Time *)
redshtab = Table[datag[[i, 1]], {i, 1, Length[datag]}];
Mean[Take[redshtab, 20]];
Mean[Take[redshtab, -20]];
fig9b = DateListPlot [MovingAverage[redshtab, 20], {{2013, 1, 1}, {2018, 1, 1}}, Frame → True,
FrameLabel → {"Time of Publication", "20 Pts Moving Average of fσ8 Redshift"},
BaseStyle → {FontFamily → "Times", 18}, FrameStyle → Directive[Black],
PlotRange → {All, {0.3, 0.8}}, PlotRange → All, PlotStyle → {PointSize → Large, Blue}];
fig8 = GraphicsGrid[{{fig9a, fig9b}}, Spacings → 0, ImageSize → 1300];
```

The `fig9a` corresponds to the left panel of Fig. 2.9, while `fig9b` corresponds to the right panel.

C.6 Reproduction of Fig. 2.12

For the reproduction of Fig. 2.12 we need to plot the best fit value of the parameter g_a along with its 1σ range for 20 point growth subsamples starting from the earliest to the latest subsample. As a first step we define an empty list which is denoted as `gtab` and apply the maximum likelihood method on each subsample appending the results on `gtab`. This is done using the following `Do` loop:

```
gtab = {};
Do[
datagen = Take[datag, {j, 19 + j}];
If[j ≥ 11,
Cijfs8 = DiagonalMatrix[datagen[[All, 3]]^2],
Wigglez = {10 + 1 - j, 11 + 1 - j, 12 + 1 - j};
Cijfs8 = DiagonalMatrix[datagen[[All, 3]]^2];
Cijfs8[[Wigglez, Wigglez]] = Cijwigglez];
InvCijfs8 = Inverse[Cijfs8];
mnga = FindMinimum[chi2corr[datagen, -1, ompl, ga, 2, σ8pl], {ga, 0, -0.1}];
gabf = mnga[[2, 1, 2]];
```

```
chimnga = mnga[[1]];
dga2 = FindRoot[chi2corr[datagen, −1, ompl, ga, 2, σ8pl] == chimnga + 1, {ga, gabf + 0.5}]
[[1, 2]] − gabf;
dga1 = FindRoot[chi2corr[datagen, −1, ompl, ga, 2, σ8pl] == chimnga + 1, {ga, gabf − 0.5}]
[[1, 2]] − gabf;
AppendTo[gtab, {gabf, dga1, dga2}], {j, 1, Length[datag] − 19}];
```

Then after the following list arrangements, the plot that shows the evolution of the best fit of g_a with time is publication is easily constructed:

```
gtaberr = Table[{{i, gtab[[i, 1]]}, ErrorBar[{gtab[[i, 2]], gtab[[i, 3]]}]}, {i, 1, Length[gtab]}];
d1 = First/@gtaberr; d4 = Table[i, {i, 2013, 2018, 0.114}];
d6 = Last/@gtaberr; d5 = Last/@d1;
d7 = Transpose[{d4, d5}]; d8 = Transpose[{d7, d6}];
figgaerrorplot = ErrorListPlot [d8, PlotRange → {All, {−1.7, 0.2}}, Frame → True,
PlotStyle → Blue, FrameLabel → {"Time of Publication", "g_a"} ,
BaseStyle → {FontFamily → "Times", 18}, FrameStyle → Directive[Black],
PlotStyle → {PointSize → Large, Blue}, ImageSize → Large];
Wigglez = {10, 11, 12};
Cijfs8 = DiagonalMatrix[datag[[All, 3]]^2];
Cijfs8[[Wigglez, Wigglez]] = Cijwigglez;
InvCijfs8 = Inverse[Cijfs8];
mnga = FindMinimum[chi2corr[datag, −1, ompl, ga, 2, σ8pl], {ga, 0, −0.1}];
gabffull = mnga[[2, 1, 2]];
chimngafull = mnga[[1]];
dga2full = FindRoot[chi2corr[datag, −1, ompl, ga, 2, σ8pl] == chimngafull + 1,
{ga, gabffull + 0.5}][[1, 2]] − gabffull;
dga1full = FindRoot[chi2corr[datag, −1, ompl, ga, 2, σ8pl] == chimngafull + 1,
{ga, gabffull − 0.5}][[1, 2]] − gabffull;
p1 = {{{2015.5, gabffull}, ErrorBar[{dga1full, dga2full}]}};
figgap1 = ErrorListPlot [p1, PlotRange → {All, {−1.7, 0.2}}, Frame → True, PlotMarkers →
{■, 15}, FrameLabel → {"Time of Publication", "g_a"} , BaseStyle → {FontFamily → "Times"
}, FrameStyle → Directive[Black], PlotStyle → {PointSize → Large, Red];
fig11 = Show[figgaerrorplot, figgap1]
```

Appendix D

Data Compilations of Chapter 3 and Numerical Algorithms

In this appendix we shortly present the basic commands that were used for the construction of the figures of Chapter 3. Moreover we present the data compilations used for the performed analysis. For a more extensive analysis regarding the corresponding code, visit the "Optimum-Redshift repository."

D.1 Data Used in the Analysis

Table D.1: The compilation of BAO data from 2009 to 2018, presented in Ref. [474].

Index	z	$D_A \times \left(r_s^{fid.}/r_s\right)$ (Mpc)	$H(z) \times \left(r_s/r_s^{fid.}\right)$ (km/sec Mpc)	$D_V \times \left(r_s^{fid.}/r_s\right)$ (Mpc)	Year	Ref.
1	0.275	-	-	1061.87 ± 29	02/11/2009	[616]
2	0.106	-	-	439.3 ± 19.6	16/06/2011	[547]
3	0.35	-	-	1356 ± 25	28/03/2012	[617]
4	0.44	-	-	1716 ± 83	28/07/2014	[489]
5	0.60	-	-	2221 ± 100	28/07/20144	[489]
6	0.73	-	-	2516 ± 86	28/07/2014	[489]
7	0.15	-	-	664 ± 25	21/01/2015	[548]
8	0.38	1100 ± 22	81.5 ± 2.6	1477 ± 16	11/07/2016	[45]
9	0.51	1309.3 ± 24.5	90.5 ± 2.7	1877 ± 19	11/07/2016	[45]
10	0.61	1418 ± 27.3	97.3 ± 2.9	2140 ± 22	11/07/2016	[45]
11	0.32	980.3 ± 15.9	78.4 ± 2.3	1270 ± 14	11/07/2016	[45]
12	0.57	1387.9 ± 22.3	96.6 ± 2.4	2033 ± 21	11/07/2016	[45]
13	0.31	931.42 ± 48	78.3 ± 4.7	1208.36 ± 33.81	06/12/2016	[618]
14	0.36	1047.04 ± 44	77.2 ± 5.7	1388.36 ± 55	06/12/2016	[618]
15	0.40	1131.34 ± 44	79.72 ± 4.9	1560.06 ± 40	06/12/2016	[618]
16	0.44	1188.78 ± 32	80.29 ± 3.4	1679.88 ± 35	06/12/2016	[618]
17	0.48	1271.43 ± 25.8	84.69 ± 3.4	1820.44 ± 39	06/12/2016	[618]
18	0.52	1336.53 ± 39	91.97 ± 7.5	1913.54 ± 47	06/12/2016	[618]
19	0.56	1385.47 ± 30.5	97.3 ± 7.9	2001.91 ± 51	06/12/2016	[618]
20	0.59	1423.43 ± 44	97.07 ± 5.8	2100.43 ± 48	06/12/2016	[618]
21	0.64	1448.81 ± 69	97.70 ± 4.8	2207.51 ± 55	06/12/2016	[618]
22	2.33	1669.7 ± 96.1	224 ± 8	-	27/03/2017	[486]
23	1.52	-	-	3843 ± 147	16/10/2017	[619]
24	0.81	1586.7 ± 63.5	-	-	17/12/2017	[620]
25	0.72	-	-	2353 ± 63	21/12/2017	[621]
26	1.52	1850 ± 110	162 ± 12	3985.2 ± 162.4	08/01/2018	[425]
27	0.978	1586.18 ± 284.93	113.72 ± 14.63	2933.59 ± 327.71	16/01/2018	[427]
28	1.230	1769.08 ± 159.67	131.44 ± 12.42	3522.04 ± 192.74	16/01/2018	[427]
29	1.526	1768.77 ± 96.59	148.11 ± 12.75	3954.31 ± 141.71	16/01/2018	[427]
30	1.944	1807.98 ± 146.46	172.63 ± 14.79	4575.17 ± 241.61	16/01/2018	[427]

Table D.2: The compilation of 41 $H(z)$ data presented in Ref. [622].

Index	z	$H(z)$ (km/sec Mpc)	σ_H	Reference
1	0.070	69	19.6	[623]
2	0.120	68.6	26.2	[623]
3	0.200	72.9	29.6	[623]
4	0.280	88.8	36.6	[623]
5	0.400	95	17	[624]
6	0.090	69	12	[624]
7	0.170	83	8	[624]
8	0.270	77	14	[624]
9	1.300	168	17	[624]
10	0.9	117	23	[624]
11	1.43	177	18	[624]
12	1.53	140	14	[624]
13	1.75	202	40	[624]
14	0.179	75	4	[43]
15	0.199	75	5	[43]
16	0.352	83	14	[43]
17	0.593	104	13	[43]
18	0.68	92	8	[43]
19	0.781	105	12	[43]
20	0.875	125	17	[43]
21	1.037	154	20	[43]
22	0.4004	77	10.02	[487]
23	0.4247	87.1	11.2	[487]
24	0.3802	83	13.5	[487]
25	0.4497	92.8	12.9	[487]
26	0.4783	80.9	9	[487]
27	1.363	160	22.6	[625]
28	1.965	186.5	50.4	[625]
29	0.440	82.6	7.8	[404]
30	0.6	87.9	6.1	[404]
31	0.73	97.3	7.0	[404]
32	0.240	79.69	6.65	[558]
33	0.430	86.45	3.68	[558]
34	0.300	81.7	6.22	[626]
35	0.350	82.7	8.4	[407]
36	0.480	97	62	[42]
37	0.88	90	40	[42]
38	0.570	92.900	7.855	[627]
39	2.300	224	8	[628]
40	2.34	222	7	[629]
41	2.36	226	8	[630]

Table D.3: The JLA binned data presented in Ref. [40].

Index	z	μ	σ_μ
1	0.01	32.9539	0.145886
2	0.012	33.879	0.167796
3	0.014	33.8421	0.0784989
4	0.016	34.1186	0.0723539
5	0.019	34.5934	0.0854606
6	0.023	34.939	0.0561251
7	0.026	35.2521	0.0610683
8	0.031	35.7485	0.0567639
9	0.037	36.0698	0.0567956
10	0.043	36.4346	0.0751431
11	0.051	36.6511	0.0929013
12	0.06	37.158	0.0620892
13	0.07	37.4302	0.0658793
14	0.082	37.9566	0.0546505
15	0.097	38.2533	0.0599337
16	0.114	38.6129	0.0374341
17	0.134	39.0679	0.0386141
18	0.158	39.3414	0.0346886
19	0.186	39.7921	0.0321403
20	0.218	40.1565	0.0329616
21	0.257	40.565	0.0317198
22	0.302	40.9053	0.0392622
23	0.355	41.4214	0.0335758
24	0.418	41.7909	0.0415207
25	0.491	42.2315	0.0393713
26	0.578	42.617	0.0359453
27	0.679	43.0527	0.0627778
28	0.799	43.5042	0.0545914
29	0.94	43.9726	0.0668276
30	1.105	44.5141	0.154604
31	1.3	44.8219	0.138452

D.2 Numerical Algorithms

D.2.1 Reproduction of Fig. 3.1

For the reproduction of Fig. 3.1 we use the same commands as in the previous appendix in order to construct Eq. (1.54) as well as to import the full compilation of Table 2.1. Then, we construct the deviations (3.1)-(3.3) through the following algorithm:

(∗ The deviation (3.1) for the Observable $f\sigma_8$ ∗)

pldfs8ga = Plot [Evaluate[Table[fσ8z[z, ompl, −1, ga, 2, σ8pl] − fσ8z[z, ompl, −1, 0, 2, σ8pl],

```
{ga, −1.5, 1.5, 0.6}]], {z, 0, 3}, Frame → True, FrameLabel → {z, "Δfσ8(z)"},
BaseStyle → FontSize → 16, PlotRange → All, Epilog → {Text["ga=1.5", {1.2, 0.05}],
Text["ga=-1.5", {1.3, −0.06}]}, ImageSize → 500];
(* Full Dataset *)
datag1 = Table[{datag[[i, 1]], datag[[i, 2]] − fσ8z[datag[[i, 1]], ompl, −1, 0, 2, σ8pl], datag[[i, 3]]},
{i, 1, Length[datag]}];
pldatag = ErrorListPlot[datag1, Frame → True, FrameLabel → {z, "Δfσ8(z)"}, PlotStyle →
{PointSize → Large, Blue}, ImageSize → Large];
datagearly = Take[datag1, 20];
(* 20 Early Data *)
pldatagearly = ErrorListPlot[datagearly, Frame → True, FrameLabel → {z, "Δfσ8(z)"},
PlotRange → {0, 0.8}, PlotStyle → {PointSize → Large, Red}, ImageSize → Large];
dataglate = Take[datag1, −20];
pldataglate = ErrorListPlot[dataglate, Frame → True, FrameLabel → {z, "Δfσ8(z)"},
PlotStyle → {PointSize → Large, Orange}, ImageSize → Large];
delfs8latga = Show[pldataglate, pldfs8ga, PlotRange → All, Epilog → {Text["ga=1.5",
{1.16, 0.06}], Text["ga=-1.5", {1.16, −0.073}]}, BaseStyle → {Large, FontFamily
→ "Times", 18}, LabelStyle → Directive[Black, Large], FrameStyle → Directive[Black, Thick]];
delfs8earlga = Show[pldatagearly, pldfs8ga, PlotRange → {−0.23, 0.13}, Epilog → {Text["ga
=1.5", {1.16, 0.06}], Text["ga=-1.5", {1.16, −0.073}]}, BaseStyle → {Large, FontFamily →
"Times", 18}, LabelStyle → Directive[Black, Large], FrameStyle → Directive[Black, Thick]];
delfs8fullga = Show[pldatag, pldfs8ga, PlotRange → {−0.23, 0.13}, Epilog → {Text["ga=1.5"
{1.17, 0.06}], Text["ga=-1.5", {1.17, −0.073}]}, BaseStyle → {Large, FontFamily → "Times"
, 18}, LabelStyle → Directive[Black, Large], FrameStyle → Directive[Black, Thick]];
delfs8ga = GraphicsGrid[{{delfs8earlga, delfs8latga, delfs8fullga}}, Spacings → 0];
```

Similar commands can be used for the reproduction of Figs. 3.2, 3.3 and 3.5.

D.2.2 Reproduction of Fig. 3.4

For the reproduction of Fig. 3.4 we use the definition (3.8) along with the theoretically predicted forms of (1.54) as follows:

```
gamin = 0; gamax = 0.1;
(* Plot of the Sensitivity Function (3.8) for the Observable fσ8 *)
pl1gaeff = Plot[((fσ8z[z, ompl, −1, gamax, 2, σ8pl] − fσ8z[z, ompl, −1, gamin, 2, σ8pl])
Veff[z, −1, 0.3]^(1/2))/((fσ8z[1.2, ompl, −1, gamax, 2, σ8pl] − fσ8z[1.2, ompl, −1, gamin, 2, σ8pl
])Veff[1.2, −1, 0.3]^(1/2)), {z, 0, 8}, Frame → True, FrameLabel → {z, "Δfσ8√Veff/Δga(z)"},
BaseStyle → FontSize → 16, PlotRange → All, Epilog → {Text["ga,min=0.0,ga,max=0.1", {4.5
, 0.5}, ]} ImageSize → 600];
```

```
wmin = −1; wmax = −0.9;
(* Plot of the Sensitivity Function (3.8) for the Observable w *)
pl1weff = Plot[((fσ8z[z, ompl, wmax, 0, 2, σ8pl] − fσ8z[z, ompl, wmin, 0, 2, σ8pl])Veff[z, −1,
0.3]^(1/2))/((fσ8z[0.8, ompl, wmax, 0, 2, σ8pl] − fσ8z[0.8, ompl, wmin, 0, 2, σ8pl])Veff[0.8, −1,
0.3]^(1/2)), {z, 0, 8}, Frame → True, FrameLabel → {z, "Δfσ8√Veff/Δw(z)"}, BaseStyle
→ FontSize → 16, PlotRange → All, Epilog → {Text ["wmin=-1.0,wmax=-0.9", {4.5, −0.5}]}];
omt = 0.30;
ommin = omt; ommax = omt + 0.01;
(* Plot of the Sensitivity Function (3.8) for the Observable Ωm,0 *)
pl1omeff = Plot[((fσ8z[z, ommax, −1, 0, 2, σ8pl] − fσ8z[z, ommin, −1, 0, 2, σ8pl])Veff[z, −1,
0.3]^(1/2))/((fσ8z[0.5, ommax, −1, 0, 2, σ8pl] − fσ8z[0.5, ommin, −1, 0, 2, σ8pl])Veff[0.5, −1
, 0.3]^(1/2)), {z, 0, 8}, Frame → True, FrameLabel → {z, "Δfσ8√Veff/ΔΩm(z)"}, BaseStyle
→ 16, PlotRange → All, Epilog → {Text ["Ωm,0 min=0.30,Ωm,0 max=0.31", {4.5, 0.5}]}];
sensstat = GraphicsGrid[{{pl1gaeff, pl1weff, pl1omeff}}, Spacings → 0, ImageSize → 1600];
```

D.2.3 Reproduction of Fig. 3.7

For the reproduction of Fig. 3.7 we need to introduce the theoretical formulas (3.11)-(3.18) as follows:

```
Tcmb = 2.7255;
c = 299792.458;
cH0 = 2997.92458;
w[a_, w0_, wa_, n_]:=w0 + wa(1 − a)^n
f[a_, w0_, wa_, n_]:=a^(−3(1+w0+wa)) e^(−3waHarmonicNumber[n]+3anwaHypergeometricPFQ[{1,1,1−n},{2,2},a])
zeq[om_?NumberQ, h_?NumberQ]:=2.5 * 10^4om h^2(Tcmb/2.7)^(−4);
aeq[om_?NumberQ, h_?NumberQ]:=1/(1 + zeq[om, h]);
H[a_?NumberQ, om_?NumberQ, w0_?NumberQ, wa_?NumberQ, n_?NumberQ, h_?NumberQ]:=
100hSqrt [a^(−3)om(1 + aeq[om, h]/a) + (1 − om(1 + aeq[om, h]))f[a, w0, wa, n]];
(* Equivalent Form of the Sound Speed (3.16) *)
cs[a_?NumberQ, obh2_?NumberQ]:=c / √(3 (1 + (31500obh2(Tcmb/2.7)^(−4)) a));
zcmb[om_?NumberQ, obh2_?NumberQ, h_?NumberQ]:=1048 (1 + 0.00124(obh2)^(−0.738))
(1 + (0.0783(obh2)^(−0.238))/(1 + 39.5(obh2)^0.763)) (om h^2)^(0.560/(1+21.1(obh2)^1.81));
(* Drag Redshift *)
zdrag[om_?NumberQ, obh2_?NumberQ, h_?NumberQ]:=1291 ((om h^2)^0.251)/(1 + 0.659(om h^2)^0.828) (1+
```

```
(0.313(omh^2)^-0.419 (1 + 0.607(omh^2)^0.674)) (obh2)^(0.238(omh^2)^0.223));
Clear[DLsol, DL, dL]
DLsol[om_?NumberQ, obh2_?NumberQ, w0_?NumberQ, wa_?NumberQ, n_?NumberQ,
h_?NumberQ]:= (DLsol[om, obh2, w0, wa, n, h] = NDSolve [{D [dL[zz]/(1 + zz), zz] == c /
H [1/(1 + zz), om, w0, wa, n, h] , dL[0] == 0}, dL, {zz, 0, 1300}, MaxSteps → Infinity])
DL[z_?NumberQ, om_?NumberQ, obh2_?NumberQ, w0_?NumberQ, wa_?NumberQ,
n_?NumberQ, h_?NumberQ]:=(dL[z]/.DLsol[om, obh2, w0, wa, n, h])[[1]]//Chop
DA[z_?NumberQ, om_?NumberQ, obh2_?NumberQ, w0_?NumberQ, wa_?NumberQ,
n_?NumberQ, h_?NumberQ]:=1/(1 + z)^2 DL[z, om, obh2, w0, wa, n, h];
(* Correction Factor *)
corrfact = 150.82/154.66;
(* Sound Horizon (3.17) Multiplied by the Correction Factor *)
rs[ze_, om_?NumberQ, obh2_?NumberQ, w0_?NumberQ, wa_?NumberQ, n_?NumberQ,
h_?NumberQ]:=NIntegrate [cs[x, obh2]/(x^2 H[x, om, w0, wa, n, h]), {x, 0, 1/(1 + ze[om, obh2, h])}] corrfact;
Dv[zbao_, om_?NumberQ, obh2_?NumberQ, w0_?NumberQ, wa_?NumberQ, n_?NumberQ,
h_?NumberQ]:= ((DL[zbao, om, obh2, w0, wa, n, h]/(1 + zbao)) ^2 c * zbao/(H [1/(1+zbao), om, w0, wa, n, h]))^(1/3);
dz[zbao_, om_, obh2_, w0_, wa_, n_, h_]:=rs[zdrag, om, obh2, w0, wa, n, h]/Dv[zbao, om, obh2, w0,
wa, n, h];
baoobs[z_, om_, w_]:=dz[z, om, obh2pl, w, 0, 2, h0pl]
```

Therefore using the above equations it is straightforward to derive the current BAO theoretical observables as

```
(* The Current BAO Theoretical Observables *)
baodv[z_, om_, w_]:=rs[zdrag, ompl, obh2pl, -1, 0, 2, h0pl]/dz[z, om, obh2pl, w, 0, 2, h0pl];
baoh[z_, om_, w_]:=H[1/(1 + z), ompl, w, 0, 2, h0pl]rs[zdrag, om, obh2pl, w, 0, 2, h0pl]/rs[zdrag,
ompl, obh2pl, -1, 0, 2, h0pl];
baoda[z_, om_, w_]:=DA[z, om, obh2pl, w, 0, 2, h0pl](rs[zdrag, ompl, obh2pl, -1, 0, 2, h0pl]/
rs[zdrag, om, obh2pl, w, 0, 2, h0pl]);
```

Furthermore, we import the BAO compilation presented in Table D.1 through the following commands

```
(* The Corresponding BAO Data of Table D.1 *)
baodvdat = {{0.978, 2933.59, 327.71}, {1.23, 3522.04, 192.74}, {1.526, 3954.31, 141.71},
{1.944, 4575, 241.61}, {1.52, 3985.2, 162.36}, {0.72, 2353, 62}, {0.35, 1356, 25},
```

```
{0.106, 439.3, 19.6}, {0.15, 664, 25}, {0.38, 1477, 16}, {0.51, 1877, 19}, {0.61, 2140, 22},
{0.32, 1270, 14}, {0.57, 2033, 21}, {0.44, 1716, 83}, {0.60, 2221, 100}, {0.73, 2516, 86},
{1.52, 3843, 147}, {0.31, 1208.36, 33.81}, {0.36, 1388.36, 55}, {0.4, 1560.06, 40},
{0.44, 1679.88, 35}, {0.48, 1820.44, 39}, {0.52, 1913.54, 47}, {0.56, 2001.91, 51},
{0.59, 2100.43, 48}, {0.64, 2207.51, 55}, {0.275, 1061.87, 29}};
baohdat = {{0.978, 113.72, 14.63}, {1.23, 131.44, 12.42}, {1.526, 148.11, 12.75},
{1.944, 172.63, 14.79}, {1.52, 162, 12}, {0.38, 81.5, 2.6}, {0.51, 90.5, 2.7}, {0.61, 97.3, 2.9},
{0.32, 78.4, 2.3}, {0.57, 96.6, 2.4}, {2.33, 224, 8}, {0.31, 78.3, 4.7}, {0.36, 77.2, 5.7},
{0.4, 79.72, 4.9}, {0.44, 80.29, 3.4}, {0.48, 84.69, 3.4}, {0.52, 91.97, 7.5}, {0.56, 97.3, 7.9},
{0.59, 97.07, 5.8}, {0.64, 97.7, 4.8}};
baodadat = {{0.978, 1586.18, 284.93}, {1.23, 1769.08, 159.67}, {1.526, 1768.77, 96.59},
{1.944, 1807.98, 146.46}, {1.52, 1850, 110}, {0.38, 1100, 22.4}, {0.51, 1309.3, 24.5},
{0.61, 1418, 27.3}, {0.32, 980.3, 15.9}, {0.57, 1387.9, 22.3}, {2.33, 1669.7, 96.1},
{0.31, 931.42, 48}, {0.36, 1047.04, 44}, {0.4, 1131.34, 44}, {0.44, 1188, 78, 32},
{0.48, 1271.43, 25.8}, {0.52, 1336.53, 39}, {0.56, 1385.47, 30.5}, {0.59, 1423.43, 44},
{0.64, 1448.81, 69}, {0.81, 1586.7, 63.5}};
```

Now we are ready to construct Fig. 3.7 with a similar algorith as for the observable for the $f\sigma_8(z)$ observable. For the $D_V \times \left(r_s^{fid.}/r_s\right)$ observable we write the following commands

```
omt = 0.30;
plbaodv = Plot [Evaluate[Table[baodv[z, om, -1] - baodv[z, omt, -1], {om, omt - 0.05,
omt + 0.05, 0.02}]], {z, 0.1, 5}, Frame → True, FrameLabel → {z, "ΔD_V(z)(r_s^fid/r_s)"} ,
BaseStyle → {Large, FontFamily → "Times", 18}, LabelStyle → Directive[Black, Large],
, FrameStyle → Directive[Black, Thick], PlotRange → All, Epilog → {Text ["Ω_m,0=0.25",
{0.5, -40}] , Text ["Ω_m,0=0.35", {0.5, 40}]}] ;
baodvdat1 = Table[{baodvdat[[i, 1]], baodvdat[[i, 2]] - baodv[baodvdat[[i, 1]], omt, -1],
baodvdat[[i, 3]]}, {i, 1, Length[baodvdat]}];
plbaodvdat1 = ErrorListPlot [baodvdat1, Frame → True, FrameLabel → {z,
"ΔD_V(z)(r_s^fid/r_s) [Mpc]"} , BaseStyle → FontSize → 16, PlotStyle → {PointSize → Large,
Blue}, ImageSize → Large] ;
dvom = Show [plbaodvdat1, plbaodv, PlotRange → {{0.1, 3}, {-200, 300}}, Epilog → {Text
["Ω_m,0=0.25", {2.5, 95}] , Text ["Ω_m,0=0.35", {2.5, -83}]} , BaseStyle → {Large, FontFamily →
"Times", 18}, LabelStyle → Directive[Black, Large], FrameStyle → Directive[Black, Thick]]
plbaodvw = Plot [Evaluate[Table[baodv[z, ompl, w] - baodv[z, ompl, -1], {w, -1.5, -0.5, 0.2}]]
, {z, 0.1, 5}, Frame → True, FrameLabel → {z, "(z)(r_s^fid/r_s) [Mpc]"} , BaseStyle → {Large,
FontFamily → "Times", 18}, LabelStyle → Directive[Black, Large], FrameStyle →
Directive[Black, Thick], PlotRange → All, Epilog → {Text["w=-1.5", {0.70, 230}],
Text["w=-0.5", {0.5, -400}]}];
dvw = Show[plbaodvdat1, plbaodvw, PlotRange → {{0.1, 3}, {-400, 400}}, Epilog →
```

```
{Text["w=-1.5", {0.70, 247}], Text["w=-0.5", {0.5, −280}]}, BaseStyle → {Large, FontFamily
→ "Times", 18}, LabelStyle → Directive[Black, Large], FrameStyle → Directive[Black, Thick]]
dvfig = GraphicsGrid[{{dvw, dvom}}, Spacings → 0, ImageSize → 1200]
```

D.2.4 Maximum Likelihood Method for BAO Data

Armed with the algorithms presented in the previous subsection it is straightforward to construct the relevant χ^2 function for the BAO data (3.21). In particular, we present the appropriate commands for the construction of the χ^2 function for the $D_V \times \left(r_s^{fid.}/r_s\right)$ compilation (similar commands can be used for the other two observables). But first we need to import the subcovariance matrix of the WiggleZ survey, recalling that the fisher matrix F_{ij} is the inverse of the covariance matrix C_{ij}, as

```
(* The Fisher Matrix of the WiggleZ Survey *)
FijbaodvWiggleZ = 10^-4 * {{2.17898878, −1.11633, 0.46982}, {−1.11633, 1.70712, −0.71847}, {0.46982, −0.71847, 1.65283}};
Cijbaodvwiggle = Inverse[FijbaodvWiggleZ];
WiggleZ = {15, 16, 17};
Cijbao = DiagonalMatrix[baodvdat[[All, 3]]^2];
Cijbao[[WiggleZ, WiggleZ]] = Cijbaodvwiggle;
(* Total Inverse Covariance Matrix *)
InvCijbao = Inverse[Cijbao];
Cijbao//MatrixForm;
(* The χ^2 Function (3.21) *)
vecbao[data_, om_, w_]:=Table[(data[[i, 2]] − baodv[data[[i, 1]], om, w]),
{i, 1, Length[data]}];
chi2bao[data_, om_, w_]:=vecbao[data, om, w].InvCijbao.vecbao[data, om, w]
```

Then, we apply the maximum likelihood method as usual using the command `FindMinimum` and derive the best fit values through

```
chi2minbaodvfull = FindMinimum[chi2bao[baodvdat, om, w], {om, .3, .31}, {w, −1, −1.1}]
```

For the construction of the $1\sigma - 3\sigma$ confidence contours in the parametric space $\Omega_{\rm m,0} - w$ that are demonstrated in Fig. 3.11 (left panel), we utilize the command `ContourPlot` as

```
contourfullbaodv = ContourPlot[chi2bao[baodvdat, om, w], {om, 0.1, 0.55}, {w, −1.35, −0.55},
Contours → {chi2minbaodvfull[[1]] + dchi[1, 2], chi2minbaodvfull[[1]] + dchi[2, 2],
chi2minbaodvfull[[1]] + dchi[3, 2]}, ContourShading → {Hue[0.6, .9, .9], Hue[0.6, .5, .9],
Hue[0.6, .2, .9], White}, ContourStyle → {Hue[0.6, .9, .9], Hue[0.6, .5, .9], Hue[0.6, .2, .9], White}]
contfullbaodv = Show [contourfullbaodv, FrameLabel → {"Ω_{m,0}", w} , PlotRange →
{{0.1, 0.55}, {−1.35, −0.55}}, PlotRangeClipping → True, BaseStyle → {FontFamily →,
```

"Times", 18}, Epilog → {{Dashed, Line[{{ompl, −2}, {ompl, 1}}]}, {Dashed, Line[{{0, −1}, {1, −1}}]}, {PointSize[Large], Red, Point[{ompl, −1}]}, {PointSize[Large], Green, Point[{chi2minbaodvfull[[2, 1, 2]], chi2minbaodvfull[[2, 2, 2]]}]}, Text["Best-fit for Full Dataset" , {0.35, −0.72}]}, FrameStyle → Directive[Black], ImageSize → Medium]

For the middle and right panel of Fig. 3.11 we present same confidence contours for low redshift $D_V \times \left(r_s^{fid.}/r_s\right)$ (with $z < 0.55$) and high redshift $D_V \times \left(r_s^{fid.}/r_s\right)$ (with $z > 0.55$). This is done using the `Select` command through the following:

lowzbaodv = Select[Sort[baodvdat, #1[[1]] < #2[[1]]&], #[[1]] < 0.55&];
highzbaodv = Select[Sort[baodvdat, #1[[1]] < #2[[1]]&], #[[1]] > 0.55&];

With similar commands one can recreate the rest of the figures of Chapter 3.

Appendix E

Analysis of the Transition Dark Energy Models Incorporating the H_0 Measurement

In this appendix we discuss the impact of including the measurement of $H_0 = 73.2 \pm 1.3\ \mathrm{km\,s^{-1}\,Mpc^{-1}}$ [518] on the different dark energy models discussed in Chapter 5 instead of the local gaussian prior of the absolute magnitude $M_c = -19.244 \pm 0.037$ mag. This task is performed in order to reveal that despite the strong constraining nature of the SH0ES measurement it is more appropriate to adopt the local prior on M due to the following reasons [541]:

- Including the H_0 prior leads to a double counting of low redshift SnIa. As we described in Chapter 5 for the determination of the H_0 value the SnIa in the redshift range $0.023 < z < 0.15$ is used. Therefore, when the SnIa dataset is used to constrain the cosmological parameters of each model, the same data are taken into account in the minimization process leading to a double counting.

- For the determination of the H_0 value, since we focus on low redshifts, a Taylor expansion is performed and an extrapolation method is used for q_0 and j_0 constant to their ΛCDM value. However, this cosmographic analysis may fail for particular dark energy models that include sudden transitions such as the LMT and $LwMT$ giving wrong values of the parameters.

- For the determination of H_0, the statistical information on M is included.

Moreover as will show below the obtained absolute magnitude M for smooth $H(z)$ deformation models are inconsistent with the measured Cepheid absolute magnitude $M_c = -19.244 \pm 0.037$ mag.

Repeating the MCMC analysis described in Chapter 5 and using the same likelihoods along with the SH0ES gaussian prior on H_0 we find the best fit values of the cosmological parameters that are illustrated in Table E.1. As we can clearly see all the considered models except the transition ones LMT and $LwMT$ produce a significantly lower value for M compared to M_c. This can also be seen if we plot (Fig. E.1) the absolute magnitude M as a function of redshift and superimpose the binned Pantheon data for all the considered models. Of course for the smooth deformation models the absolute magnitude is constant. More specifically, the wCDM and CPL models give a H_0 best fit value that is inconsistent with the SH0ES measurement [518] at more than 2.4σ, in contrast to the PEDE dark energy model that gives a value consistent

Parameters	ΛCDM	wCDM	CPL	$LwMT$ ($z_t \geq 0.01$)	PEDE	LMT ($z_t = 0.01$)
$\Omega_{\rm m,0}$	$0.3022^{+0.0050}_{-0.0052}$	$0.2967^{+0.0067}_{-0.0064}$	$0.2951^{+0.0063}_{-0.0067}$	$0.2989^{+0.0055}_{-0.0060}$	0.281 ± 0.005	$0.3021^{+0.0053}_{-0.0052}$
n_s	0.9705 ± 0.0037	0.9684 ± 0.004	0.9668 ± 0.0040	0.9706 ± 0.0037	$0.9621^{+0.0036}_{-0.0034}$	0.9705 ± 0.0038
H_0	68.36 ± 0.4	$69.17^{+0.65}_{-0.76}$	69.50 ± 0.71	68.71 ± 0.5	$71.69^{+0.45}_{-0.46}$	$68.36^{+0.40}_{-0.41}$
σ_8	$0.8075^{+0.0058}_{-0.0064}$	$0.8183^{+0.0089}_{-0.01}$	0.8258 ± 0.0099	0.8098 ± 0.0064	$0.8531^{0.0064}_{-0.0058}$	$0.8086^{+0.0058}_{-0.0064}$
M	-19.40 ± 0.01	-19.38 ± 0.02	$-19.37^{+0.017}_{-0.018}$	-19.24	-19.34 ± 0.01	-19.24
ΔM	-	-	-	-0.1652 ± 0.011	-	-0.159 ± 0.011
$M_> \equiv M_c + \Delta M$	-	-	-	-19.405 ± 0.011	-	-19.40 ± 0.011
Δw	-	-	-	> -0.7	-	-
a_t	-	-	-	> 0.98	-	-
w_0	-	$-1.038^{+0.031}_{-0.018}$	$-0.9576^{+0.075}_{-0.078}$	-	-	-
w_a	-	-	$-0.38^{+0.32}_{-0.27}$	-	-	-
χ^2	3849	3846	3845	3846	3862	3850
$\Delta\chi^2$	-	-3	-4	-3	$+13$	$+1$

Table E.1: The 1σ constrains of the parameters for all dark energy models in question when the SH0ES gaussian prior $H_0 = 73.2 \pm 1.3$ km s^{-1} Mpc^{-1} is imposed, using the CMB+BAO+Pantheon+RSD likelihoods.

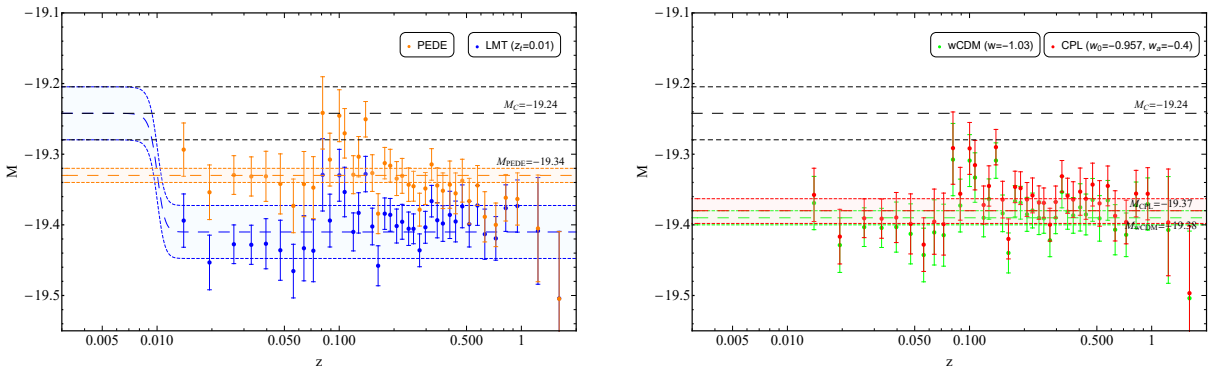

Figure E.1: The best fit absolute magnitude M of the binned Pantheon data as a function of the redshift z. In the left panel we show the corresponding best fit data for the LMT model with $z_t = 0.01$ (blue points) and PEDE models (orange points). In the right panel we show the corresponding best fit data for the $wCDM$ model with $w = -1.03$ (green points) and CPL models (red points). From Ref. [536].

with the SH0ES measurement at the 1σ level in agreement with previous studies. Conclusively, although in this case the majority of dark energy models (except PEDE and LMT) display a better quality of fit to the data than that of ΛCDM (cyan row of Table E.1), they fail to give an M value consistent with the M_c measurement that lies in the core of the H_0 problem. For consistency we also show the $1\sigma - 2\sigma$ confidence contours in Fig. E.2.

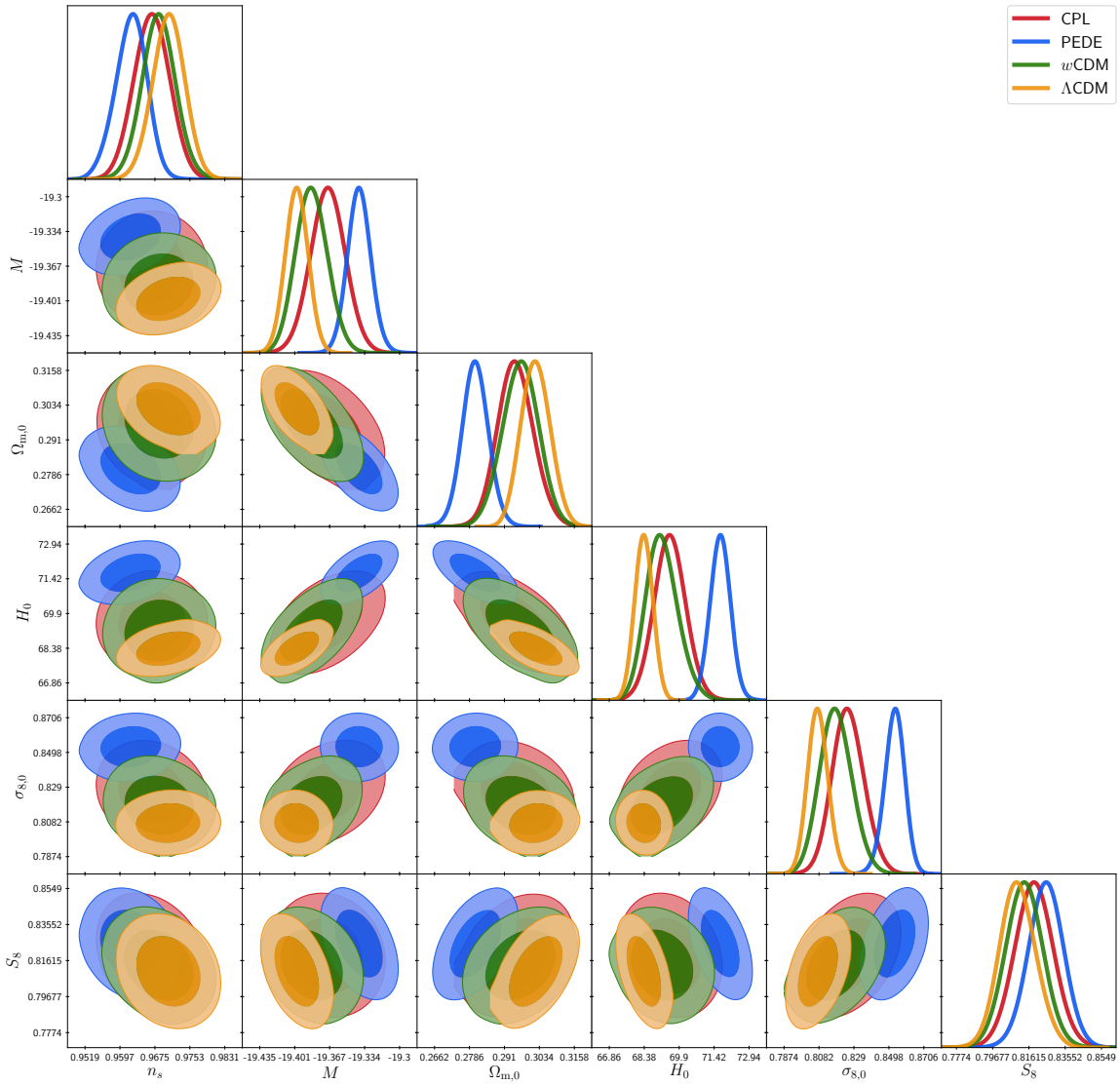

Figure E.2: The $1\sigma-2\sigma$ confidence contours for the common parameters of the ΛCDM, wCDM, CPL and PEDE dark energy model corresponding to the constraints of Table E.1, imposing the SH0ES gaussian prior on $H_0 = 73.2 \pm 1.3$ km s^{-1} Mpc^{-1}. In this plot $\sigma_{8,0} \equiv \sigma_8$. From Ref. [536].

Appendix F

Washington Experiment Data

In this appendix we present the data of the Washington experiment that were used for the analysis of Chapter 6. In particular, in Table F.1 we present the distance between the attractor and the detector in mm denoted as r, the torque residuals δ_τ along with their corresponding 1σ values as well as the different setups using different thickness for the attractor, denoted as Experiments I, II and III respectively.

Table F.1: The torque residuals used for the maximum likelihood method of Chapter 6 presented in Ref. [566].

r (mm)	$\delta_\tau \equiv \tau - \tau_N$ (f N $\cdot$ m)	1σ Errors of δ_τ	Experiment
0.062	0.039	0.036	I
0.065	0.036	0.023	I
0.067	-0.008	0.014	I
0.068	-0.007	0.006	I
0.07	-0.018	0.012	I
0.073	-0.002	0.01	I
0.077	0.032	0.014	I
0.084	0.009	0.007	I
0.095	0.005	0.006	I
0.106	-0.004	0.008	I
0.114	-0.006	0.005	I
0.146	-0.001	0.006	I
0.237	0.002	0.006	I
0.379	0.007	0.006	I
0.577	-0.007	0.003	I
0.915	0.	0.007	I
1.301	0.003	0.005	I
1.995	0.004	0.006	I
3.021	0.008	0.006	I
4.027	0.	0.005	I
5.04	0.001	0.004	I
8.512	0.001	0.004	I
0.065	0.012	0.018	II

0.067	0.016	0.027	II
0.069	0.029	0.035	II
0.069	-0.021	0.015	II
0.072	0.014	0.012	II
0.075	0.009	0.02	II
0.079	0.01	0.014	II
0.082	-0.023	0.01	II
0.085	0.011	0.029	II
0.087	0.011	0.017	II
0.089	-0.002	0.009	II
0.091	0.012	0.014	II
0.095	0.001	0.01	II
0.095	0.001	0.007	II
0.099	0.004	0.007	II
0.106	-0.002	0.007	II
0.122	0.	0.004	II
0.132	0.006	0.008	II
0.145	0.005	0.009	II
0.179	-0.003	0.005	II
0.222	-0.006	0.007	II
0.274	0.002	0.005	II
0.322	-0.001	0.006	II
0.531	0.011	0.006	II
1.024	0.007	0.005	II
1.221	0.005	0.005	II
2.014	0.001	0.005	II
3.021	0.002	0.003	II
4.014	-0.002	0.005	II
4.983	0.004	0.004	II
5.981	-0.005	0.006	II
8.054	0.007	0.006	II
0.057	0.075	0.05	III
0.06	0.035	0.036	III
0.06	0.013	0.028	III
0.061	0.006	0.03	III
0.064	0.016	0.026	III
0.064	-0.021	0.043	III
0.065	-0.016	0.019	III
0.069	0.004	0.014	III
0.07	0.012	0.023	III
0.07	0.025	0.023	III
0.072	-0.023	0.02	III
0.076	-0.014	0.016	III
0.081	0.009	0.011	III
0.085	-0.005	0.011	III
0.098	-0.006	0.01	III

0.116	0.002	0.007	III
0.131	-0.022	0.01	III
0.151	0.013	0.007	III
0.162	0.005	0.007	III
0.176	-0.007	0.006	III
0.205	-0.004	0.005	III
0.23	-0.004	0.007	III
0.322	-0.002	0.005	III
0.548	0.	0.009	III
0.777	-0.004	0.005	III
1.044	-0.006	0.007	III
1.168	-0.013	0.005	III
1.958	-0.002	0.005	III
2.423	-0.01	0.006	III
2.957	0.01	0.006	III
3.784	-0.005	0.006	III
4.993	0.002	0.006	III
6.416	-0.002	0.005	III

Bibliography

[1] A. Einstein, "Erklärung der Perihelbewegung des Merkur aus der allgemeinen Relativitätstheorie," *Sitzungsberichte der Königlich Preußischen Akademie der Wissenschaften (Berlin* (Jan., 1915) 831–839.

[2] F. W. Dyson, A. S. Eddington, and C. Davidson, "A Determination of the Deflection of Light by the Sun's Gravitational Field, from Observations Made at the Total Eclipse of May 29, 1919," *Philosophical Transactions of the Royal Society of London Series A* **220** (Jan., 1920) 291–333.

[3] S. W. Hawking, "Black holes in general relativity," *Commun. Math. Phys.* **25** (1972) 152–166.

[4] J. M. Bardeen, B. Carter, and S. W. Hawking, "The Four laws of black hole mechanics," *Commun. Math. Phys.* **31** (1973) 161–170.

[5] S. W. Hawking, "Black Holes and Thermodynamics," *Phys. Rev. D* **13** (1976) 191–197.

[6] R. Penrose, "Gravitational collapse: The role of general relativity," *Riv. Nuovo Cim.* **1** (1969) 252–276.

[7] R. Penrose, "Gravitational collapse and space-time singularities," *Phys. Rev. Lett.* **14** (1965) 57–59.

[8] **Event Horizon Telescope** Collaboration, K. Akiyama *et al.*, "First M87 Event Horizon Telescope Results. I. The Shadow of the Supermassive Black Hole," *Astrophys. J. Lett.* **875** (2019) L1, arXiv:1906.11238 [astro-ph.GA].

[9] **LIGO Scientific, Virgo** Collaboration, B. P. Abbott *et al.*, "Observation of Gravitational Waves from a Binary Black Hole Merger," *Phys. Rev. Lett.* **116** no. 6, (2016) 061102, arXiv:1602.03837 [gr-qc].

[10] **LIGO Scientific, Virgo** Collaboration, B. P. Abbott *et al.*, "GW170817: Observation of Gravitational Waves from a Binary Neutron Star Inspiral," *Phys. Rev. Lett.* **119** no. 16, (2017) 161101, arXiv:1710.05832 [gr-qc].

[11] **LIGO Scientific, KAGRA, VIRGO** Collaboration, R. Abbott *et al.*, "Observation of Gravitational Waves from Two Neutron Star–Black Hole Coalescences," *Astrophys. J. Lett.* **915** no. 1, (2021) L5, arXiv:2106.15163 [astro-ph.HE].

[12] G. Gamow, "Expanding universe and the origin of elements," *Phys. Rev.* **70** (Oct, 1946) 572–573. https://link.aps.org/doi/10.1103/PhysRev.70.572.2.

[13] R. A. Alpher, H. Bethe, and G. Gamow, "The origin of chemical elements," *Phys. Rev.* **73** (Apr, 1948) 803–804. https://link.aps.org/doi/10.1103/PhysRev.73.803.

[14] B. Ratra, M. S. Vogeley, and M. S. Vogeley, "The Beginning and Evolution of the Universe," *Publ. Astron. Soc. Pac.* **120** (2008) 235–265, arXiv:0706.1565 [astro-ph].

[15] D. Clowe, A. Gonzalez, and M. Markevitch, "Weak lensing mass reconstruction of the interacting cluster 1E0657-558: Direct evidence for the existence of dark matter," *Astrophys. J.* **604** (2004) 596–603, arXiv:astro-ph/0312273.

[16] D. Clowe, M. Bradac, A. H. Gonzalez, M. Markevitch, S. W. Randall, C. Jones, and D. Zaritsky, "A direct empirical proof of the existence of dark matter," *Astrophys. J. Lett.* **648** (2006) L109–L113, arXiv:astro-ph/0608407.

[17] **Planck** Collaboration, P. A. R. Ade *et al.*, "Planck 2015 results. XIII. Cosmological parameters," *Astron. Astrophys.* **594** (2016) A13, arXiv:1502.01589 [astro-ph.CO].

[18] **Planck** Collaboration, N. Aghanim *et al.*, "Planck 2018 results. VI. Cosmological parameters," *Astron. Astrophys.* **641** (2020) A6, arXiv:1807.06209 [astro-ph.CO].

[19] G. Steigman and M. S. Turner, "Cosmological Constraints on the Properties of Weakly Interacting Massive Particles," *Nucl. Phys. B* **253** (1985) 375–386.

[20] G. Bertone, "The moment of truth for WIMP Dark Matter," *Nature* **468** (2010) 389–393, arXiv:1011.3532 [astro-ph.CO].

[21] K. Griest, "Galactic Microlensing as a Method of Detecting Massive Compact Halo Objects," *Astrophys. J.* **366** (1991) 412–421.

[22] **MACHO** Collaboration, C. Alcock *et al.*, "The MACHO project: Microlensing results from 5.7 years of LMC observations," *Astrophys. J.* **542** (2000) 281–307, arXiv:astro-ph/0001272.

[23] B. J. Carr and S. W. Hawking, "Black holes in the early Universe," *Mon. Not. Roy. Astron. Soc.* **168** (1974) 399–415.

[24] B. Carr and F. Kuhnel, "Primordial Black Holes as Dark Matter: Recent Developments," *Ann. Rev. Nucl. Part. Sci.* **70** (2020) 355–394, arXiv:2006.02838 [astro-ph.CO].

[25] A. M. Green and B. J. Kavanagh, "Primordial Black Holes as a dark matter candidate," *J. Phys. G* **48** no. 4, (2021) 4, arXiv:2007.10722 [astro-ph.CO].

[26] I. Dalianis, A. Kehagias, and G. Tringas, "Primordial black holes from α-attractors," *JCAP* **01** (2019) 037, arXiv:1805.09483 [astro-ph.CO].

[27] M. Dine, W. Fischler, and M. Srednicki, "A Simple Solution to the Strong CP Problem with a Harmless Axion," *Phys. Lett. B* **104** (1981) 199–202.

[28] R. D. Peccei, "The Strong CP problem and axions," *Lect. Notes Phys.* **741** (2008) 3–17, arXiv:hep-ph/0607268.

[29] L. Bergstrom, "Dark Matter Candidates," *New J. Phys.* **11** (2009) 105006, arXiv:0903.4849 [hep-ph].

[30] H. Goldberg and L. J. Hall, "A New Candidate for Dark Matter," *Phys. Lett. B* **174** (1986) 151.

[31] Y. Hochberg, E. Kuflik, T. Volansky, and J. G. Wacker, "Mechanism for Thermal Relic Dark Matter of Strongly Interacting Massive Particles," *Phys. Rev. Lett.* **113** (2014) 171301, arXiv:1402.5143 [hep-ph].

[32] S. M. Carroll, "The Cosmological constant," *Living Rev. Rel.* **4** (2001) 1, arXiv:astro-ph/0004075.

[33] A. Einstein, "Kosmologische Betrachtungen zur allgemeinen Relativitätstheorie," *Sitzungsberichte der Königlich Preußischen Akademie der Wissenschaften (Berlin* (Jan., 1917) 142–152.

[34] G. Lemaître, "Un Univers homogène de masse constante et de rayon croissant rendant compte de la vitesse radiale des nébuleuses extra-galactiques," *Annales de la Société Scientifique de Bruxelles* **47** (Jan., 1927) 49–59.

[35] A. S. Eddington, "On the Instability of Einstein's Spherical World," *Mon. Not. Roy. Astron. Soc.* **90** (1930) 668–678.

[36] E. Hubble, "A relation between distance and radial velocity among extra-galactic nebulae," *Proc. Nat. Acad. Sci.* **15** (1929) 168–173.

[37] **Supernova Cosmology Project** Collaboration, S. Perlmutter *et al.*, "Measurements of Ω and Λ from 42 high redshift supernovae," *Astrophys. J.* **517** (1999) 565–586, arXiv:astro-ph/9812133.

[38] **Supernova Search Team** Collaboration, A. G. Riess *et al.*, "Observational evidence from supernovae for an accelerating universe and a cosmological constant," *Astron. J.* **116** (1998) 1009–1038, arXiv:astro-ph/9805201.

[39] **WMAP** Collaboration, G. Hinshaw *et al.*, "Nine-Year Wilkinson Microwave Anisotropy Probe (WMAP) Observations: Cosmological Parameter Results," *Astrophys. J. Suppl.* **208** (2013) 19, arXiv:1212.5226 [astro-ph.CO].

[40] **SDSS** Collaboration, M. Betoule *et al.*, "Improved cosmological constraints from a joint analysis of the SDSS-II and SNLS supernova samples," *Astron. Astrophys.* **568** (2014) A22, arXiv:1401.4064 [astro-ph.CO].

[41] D. M. Scolnic *et al.*, "The Complete Light-curve Sample of Spectroscopically Confirmed SNe Ia from Pan-STARRS1 and Cosmological Constraints from the Combined Pantheon Sample," *Astrophys. J.* **859** no. 2, (2018) 101, arXiv:1710.00845 [astro-ph.CO].

[42] D. Stern, R. Jimenez, L. Verde, M. Kamionkowski, and S. A. Stanford, "Cosmic Chronometers: Constraining the Equation of State of Dark Energy. I: H(z) Measurements," *JCAP* **02** (2010) 008, arXiv:0907.3149 [astro-ph.CO].

[43] M. Moresco *et al.*, "Improved constraints on the expansion rate of the Universe up to z˜1.1 from the spectroscopic evolution of cosmic chronometers," *JCAP* **08** (2012) 006, arXiv:1201.3609 [astro-ph.CO].

[44] A. Gómez-Valent and L. Amendola, "H_0 from cosmic chronometers and Type Ia supernovae, with Gaussian Processes and the novel Weighted Polynomial Regression method," *JCAP* **04** (2018) 051, arXiv:1802.01505 [astro-ph.CO].

[45] **BOSS** Collaboration, S. Alam *et al.*, "The clustering of galaxies in the completed SDSS-III Baryon Oscillation Spectroscopic Survey: cosmological analysis of the DR12 galaxy sample," *Mon. Not. Roy. Astron. Soc.* **470** no. 3, (2017) 2617–2652, arXiv:1607.03155 [astro-ph.CO].

[46] E. Aubourg *et al.*, "Cosmological implications of baryon acoustic oscillation measurements," *Phys. Rev. D* **92** no. 12, (2015) 123516, arXiv:1411.1074 [astro-ph.CO].

[47] S. Basilakos and S. Nesseris, "Testing Einstein's gravity and dark energy with growth of matter perturbations: Indications for new physics?," *Phys. Rev. D* **94** no. 12, (2016) 123525, arXiv:1610.00160 [astro-ph.CO].

[48] A. Quelle and A. L. Maroto, "On the tension between growth rate and CMB data," *Eur. Phys. J. C* **80** no. 5, (2020) 369, arXiv:1908.00900 [astro-ph.CO].

[49] E. Baxter *et al.*, "Joint measurement of lensing–galaxy correlations using SPT and DES SV data," *Mon. Not. Roy. Astron. Soc.* **461** no. 4, (2016) 4099–4114, arXiv:1602.07384 [astro-ph.CO].

[50] G. Efstathiou and P. Lemos, "Statistical inconsistencies in the KiDS-450 data set," *Mon. Not. Roy. Astron. Soc.* **476** no. 1, (2018) 151–157, arXiv:1707.00483 [astro-ph.CO].

[51] D. Rapetti, S. W. Allen, A. Mantz, and H. Ebeling, "Constraints on modified gravity from the observed X-ray luminosity function of galaxy clusters," *Mon. Not. Roy. Astron. Soc.* **400** (2009) 699, arXiv:0812.2259 [astro-ph].

[52] **DSDD** Collaboration, E. Rozo *et al.*, "Cosmological Constraints from the SDSS maxBCG Cluster Catalog," *Astrophys. J.* **708** (2010) 645–660, arXiv:0902.3702 [astro-ph.CO].

[53] **Planck** Collaboration, P. A. R. Ade *et al.*, "Planck 2015 results. XXIV. Cosmology from Sunyaev-Zeldovich cluster counts," *Astron. Astrophys.* **594** (2016) A24, arXiv:1502.01597 [astro-ph.CO].

[54] L. Salvati, M. Douspis, and N. Aghanim, "Constraints from thermal Sunyaev-Zel'dovich cluster counts and power spectrum combined with CMB," *Astron. Astrophys.* **614** (2018) A13, arXiv:1708.00697 [astro-ph.CO].

[55] **DES** Collaboration, M. Costanzi *et al.*, "Methods for cluster cosmology and application to the SDSS in preparation for DES Year 1 release," *Mon. Not. Roy. Astron. Soc.* **488** no. 4, (2019) 4779–4800, arXiv:1810.09456 [astro-ph.CO].

[56] S. Weinberg, "The Cosmological Constant Problem," *Rev. Mod. Phys.* **61** (1989) 1–23.

[57] J. Martin, "Everything You Always Wanted To Know About The Cosmological Constant Problem (But Were Afraid To Ask)," *Comptes Rendus Physique* **13** (2012) 566–665, arXiv:1205.3365 [astro-ph.CO].

[58] V. Sahni, "The Cosmological constant problem and quintessence," *Class. Quant. Grav.* **19** (2002) 3435–3448, arXiv:astro-ph/0202076.

[59] M. Trodden and S. M. Carroll, "TASI lectures: Introduction to cosmology," in *Theoretical Advanced Study Institute in Elementary Particle Physics (TASI 2002): Particle Physics and Cosmology: The Quest for Physics Beyond the Standard Model(s)*, pp. 703–793. 1, 2004. arXiv:astro-ph/0401547.

[60] E. J. Copeland, M. Sami, and S. Tsujikawa, "Dynamics of dark energy," *Int. J. Mod. Phys. D* **15** (2006) 1753–1936, arXiv:hep-th/0603057.

[61] S. P.J, *Critical Problems in Physics*. Princeton University Press, 1997.

[62] H. E. S. Velten, R. F. vom Marttens, and W. Zimdahl, "Aspects of the cosmological "coincidence problem"," *Eur. Phys. J. C* **74** no. 11, (2014) 3160, arXiv:1410.2509 [astro-ph.CO].

[63] A. G. Riess *et al.*, "A Comprehensive Measurement of the Local Value of the Hubble Constant with 1 km/s/Mpc Uncertainty from the Hubble Space Telescope and the SH0ES Team," arXiv:2112.04510 [astro-ph.CO].

[64] K. C. Wong *et al.*, "H0LiCOW – XIII. A 2.4 per cent measurement of H0 from lensed quasars: 5.3σ tension between early- and late-Universe probes," *Mon. Not. Roy. Astron. Soc.* **498** no. 1, (2020) 1420–1439, arXiv:1907.04869 [astro-ph.CO].

[65] A. G. Riess, "The Expansion of the Universe is Faster than Expected," *Nature Rev. Phys.* **2** no. 1, (2019) 10–12, arXiv:2001.03624 [astro-ph.CO].

[66] E. Macaulay, I. K. Wehus, and H. K. Eriksen, "Lower Growth Rate from Recent Redshift Space Distortion Measurements than Expected from Planck," *Phys. Rev. Lett.* **111** no. 16, (2013) 161301, arXiv:1303.6583 [astro-ph.CO].

[67] A. Johnson, C. Blake, J. Dossett, J. Koda, D. Parkinson, and S. Joudaki, "Searching for Modified Gravity: Scale and Redshift Dependent Constraints from Galaxy Peculiar Velocities," *Mon. Not. Roy. Astron. Soc.* **458** no. 3, (2016) 2725–2744, arXiv:1504.06885 [astro-ph.CO].

[68] S. Nesseris, G. Pantazis, and L. Perivolaropoulos, "Tension and constraints on modified gravity parametrizations of $G_{\rm eff}(z)$ from growth rate and Planck data," *Phys. Rev. D* **96** no. 2, (2017) 023542, arXiv:1703.10538 [astro-ph.CO].

[69] S. Basilakos and S. Nesseris, "Conjoined constraints on modified gravity from the expansion history and cosmic growth," *Phys. Rev. D* **96** no. 6, (2017) 063517, arXiv:1705.08797 [astro-ph.CO].

[70] L. Kazantzidis and L. Perivolaropoulos, "Evolution of the $f\sigma_8$ tension with the Planck15/ΛCDM determination and implications for modified gravity theories," *Phys. Rev. D* **97** no. 10, (2018) 103503, arXiv:1803.01337 [astro-ph.CO].

[71] B. Sagredo, S. Nesseris, and D. Sapone, "Internal Robustness of Growth Rate data," *Phys. Rev. D* **98** no. 8, (2018) 083543, arXiv:1806.10822 [astro-ph.CO].

[72] L. Perivolaropoulos and L. Kazantzidis, "Hints of modified gravity in cosmos and in the lab?," *Int. J. Mod. Phys. D* **28** no. 05, (2019) 1942001, arXiv:1904.09462 [gr-qc].

[73] L. Kazantzidis and L. Perivolaropoulos, "σ_8 Tension. Is Gravity Getting Weaker at Low z? Observational Evidence and Theoretical Implications," arXiv:1907.03176 [astro-ph.CO].

[74] D. Benisty, "Quantifying the S_8 tension with the Redshift Space Distortion data set," *Phys. Dark Univ.* **31** (2021) 100766, arXiv:2005.03751 [astro-ph.CO].

[75] H. Hildebrandt *et al.*, "KiDS-450: Cosmological parameter constraints from tomographic weak gravitational lensing," *Mon. Not. Roy. Astron. Soc.* **465** (2017) 1454, arXiv:1606.05338 [astro-ph.CO].

[76] F. Köhlinger *et al.*, "KiDS-450: The tomographic weak lensing power spectrum and constraints on cosmological parameters," *Mon. Not. Roy. Astron. Soc.* **471** no. 4, (2017) 4412–4435, arXiv:1706.02892 [astro-ph.CO].

[77] S. Joudaki *et al.*, "KiDS-450 + 2dFLenS: Cosmological parameter constraints from weak gravitational lensing tomography and overlapping redshift-space galaxy clustering," *Mon. Not. Roy. Astron. Soc.* **474** no. 4, (2018) 4894–4924, arXiv:1707.06627 [astro-ph.CO].

[78] **DES** Collaboration, T. M. C. Abbott *et al.*, "Dark Energy Survey year 1 results: Cosmological constraints from galaxy clustering and weak lensing," *Phys. Rev. D* **98** no. 4, (2018) 043526, arXiv:1708.01530 [astro-ph.CO].

[79] **DES** Collaboration, T. M. C. Abbott *et al.*, "Dark Energy Survey Year 1 Results: Constraints on Extended Cosmological Models from Galaxy Clustering and Weak Lensing," *Phys. Rev. D* **99** no. 12, (2019) 123505, arXiv:1810.02499 [astro-ph.CO].

[80] M. Asgari *et al.*, "KiDS+VIKING-450 and DES-Y1 combined: Mitigating baryon feedback uncertainty with COSEBIs," *Astron. Astrophys.* **634** (2020) A127, arXiv:1910.05336 [astro-ph.CO].

[81] **DES** Collaboration, T. M. C. Abbott *et al.*, "Dark Energy Survey Year 1 Results: Cosmological constraints from cluster abundances and weak lensing," *Phys. Rev. D* **102** no. 2, (2020) 023509, arXiv:2002.11124 [astro-ph.CO].

[82] C. Heymans *et al.*, "KiDS-1000 Cosmology: Multi-probe weak gravitational lensing and spectroscopic galaxy clustering constraints," *Astron. Astrophys.* **646** (2021) A140, arXiv:2007.15632 [astro-ph.CO].

[83] **SPT** Collaboration, T. de Haan *et al.*, "Cosmological Constraints from Galaxy Clusters in the 2500 square-degree SPT-SZ Survey," *Astrophys. J.* **832** no. 1, (2016) 95, arXiv:1603.06522 [astro-ph.CO].

[84] H. Böhringer, G. Chon, and M. Fukugita, "The extended ROSAT-ESO Flux-Limited X-ray Galaxy Cluster Survey (REFLEX II) VII The Mass Function of Galaxy Clusters," *Astron. Astrophys.* **608** (2017) A65, arXiv:1708.02449 [astro-ph.CO].

[85] F. Skara and L. Perivolaropoulos, "Tension of the E_G statistic and redshift space distortion data with the Planck - ΛCDM model and implications for weakening gravity," *Phys. Rev. D* **101** no. 6, (2020) 063521, arXiv:1911.10609 [astro-ph.CO].

[86] L. Perivolaropoulos, "Six Puzzles for LCDM Cosmology," arXiv:0811.4684 [astro-ph].

[87] T. Buchert, A. A. Coley, H. Kleinert, B. F. Roukema, and D. L. Wiltshire, "Observational Challenges for the Standard FLRW Model," *Int. J. Mod. Phys. D* **25** no. 03, (2016) 1630007, arXiv:1512.03313 [astro-ph.CO].

[88] D. Huterer and D. L. Shafer, "Dark energy two decades after: Observables, probes, consistency tests," *Rept. Prog. Phys.* **81** no. 1, (2018) 016901, arXiv:1709.01091 [astro-ph.CO].

[89] E. Di Valentino and S. Bridle, "Exploring the Tension between Current Cosmic Microwave Background and Cosmic Shear Data," *Symmetry* **10** no. 11, (2018) 585.

[90] M. Ishak, "Testing General Relativity in Cosmology," *Living Rev. Rel.* **22** no. 1, (2019) 1, arXiv:1806.10122 [astro-ph.CO].

[91] E. Di Valentino, O. Mena, S. Pan, L. Visinelli, W. Yang, A. Melchiorri, D. F. Mota, A. G. Riess, and J. Silk, "In the Realm of the Hubble tension − a Review of Solutions," arXiv:2103.01183 [astro-ph.CO].

[92] L. Perivolaropoulos and F. Skara, "Challenges for ΛCDM: An update," arXiv:2105.05208 [astro-ph.CO].

[93] **CANTATA** Collaboration, E. N. Saridakis *et al.*, "Modified Gravity and Cosmology: An Update by the CANTATA Network," arXiv:2105.12582 [gr-qc].

[94] A. Theodoropoulos and L. Perivolaropoulos, "The Hubble Tension, the M Crisis of Late Time H(z) Deformation Models and the Reconstruction of Quintessence Lagrangians," *Universe* **7** no. 8, (2021) 300, arXiv:2109.06256 [astro-ph.CO].

[95] J. D. Barrow and F. J. Tipler, *The Anthropic Cosmological Principle*. Oxford U. Pr., Oxford, 1988.

[96] S. Weinberg, "Anthropic Bound on the Cosmological Constant," *Phys. Rev. Lett.* **59** (1987) 2607.

[97] L. Susskind, "The Anthropic landscape of string theory," arXiv:hep-th/0302219.

[98] B. Carter, "Anthropic principle in cosmology," in *Colloquium on Cosmology: Facts and Problems*, pp. 173–179. 6, 2006. arXiv:gr-qc/0606117.

[99] M. S. Turner and M. J. White, "CDM models with a smooth component," *Phys. Rev. D* **56** no. 8, (1997) R4439, arXiv:astro-ph/9701138.

[100] A. A. Starobinsky, "How to determine an effective potential for a variable cosmological term," *JETP Lett.* **68** (1998) 757–763, arXiv:astro-ph/9810431.

[101] M. Chevallier and D. Polarski, "Accelerating universes with scaling dark matter," *Int. J. Mod. Phys. D* **10** (2001) 213–224, arXiv:gr-qc/0009008.

[102] D. Huterer and M. S. Turner, "Probing the dark energy: Methods and strategies," *Phys. Rev. D* **64** (2001) 123527, arXiv:astro-ph/0012510.

[103] E. V. Linder, "Exploring the expansion history of the universe," *Phys. Rev. Lett.* **90** (2003) 091301, arXiv:astro-ph/0208512.

[104] P. S. Corasaniti and E. J. Copeland, "A Model independent approach to the dark energy equation of state," *Phys. Rev. D* **67** (2003) 063521, arXiv:astro-ph/0205544.

[105] V. Sahni and A. Starobinsky, "Reconstructing Dark Energy," *Int. J. Mod. Phys. D* **15** (2006) 2105–2132, arXiv:astro-ph/0610026.

[106] P. J. E. Peebles and B. Ratra, "Cosmology with a Time Variable Cosmological Constant," *Astrophys. J. Lett.* **325** (1988) L17.

[107] J. C. Carvalho, J. A. S. Lima, and I. Waga, "On the cosmological consequences of a time dependent lambda term," *Phys. Rev. D* **46** (1992) 2404–2407.

[108] P. Wang and X.-H. Meng, "Can vacuum decay in our universe?," *Class. Quant. Grav.* **22** (2005) 283–294, arXiv:astro-ph/0408495.

[109] S. Basilakos, "Cosmological implications and structure formation from a time varying vacuum," *Mon. Not. Roy. Astron. Soc.* **395** (2009) 2347, arXiv:0903.0452 [astro-ph.CO].

[110] J. Sola, "Cosmologies with a time dependent vacuum," *J. Phys. Conf. Ser.* **283** (2011) 012033, arXiv:1102.1815 [astro-ph.CO].

[111] E. L. D. Perico, J. A. S. Lima, S. Basilakos, and J. Sola, "Complete Cosmic History with a dynamical $\Lambda = \Lambda(H)$ term," *Phys. Rev. D* **88** (2013) 063531, arXiv:1306.0591 [astro-ph.CO].

[112] J. Solà, A. Gómez-Valent, and J. de Cruz Pérez, "The H_0 tension in light of vacuum dynamics in the Universe," *Phys. Lett. B* **774** (2017) 317–324, arXiv:1705.06723 [astro-ph.CO].

[113] A. Gómez-Valent and J. Solà Peracaula, "Density perturbations for running vacuum: a successful approach to structure formation and to the σ_8-tension," *Mon. Not. Roy. Astron. Soc.* **478** no. 1, (2018) 126–145, arXiv:1801.08501 [astro-ph.CO].

[114] G. Papagiannopoulos, P. Tsiapi, S. Basilakos, and A. Paliathanasis, "Dynamics and cosmological evolution in Λ-varying cosmology," *Eur. Phys. J. C* **80** no. 1, (2020) 55, arXiv:1911.12431 [gr-qc].

[115] B. Ratra and P. J. E. Peebles, "Cosmological Consequences of a Rolling Homogeneous Scalar Field," *Phys. Rev. D* **37** (1988) 3406.

[116] C. Wetterich, "Cosmology and the Fate of Dilatation Symmetry," *Nucl. Phys. B* **302** (1988) 668–696, arXiv:1711.03844 [hep-th].

[117] E. J. Copeland, A. R. Liddle, and D. Wands, "Exponential potentials and cosmological scaling solutions," *Phys. Rev. D* **57** (1998) 4686–4690, arXiv:gr-qc/9711068.

[118] P. G. Ferreira and M. Joyce, "Cosmology with a primordial scaling field," *Phys. Rev. D* **58** (1998) 023503, arXiv:astro-ph/9711102.

[119] P. G. Ferreira and M. Joyce, "Structure formation with a selftuning scalar field," *Phys. Rev. Lett.* **79** (1997) 4740–4743, arXiv:astro-ph/9707286.

[120] R. R. Caldwell, R. Dave, and P. J. Steinhardt, "Cosmological imprint of an energy component with general equation of state," *Phys. Rev. Lett.* **80** (1998) 1582–1585, arXiv:astro-ph/9708069.

[121] S. M. Carroll, "Quintessence and the rest of the world," *Phys. Rev. Lett.* **81** (1998) 3067–3070, arXiv:astro-ph/9806099.

[122] A. R. Liddle and R. J. Scherrer, "A Classification of scalar field potentials with cosmological scaling solutions," *Phys. Rev. D* **59** (1999) 023509, arXiv:astro-ph/9809272.

[123] I. Zlatev, L.-M. Wang, and P. J. Steinhardt, "Quintessence, cosmic coincidence, and the cosmological constant," *Phys. Rev. Lett.* **82** (1999) 896–899, arXiv:astro-ph/9807002.

[124] V. Sahni and L.-M. Wang, "A New cosmological model of quintessence and dark matter," *Phys. Rev. D* **62** (2000) 103517, arXiv:astro-ph/9910097.

[125] T. Barreiro, E. J. Copeland, and N. J. Nunes, "Quintessence arising from exponential potentials," *Phys. Rev. D* **61** (2000) 127301, arXiv:astro-ph/9910214.

[126] P. Brax and J. Martin, "The Robustness of quintessence," *Phys. Rev. D* **61** (2000) 103502, arXiv:astro-ph/9912046.

[127] L. A. Urena-Lopez and T. Matos, "A New cosmological tracker solution for quintessence," *Phys. Rev. D* **62** (2000) 081302, arXiv:astro-ph/0003364.

[128] M. Axenides and K. Dimopoulos, "Hybrid dark sector: Locked quintessence and dark matter," *JCAP* **07** (2004) 010, arXiv:hep-ph/0401238.

[129] T. Chiba, A. De Felice, and S. Tsujikawa, "Observational constraints on quintessence: thawing, tracker, and scaling models," *Phys. Rev. D* **87** no. 8, (2013) 083505, arXiv:1210.3859 [astro-ph.CO].

[130] S. Tsujikawa, "Quintessence: A Review," *Class. Quant. Grav.* **30** (2013) 214003, arXiv:1304.1961 [gr-qc].

[131] R. R. Caldwell, "A Phantom menace?," *Phys. Lett. B* **545** (2002) 23–29, arXiv:astro-ph/9908168.

[132] B. McInnes, "What if w < -1 ?," in *18th IAP Colloquium on the Nature of Dark Energy: Observational and Theoretical Results on the Accelerating Universe*. 10, 2002. arXiv:astro-ph/0210321.

[133] S. M. Carroll, M. Hoffman, and M. Trodden, "Can the dark energy equation of state parameter w be less than -1?," *Phys. Rev. D* **68** (2003) 023509, arXiv:astro-ph/0301273.

[134] P. Singh, M. Sami, and N. Dadhich, "Cosmological dynamics of phantom field," *Phys. Rev. D* **68** (2003) 023522, arXiv:hep-th/0305110.

[135] L. P. Chimento and R. Lazkoz, "On the link between phantom and standard cosmologies," *Phys. Rev. Lett.* **91** (2003) 211301, arXiv:gr-qc/0307111.

[136] P. F. Gonzalez-Diaz and C. L. Siguenza, "Phantom thermodynamics," *Nucl. Phys. B* **697** (2004) 363–386, arXiv:astro-ph/0407421.

[137] C. Armendariz-Picon, V. F. Mukhanov, and P. J. Steinhardt, "Essentials of k essence," *Phys. Rev. D* **63** (2001) 103510, arXiv:astro-ph/0006373.

[138] P. F. Gonzalez-Diaz, "K-essential phantom energy: Doomsday around the corner?," *Phys. Lett. B* **586** (2004) 1–4, arXiv:astro-ph/0312579.

[139] S. Capozziello, R. de Ritis, and A. A. Marino, "Recovering the effective cosmological constant in extended gravity theories," *Gen. Rel. Grav.* **30** (1998) 1247–1272, arXiv:gr-qc/9804053.

[140] J.-P. Uzan, "Cosmological scaling solutions of nonminimally coupled scalar fields," *Phys. Rev. D* **59** (1999) 123510, arXiv:gr-qc/9903004.

[141] T. Chiba, "Quintessence, the gravitational constant, and gravity," *Phys. Rev. D* **60** (1999) 083508, arXiv:gr-qc/9903094.

[142] L. Amendola, "Scaling solutions in general nonminimal coupling theories," *Phys. Rev. D* **60** (1999) 043501, arXiv:astro-ph/9904120.

[143] F. Perrotta, C. Baccigalupi, and S. Matarrese, "Extended quintessence," *Phys. Rev. D* **61** (1999) 023507, arXiv:astro-ph/9906066.

[144] N. Bartolo and M. Pietroni, "Scalar tensor gravity and quintessence," *Phys. Rev. D* **61** (2000) 023518, arXiv:hep-ph/9908521.

[145] Y. Fujii, "Quintessence, scalar tensor theories and nonNewtonian gravity," *Phys. Rev. D* **62** (2000) 044011, arXiv:gr-qc/9911064.

[146] B. Boisseau, G. Esposito-Farese, D. Polarski, and A. A. Starobinsky, "Reconstruction of a scalar tensor theory of gravity in an accelerating universe," *Phys. Rev. Lett.* **85** (2000) 2236, arXiv:gr-qc/0001066.

[147] G. Esposito-Farese and D. Polarski, "Scalar tensor gravity in an accelerating universe," *Phys. Rev. D* **63** (2001) 063504, arXiv:gr-qc/0009034.

[148] L. Perivolaropoulos, "Crossing the phantom divide barrier with scalar tensor theories," *JCAP* **10** (2005) 001, arXiv:astro-ph/0504582.

[149] A. Coc, K. A. Olive, J.-P. Uzan, and E. Vangioni, "Big bang nucleosynthesis constraints on scalar-tensor theories of gravity," *Phys. Rev. D* **73** (2006) 083525, arXiv:astro-ph/0601299.

[150] S. Nesseris and L. Perivolaropoulos, "The Limits of Extended Quintessence," *Phys. Rev. D* **75** (2007) 023517, arXiv:astro-ph/0611238.

[151] A. Y. Kamenshchik, U. Moschella, and V. Pasquier, "An Alternative to quintessence," *Phys. Lett. B* **511** (2001) 265–268, arXiv:gr-qc/0103004.

[152] J. C. Fabris, S. V. B. Goncalves, and P. E. de Souza, "Density perturbations in a universe dominated by the Chaplygin gas," *Gen. Rel. Grav.* **34** (2002) 53–63, arXiv:gr-qc/0103083.

[153] N. Bilic, G. B. Tupper, and R. D. Viollier, "Unification of dark matter and dark energy: The Inhomogeneous Chaplygin gas," *Phys. Lett. B* **535** (2002) 17–21, arXiv:astro-ph/0111325.

[154] M. C. Bento, O. Bertolami, and A. A. Sen, "Generalized Chaplygin gas, accelerated expansion and dark energy matter unification," *Phys. Rev. D* **66** (2002) 043507, arXiv:gr-qc/0202064.

[155] W. Yang, S. Pan, S. Vagnozzi, E. Di Valentino, D. F. Mota, and S. Capozziello, "Dawn of the dark: unified dark sectors and the EDGES Cosmic Dawn 21-cm signal," *JCAP* **11** (2019) 044, arXiv:1907.05344 [astro-ph.CO].

[156] S. Capozziello, "Curvature quintessence," *Int. J. Mod. Phys. D* **11** (2002) 483–492, arXiv:gr-qc/0201033.

[157] S. M. Carroll, V. Duvvuri, M. Trodden, and M. S. Turner, "Is cosmic speed - up due to new gravitational physics?," *Phys. Rev. D* **70** (2004) 043528, arXiv:astro-ph/0306438.

[158] S. Capozziello, V. F. Cardone, S. Carloni, and A. Troisi, "Curvature quintessence matched with observational data," *Int. J. Mod. Phys. D* **12** (2003) 1969–1982, arXiv:astro-ph/0307018.

[159] G. Allemandi, A. Borowiec, and M. Francaviglia, "Accelerated cosmological models in Ricci squared gravity," *Phys. Rev. D* **70** (2004) 103503, arXiv:hep-th/0407090.

[160] S. Carloni, P. K. S. Dunsby, S. Capozziello, and A. Troisi, "Cosmological dynamics of R**n gravity," *Class. Quant. Grav.* **22** (2005) 4839–4868, arXiv:gr-qc/0410046.

[161] S. Nojiri and S. D. Odintsov, "Introduction to modified gravity and gravitational alternative for dark energy," *eConf* **C0602061** (2006) 06, arXiv:hep-th/0601213.

[162] L. Amendola, D. Polarski, and S. Tsujikawa, "Are f(R) dark energy models cosmologically viable ?," *Phys. Rev. Lett.* **98** (2007) 131302, arXiv:astro-ph/0603703.

[163] S. Capozziello, S. Nojiri, S. D. Odintsov, and A. Troisi, "Cosmological viability of f(R)-gravity as an ideal fluid and its compatibility with a matter dominated phase," *Phys. Lett. B* **639** (2006) 135–143, arXiv:astro-ph/0604431.

[164] V. Faraoni, "Solar System experiments do not yet veto modified gravity models," *Phys. Rev. D* **74** (2006) 023529, arXiv:gr-qc/0607016.

[165] S. Nojiri and S. D. Odintsov, "Modified f(R) gravity consistent with realistic cosmology: From matter dominated epoch to dark energy universe," *Phys. Rev. D* **74** (2006) 086005, arXiv:hep-th/0608008.

[166] L. Amendola, R. Gannouji, D. Polarski, and S. Tsujikawa, "Conditions for the cosmological viability of f(R) dark energy models," *Phys. Rev. D* **75** (2007) 083504, arXiv:gr-qc/0612180.

[167] S. Fay, S. Nesseris, and L. Perivolaropoulos, "Can f(R) Modified Gravity Theories Mimic a LCDM Cosmology?," *Phys. Rev. D* **76** (2007) 063504, arXiv:gr-qc/0703006.

[168] W. Hu and I. Sawicki, "Models of f(R) Cosmic Acceleration that Evade Solar-System Tests," *Phys. Rev. D* **76** (2007) 064004, arXiv:0705.1158 [astro-ph].

[169] A. A. Starobinsky, "Disappearing cosmological constant in f(R) gravity," *JETP Lett.* **86** (2007) 157–163, arXiv:0706.2041 [astro-ph].

[170] T. P. Sotiriou and V. Faraoni, "f(R) Theories Of Gravity," *Rev. Mod. Phys.* **82** (2010) 451–497, arXiv:0805.1726 [gr-qc].

[171] S. Nojiri and S. D. Odintsov, "Dark energy, inflation and dark matter from modified F(R) gravity," *TSPU Bulletin* **N8(110)** (2011) 7–19, arXiv:0807.0685 [hep-th].

[172] A. De Felice and S. Tsujikawa, "f(R) theories," *Living Rev. Rel.* **13** (2010) 3, arXiv:1002.4928 [gr-qc].

[173] S. Nojiri and S. D. Odintsov, "Unified cosmic history in modified gravity: from F(R) theory to Lorentz non-invariant models," *Phys. Rept.* **505** (2011) 59–144, arXiv:1011.0544 [gr-qc].

[174] E. Elizalde, S. Nojiri, S. D. Odintsov, L. Sebastiani, and S. Zerbini, "Non-singular exponential gravity: a simple theory for early- and late-time accelerated expansion," *Phys. Rev. D* **83** (2011) 086006, arXiv:1012.2280 [hep-th].

[175] A. Aviles, A. Bravetti, S. Capozziello, and O. Luongo, "Updated constraints on f(R) gravity from cosmography," *Phys. Rev. D* **87** no. 4, (2013) 044012, arXiv:1210.5149 [gr-qc].

[176] S. Basilakos, S. Nesseris, and L. Perivolaropoulos, "Observational constraints on viable f(R) parametrizations with geometrical and dynamical probes," *Phys. Rev. D* **87** no. 12, (2013) 123529, arXiv:1302.6051 [astro-ph.CO].

[177] M. O'Dwyer, S. E. Joras, and I. Waga, "γ gravity: Steepness control," *Phys. Rev. D* **88** no. 6, (2013) 063520, arXiv:1305.4654 [astro-ph.CO].

[178] S. D. Odintsov, V. K. Oikonomou, and L. Sebastiani, "Unification of Constant-roll Inflation and Dark Energy with Logarithmic R^2-corrected and Exponential $F(R)$ Gravity," *Nucl. Phys. B* **923** (2017) 608–632, arXiv:1708.08346 [gr-qc].

[179] A. de la Cruz-Dombriz, P. K. S. Dunsby, S. Kandhai, and D. Sáez-Gómez, "Theoretical and observational constraints of viable f(R) theories of gravity," *Phys. Rev. D* **93** no. 8, (2016) 084016, arXiv:1511.00102 [gr-qc].

[180] C. Álvarez Luna, S. Basilakos, and S. Nesseris, "Cosmological constraints on γ-gravity models," *Phys. Rev. D* **98** no. 2, (2018) 023516, arXiv:1805.02926 [astro-ph.CO].

[181] R. Ferraro and F. Fiorini, "Modified teleparallel gravity: Inflation without inflaton," *Phys. Rev. D* **75** (2007) 084031, arXiv:gr-qc/0610067.

[182] G. R. Bengochea and R. Ferraro, "Dark torsion as the cosmic speed-up," *Phys. Rev. D* **79** (2009) 124019, arXiv:0812.1205 [astro-ph].

[183] E. V. Linder, "Einstein's Other Gravity and the Acceleration of the Universe," *Phys. Rev. D* **81** (2010) 127301, arXiv:1005.3039 [astro-ph.CO]. [Erratum: Phys.Rev.D 82, 109902 (2010)].

[184] S.-H. Chen, J. B. Dent, S. Dutta, and E. N. Saridakis, "Cosmological perturbations in f(T) gravity," *Phys. Rev. D* **83** (2011) 023508, arXiv:1008.1250 [astro-ph.CO].

[185] S. Nesseris, S. Basilakos, E. N. Saridakis, and L. Perivolaropoulos, "Viable $f(T)$ models are practically indistinguishable from ΛCDM," *Phys. Rev. D* **88** (2013) 103010, arXiv:1308.6142 [astro-ph.CO].

[186] Y.-F. Cai, S. Capozziello, M. De Laurentis, and E. N. Saridakis, "f(T) teleparallel gravity and cosmology," *Rept. Prog. Phys.* **79** no. 10, (2016) 106901, arXiv:1511.07586 [gr-qc].

[187] S. Basilakos, S. Nesseris, F. K. Anagnostopoulos, and E. N. Saridakis, "Updated constraints on $f(T)$ models using direct and indirect measurements of the Hubble parameter," *JCAP* **08** (2018) 008, arXiv:1803.09278 [astro-ph.CO].

[188] S.-F. Yan, P. Zhang, J.-W. Chen, X.-Z. Zhang, Y.-F. Cai, and E. N. Saridakis, "Interpreting cosmological tensions from the effective field theory of torsional gravity," arXiv:1909.06388 [astro-ph.CO].

[189] C. Escamilla-Rivera and J. Levi Said, "Cosmological viable models in $f(T, B)$ theory as solutions to the H_0 tension," *Class. Quant. Grav.* **37** no. 16, (2020) 165002, arXiv:1909.10328 [gr-qc].

[190] S. Bahamonde, K. F. Dialektopoulos, C. Escamilla-Rivera, G. Farrugia, V. Gakis, M. Hendry, M. Hohmann, J. L. Said, J. Mifsud, and E. Di Valentino, "Teleparallel Gravity: From Theory to Cosmology," arXiv:2106.13793 [gr-qc].

[191] T. Kaluza, "Zum Unitätsproblem der Physik," *Sitzungsber. Preuss. Akad. Wiss. Berlin (Math. Phys.)* **1921** (1921) 966–972, arXiv:1803.08616 [physics.hist-ph].

[192] N. Arkani-Hamed, S. Dimopoulos, and G. R. Dvali, "The Hierarchy problem and new dimensions at a millimeter," *Phys. Lett. B* **429** (1998) 263–272, arXiv:hep-ph/9803315.

[193] I. Antoniadis, N. Arkani-Hamed, S. Dimopoulos, and G. R. Dvali, "New dimensions at a millimeter to a Fermi and superstrings at a TeV," *Phys. Lett. B* **436** (1998) 257–263, arXiv:hep-ph/9804398.

[194] G. R. Dvali, G. Gabadadze, and M. Porrati, "4-D gravity on a brane in 5-D Minkowski space," *Phys. Lett. B* **485** (2000) 208–214, arXiv:hep-th/0005016.

[195] V. Sahni and Y. Shtanov, "Brane world models of dark energy," *JCAP* **11** (2003) 014, arXiv:astro-ph/0202346.

[196] A. Lue and G. D. Starkman, "How a brane cosmological constant can trick us into thinking that W < -1," *Phys. Rev. D* **70** (2004) 101501, arXiv:astro-ph/0408246.

[197] R. Lazkoz, R. Maartens, and E. Majerotto, "Observational constraints on phantom-like braneworld cosmologies," *Phys. Rev. D* **74** (2006) 083510, arXiv:astro-ph/0605701.

[198] L. Lombriser, W. Hu, W. Fang, and U. Seljak, "Cosmological Constraints on DGP Braneworld Gravity with Brane Tension," *Phys. Rev. D* **80** (2009) 063536, arXiv:0905.1112 [astro-ph.CO].

[199] R. Maartens and K. Koyama, "Brane-World Gravity," *Living Rev. Rel.* **13** (2010) 5, arXiv:1004.3962 [hep-th].

[200] T. Azizi, M. Sadegh Movahed, and K. Nozari, "Observational Constraints on the Normal Branch of a Warped DGP Cosmology," *New Astron.* **17** (2012) 424–432, arXiv:1111.3195 [astro-ph.CO].

[201] L. Xu, "Confronting DGP braneworld gravity with cosmico observations after Planck data," *JCAP* **02** (2014) 048, arXiv:1312.4679 [astro-ph.CO].

[202] S. Bag, V. Sahni, A. Shafieloo, and Y. Shtanov, "Phantom braneworld and the Hubble tension," arXiv:2107.03271 [astro-ph.CO].

[203] J. Sola, A. Gomez-Valent, J. d. C. Perez, and C. Moreno-Pulido, "Brans-Dicke gravity with a cosmological constant smoothes out ΛCDM tensions," arXiv:1909.02554 [astro-ph.CO].

[204] D. Comelli, M. Pietroni, and A. Riotto, "Dark energy and dark matter," *Phys. Lett. B* **571** (2003) 115–120, arXiv:hep-ph/0302080.

[205] G. Huey and B. D. Wandelt, "Interacting quintessence. The Coincidence problem and cosmic acceleration," *Phys. Rev. D* **74** (2006) 023519, arXiv:astro-ph/0407196.

[206] R.-G. Cai and A. Wang, "Cosmology with interaction between phantom dark energy and dark matter and the coincidence problem," *JCAP* **03** (2005) 002, arXiv:hep-th/0411025.

[207] D. Pavon and W. Zimdahl, "Holographic dark energy and cosmic coincidence," *Phys. Lett. B* **628** (2005) 206–210, arXiv:gr-qc/0505020.

[208] J.-H. He and B. Wang, "Effects of the interaction between dark energy and dark matter on cosmological parameters," *JCAP* **06** (2008) 010, arXiv:0801.4233 [astro-ph].

[209] B. Wang, E. Abdalla, F. Atrio-Barandela, and D. Pavon, "Dark Matter and Dark Energy Interactions: Theoretical Challenges, Cosmological Implications and Observational Signatures," *Rept. Prog. Phys.* **79** no. 9, (2016) 096901, arXiv:1603.08299 [astro-ph.CO].

[210] S. Kumar and R. C. Nunes, "Echo of interactions in the dark sector," *Phys. Rev. D* **96** no. 10, (2017) 103511, arXiv:1702.02143 [astro-ph.CO].

[211] S. Kumar, R. C. Nunes, and S. K. Yadav, "Dark sector interaction: a remedy of the tensions between CMB and LSS data," *Eur. Phys. J. C* **79** no. 7, (2019) 576, arXiv:1903.04865 [astro-ph.CO].

[212] E. Di Valentino, C. Bøehm, E. Hivon, and F. R. Bouchet, "Reducing the H_0 and σ_8 tensions with Dark Matter-neutrino interactions," *Phys. Rev.* **D97** no. 4, (2018) 043513, arXiv:1710.02559 [astro-ph.CO].

[213] A. G. Cohen, D. B. Kaplan, and A. E. Nelson, "Effective field theory, black holes, and the cosmological constant," *Phys. Rev. Lett.* **82** (1999) 4971–4974, arXiv:hep-th/9803132.

[214] S. Nojiri and S. D. Odintsov, "Unifying phantom inflation with late-time acceleration: Scalar phantom-non-phantom transition model and generalized holographic dark energy," *Gen. Rel. Grav.* **38** (2006) 1285–1304, arXiv:hep-th/0506212.

[215] M. Li, "A Model of holographic dark energy," *Phys. Lett. B* **603** (2004) 1, arXiv:hep-th/0403127.

[216] W.-M. Dai, Y.-Z. Ma, and H.-J. He, "Reconciling Hubble Constant Discrepancy from Holographic Dark Energy," *Phys. Rev. D* **102** (2020) 121302, arXiv:2003.03602 [astro-ph.CO].

[217] T. Karwal and M. Kamionkowski, "Dark energy at early times, the Hubble parameter, and the string axiverse," *Phys. Rev. D* **94** no. 10, (2016) 103523, arXiv:1608.01309 [astro-ph.CO].

[218] V. Poulin, T. L. Smith, T. Karwal, and M. Kamionkowski, "Early Dark Energy Can Resolve The Hubble Tension," *Phys. Rev. Lett.* **122** no. 22, (2019) 221301, arXiv:1811.04083 [astro-ph.CO].

[219] P. Agrawal, F.-Y. Cyr-Racine, D. Pinner, and L. Randall, "Rock 'n' Roll Solutions to the Hubble Tension," arXiv:1904.01016 [astro-ph.CO].

[220] M.-X. Lin, G. Benevento, W. Hu, and M. Raveri, "Acoustic Dark Energy: Potential Conversion of the Hubble Tension," *Phys. Rev. D* **100** no. 6, (2019) 063542, arXiv:1905.12618 [astro-ph.CO].

[221] T. L. Smith, V. Poulin, and M. A. Amin, "Oscillating scalar fields and the Hubble tension: a resolution with novel signatures," *Phys. Rev. D* **101** no. 6, (2020) 063523, arXiv:1908.06995 [astro-ph.CO].

[222] J. Sakstein and M. Trodden, "Early Dark Energy from Massive Neutrinos as a Natural Resolution of the Hubble Tension," *Phys. Rev. Lett.* **124** no. 16, (2020) 161301, arXiv:1911.11760 [astro-ph.CO].

[223] M. Braglia, W. T. Emond, F. Finelli, A. E. Gumrukcuoglu, and K. Koyama, "Unified framework for early dark energy from α-attractors," *Phys. Rev. D* **102** no. 8, (2020) 083513, arXiv:2005.14053 [astro-ph.CO].

[224] K. L. Pandey, T. Karwal, and S. Das, "Alleviating the H_0 and σ_8 anomalies with a decaying dark matter model," arXiv:1902.10636 [astro-ph.CO].

[225] R. A. Battye, M. Bucher, and D. Spergel, "Domain wall dominated universes," arXiv:astro-ph/9908047.

[226] A. Friedland, H. Murayama, and M. Perelstein, "Domain walls as dark energy," *Phys. Rev. D* **67** (2003) 043519, arXiv:astro-ph/0205520.

[227] L. Conversi, A. Melchiorri, L. Mersini-Houghton, and J. Silk, "Are domain walls ruled out?," *Astropart. Phys.* **21** (2004) 443–449, arXiv:astro-ph/0402529.

[228] S. Nesseris, D. Sapone, and S. Sypsas, "Evaporating primordial black holes as varying dark energy," *Phys. Dark Univ.* **27** (2020) 100413, arXiv:1907.05608 [astro-ph.CO].

[229] A. Banihashemi, N. Khosravi, and A. H. Shirazi, "Phase transition in the dark sector as a proposal to lessen cosmological tensions," *Phys. Rev. D* **101** no. 12, (2020) 123521, arXiv:1808.02472 [astro-ph.CO].

[230] R.-Y. Guo, J.-F. Zhang, and X. Zhang, "Can the H_0 tension be resolved in extensions to ΛCDM cosmology?," *JCAP* **02** (2019) 054, arXiv:1809.02340 [astro-ph.CO].

[231] W. Yang, S. Pan, E. Di Valentino, E. N. Saridakis, and S. Chakraborty, "Observational constraints on one-parameter dynamical dark-energy parametrizations and the H_0 tension," *Phys. Rev. D* **99** no. 4, (2019) 043543, arXiv:1810.05141 [astro-ph.CO].

[232] X. Li, A. Shafieloo, V. Sahni, and A. A. Starobinsky, "Revisiting Metastable Dark Energy and Tensions in the Estimation of Cosmological Parameters," *Astrophys. J.* **887** (4, 2019) 153, arXiv:1904.03790 [astro-ph.CO].

[233] R. E. Keeley, S. Joudaki, M. Kaplinghat, and D. Kirkby, "Implications of a transition in the dark energy equation of state for the H_0 and σ_8 tensions," *JCAP* **12** (2019) 035, arXiv:1905.10198 [astro-ph.CO].

[234] X. Li and A. Shafieloo, "A Simple Phenomenological Emergent Dark Energy Model can Resolve the Hubble Tension," *Astrophys. J. Lett.* **883** no. 1, (2019) L3, arXiv:1906.08275 [astro-ph.CO].

[235] E. Di Valentino, R. Z. Ferreira, L. Visinelli, and U. Danielsson, "Late time transitions in the quintessence field and the H_0 tension," *Phys. Dark Univ.* **26** (2019) 100385, arXiv:1906.11255 [astro-ph.CO].

[236] S. Pan, W. Yang, E. Di Valentino, A. Shafieloo, and S. Chakraborty, "Reconciling H_0 tension in a six parameter space?," *JCAP* **06** no. 06, (2020) 062, arXiv:1907.12551 [astro-ph.CO].

[237] E. Di Valentino, A. Melchiorri, and J. Silk, "Cosmological constraints in extended parameter space from the Planck 2018 Legacy release," *JCAP* **01** (2020) 013, arXiv:1908.01391 [astro-ph.CO].

[238] X. Li and A. Shafieloo, "Evidence for Emergent Dark Energy," *Astrophys. J.* **902** no. 1, (2020) 58, arXiv:2001.05103 [astro-ph.CO].

[239] W. Yang, E. Di Valentino, S. Pan, S. Basilakos, and A. Paliathanasis, "Metastable dark energy models in light of *Planck* 2018 data: Alleviating the H_0 tension," *Phys. Rev. D* **102** no. 6, (2020) 063503, arXiv:2001.04307 [astro-ph.CO].

[240] E. Di Valentino, A. Mukherjee, and A. A. Sen, "Dark Energy with Phantom Crossing and the H_0 Tension," *Entropy* **23** no. 4, (2021) 404, arXiv:2005.12587 [astro-ph.CO].

[241] E. Di Valentino, E. V. Linder, and A. Melchiorri, "H_0 ex machina: Vacuum metamorphosis and beyond H_0," *Phys. Dark Univ.* **30** (2020) 100733, arXiv:2006.16291 [astro-ph.CO].

[242] W. Yang, E. Di Valentino, S. Pan, and O. Mena, "Emergent Dark Energy, neutrinos and cosmological tensions," *Phys. Dark Univ.* **31** (2021) 100762, arXiv:2007.02927 [astro-ph.CO].

[243] W. Yang, E. Di Valentino, S. Pan, A. Shafieloo, and X. Li, "Generalized emergent dark energy model and the Hubble constant tension," *Phys. Rev. D* **104** no. 6, (2021) 063521, arXiv:2103.03815 [astro-ph.CO].

[244] N. Copernicus, *De revolutionibus orbium coelestium*. 1543.

[245] J.-P. Uzan, C. Clarkson, and G. F. R. Ellis, "Time drift of cosmological redshifts as a test of the Copernican principle," *Phys. Rev. Lett.* **100** (2008) 191303, arXiv:0801.0068 [astro-ph].

[246] K. Bolejko and J. S. B. Wyithe, "Testing the Copernican Principle Via Cosmological Observations," *JCAP* **02** (2009) 020, arXiv:0807.2891 [astro-ph].

[247] T. Clifton, P. G. Ferreira, and K. Land, "Living in a Void: Testing the Copernican Principle with Distant Supernovae," *Phys. Rev. Lett.* **101** (2008) 131302, arXiv:0807.1443 [astro-ph].

[248] F. S. Labini and Y. V. Baryshev, "Testing the Copernican and Cosmological Principles in the local universe with galaxy surveys," *JCAP* **06** (2010) 021, arXiv:1006.0801 [astro-ph.CO].

[249] P. Zhang and A. Stebbins, "Confirmation of the Copernican Principle at Gpc Radial Scale and above from the Kinetic Sunyaev Zel'dovich Effect Power Spectrum," *Phys. Rev. Lett.* **107** (2011) 041301, arXiv:1009.3967 [astro-ph.CO].

[250] S. February, C. Clarkson, and R. Maartens, "Galaxy correlations and the BAO in a void universe: structure formation as a test of the Copernican Principle," *JCAP* **03** (2013) 023, arXiv:1206.1602 [astro-ph.CO].

[251] H. L. Bester, J. Larena, and N. T. Bishop, "Testing the Copernican principle with future radio-astronomy observations," arXiv:1705.00994 [astro-ph.CO].

[252] C. A. P. Bengaly, R. Maartens, and M. G. Santos, "Probing the Cosmological Principle in the counts of radio galaxies at different frequencies," *JCAP* **04** (2018) 031, arXiv:1710.08804 [astro-ph.CO].

[253] S. Alexander, L. Jenks, P. Jiroušek, J. a. Magueijo, and T. Złośnik, "Gravity waves in parity-violating Copernican Universes," *Phys. Rev. D* **102** no. 4, (2020) 044039, arXiv:2001.06373 [gr-qc].

[254] K. Migkas, G. Schellenberger, T. H. Reiprich, F. Pacaud, M. E. Ramos-Ceja, and L. Lovisari, "Probing cosmic isotropy with a new X-ray galaxy cluster sample through the $L_{\rm X} - T$ scaling relation," *Astron. Astrophys.* **636** (2020) A15, arXiv:2004.03305 [astro-ph.CO].

[255] N. J. Secrest, S. von Hausegger, M. Rameez, R. Mohayaee, S. Sarkar, and J. Colin, "A Test of the Cosmological Principle with Quasars," *Astrophys. J. Lett.* **908** no. 2, (2021) L51, arXiv:2009.14826 [astro-ph.CO].

[256] K. Migkas, F. Pacaud, G. Schellenberger, J. Erler, N. T. Nguyen-Dang, T. H. Reiprich, M. E. Ramos-Ceja, and L. Lovisari, "Cosmological implications of the anisotropy of ten galaxy cluster scaling relations," *Astron. Astrophys.* **649** (2021) A151, arXiv:2103.13904 [astro-ph.CO].

[257] R. Arjona and S. Nesseris, "A complementary consistency test of the Copernican principle via Noether's Theorem and machine learning forecasts," arXiv:2105.09049 [astro-ph.CO].

[258] T. Nadolny, R. Durrer, M. Kunz, and H. Padmanabhan, "A new test of the Cosmological Principle: measuring our peculiar velocity and the large scale anisotropy independently," arXiv:2106.05284 [astro-ph.CO].

[259] D. Camarena, V. Marra, Z. Sakr, and C. Clarkson, "The Copernican principle in light of the latest cosmological data," arXiv:2107.02296 [astro-ph.CO].

[260] M.-N. Celerier, "Do we really see a cosmological constant in the supernovae data?," *Astron. Astrophys.* **353** (2000) 63–71, arXiv:astro-ph/9907206.

[261] H. Alnes, M. Amarzguioui, and O. Gron, "An inhomogeneous alternative to dark energy?," *Phys. Rev. D* **73** (2006) 083519, arXiv:astro-ph/0512006.

[262] K. Enqvist and T. Mattsson, "The effect of inhomogeneous expansion on the supernova observations," *JCAP* **02** (2007) 019, arXiv:astro-ph/0609120.

[263] J. Garcia-Bellido and T. Haugboelle, "Confronting Lemaitre-Tolman-Bondi models with Observational Cosmology," *JCAP* **04** (2008) 003, arXiv:0802.1523 [astro-ph].

[264] S. February, J. Larena, M. Smith, and C. Clarkson, "Rendering Dark Energy Void," *Mon. Not. Roy. Astron. Soc.* **405** (2010) 2231, arXiv:0909.1479 [astro-ph.CO].

[265] T. Biswas, A. Notari, and W. Valkenburg, "Testing the Void against Cosmological data: fitting CMB, BAO, SN and H0," *JCAP* **11** (2010) 030, arXiv:1007.3065 [astro-ph.CO].

[266] S. Nadathur and S. Sarkar, "Reconciling the local void with the CMB," *Phys. Rev. D* **83** (2011) 063506, arXiv:1012.3460 [astro-ph.CO].

[267] K. Bolejko and R. A. Sussman, "Cosmic spherical void via coarse-graining and averaging non-spherical structures," *Phys. Lett. B* **697** (2011) 265–270, arXiv:1008.3420 [astro-ph.CO].

[268] V. Marra, L. Amendola, I. Sawicki, and W. Valkenburg, "Cosmic variance and the measurement of the local Hubble parameter," *Phys. Rev. Lett.* **110** no. 24, (2013) 241305, arXiv:1303.3121 [astro-ph.CO].

[269] R. Wojtak, A. Knebe, W. A. Watson, I. T. Iliev, S. Heß, D. Rapetti, G. Yepes, and S. Gottlöber, "Cosmic variance of the local Hubble flow in large-scale cosmological simulations," *Mon. Not. Roy. Astron. Soc.* **438** no. 2, (2014) 1805–1812, arXiv:1312.0276 [astro-ph.CO].

[270] S. Heß and F.-S. Kitaura, "Cosmic flows and the expansion of the local Universe from non-linear phase–space reconstructions," *Mon. Not. Roy. Astron. Soc.* **456** no. 4, (2016) 4247–4255, arXiv:1412.7310 [astro-ph.CO].

[271] I. Odderskov, S. M. Koksbang, and S. Hannestad, "The local value of H_0 in an inhomogeneous universe," *JCAP* **02** (2016) 001, arXiv:1601.07356 [astro-ph.CO].

[272] I. Odderskov, S. Hannestad, and J. Brandbyge, "The variance of the locally measured Hubble parameter explained with different estimators," *JCAP* **03** (2017) 022, arXiv:1701.05391 [astro-ph.CO].

[273] H.-Y. Wu and D. Huterer, "Sample variance in the local measurements of the Hubble constant," *Mon. Not. Roy. Astron. Soc.* **471** no. 4, (2017) 4946–4955, arXiv:1706.09723 [astro-ph.CO].

[274] D. Camarena and V. Marra, "Impact of the cosmic variance on H_0 on cosmological analyses," *Phys. Rev. D* **98** no. 2, (2018) 023537, arXiv:1805.09900 [astro-ph.CO].

[275] A. G. Riess, S. Casertano, D. Kenworthy, D. Scolnic, and L. Macri, "Seven Problems with the Claims Related to the Hubble Tension in arXiv:1810.02595," arXiv:1810.03526 [astro-ph.CO].

[276] W. J. Frith, G. S. Busswell, R. Fong, N. Metcalfe, and T. Shanks, "The local hole in the galaxy distribution: Evidence from 2MASS," *Mon. Not. Roy. Astron. Soc.* **345** (2003) 1049, arXiv:astro-ph/0302331.

[277] W. J. Frith, N. Metcalfe, and T. Shanks, "New h-band galaxy number counts: a large local hole in the galaxy distribution?," *Mon. Not. Roy. Astron. Soc.* **371** (2006) 1601–1609, arXiv:astro-ph/0509875.

[278] R. C. Keenan, A. J. Barger, and L. L. Cowie, "Evidence for a ˜300 Megaparsec Scale Under-density in the Local Galaxy Distribution," *Astrophys. J.* **775** (2013) 62, arXiv:1304.2884 [astro-ph.CO].

[279] J. R. Whitbourn and T. Shanks, "The Local Hole revealed by galaxy counts and redshifts," *Mon. Not. Roy. Astron. Soc.* **437** (2014) 2146–2162, arXiv:1307.4405 [astro-ph.CO].

[280] **Extragalactic Astronomy Group, Durham University** Collaboration, J. R. Whitbourn and T. Shanks, "The galaxy luminosity function and the Local Hole," *Mon. Not. Roy. Astron. Soc.* **459** no. 1, (2016) 496–507, arXiv:1603.02322 [astro-ph.CO].

[281] T. Shanks, L. Hogarth, and N. Metcalfe, "Gaia Cepheid parallaxes and 'Local Hole' relieve H_0 tension," *Mon. Not. Roy. Astron. Soc.* **484** no. 1, (2019) L64–L68, arXiv:1810.02595 [astro-ph.CO].

[282] T. Shanks, L. Hogarth, and N. Metcalfe, "H_0 Tension: Response to Riess et al arXiv:1810.03526," arXiv:1810.07628 [astro-ph.CO].

[283] V. V. Lukovi´c, B. S. Haridasu, and N. Vittorio, "Exploring the evidence for a large local void with supernovae Ia data," *Mon. Not. Roy. Astron. Soc.* **491** no. 2, (2020) 2075–2087, arXiv:1907.11219 [astro-ph.CO].

[284] T. Shanks, L. M. Hogarth, N. Metcalfe, and J. Whitbourn, "Local Hole revisited: evidence for bulk motions and self-consistent outflow," *Mon. Not. Roy. Astron. Soc.* **490** no. 4, (2019) 4715–4720, arXiv:1909.01878 [astro-ph.CO].

[285] L. Kazantzidis and L. Perivolaropoulos, "Hints of a Local Matter Underdensity or Modified Gravity in the Low z Pantheon data," *Phys. Rev. D* **102** no. 2, (2020) 023520, arXiv:2004.02155 [astro-ph.CO].

[286] H. Böhringer, G. Chon, and C. A. Collins, "Observational evidence for a local underdensity in the Universe and its effect on the measurement of the Hubble Constant," *Astron. Astrophys.* **633** (2020) A19, arXiv:1907.12402 [astro-ph.CO].

[287] S. Weinberg, *Gravitation and Cosmology: Principles and Applications of the General Theory of Relativity*. John Wiley and Sons, New York, 1972.

[288] P. Kanti, *Lecture notes for the course of Cosmology*. 2014.

[289] H. Weyl, *Gruppentheorie und Quantenmechanik*. Hirzel Leipzig, 1923.

[290] M. P. Hobson, G. P. Efstathiou, and A. N. Lasenby, *General Relativity: An Introduction for Physicists*. Cambridge University Press, 2006.

[291] J. Frieman, M. Turner, and D. Huterer, "Dark Energy and the Accelerating Universe," *Ann. Rev. Astron. Astrophys.* **46** (2008) 385–432, arXiv:0803.0982 [astro-ph].

[292] M. Hamuy, M. M. Phillips, N. B. Suntzeff, R. A. Schommer, J. Maza, and R. Aviles, "The Hubble diagram of the Calan/Tololo type IA supernovae and the value of HO," *Astron. J.* **112** (1996) 2398, arXiv:astro-ph/9609062.

[293] S. Perlmutter, "Supernovae, dark energy, and the accelerating universe," *Physics Today* **56** no. 4, (2003) 53–60, https://doi.org/10.1063/1.1580050. https://doi.org/10.1063/1.1580050.

[294] E. Bertschinger, "On the Growth of Perturbations as a Test of Dark Energy," *Astrophys. J.* **648** (2006) 797–806, arXiv:astro-ph/0604485.

[295] S. Nesseris and L. Perivolaropoulos, "Crossing the Phantom Divide: Theoretical Implications and Observational Status," *JCAP* **01** (2007) 018, arXiv:astro-ph/0610092.

[296] E. J. Ruiz and D. Huterer, "Testing the dark energy consistency with geometry and growth," *Phys. Rev. D* **91** (2015) 063009, arXiv:1410.5832 [astro-ph.CO].

[297] B. Daniel, *Cosmology Lecture Notes*. http://cosmology.amsterdam/education/cosmology/.

[298] S. Dodelson, *Modern Cosmology*. Academic Press, Amsterdam, 2003.

[299] J. A. Peacock, *Cosmological Physics*. 1999.

[300] S. Tsujikawa, "Matter density perturbations and effective gravitational constant in modified gravity models of dark energy," *Phys. Rev. D* **76** (2007) 023514, arXiv:0705.1032 [astro-ph].

[301] S. Nesseris, "Matter density perturbations in modified gravity models with arbitrary coupling between matter and geometry," *Phys. Rev. D* **79** (2009) 044015, arXiv:0811.4292 [astro-ph].

[302] A. De Felice, S. Mukohyama, and S. Tsujikawa, "Density perturbations in general modified gravitational theories," *Phys. Rev. D* **82** (2010) 023524, arXiv:1006.0281 [astro-ph.CO].

[303] S. Nesseris and D. Sapone, "Accuracy of the growth index in the presence of dark energy perturbations," *Phys. Rev. D* **92** no. 2, (2015) 023013, arXiv:1505.06601 [astro-ph.CO].

[304] J. M. Bardeen, "Gauge Invariant Cosmological Perturbations," *Phys. Rev. D* **22** (1980) 1882–1905.

[305] C.-P. Ma and E. Bertschinger, "Cosmological perturbation theory in the synchronous and conformal Newtonian gauges," *Astrophys. J.* **455** (1995) 7–25, arXiv:astro-ph/9506072.

[306] A. A. Starobinsky, "A New Type of Isotropic Cosmological Models Without Singularity," *Phys. Lett. B* **91** (1980) 99–102.

[307] A. H. Guth, "The Inflationary Universe: A Possible Solution to the Horizon and Flatness Problems," *Phys. Rev. D* **23** (1981) 347–356.

[308] D. Kazanas, "Dynamics of the Universe and Spontaneous Symmetry Breaking," *Astrophys. J. Lett.* **241** (1980) L59–L63.

[309] A. D. Linde, "A New Inflationary Universe Scenario: A Possible Solution of the Horizon, Flatness, Homogeneity, Isotropy and Primordial Monopole Problems," *Phys. Lett. B* **108** (1982) 389–393.

[310] A. Albrecht and P. J. Steinhardt, "Cosmology for Grand Unified Theories with Radiatively Induced Symmetry Breaking," *Phys. Rev. Lett.* **48** (1982) 1220–1223.

[311] F. Bernardeau, S. Colombi, E. Gaztanaga, and R. Scoccimarro, "Large scale structure of the universe and cosmological perturbation theory," *Phys. Rept.* **367** (2002) 1–248, arXiv:astro-ph/0112551.

[312] D. N. Schramm and M. S. Turner, "Big Bang Nucleosynthesis Enters the Precision Era," *Rev. Mod. Phys.* **70** (1998) 303–318, arXiv:astro-ph/9706069.

[313] G. Steigman, "Primordial Nucleosynthesis in the Precision Cosmology Era," *Ann. Rev. Nucl. Part. Sci.* **57** (2007) 463–491, arXiv:0712.1100 [astro-ph].

[314] F. Iocco, G. Mangano, G. Miele, O. Pisanti, and P. D. Serpico, "Primordial Nucleosynthesis: from precision cosmology to fundamental physics," *Phys. Rept.* **472** (2009) 1–76, arXiv:0809.0631 [astro-ph].

[315] R. H. Cyburt, B. D. Fields, K. A. Olive, and T.-H. Yeh, "Big Bang Nucleosynthesis: 2015," *Rev. Mod. Phys.* **88** (2016) 015004, arXiv:1505.01076 [astro-ph.CO].

[316] E. Bianchi and C. Rovelli, "Why all these prejudices against a constant?," arXiv:1002.3966 [astro-ph.CO].

[317] E. Kourkchi, R. B. Tully, G. S. Anand, H. M. Courtois, A. Dupuy, J. D. Neill, L. Rizzi, and M. Seibert, "Cosmicflows-4: The Calibration of Optical and Infrared Tully–Fisher Relations," *Astrophys. J.* **896** no. 1, (2020) 3, arXiv:2004.14499 [astro-ph.GA].

[318] J. Schombert, S. McGaugh, and F. Lelli, "Using the Baryonic Tully–Fisher Relation to Measure H o," *Astron. J.* **160** no. 2, (2020) 71, arXiv:2006.08615 [astro-ph.CO].

[319] T. de Jaeger, B. E. Stahl, W. Zheng, A. V. Filippenko, A. G. Riess, and L. Galbany, "A measurement of the Hubble constant from Type II supernovae," *Mon. Not. Roy. Astron. Soc.* **496** no. 3, (2020) 3402–3411, arXiv:2006.03412 [astro-ph.CO].

[320] K. Liao, A. Shafieloo, R. E. Keeley, and E. V. Linder, "A model-independent determination of the Hubble constant from lensed quasars and supernovae using Gaussian process regression," *Astrophys. J. Lett.* **886** no. 1, (2019) L23, arXiv:1908.04967 [astro-ph.CO].

[321] K. Liao, A. Shafieloo, R. E. Keeley, and E. V. Linder, "Determining Model-independent H 0 and Consistency Tests," *Astrophys. J. Lett.* **895** no. 2, (2020) L29, arXiv:2002.10605 [astro-ph.CO].

[322] W. L. Freedman *et al.*, "The Carnegie-Chicago Hubble Program. VIII. An Independent Determination of the Hubble Constant Based on the Tip of the Red Giant Branch," arXiv:1907.05922 [astro-ph.CO].

[323] W. L. Freedman, B. F. Madore, T. Hoyt, I. S. Jang, R. Beaton, M. G. Lee, A. Monson, J. Neeley, and J. Rich, "Calibration of the Tip of the Red Giant Branch (TRGB)," arXiv:2002.01550 [astro-ph.GA].

[324] D. Fernández Arenas, E. Terlevich, R. Terlevich, J. Melnick, R. Chávez, F. Bresolin, E. Telles, M. Plionis, and S. Basilakos, "An independent determination of the local Hubble constant," *Mon. Not. Roy. Astron. Soc.* **474** no. 1, (2018) 1250–1276, arXiv:1710.05951 [astro-ph.CO].

[325] K. Dutta, A. Roy, Ruchika, A. A. Sen, and M. M. Sheikh-Jabbari, "Cosmology with low-redshift observations: No signal for new physics," *Phys. Rev. D* **100** no. 10, (2019) 103501, arXiv:1908.07267 [astro-ph.CO].

[326] **LIGO Scientific, Virgo, 1M2H, Dark Energy Camera GW-E, DES, DLT40, Las Cumbres Observatory, VINROUGE, MASTER** Collaboration, B. P. Abbott *et al.*, "A gravitational-wave standard siren measurement of the Hubble constant," *Nature* **551** no. 7678, (2017) 85–88, arXiv:1710.05835 [astro-ph.CO].

[327] K. Hotokezaka, E. Nakar, O. Gottlieb, S. Nissanke, K. Masuda, G. Hallinan, K. P. Mooley, and A. T. Deller, "A Hubble constant measurement from superluminal motion of the jet in GW170817," *Nature Astron.* **3** no. 10, (2019) 940–944, arXiv:1806.10596 [astro-ph.CO].

[328] **LIGO Scientific, Virgo** Collaboration, R. Abbott *et al.*, "GW190814: Gravitational Waves from the Coalescence of a 23 Solar Mass Black Hole with a 2.6 Solar Mass Compact Object," *Astrophys. J. Lett.* **896** no. 2, (2020) L44, arXiv:2006.12611 [astro-ph.HE].

[329] **LIGO Scientific, VIRGO, KAGRA** Collaboration, R. Abbott *et al.*, "Constraints on the cosmic expansion history from GWTC-3," arXiv:2111.03604 [astro-ph.CO].

[330] H. Hildebrandt *et al.*, "KiDS+VIKING-450: Cosmic shear tomography with optical and infrared data," *Astron. Astrophys.* **633** (2020) A69, arXiv:1812.06076 [astro-ph.CO].

[331] S. Joudaki *et al.*, "KiDS+VIKING-450 and DES-Y1 combined: Cosmology with cosmic shear," *Astron. Astrophys.* **638** (2020) L1, arXiv:1906.09262 [astro-ph.CO].

[332] A. H. Wright, H. Hildebrandt, J. L. van den Busch, C. Heymans, B. Joachimi, A. Kannawadi, and K. Kuijken, "KiDS+VIKING-450: Improved cosmological parameter constraints from redshift calibration with self-organising maps," *Astron. Astrophys.* **640** (2020) L14, arXiv:2005.04207 [astro-ph.CO].

[333] **KiDS** Collaboration, M. Asgari *et al.*, "KiDS-1000 Cosmology: Cosmic shear constraints and comparison between two point statistics," *Astron. Astrophys.* **645** (2021) A104, arXiv:2007.15633 [astro-ph.CO].

[334] M. White *et al.*, "Cosmological constraints from the tomographic cross-correlation of DESI Luminous Red Galaxies and Planck CMB lensing," *JCAP* **02** no. 02, (2022) 007, arXiv:2111.09898 [astro-ph.CO].

[335] G. F. Lesci *et al.*, "AMICO galaxy clusters in KiDS-DR3: cosmological constraints from counts and stacked weak-lensing," arXiv:2012.12273 [astro-ph.CO].

[336] G. E. Addison, Y. Huang, D. J. Watts, C. L. Bennett, M. Halpern, G. Hinshaw, and J. L. Weiland, "Quantifying discordance in the 2015 Planck CMB spectrum," *Astrophys. J.* **818** no. 2, (2016) 132, arXiv:1511.00055 [astro-ph.CO].

[337] **Planck** Collaboration, N. Aghanim *et al.*, "Planck 2018 results. V. CMB power spectra and likelihoods," *Astron. Astrophys.* **641** (2020) A5, arXiv:1907.12875 [astro-ph.CO].

[338] G. E. Addison, D. J. Watts, C. L. Bennett, M. Halpern, G. Hinshaw, and J. L. Weiland, "Elucidating ΛCDM: Impact of Baryon Acoustic Oscillation Measurements on the Hubble Constant Discrepancy," *Astrophys. J.* **853** no. 2, (2018) 119, arXiv:1707.06547 [astro-ph.CO].

[339] A. Cuceu, J. Farr, P. Lemos, and A. Font-Ribera, "Baryon Acoustic Oscillations and the Hubble Constant: Past, Present and Future," *JCAP* **10** (2019) 044, arXiv:1906.11628 [astro-ph.CO].

[340] S. Nesseris and L. Perivolaropoulos, "A Comparison of cosmological models using recent supernova data," *Phys. Rev. D* **70** (2004) 043531, arXiv:astro-ph/0401556.

[341] G. Pantazis, S. Nesseris, and L. Perivolaropoulos, "Comparison of thawing and freezing dark energy parametrizations," *Phys. Rev. D* **93** no. 10, (2016) 103503, arXiv:1603.02164 [astro-ph.CO].

[342] J. Yoo and Y. Watanabe, "Theoretical Models of Dark Energy," *Int. J. Mod. Phys. D* **21** (2012) 1230002, arXiv:1212.4726 [astro-ph.CO].

[343] L. Perivolaropoulos, "Constraints on linear negative potentials in quintessence and phantom models from recent supernova data," *Phys. Rev. D* **71** (2005) 063503, arXiv:astro-ph/0412308.

[344] J. A. Frieman, C. T. Hill, A. Stebbins, and I. Waga, "Cosmology with ultralight pseudo Nambu-Goldstone bosons," *Phys. Rev. Lett.* **75** (1995) 2077–2080, arXiv:astro-ph/9505060.

[345] K. Choi, "String or M theory axion as a quintessence," *Phys. Rev. D* **62** (2000) 043509, arXiv:hep-ph/9902292.

[346] P. Brax and J. Martin, "Quintessence and supergravity," *Phys. Lett. B* **468** (1999) 40–45, arXiv:astro-ph/9905040.

[347] A. Albrecht and C. Skordis, "Phenomenology of a realistic accelerating universe using only Planck scale physics," *Phys. Rev. Lett.* **84** (2000) 2076–2079, arXiv:astro-ph/9908085.

[348] J. Garriga, L. Pogosian, and T. Vachaspati, "Forecasting cosmic doomsday from CMB / LSS cross - correlations," *Phys. Rev. D* **69** (2004) 063511, arXiv:astro-ph/0311412.

[349] R. R. Caldwell, M. Kamionkowski, and N. N. Weinberg, "Phantom energy and cosmic doomsday," *Phys. Rev. Lett.* **91** (2003) 071301, arXiv:astro-ph/0302506.

[350] S. Tsujikawa, "Dark energy: investigation and modeling," arXiv:1004.1493 [astro-ph.CO].

[351] K. Tomita, "A local void and the accelerating universe," *Mon. Not. Roy. Astron. Soc.* **326** (2001) 287, arXiv:astro-ph/0011484.

[352] D. J. Schwarz, "Accelerated expansion without dark energy," in *18th IAP Colloquium on the Nature of Dark Energy: Observational and Theoretical Results on the Accelerating Universe*. 9, 2002. arXiv:astro-ph/0209584.

[353] E. Barausse, S. Matarrese, and A. Riotto, "The Effect of inhomogeneities on the luminosity distance-redshift relation: Is dark energy necessary in a perturbed Universe?," *Phys. Rev. D* **71** (2005) 063537, arXiv:astro-ph/0501152.

[354] J. W. Moffat, "Cosmic microwave background, accelerating Universe and inhomogeneous cosmology," *JCAP* **10** (2005) 012, arXiv:astro-ph/0502110.

[355] D. L. Wiltshire, "Viable inhomogeneous model universe without dark energy from primordial inflation," arXiv:gr-qc/0503099.

[356] P. Hunt and S. Sarkar, "Constraints on large scale inhomogeneities from WMAP-5 and SDSS: confrontation with recent observations," *Mon. Not. Roy. Astron. Soc.* **401** (2010) 547, arXiv:0807.4508 [astro-ph].

[357] V. Marra and A. Notari, "Observational constraints on inhomogeneous cosmological models without dark energy," *Class. Quant. Grav.* **28** (2011) 164004, arXiv:1102.1015 [astro-ph.CO].

[358] J. Grande and L. Perivolaropoulos, "Generalized LTB model with Inhomogeneous Isotropic Dark Energy: Observational Constraints," *Phys. Rev. D* **84** (2011) 023514, arXiv:1103.4143 [astro-ph.CO].

[359] G. Lemaitre, "The expanding universe," *Annales Soc. Sci. Bruxelles A* **53** (1933) 51–85.

[360] R. C. Tolman, "Effect of imhomogeneity on cosmological models," *Proc. Nat. Acad. Sci.* **20** (1934) 169–176.

[361] H. Bondi, "Spherically symmetrical models in general relativity," *Mon. Not. Roy. Astron. Soc.* **107** (1947) 410–425.

[362] G. D'Amico, C. de Rham, S. Dubovsky, G. Gabadadze, D. Pirtskhalava, and A. J. Tolley, "Massive Cosmologies," *Phys. Rev. D* **84** (2011) 124046, arXiv:1108.5231 [hep-th].

[363] G. D'Amico, G. Gabadadze, L. Hui, and D. Pirtskhalava, "Quasidilaton: Theory and cosmology," *Phys. Rev. D* **87** (2013) 064037, arXiv:1206.4253 [hep-th].

[364] Q.-G. Huang, Y.-S. Piao, and S.-Y. Zhou, "Mass-Varying Massive Gravity," *Phys. Rev. D* **86** (2012) 124014, arXiv:1206.5678 [hep-th].

[365] G. Leon, J. Saavedra, and E. N. Saridakis, "Cosmological behavior in extended nonlinear massive gravity," *Class. Quant. Grav.* **30** (2013) 135001, arXiv:1301.7419 [astro-ph.CO].

[366] C. G. Callan, Jr., E. J. Martinec, M. J. Perry, and D. Friedan, "Strings in Background Fields," *Nucl. Phys. B* **262** (1985) 593–609.

[367] E. S. Fradkin and A. A. Tseytlin, "Quantum String Theory Effective Action," *Nucl. Phys. B* **261** (1985) 1–27. [Erratum: Nucl.Phys.B 269, 745–745 (1986)].

[368] R. P. Woodard, "Avoiding dark energy with 1/r modifications of gravity," *Lect. Notes Phys.* **720** (2007) 403–433, arXiv:astro-ph/0601672.

[369] F. W. Hehl, P. Von Der Heyde, G. D. Kerlick, and J. M. Nester, "General Relativity with Spin and Torsion: Foundations and Prospects," *Rev. Mod. Phys.* **48** (1976) 393–416.

[370] C. G. Tsagas, "Large-scale peculiar motions and cosmic acceleration," *Mon. Not. Roy. Astron. Soc.* **405** (2010) 503, arXiv:0902.3232 [astro-ph.CO].

[371] C. G. Tsagas, "Peculiar motions, accelerated expansion and the cosmological axis," *Phys. Rev. D* **84** (2011) 063503, arXiv:1107.4045 [astro-ph.CO].

[372] C. G. Tsagas and M. I. Kadiltzoglou, "Deceleration parameter in tilted Friedmann universes," *Phys. Rev. D* **92** no. 4, (2015) 043515, arXiv:1507.04266 [gr-qc].

[373] R. Watkins, H. A. Feldman, and M. J. Hudson, "Consistently Large Cosmic Flows on Scales of 100 Mpc/h: a Challenge for the Standard LCDM Cosmology," *Mon. Not. Roy. Astron. Soc.* **392** (2009) 743–756, arXiv:0809.4041 [astro-ph].

[374] A. Nusser and M. Davis, "The cosmological bulk flow: consistency with ΛCDM and $z \approx 0$ constraints on σ_8 and γ," *Astrophys. J.* **736** (2011) 93, arXiv:1101.1650 [astro-ph.CO].

[375] J. Colin, R. Mohayaee, S. Sarkar, and A. Shafieloo, "Probing the anisotropic local universe and beyond with SNe Ia data," *Mon. Not. Roy. Astron. Soc.* **414** (2011) 264–271, arXiv:1011.6292 [astro-ph.CO].

[376] M. I. Scrimgeour *et al.*, "The 6dF Galaxy Survey: Bulk Flows on $50 - 70h^{-1}$ Mpc scales," *Mon. Not. Roy. Astron. Soc.* **455** no. 1, (2016) 386–401, arXiv:1511.06930 [astro-ph.CO].

[377] J. Ehlers, "Contributions to the relativistic mechanics of continuous media," *Abh. Akad. Wiss. Lit. Mainz. Nat. Kl.* **11** (1961) 793–837.

[378] G. F. R. Ellis, *Cargese lectures in Physics*. Gordon and Breach., 1973.

[379] C. G. Tsagas, A. Challinor, and R. Maartens, "Relativistic cosmology and large-scale structure," *Physics Reports* **465** (2007) 61–147.

[380] G. F. R. Ellis, R. Maartens, and M. A. H. MacCallum, *Relativistic Cosmology*. Cambridge University Press, 2012.

[381] R. Maartens, "Covariant velocity and density perturbations in quasiNewtonian cosmologies," *Phys. Rev. D* **58** (1998) 124006, arXiv:astro-ph/9808235.

[382] C. G. Tsagas, "The peculiar Jeans length," *Eur. Phys. J. C* **81** no. 8, (2021) 753, arXiv:2103.15884 [gr-qc].

[383] K. Asvesta, L. Kazantzidis, L. Perivolaropoulos, and C. G. Tsagas, "Observational constraints on the deceleration parameter in a tilted universe," arXiv:2202.00962 [astro-ph.CO].

[384] Y.-G. Gong and A. Wang, "Reconstruction of the deceleration parameter and the equation of state of dark energy," *Phys. Rev. D* **75** (2007) 043520, arXiv:astro-ph/0612196.

[385] N. Kaiser, "Clustering in real space and in redshift space," *Mon. Not. Roy. Astron. Soc.* **227** (1987) 1–27.

[386] A. J. S. Hamilton, "Linear redshift distortions: A Review," in *Ringberg Workshop on Large Scale Structure*. 8, 1997. arXiv:astro-ph/9708102.

[387] S. Saito, "Lecture notes in cosmology," June, 2016.

[388] J. C. Jackson, "A Critique of Rees's Theory of Primordial Gravitational Radiation," *Monthly Notices of the Royal Astronomical Society* **156** no. 1, (02, 1972) 1P–5P. https://doi.org/10.1093/mnras/156.1.1P.

[389] N. Padmanabhan and M. J. White, "Constraining Anisotropic Baryon Oscillations," *Phys. Rev. D* **77** (2008) 123540, arXiv:0804.0799 [astro-ph].

[390] X.-D. Li, C. Park, C. G. Sabiu, H. Park, D. H. Weinberg, D. P. Schneider, J. Kim, and S. E. Hong, "Cosmological constraints from the redshift dependence of the Alcock-Paczynski effect: application to the SDSS-III BOSS DR12 galaxies," *Astrophys. J.* **832** no. 2, (2016) 103, arXiv:1609.05476 [astro-ph.CO].

[391] M. J. Wilson, "Geometric and growth rate tests of General Relativity with recovered linear cosmological perturbations," other thesis, 10, 2016.

[392] S. Alam, S. Ho, and A. Silvestri, "Testing deviations from ΛCDM with growth rate measurements from six large-scale structure surveys at z =0.06–1," *Mon. Not. Roy. Astron. Soc.* **456** no. 4, (2016) 3743–3756, arXiv:1509.05034 [astro-ph.CO].

[393] C. Alcock and B. Paczynski, "An evolution free test for non-zero cosmological constant," *Nature* **281** (1979) 358–359.

[394] **Planck** Collaboration, P. A. R. Ade *et al.*, "Planck 2013 results. I. Overview of products and scientific results," *Astron. Astrophys.* **571** (2014) A1, arXiv:1303.5062 [astro-ph.CO].

[395] **2dFGRS** Collaboration, W. J. Percival *et al.*, "The 2dF Galaxy Redshift Survey: Spherical harmonics analysis of fluctuations in the final catalogue," *Mon. Not. Roy. Astron. Soc.* **353** (2004) 1201, arXiv:astro-ph/0406513.

[396] Y.-S. Song and W. J. Percival, "Reconstructing the history of structure formation using Redshift Distortions," *JCAP* **10** (2009) 004, arXiv:0807.0810 [astro-ph].

[397] **SDSS** Collaboration, M. Tegmark *et al.*, "Cosmological Constraints from the SDSS Luminous Red Galaxies," *Phys. Rev. D* **74** (2006) 123507, arXiv:astro-ph/0608632.

[398] L. Guzzo *et al.*, "A test of the nature of cosmic acceleration using galaxy redshift distortions," *Nature* **451** (2008) 541–545, arXiv:0802.1944 [astro-ph].

[399] M. Davis, A. Nusser, K. Masters, C. Springob, J. P. Huchra, and G. Lemson, "Local Gravity versus Local Velocity: Solutions for β and nonlinear bias," *Mon. Not. Roy. Astron. Soc.* **413** (2011) 2906, arXiv:1011.3114 [astro-ph.CO].

[400] M. J. Hudson and S. J. Turnbull, "The growth rate of cosmic structure from peculiar velocities at low and high redshifts," *Astrophys. J. Lett.* **751** (2013) L30, arXiv:1203.4814 [astro-ph.CO].

[401] S. J. Turnbull, M. J. Hudson, H. A. Feldman, M. Hicken, R. P. Kirshner, and R. Watkins, "Cosmic flows in the nearby universe from Type Ia Supernovae," *Mon. Not. Roy. Astron. Soc.* **420** (2012) 447–454, arXiv:1111.0631 [astro-ph.CO].

[402] L. Samushia, W. J. Percival, and A. Raccanelli, "Interpreting large-scale redshift-space distortion measurements," *Mon. Not. Roy. Astron. Soc.* **420** (2012) 2102–2119, arXiv:1102.1014 [astro-ph.CO].

[403] F. Beutler, C. Blake, M. Colless, D. H. Jones, L. Staveley-Smith, G. B. Poole, L. Campbell, Q. Parker, W. Saunders, and F. Watson, "The 6dF Galaxy Survey: $z \approx 0$ measurement of the growth rate and σ_8," *Mon. Not. Roy. Astron. Soc.* **423** (2012) 3430–3444, arXiv:1204.4725 [astro-ph.CO].

[404] C. Blake *et al.*, "The WiggleZ Dark Energy Survey: Joint measurements of the expansion and growth history at z < 1," *Mon. Not. Roy. Astron. Soc.* **425** (2012) 405–414, arXiv:1204.3674 [astro-ph.CO].

[405] R. Tojeiro *et al.*, "The clustering of galaxies in the SDSS-III Baryon Oscillation Spectroscopic Survey: measuring structure growth using passive galaxies," *Mon. Not. Roy. Astron. Soc.* **424** (2012) 2339, arXiv:1203.6565 [astro-ph.CO].

[406] S. de la Torre *et al.*, "The VIMOS Public Extragalactic Redshift Survey (VIPERS). Galaxy clustering and redshift-space distortions at z=0.8 in the first data release," *Astron. Astrophys.* **557** (2013) A54, arXiv:1303.2622 [astro-ph.CO].

[407] C.-H. Chuang and Y. Wang, "Modeling the Anisotropic Two-Point Galaxy Correlation Function on Small Scales and Improved Measurements of $H(z)$, $D_A(z)$, and $\beta(z)$ from the Sloan Digital Sky Survey DR7 Luminous Red Galaxies," *Mon. Not. Roy. Astron. Soc.* **435** (2013) 255–262, arXiv:1209.0210 [astro-ph.CO].

[408] C. Blake *et al.*, "Galaxy And Mass Assembly (GAMA): improved cosmic growth measurements using multiple tracers of large-scale structure," *Mon. Not. Roy. Astron. Soc.* **436** (2013) 3089, arXiv:1309.5556 [astro-ph.CO].

[409] A. G. Sanchez *et al.*, "The clustering of galaxies in the SDSS-III Baryon Oscillation Spectroscopic Survey: cosmological implications of the full shape of the clustering wedges in the data release 10 and 11 galaxy samples," *Mon. Not. Roy. Astron. Soc.* **440** no. 3, (2014) 2692–2713, arXiv:1312.4854 [astro-ph.CO].

[410] C. Howlett, A. Ross, L. Samushia, W. Percival, and M. Manera, "The clustering of the SDSS main galaxy sample – II. Mock galaxy catalogues and a measurement of the growth of structure from redshift space distortions at $z = 0.15$" *Mon. Not. Roy. Astron. Soc.* **449** no. 1, (2015) 848–866, arXiv:1409.3238 [astro-ph.CO].

[411] M. Feix, A. Nusser, and E. Branchini, "Growth Rate of Cosmological Perturbations at z∼0.1 from a New Observational Test," *Phys. Rev. Lett.* **115** no. 1, (2015) 011301, arXiv:1503.05945 [astro-ph.CO].

[412] T. Okumura *et al.*, "The Subaru FMOS galaxy redshift survey (FastSound). IV. New constraint on gravity theory from redshift space distortions at $z \sim 1.4$," *Publ. Astron. Soc. Jap.* **68** no. 3, (2016) 38, arXiv:1511.08083 [astro-ph.CO].

[413] C.-H. Chuang *et al.*, "The clustering of galaxies in the SDSS-III Baryon Oscillation Spectroscopic Survey: single-probe measurements from CMASS anisotropic galaxy clustering," *Mon. Not. Roy. Astron. Soc.* **461** no. 4, (2016) 3781–3793, arXiv:1312.4889 [astro-ph.CO].

[414] **BOSS** Collaboration, F. Beutler *et al.*, "The clustering of galaxies in the completed SDSS-III Baryon Oscillation Spectroscopic Survey: Anisotropic galaxy clustering in Fourier-space," *Mon. Not. Roy. Astron. Soc.* **466** no. 2, (2017) 2242–2260, arXiv:1607.03150 [astro-ph.CO].

[415] H. Gil-Marín, W. J. Percival, L. Verde, J. R. Brownstein, C.-H. Chuang, F.-S. Kitaura, S. A. Rodríguez-Torres, and M. D. Olmstead, "The clustering of galaxies in the SDSS-III Baryon Oscillation Spectroscopic Survey: RSD measurement from the power spectrum and bispectrum of the DR12 BOSS galaxies," *Mon. Not. Roy. Astron. Soc.* **465** no. 2, (2017) 1757–1788, arXiv:1606.00439 [astro-ph.CO].

[416] A. J. Hawken *et al.*, "The VIMOS Public Extragalactic Redshift Survey: Measuring the growth rate of structure around cosmic voids," *Astron. Astrophys.* **607** (2017) A54, arXiv:1611.07046 [astro-ph.CO].

[417] D. Huterer, D. Shafer, D. Scolnic, and F. Schmidt, "Testing ΛCDM at the lowest redshifts with SN Ia and galaxy velocities," *JCAP* **05** (2017) 015, arXiv:1611.09862 [astro-ph.CO].

[418] S. de la Torre *et al.*, "The VIMOS Public Extragalactic Redshift Survey (VIPERS). Gravity test from the combination of redshift-space distortions and galaxy-galaxy lensing at $0.5 < z < 1.2$," *Astron. Astrophys.* **608** (2017) A44, arXiv:1612.05647 [astro-ph.CO].

[419] A. Pezzotta *et al.*, "The VIMOS Public Extragalactic Redshift Survey (VIPERS): The growth of structure at $0.5 < z < 1.2$ from redshift-space distortions in the clustering of the PDR-2 final sample," *Astron. Astrophys.* **604** (2017) A33, arXiv:1612.05645 [astro-ph.CO].

[420] M. Feix, E. Branchini, and A. Nusser, "Speed from light: growth rate and bulk flow at z $\sim$ 0.1 from improved SDSS DR13 photometry," *Mon. Not. Roy. Astron. Soc.* **468** no. 2, (2017) 1420–1425, arXiv:1612.07809 [astro-ph.CO].

[421] C. Howlett, L. Staveley-Smith, P. J. Elahi, T. Hong, T. H. Jarrett, D. H. Jones, B. S. Koribalski, L. M. Macri, K. L. Masters, and C. M. Springob, "2MTF – VI. Measuring the velocity power spectrum," *Mon. Not. Roy. Astron. Soc.* **471** no. 3, (2017) 3135–3151, arXiv:1706.05130 [astro-ph.CO].

[422] F. G. Mohammad *et al.*, "The VIMOS Public Extragalactic Redshift Survey (VIPERS). An unbiased estimate of the growth rate of structure at $\langle z \rangle = 0.85$ using the clustering of luminous blue galaxies," *Astron. Astrophys.* **610** (2018) A59, arXiv:1708.00026 [astro-ph.CO].

[423] Y. Wang, G.-B. Zhao, C.-H. Chuang, M. Pellejero-Ibanez, C. Zhao, F.-S. Kitaura, and S. Rodriguez-Torres, "The clustering of galaxies in the completed SDSS-III Baryon Oscillation Spectroscopic Survey: a tomographic analysis of structure growth and expansion rate from anisotropic galaxy clustering," *Mon. Not. Roy. Astron. Soc.* **481** no. 3, (2018) 3160–3166, arXiv:1709.05173 [astro-ph.CO].

[424] F. Shi *et al.*, "Mapping the Real Space Distributions of Galaxies in SDSS DR7: II. Measuring the growth rate, clustering amplitude of matter and biases of galaxies at redshift 0.1," *Astrophys. J.* **861** no. 2, (2018) 137, arXiv:1712.04163 [astro-ph.CO].

[425] H. Gil-Marín *et al.*, "The clustering of the SDSS-IV extended Baryon Oscillation Spectroscopic Survey DR14 quasar sample: structure growth rate measurement from the anisotropic quasar power spectrum in the redshift range $0.8 < z < 2.2$," *Mon. Not. Roy. Astron. Soc.* **477** no. 2, (2018) 1604–1638, arXiv:1801.02689 [astro-ph.CO].

[426] J. Hou *et al.*, "The clustering of the SDSS-IV extended Baryon Oscillation Spectroscopic Survey DR14 quasar sample: anisotropic clustering analysis in configuration-space," *Mon. Not. Roy. Astron. Soc.* **480** no. 2, (2018) 2521–2534, arXiv:1801.02656 [astro-ph.CO].

[427] G.-B. Zhao *et al.*, "The clustering of the SDSS-IV extended Baryon Oscillation Spectroscopic Survey DR14 quasar sample: a tomographic measurement of cosmic structure growth and expansion rate based on optimal redshift weights," *Mon. Not. Roy. Astron. Soc.* **482** no. 3, (2019) 3497–3513, arXiv:1801.03043 [astro-ph.CO].

[428] S. Nesseris and L. Perivolaropoulos, "Testing Lambda CDM with the Growth Function delta(a): Current Constraints," *Phys. Rev. D* **77** (2008) 023504, arXiv:0710.1092 [astro-ph].

[429] B. C. Paul and P. Thakur, "Observational constraints on modified Chaplygin gas from cosmic growth," *JCAP* **11** (2013) 052, arXiv:1306.4808 [astro-ph.CO].

[430] A. Pouri, S. Basilakos, and M. Plionis, "Precision growth index using the clustering of cosmic structures and growth data," *JCAP* **08** (2014) 042, arXiv:1402.0964 [astro-ph.CO].

[431] S. Nesseris and D. Sapone, "Novel null-test for the Λ cold dark matter model with growth-rate data," *Int. J. Mod. Phys. D* **24** no. 06, (2015) 1550045, arXiv:1409.3697 [astro-ph.CO].

[432] T. Baker, P. G. Ferreira, C. D. Leonard, and M. Motta, "New Gravitational Scales in Cosmological Surveys," *Phys. Rev. D* **90** no. 12, (2014) 124030, arXiv:1409.8284 [astro-ph.CO].

[433] S. Basilakos, "The growth index of matter perturbations using the clustering of dark energy," *Mon. Not. Roy. Astron. Soc.* **449** no. 2, (2015) 2151–2155, arXiv:1412.2234 [astro-ph.CO].

[434] A. Mehrabi, S. Basilakos, M. Malekjani, and Z. Davari, "Growth of matter perturbations in clustered holographic dark energy cosmologies," *Phys. Rev. D* **92** no. 12, (2015) 123513, arXiv:1510.03996 [astro-ph.CO].

[435] J. Pérez-Romero and S. Nesseris, "Cosmological constraints and comparison of viable $f(R)$ models," *Phys. Rev. D* **97** no. 2, (2018) 023525, arXiv:1710.05634 [astro-ph.CO].

[436] A. Gomez-Valent and J. Sola, "Relaxing the σ_8-tension through running vacuum in the Universe," *EPL* **120** no. 3, (2017) 39001, arXiv:1711.00692 [astro-ph.CO].

[437] B. L'Huillier, A. Shafieloo, and H. Kim, "Model-independent cosmological constraints from growth and expansion," *Mon. Not. Roy. Astron. Soc.* **476** no. 3, (2018) 3263–3268, arXiv:1712.04865 [astro-ph.CO].

[438] L. Amendola, V. Marra, and M. Quartin, "Internal Robustness: systematic search for systematic bias in SN Ia data," *Mon. Not. Roy. Astron. Soc.* **430** (2013) 1867–1879, arXiv:1209.1897 [astro-ph.CO].

[439] C. J. Copi, A. N. Davis, and L. M. Krauss, "A New nucleosynthesis constraint on the variation of G," *Phys. Rev. Lett.* **92** (2004) 171301, arXiv:astro-ph/0311334.

[440] D. Larson *et al.*, "Seven-Year Wilkinson Microwave Anisotropy Probe (WMAP) Observations: Power Spectra and WMAP-Derived Parameters," *Astrophys. J. Suppl.* **192** (2011) 16, arXiv:1001.4635 [astro-ph.CO].

[441] V. Silveira and I. Waga, "Decaying Lambda cosmologies and power spectrum," *Phys. Rev. D* **50** (1994) 4890–4894.

[442] W. J. Percival, "Cosmological structure formation in a homogeneous dark energy background," *Astron. Astrophys.* **443** (2005) 819, arXiv:astro-ph/0508156.

[443] A. Bueno belloso, J. Garcia-Bellido, and D. Sapone, "A parametrization of the growth index of matter perturbations in various Dark Energy models and observational prospects using a Euclid-like survey," *JCAP* **10** (2011) 010, arXiv:1105.4825 [astro-ph.CO].

[444] L.-M. Wang and P. J. Steinhardt, "Cluster abundance constraints on quintessence models," *Astrophys. J.* **508** (1998) 483–490, arXiv:astro-ph/9804015.

[445] E. V. Linder, "Cosmic growth history and expansion history," *Phys. Rev. D* **72** (2005) 043529, arXiv:astro-ph/0507263.

[446] D. Polarski and R. Gannouji, "On the growth of linear perturbations," *Phys. Lett. B* **660** (2008) 439–443, arXiv:0710.1510 [astro-ph].

[447] R. Gannouji and D. Polarski, "The growth of matter perturbations in some scalar-tensor DE models," *JCAP* **05** (2008) 018, arXiv:0802.4196 [astro-ph].

[448] D. Polarski, A. A. Starobinsky, and H. Giacomini, "When is the growth index constant?," *JCAP* **12** (2016) 037, arXiv:1610.00363 [astro-ph.CO].

[449] W. H. Press, S. A. Teukolsky, W. T. Vetterling, and B. P. Flannery, *Numerical Recipes 3rd Edition: The Art of Scientific Computing*. Cambridge University Press, USA, 3 ed., 2007.

[450] M. O. Farooq, "Observational constraints on dark energy cosmological model parameters," other thesis, 9, 2013.

[451] R. Gannouji, B. Moraes, and D. Polarski, "The growth of matter perturbations in f(R) models," *JCAP* **02** (2009) 034, arXiv:0809.3374 [astro-ph].

[452] R. Gannouji, L. Kazantzidis, L. Perivolaropoulos, and D. Polarski, "Consistency of modified gravity with a decreasing $G_{\rm eff}(z)$ in a ΛCDM background," *Phys. Rev. D* **98** no. 10, (2018) 104044, arXiv:1809.07034 [gr-qc].

[453] R. Gannouji and D. Polarski, "Consistency of the expansion of the Universe with density perturbations," *Phys. Rev. D* **98** no. 8, (2018) 083533, arXiv:1805.08230 [astro-ph.CO].

[454] L. Amendola, P. S. Corasaniti, and F. Occhionero, "Time variability of the gravitational constant and type Ia supernovae," arXiv:astro-ph/9907222.

[455] E. Gaztanaga, E. Garcia-Berro, J. Isern, E. Bravo, and I. Dominguez, "Bounds on the possible evolution of the gravitational constant from cosmological type Ia supernovae," *Phys. Rev. D* **65** (2002) 023506, arXiv:astro-ph/0109299.

[456] S. Nesseris and L. Perivolaropoulos, "Evolving newton's constant, extended gravity theories and snia data analysis," *Phys. Rev. D* **73** (2006) 103511, arXiv:astro-ph/0602053.

[457] B. S. Wright and B. Li, "Type Ia supernovae, standardizable candles, and gravity," *Phys. Rev. D* **97** no. 8, (2018) 083505, arXiv:1710.07018 [astro-ph.CO].

[458] D. Sapone, S. Nesseris, and C. A. P. Bengaly, "Is there any measurable redshift dependence on the SN Ia absolute magnitude?," *Phys. Dark Univ.* **32** (2021) 100814, arXiv:2006.05461 [astro-ph.CO].

[459] T. Giannantonio, M. Martinelli, A. Silvestri, and A. Melchiorri, "New constraints on parametrised modified gravity from correlations of the CMB with large scale structure," *JCAP* **04** (2010) 030, arXiv:0909.2045 [astro-ph.CO].

[460] L. Pogosian, P. S. Corasaniti, C. Stephan-Otto, R. Crittenden, and R. Nichol, "Tracking dark energy with the ISW effect: Short and long-term predictions," *Phys. Rev. D* **72** (2005) 103519, arXiv:astro-ph/0506396.

[461] S. Ho, C. Hirata, N. Padmanabhan, U. Seljak, and N. Bahcall, "Correlation of CMB with large-scale structure: I. ISW Tomography and Cosmological Implications," *Phys. Rev. D* **78** (2008) 043519, arXiv:0801.0642 [astro-ph].

[462] A. Lewis, A. Challinor, and A. Lasenby, "Efficient computation of CMB anisotropies in closed FRW models," *Astrophys. J.* **538** (2000) 473–476, arXiv:astro-ph/9911177.

[463] J. Lesgourgues, "The Cosmic Linear Anisotropy Solving System (CLASS) I: Overview," arXiv:1104.2932 [astro-ph.IM].

[464] D. Blas, J. Lesgourgues, and T. Tram, "The Cosmic Linear Anisotropy Solving System (CLASS) II: Approximation schemes," *JCAP* **07** (2011) 034, arXiv:1104.2933 [astro-ph.CO].

[465] G.-B. Zhao, L. Pogosian, A. Silvestri, and J. Zylberberg, "Searching for modified growth patterns with tomographic surveys," *Phys. Rev. D* **79** (2009) 083513, arXiv:0809.3791 [astro-ph].

[466] A. Hojjati, L. Pogosian, and G.-B. Zhao, "Testing gravity with CAMB and CosmoMC," *JCAP* **08** (2011) 005, arXiv:1106.4543 [astro-ph.CO].

[467] A. Zucca, L. Pogosian, A. Silvestri, and G.-B. Zhao, "MGCAMB with massive neutrinos and dynamical dark energy," *JCAP* **05** (2019) 001, arXiv:1901.05956 [astro-ph.CO].

[468] M. Zumalacárregui, E. Bellini, I. Sawicki, J. Lesgourgues, and P. G. Ferreira, "hi_class: Horndeski in the Cosmic Linear Anisotropy Solving System," *JCAP* **08** (2017) 019, arXiv:1605.06102 [astro-ph.CO].

[469] E. Bellini, I. Sawicki, and M. Zumalacárregui, "hi_class: Background Evolution, Initial Conditions and Approximation Schemes," *JCAP* **02** (2020) 008, arXiv:1909.01828 [astro-ph.CO].

[470] A. Lewis and S. Bridle, "Cosmological parameters from CMB and other data: A Monte Carlo approach," *Phys. Rev. D* **66** (2002) 103511, arXiv:astro-ph/0205436.

[471] A. Lewis, "Efficient sampling of fast and slow cosmological parameters," *Phys. Rev. D* **87** no. 10, (2013) 103529, arXiv:1304.4473 [astro-ph.CO].

[472] S. Nesseris, C. Blake, T. Davis, and D. Parkinson, "The WiggleZ Dark Energy Survey: constraining the evolution of Newton's constant using the growth rate of structure," *JCAP* **07** (2011) 037, arXiv:1107.3659 [astro-ph.CO].

[473] S. Nesseris and J. Garcia-Bellido, "A new perspective on Dark Energy modeling via Genetic Algorithms," *JCAP* **11** (2012) 033, arXiv:1205.0364 [astro-ph.CO].

[474] L. Kazantzidis, L. Perivolaropoulos, and F. Skara, "Constraining power of cosmological observables: blind redshift spots and optimal ranges," *Phys. Rev. D* **99** no. 6, (2019) 063537, arXiv:1812.05356 [astro-ph.CO].

[475] H. A. Feldman, N. Kaiser, and J. A. Peacock, "Power spectrum analysis of three-dimensional redshift surveys," *Astrophys. J.* **426** (1994) 23–37, arXiv:astro-ph/9304022.

[476] S. F. Huelga, C. Macchiavello, T. Pellizzari, A. K. Ekert, M. B. Plenio, and J. I. Cirac, "On the improvement of frequency standards with quantum entanglement," *Phys. Rev. Lett.* **79** (1997) 3865, arXiv:quant-ph/9707014.

[477] F. B. Abdalla and S. Rawlings, "Probing dark energy with baryonic oscillations and future radio surveys of neutral hydrogen," *Mon. Not. Roy. Astron. Soc.* **360** (2005) 27–40, arXiv:astro-ph/0411342.

[478] A. R. Duffy, "Probing the nature of dark energy through galaxy redshift surveys with radio telescopes," *Annalen Phys.* **526** (2014) 283–293, arXiv:1405.7465 [astro-ph.CO].

[479] L. Amendola *et al.*, "Cosmology and fundamental physics with the Euclid satellite," *Living Rev. Rel.* **21** no. 1, (2018) 2, arXiv:1606.00180 [astro-ph.CO].

[480] D. J. Eisenstein, H.-j. Seo, and M. J. White, "On the Robustness of the Acoustic Scale in the Low-Redshift Clustering of Matter," *Astrophys. J.* **664** (2007) 660–674, arXiv:astro-ph/0604361.

[481] **SDSS** Collaboration, D. J. Eisenstein *et al.*, "Detection of the Baryon Acoustic Peak in the Large-Scale Correlation Function of SDSS Luminous Red Galaxies," *Astrophys. J.* **633** (2005) 560–574, arXiv:astro-ph/0501171.

[482] **2dFGRS** Collaboration, S. Cole *et al.*, "The 2dF Galaxy Redshift Survey: Power-spectrum analysis of the final dataset and cosmological implications," *Mon. Not. Roy. Astron. Soc.* **362** (2005) 505–534, arXiv:astro-ph/0501174.

[483] P. J. E. Peebles, *The large-scale structure of the universe*. 1980.

[484] D. J. Eisenstein and W. Hu, "Baryonic features in the matter transfer function," *Astrophys. J.* **496** (1998) 605, arXiv:astro-ph/9709112.

[485] J. Hamann, S. Hannestad, J. Lesgourgues, C. Rampf, and Y. Y. Y. Wong, "Cosmological parameters from large scale structure - geometric versus shape information," *JCAP* **07** (2010) 022, arXiv:1003.3999 [astro-ph.CO].

[486] J. E. Bautista *et al.*, "Measurement of baryon acoustic oscillation correlations at $z = 2.3$ with SDSS DR12 Lyα-Forests," *Astron. Astrophys.* **603** (2017) A12, arXiv:1702.00176 [astro-ph.CO].

[487] M. Moresco, L. Pozzetti, A. Cimatti, R. Jimenez, C. Maraston, L. Verde, D. Thomas, A. Citro, R. Tojeiro, and D. Wilkinson, "A 6% measurement of the Hubble parameter at $z \sim 0.45$: direct evidence of the epoch of cosmic re-acceleration," *JCAP* **05** (2016) 014, arXiv:1601.01701 [astro-ph.CO].

[488] N. Borghi, M. Moresco, and A. Cimatti, "Towards a Better Understanding of Cosmic Chronometers: A new measurement of $H(z)$ at $z \sim 0.7$," arXiv:2110.04304 [astro-ph.CO].

[489] E. A. Kazin *et al.*, "The WiggleZ Dark Energy Survey: improved distance measurements to z = 1 with reconstruction of the baryonic acoustic feature," *Mon. Not. Roy. Astron. Soc.* **441** no. 4, (2014) 3524–3542, arXiv:1401.0358 [astro-ph.CO].

[490] P. A. Mazzali, F. K. Ropke, S. Benetti, and W. Hillebrandt, "A Common Explosion Mechanism for Type Ia Supernovae," *Science* **315** (2007) 825, arXiv:astro-ph/0702351.

[491] B. F. Schutz, "Determining the Hubble constant from gravitational wave observations," *Nature* **323** no. 6086, (Sept., 1986) 310–311.

[492] D. E. Holz and S. A. Hughes, "Using gravitational-wave standard sirens," *Astrophys. J.* **629** (2005) 15–22, arXiv:astro-ph/0504616.

[493] N. Dalal, D. E. Holz, S. A. Hughes, and B. Jain, "Short grb and binary black hole standard sirens as a probe of dark energy," *Phys. Rev. D* **74** (2006) 063006, arXiv:astro-ph/0601275.

[494] S. Nissanke, D. E. Holz, N. Dalal, S. A. Hughes, J. L. Sievers, and C. M. Hirata, "Determining the Hubble constant from gravitational wave observations of merging compact binaries," arXiv:1307.2638 [astro-ph.CO].

[495] E. Garcia-Berro, E. Gaztanaga, J. Isern, O. Benvenuto, and L. Althaus, "On the evolution of cosmological type ia supernovae and the gravitational constant," arXiv:astro-ph/9907440.

[496] E. Belgacem, Y. Dirian, S. Foffa, and M. Maggiore, "Gravitational-wave luminosity distance in modified gravity theories," *Phys. Rev. D* **97** no. 10, (2018) 104066, arXiv:1712.08108 [astro-ph.CO].

[497] L. Kazantzidis, H. Koo, S. Nesseris, L. Perivolaropoulos, and A. Shafieloo, "Hints for possible low redshift oscillation around the best-fitting ΛCDM model in the expansion history of the Universe," *Mon. Not. Roy. Astron. Soc.* **501** no. 3, (2021) 3421–3426, arXiv:2010.03491 [astro-ph.CO].

[498] **SNLS** Collaboration, A. Conley *et al.*, "Supernova Constraints and Systematic Uncertainties from the First 3 Years of the Supernova Legacy Survey," *Astrophys. J. Suppl.* **192** (2011) 1, arXiv:1104.1443 [astro-ph.CO].

[499] N. Kaiser and M. J. Hudson, "On the perturbation of the luminosity distance by peculiar motions," *Mon. Not. Roy. Astron. Soc.* **450** no. 1, (2015) 883–895, arXiv:1411.6339 [astro-ph.CO].

[500] D. Zhao, Y. Zhou, and Z. Chang, "Anisotropy of the Universe via the Pantheon supernovae sample revisited," *Mon. Not. Roy. Astron. Soc.* **486** no. 4, (2019) 5679–5689, arXiv:1903.12401 [astro-ph.CO].

[501] A. G. Riess, S. Casertano, W. Yuan, L. M. Macri, and D. Scolnic, "Large Magellanic Cloud Cepheid Standards Provide a 1% Foundation for the Determination of the Hubble Constant and Stronger Evidence for Physics beyond ΛCDM," *Astrophys. J.* **876** no. 1, (2019) 85, arXiv:1903.07603 [astro-ph.CO].

[502] I. Antoniou and L. Perivolaropoulos, "Searching for a Cosmological Preferred Axis: Union2 Data Analysis and Comparison with Other Probes," *JCAP* **12** (2010) 012, arXiv:1007.4347 [astro-ph.CO].

[503] E. O. Colgáin, "A hint of matter underdensity at low z?," *JCAP* **09** (2019) 006, arXiv:1903.11743 [astro-ph.CO].

[504] D. J. Schwarz and B. Weinhorst, "(An)isotropy of the Hubble diagram: Comparing hemispheres," *Astron. Astrophys.* **474** (2007) 717–729, arXiv:0706.0165 [astro-ph].

[505] R.-G. Cai and Z.-L. Tuo, "Direction Dependence of the Deceleration Parameter," *JCAP* **02** (2012) 004, arXiv:1109.0941 [astro-ph.CO].

[506] Z. Chang and H.-N. Lin, "Comparison between hemisphere comparison method and dipole-fitting method in tracing the anisotropic expansion of the Universe use the Union2 dataset," *Mon. Not. Roy. Astron. Soc.* **446** (2015) 2952–2958, arXiv:1411.1466 [astro-ph.CO].

[507] H.-K. Deng and H. Wei, "Null signal for the cosmic anisotropy in the Pantheon supernovae data," *Eur. Phys. J. C* **78** no. 9, (2018) 755, arXiv:1806.02773 [astro-ph.CO].

[508] A. Mariano and L. Perivolaropoulos, "Is there correlation between Fine Structure and Dark Energy Cosmic Dipoles?," *Phys. Rev. D* **86** (2012) 083517, arXiv:1206.4055 [astro-ph.CO].

[509] H.-N. Lin, S. Wang, Z. Chang, and X. Li, "Testing the isotropy of the Universe by using the JLA compilation of type-Ia supernovae," *Mon. Not. Roy. Astron. Soc.* **456** no. 2, (2016) 1881–1885, arXiv:1504.03428 [astro-ph.CO].

[510] U. Feindt *et al.*, "Measuring cosmic bulk flows with Type Ia Supernovae from the Nearby Supernova Factory," *Astron. Astrophys.* **560** (2013) A90, arXiv:1310.4184 [astro-ph.CO].

[511] S. Appleby and A. Shafieloo, "Testing local anisotropy using the method of smoothed residuals I — methodology," *JCAP* **03** (2014) 007, arXiv:1312.3415 [astro-ph.CO].

[512] S. Appleby and A. Shafieloo, "Testing Isotropy in the Local Universe," *JCAP* **10** (2014) 070, arXiv:1405.4595 [astro-ph.CO].

[513] Z. Chang, D. Zhao, and Y. Zhou, "Constraining the anisotropy of the Universe with the Pantheon supernovae sample," *Chin. Phys. C* **43** no. 12, (2019) 125102, arXiv:1910.06883 [astro-ph.CO].

[514] D. Saadeh, S. M. Feeney, A. Pontzen, H. V. Peiris, and J. D. McEwen, "How isotropic is the Universe?," *Phys. Rev. Lett.* **117** no. 13, (2016) 131302, arXiv:1605.07178 [astro-ph.CO].

[515] Z. Q. Sun and F. Y. Wang, "Testing the anisotropy of cosmic acceleration from Pantheon supernovae sample," *Mon. Not. Roy. Astron. Soc.* **478** no. 4, (2018) 5153–5158, arXiv:1805.09195 [astro-ph.CO].

[516] U. Andrade, C. A. P. Bengaly, B. Santos, and J. S. Alcaniz, "A Model-independent Test of Cosmic Isotropy with Low-z Pantheon Supernovae," *Astrophys. J.* **865** no. 2, (2018) 119, arXiv:1806.06990 [astro-ph.CO].

[517] S. Prince, *Computer Vision: Models, Learning, and Inference*. Cambridge University Press, 2012.

[518] A. G. Riess, S. Casertano, W. Yuan, J. B. Bowers, L. Macri, J. C. Zinn, and D. Scolnic, "Cosmic Distances Calibrated to 1% Precision with Gaia EDR3 Parallaxes and Hubble Space Telescope Photometry of 75 Milky Way Cepheids Confirm Tension with ΛCDM," *Astrophys. J. Lett.* **908** no. 1, (2021) L6, arXiv:2012.08534 [astro-ph.CO].

[519] J. Soltis, S. Casertano, and A. G. Riess, "The Parallax of ω Centauri Measured from Gaia EDR3 and a Direct, Geometric Calibration of the Tip of the Red Giant Branch and the Hubble Constant," *Astrophys. J. Lett.* **908** no. 1, (2021) L5, arXiv:2012.09196 [astro-ph.GA].

[520] D. W. Pesce *et al.*, "The Megamaser Cosmology Project. XIII. Combined Hubble constant constraints," *Astrophys. J. Lett.* **891** no. 1, (2020) L1, arXiv:2001.09213 [astro-ph.CO].

[521] J. P. Blakeslee, J. B. Jensen, C.-P. Ma, P. A. Milne, and J. E. Greene, "The Hubble Constant from Infrared Surface Brightness Fluctuation Distances," *Astrophys. J.* **911** no. 1, (2021) 65, arXiv:2101.02221 [astro-ph.CO].

[522] J. L. Bernal, L. Verde, and A. G. Riess, "The trouble with H_0," *JCAP* **10** (2016) 019, arXiv:1607.05617 [astro-ph.CO].

[523] K. Aylor, M. Joy, L. Knox, M. Millea, S. Raghunathan, and W. L. K. Wu, "Sounds Discordant: Classical Distance Ladder & ΛCDM -based Determinations of the Cosmological Sound Horizon," *Astrophys. J.* **874** no. 1, (2019) 4, arXiv:1811.00537 [astro-ph.CO].

[524] L. Knox and M. Millea, "Hubble constant hunter's guide," *Phys. Rev. D* **101** no. 4, (2020) 043533, arXiv:1908.03663 [astro-ph.CO].

[525] F. D'Eramo, R. Z. Ferreira, A. Notari, and J. L. Bernal, "Hot Axions and the H_0 tension," *JCAP* **11** (2018) 014, arXiv:1808.07430 [hep-ph].

[526] S. Carneiro, P. C. de Holanda, C. Pigozzo, and F. Sobreira, "Is the H_0 tension suggesting a fourth neutrino generation?," *Phys. Rev. D* **100** no. 2, (2019) 023505, arXiv:1812.06064 [astro-ph.CO].

[527] S. Vagnozzi, "New physics in light of the H_0 tension: An alternative view," *Phys. Rev. D* **102** no. 2, (2020) 023518, arXiv:1907.07569 [astro-ph.CO].

[528] M. Escudero and S. J. Witte, "A CMB search for the neutrino mass mechanism and its relation to the Hubble tension," *Eur. Phys. J. C* **80** no. 4, (2020) 294, arXiv:1909.04044 [astro-ph.CO].

[529] N. Blinov and G. Marques-Tavares, "Interacting radiation after Planck and its implications for the Hubble Tension," *JCAP* **09** (2020) 029, arXiv:2003.08387 [astro-ph.CO].

[530] O. Seto and Y. Toda, "Comparing early dark energy and extra radiation solutions to the Hubble tension with BBN," *Phys. Rev. D* **103** no. 12, (2021) 123501, arXiv:2101.03740 [astro-ph.CO].

[531] K. Jedamzik, L. Pogosian, and G.-B. Zhao, "Why reducing the cosmic sound horizon alone can not fully resolve the Hubble tension," *Commun. in Phys.* **4** (2021) 123, arXiv:2010.04158 [astro-ph.CO].

[532] A. Banerjee, H. Cai, L. Heisenberg, E. O. Colgáin, M. M. Sheikh-Jabbari, and T. Yang, "Hubble sinks in the low-redshift swampland," *Phys. Rev. D* **103** no. 8, (2021) L081305, arXiv:2006.00244 [astro-ph.CO].

[533] G. Alestas and L. Perivolaropoulos, "Late-time approaches to the Hubble tension deforming H(z), worsen the growth tension," *Mon. Not. Roy. Astron. Soc.* **504** no. 3, (2021) 3956, arXiv:2103.04045 [astro-ph.CO].

[534] G. Alestas, L. Kazantzidis, and L. Perivolaropoulos, "$w - M$ phantom transition at z_t <0.1 as a resolution of the Hubble tension," *Phys. Rev. D* **103** no. 8, (2021) 083517, arXiv:2012.13932 [astro-ph.CO].

[535] V. Marra and L. Perivolaropoulos, "Rapid transition of Geff at zt≃0.01 as a possible solution of the Hubble and growth tensions," *Phys. Rev. D* **104** no. 2, (2021) L021303, arXiv:2102.06012 [astro-ph.CO].

[536] G. Alestas, D. Camarena, E. Di Valentino, L. Kazantzidis, V. Marra, S. Nesseris, and L. Perivolaropoulos, "Late-transition vs smooth $H(z)$ deformation models for the resolution of the Hubble crisis," arXiv:2110.04336 [astro-ph.CO].

[537] G. Alestas, I. Antoniou, and L. Perivolaropoulos, "Hints for a Gravitational Transition in Tully–Fisher Data," *Universe* **7** no. 10, (2021) 366, arXiv:2104.14481 [astro-ph.CO].

[538] L. Perivolaropoulos and F. Skara, "Hubble tension or a transition of the Cepheid SnIa calibrator parameters?," arXiv:2109.04406 [astro-ph.CO].

[539] A. G. Riess *et al.*, "A Redetermination of the Hubble Constant with the Hubble Space Telescope from a Differential Distance Ladder," *Astrophys. J.* **699** (2009) 539–563, arXiv:0905.0695 [astro-ph.CO].

[540] M. Visser, "Jerk and the cosmological equation of state," *Class. Quant. Grav.* **21** (2004) 2603–2616, arXiv:gr-qc/0309109.

[541] D. Camarena and V. Marra, "On the use of the local prior on the absolute magnitude of Type Ia supernovae in cosmological inference," *Mon. Not. Roy. Astron. Soc.* **504** (2021) 5164–5171, arXiv:2101.08641 [astro-ph.CO].

[542] G. Efstathiou, "To H0 or not to H0?," *Mon. Not. Roy. Astron. Soc.* **505** no. 3, (2021) 3866–3872, arXiv:2103.08723 [astro-ph.CO].

[543] D. Camarena and V. Marra, "A new method to build the (inverse) distance ladder," *Mon. Not. Roy. Astron. Soc.* **495** no. 3, (2020) 2630–2644, arXiv:1910.14125 [astro-ph.CO].

[544] D. Camarena and V. Marra, "Local determination of the Hubble constant and the deceleration parameter," *Phys. Rev. Res.* **2** no. 1, (2020) 013028, arXiv:1906.11814 [astro-ph.CO].

[545] B. Audren, J. Lesgourgues, K. Benabed, and S. Prunet, "Conservative Constraints on Early Cosmology: an illustration of the Monte Python cosmological parameter inference code," *JCAP* **02** (2013) 001, arXiv:1210.7183 [astro-ph.CO].

[546] T. Brinckmann and J. Lesgourgues, "MontePython 3: boosted MCMC sampler and other features," *Phys. Dark Univ.* **24** (2019) 100260, arXiv:1804.07261 [astro-ph.CO].

[547] F. Beutler, C. Blake, M. Colless, D. H. Jones, L. Staveley-Smith, L. Campbell, Q. Parker, W. Saunders, and F. Watson, "The 6dF Galaxy Survey: Baryon Acoustic Oscillations and the Local Hubble Constant," *Mon. Not. Roy. Astron. Soc.* **416** (2011) 3017–3032, arXiv:1106.3366 [astro-ph.CO].

[548] A. J. Ross, L. Samushia, C. Howlett, W. J. Percival, A. Burden, and M. Manera, "The clustering of the SDSS DR7 main Galaxy sample – I. A 4 per cent distance measure at $z = 0.15$" *Mon. Not. Roy. Astron. Soc.* **449** no. 1, (2015) 835–847, arXiv:1409.3242 [astro-ph.CO].

[549] M. Blomqvist *et al.*, "Baryon acoustic oscillations from the cross-correlation of Lyα absorption and quasars in eBOSS DR14," *Astron. Astrophys.* **629** (2019) A86, arXiv:1904.03430 [astro-ph.CO].

[550] V. de Sainte Agathe *et al.*, "Baryon acoustic oscillations at z = 2.34 from the correlations of Lyα absorption in eBOSS DR14," *Astron. Astrophys.* **629** (2019) A85, arXiv:1904.03400 [astro-ph.CO].

[551] R. Arjona, J. García-Bellido, and S. Nesseris, "Cosmological constraints on nonadiabatic dark energy perturbations," *Phys. Rev. D* **102** no. 10, (2020) 103526, arXiv:2006.01762 [astro-ph.CO].

[552] H. Akaike, "A New Look at the Statistical Model Identification," *IEEE Transactions on Automatic Control* **19** (Jan., 1974) 716–723.

[553] S. Nesseris and J. Garcia-Bellido, "Is the Jeffreys' scale a reliable tool for Bayesian model comparison in cosmology?," *JCAP* **08** (2013) 036, arXiv:1210.7652 [astro-ph.CO].

[554] A. Heavens, Y. Fantaye, A. Mootoovaloo, H. Eggers, Z. Hosenie, S. Kroon, and E. Sellentin, "Marginal Likelihoods from Monte Carlo Markov Chains," arXiv:1704.03472 [stat.CO].

[555] P. C. Mahalanobis, "On the generalized distance in statistics," National Institute of Science of India. 1936.

[556] R. Trotta, "Bayes in the sky: Bayesian inference and model selection in cosmology," *Contemp. Phys.* **49** (2008) 71–104, arXiv:0803.4089 [astro-ph].

[557] J. Alvey, N. Sabti, M. Escudero, and M. Fairbairn, "Improved BBN Constraints on the Variation of the Gravitational Constant," *Eur. Phys. J. C* **80** no. 2, (2020) 148, arXiv:1910.10730 [astro-ph.CO].

[558] E. Gaztanaga, A. Cabre, and L. Hui, "Clustering of Luminous Red Galaxies IV: Baryon Acoustic Peak in the Line-of-Sight Direction and a Direct Measurement of H(z)," *Mon. Not. Roy. Astron. Soc.* **399** (2009) 1663–1680, arXiv:0807.3551 [astro-ph].

[559] J.-P. Uzan, "The Fundamental Constants and Their Variation: Observational Status and Theoretical Motivations," *Rev. Mod. Phys.* **75** (2003) 403, arXiv:hep-ph/0205340.

[560] S. R. Coleman, "The Fate of the False Vacuum. 1. Semiclassical Theory," *Phys. Rev. D* **15** (1977) 2929–2936. [Erratum: Phys.Rev.D 16, 1248 (1977)].

[561] A. V. Patwardhan and G. M. Fuller, "Late-time vacuum phase transitions: Connecting sub-eV scale physics with cosmological structure formation," *Phys. Rev. D* **90** no. 6, (2014) 063009, arXiv:1401.1923 [astro-ph.CO].

[562] P. Kroupa, B. Famaey, K. S. de Boer, J. Dabringhausen, M. S. Pawlowski, C. M. Boily, H. Jerjen, D. Forbes, G. Hensler, and M. Metz, "Local-Group tests of dark-matter Concordance Cosmology: Towards a new paradigm for structure formation?," *Astron. Astrophys.* **523** (2010) A32, arXiv:1006.1647 [astro-ph.CO].

[563] D. H. Weinberg, J. S. Bullock, F. Governato, R. Kuzio de Naray, and A. H. G. Peter, "Cold dark matter: controversies on small scales," *Proc. Nat. Acad. Sci.* **112** (2015) 12249–12255, arXiv:1306.0913 [astro-ph.CO].

[564] A. Del Popolo and M. Le Delliou, "Small scale problems of the ΛCDM model: a short review," *Galaxies* **5** no. 1, (2017) 17, arXiv:1606.07790 [astro-ph.CO].

[565] J. S. Bullock and M. Boylan-Kolchin, "Small-Scale Challenges to the ΛCDM Paradigm," *Ann. Rev. Astron. Astrophys.* **55** (2017) 343–387, arXiv:1707.04256 [astro-ph.CO].

[566] L. Perivolaropoulos, "Submillimeter spatial oscillations of Newton's constant: Theoretical models and laboratory tests," *Phys. Rev. D* **95** no. 8, (2017) 084050, arXiv:1611.07293 [gr-qc].

[567] I. Antoniou and L. Perivolaropoulos, "Constraints on spatially oscillating sub-mm forces from the Stanford Optically Levitated Microsphere Experiment data," *Phys. Rev. D* **96** no. 10, (2017) 104002, arXiv:1708.02117 [gr-qc].

[568] C. D. Hoyle, D. J. Kapner, B. R. Heckel, E. G. Adelberger, J. H. Gundlach, U. Schmidt, and H. E. Swanson, "Sub-millimeter tests of the gravitational inverse-square law," *Phys. Rev. D* **70** (2004) 042004, arXiv:hep-ph/0405262.

[569] D. J. Kapner, T. S. Cook, E. G. Adelberger, J. H. Gundlach, B. R. Heckel, C. D. Hoyle, and H. E. Swanson, "Tests of the gravitational inverse-square law below the dark-energy length scale," *Phys. Rev. Lett.* **98** (2007) 021101, arXiv:hep-ph/0611184.

[570] A. D. Rider, D. C. Moore, C. P. Blakemore, M. Louis, M. Lu, and G. Gratta, "Search for Screened Interactions Associated with Dark Energy Below the 100 μm Length Scale," *Phys. Rev. Lett.* **117** no. 10, (2016) 101101, arXiv:1604.04908 [hep-ex].

[571] E. G. Adelberger, B. R. Heckel, S. A. Hoedl, C. D. Hoyle, D. J. Kapner, and A. Upadhye, "Particle Physics Implications of a Recent Test of the Gravitational Inverse Sqaure Law," *Phys. Rev. Lett.* **98** (2007) 131104, arXiv:hep-ph/0611223.

[572] L. Perivolaropoulos, "PPN Parameter gamma and Solar System Constraints of Massive Brans-Dicke Theories," *Phys. Rev. D* **81** (2010) 047501, arXiv:0911.3401 [gr-qc].

[573] M. Hohmann, L. Jarv, P. Kuusk, and E. Randla, "Post-Newtonian parameters γ and β of scalar-tensor gravity with a general potential," *Phys. Rev. D* **88** no. 8, (2013) 084054, arXiv:1309.0031 [gr-qc]. [Erratum: Phys.Rev.D 89, 069901 (2014)].

[574] L. Järv, P. Kuusk, M. Saal, and O. Vilson, "Invariant quantities in the scalar-tensor theories of gravitation," *Phys. Rev. D* **91** no. 2, (2015) 024041, arXiv:1411.1947 [gr-qc].

[575] S. Capozziello, A. Stabile, and A. Troisi, "A General solution in the Newtonian limit of f(R)- gravity," *Mod. Phys. Lett. A* **24** (2009) 659–665, arXiv:0901.0448 [gr-qc].

[576] C. P. L. Berry and J. R. Gair, "Linearized f(R) Gravity: Gravitational Radiation and Solar System Tests," *Phys. Rev. D* **83** (2011) 104022, arXiv:1104.0819 [gr-qc]. [Erratum: Phys.Rev.D 85, 089906 (2012)].

[577] G. O. Schellstede, "On the Newtonian limit of metric f(R) gravity," *General Relativity and Gravitation* **48** no. 9, (Sept., 2016) 118.

[578] S. Nojiri and S. D. Odintsov, "Newton potential in deSitter brane world," *Phys. Lett. B* **548** (2002) 215–223, arXiv:hep-th/0209066.

[579] K. A. Bronnikov, S. A. Kononogov, and V. N. Melnikov, "Brane world corrections to Newton's law," *Gen. Rel. Grav.* **38** (2006) 1215–1232, arXiv:gr-qc/0601114.

[580] R. Benichou and J. Estes, "The Fate of Newton's Law in Brane-World Scenarios," *Phys. Lett. B* **712** (2012) 456–459, arXiv:1112.0565 [hep-th].

[581] A. Donini and S. G. Marimón, "Micro-orbits in a many-brane model and deviations from Newton's $1/r^2$ law," *Eur. Phys. J. C* **76** no. 12, (2016) 696, arXiv:1609.05654 [hep-ph].

[582] N. Arkani-Hamed, S. Dimopoulos, and G. R. Dvali, "Phenomenology, astrophysics and cosmology of theories with submillimeter dimensions and TeV scale quantum gravity," *Phys. Rev. D* **59** (1999) 086004, arXiv:hep-ph/9807344.

[583] E. G. Floratos and G. K. Leontaris, "Low scale unification, Newton's law and extra dimensions," *Phys. Lett. B* **465** (1999) 95–100, arXiv:hep-ph/9906238.

[584] A. Kehagias and K. Sfetsos, "Deviations from the 1/r**2 Newton law due to extra dimensions," *Phys. Lett. B* **472** (2000) 39–44, arXiv:hep-ph/9905417.

[585] L. Perivolaropoulos and C. Sourdis, "Cosmological effects of radion oscillations," *Phys. Rev. D* **66** (2002) 084018, arXiv:hep-ph/0204155.

[586] A. Conroy, T. Koivisto, A. Mazumdar, and A. Teimouri, "Generalized quadratic curvature, non-local infrared modifications of gravity and Newtonian potentials," *Class. Quant. Grav.* **32** no. 1, (2015) 015024, arXiv:1406.4998 [hep-th].

[587] J. Edholm, A. S. Koshelev, and A. Mazumdar, "Behavior of the Newtonian potential for ghost-free gravity and singularity-free gravity," *Phys. Rev. D* **94** no. 10, (2016) 104033, arXiv:1604.01989 [gr-qc].

[588] J. Edholm and A. Conroy, "Newtonian Potential and Geodesic Completeness in Infinite Derivative Gravity," *Phys. Rev. D* **96** no. 4, (2017) 044012, arXiv:1705.02382 [gr-qc].

[589] T. Biswas, E. Gerwick, T. Koivisto, and A. Mazumdar, "Towards singularity and ghost free theories of gravity," *Phys. Rev. Lett.* **108** (2012) 031101, arXiv:1110.5249 [gr-qc].

[590] M. H. Goroff and A. Sagnotti, "The Ultraviolet Behavior of Einstein Gravity," *Nucl. Phys.* **B266** (1986) 709–736.

[591] K. S. Stelle, "Classical Gravity with Higher Derivatives," *Gen. Rel. Grav.* **9** (1978) 353–371.

[592] L. Modesto, "Super-renormalizable Quantum Gravity," *Phys. Rev.* **D86** (2012) 044005, arXiv:1107.2403 [hep-th].

[593] L. Amendola, N. Burzilla, and H. Nersisyan, "Quantum Gravity inspired nonlocal gravity model," *Phys. Rev. D* **96** no. 8, (2017) 084031, arXiv:1707.04628 [gr-qc].

[594] G. Calcagni and G. Nardelli, "Non-local gravity and the diffusion equation," *Phys. Rev. D* **82** (2010) 123518, arXiv:1004.5144 [hep-th].

[595] A. O. Barvinsky, "Dark energy and dark matter from nonlocal ghost-free gravity theory," *Phys. Lett. B* **710** (2012) 12–16, arXiv:1107.1463 [hep-th].

[596] S. Park and S. Dodelson, "Structure formation in a nonlocally modified gravity model," *Phys. Rev. D* **87** no. 2, (2013) 024003, arXiv:1209.0836 [astro-ph.CO].

[597] Y. Dirian, S. Foffa, M. Kunz, M. Maggiore, and V. Pettorino, "Non-local gravity and comparison with observational datasets. II. Updated results and Bayesian model comparison with ΛCDM," *JCAP* **05** (2016) 068, arXiv:1602.03558 [astro-ph.CO].

[598] R. D'Agostino and O. Luongo, "Growth of matter perturbations in nonminimal teleparallel dark energy," *Phys. Rev. D* **98** no. 12, (2018) 124013, arXiv:1807.10167 [gr-qc].

[599] M. Gonzalez-Espinoza, G. Otalora, J. Saavedra, and N. Videla, "Growth of matter overdensities in non-minimal torsion-matter coupling theories," *Eur. Phys. J. C* **78** no. 10, (2018) 799, arXiv:1808.01941 [gr-qc].

[600] E. V. Linder, "No Slip Gravity," *JCAP* **03** (2018) 005, arXiv:1801.01503 [astro-ph.CO].

[601] J. Kennedy, L. Lombriser, and A. Taylor, "Reconstructing Horndeski theories from phenomenological modified gravity and dark energy models on cosmological scales," *Phys. Rev. D* **98** no. 4, (2018) 044051, arXiv:1804.04582 [astro-ph.CO].

[602] R. Gannouji, L. Perivolaropoulos, D. Polarski, and F. Skara, "Weak gravity on a ΛCDM background," *Phys. Rev. D* **103** no. 6, (2021) 063509, arXiv:2011.01517 [gr-qc].

[603] G. D'Amico, Z. Huang, M. Mancarella, and F. Vernizzi, "Weakening Gravity on Redshift-Survey Scales with Kinetic Matter Mixing," *JCAP* **02** (2017) 014, arXiv:1609.01272 [astro-ph.CO].

[604] G. Alestas, L. Perivolaropoulos, and K. Tanidis, "Constraining a late time transition of G_{eff} using low-z galaxy survey data," arXiv:2201.05846 [astro-ph.CO].

[605] L. Perivolaropoulos, "Is the Hubble crisis connected with the extinction of dinosaurs?," arXiv:2201.08997 [astro-ph.EP].

[606] **EUCLID** Collaboration, R. Laureijs *et al.*, "Euclid Definition Study Report," arXiv:1110.3193 [astro-ph.CO].

[607] **LSST** Collaboration, P. Marshall *et al.*, "Science-Driven Optimization of the LSST Observing Strategy," arXiv:1708.04058 [astro-ph.IM].

[608] K. Abazajian *et al.*, "CMB-S4 Science Case, Reference Design, and Project Plan," arXiv:1907.04473 [astro-ph.IM].

[609] J. P. Gardner *et al.*, "The James Webb Space Telescope," *Space Sci. Rev.* **123** (2006) 485, arXiv:astro-ph/0606175.

[610] D. Baumann, "Cosmology - part iii mathematical tripos," 2012.

[611] U. Seljak and M. Zaldarriaga, "A Line of sight integration approach to cosmic microwave background anisotropies," *Astrophys. J.* **469** (1996) 437–444, arXiv:astro-ph/9603033.

[612] M. Kaplinghat, L. Knox, and C. Skordis, "Rapid calculation of theoretical cmb angular power spectra," *Astrophys. J.* **578** (2002) 665, arXiv:astro-ph/0203413.

[613] M. Doran, "CMBEASY: an object oriented code for the cosmic microwave background," *JCAP* **10** (2005) 011, arXiv:astro-ph/0302138.

[614] J. Goodman and J. Weare, "Ensemble samplers with affine invariance," *Communications in Applied Mathematics and Computational Science* **5** no. 1, (Jan., 2010) 65–80.

[615] D. Foreman-Mackey, D. W. Hogg, D. Lang, and J. Goodman, "emcee: The MCMC Hammer," *Publ. Astron. Soc. Pac.* **125** (2013) 306–312, arXiv:1202.3665 [astro-ph.IM].

[616] **SDSS** Collaboration, W. J. Percival *et al.*, "Baryon Acoustic Oscillations in the Sloan Digital Sky Survey Data Release 7 Galaxy Sample," *Mon. Not. Roy. Astron. Soc.* **401** (2010) 2148–2168, arXiv:0907.1660 [astro-ph.CO].

[617] K. T. Mehta, A. J. Cuesta, X. Xu, D. J. Eisenstein, and N. Padmanabhan, "A 2% Distance to z = 0.35 by Reconstructing Baryon Acoustic Oscillations - III : Cosmological Measurements and Interpretation," *Mon. Not. Roy. Astron. Soc.* **427** (2012) 2168, arXiv:1202.0092 [astro-ph.CO].

[618] **BOSS** Collaboration, G.-B. Zhao *et al.*, "The clustering of galaxies in the completed SDSS-III Baryon Oscillation Spectroscopic Survey: tomographic BAO analysis of DR12 combined sample in Fourier space," *Mon. Not. Roy. Astron. Soc.* **466** no. 1, (2017) 762–779, arXiv:1607.03153 [astro-ph.CO].

[619] M. Ata *et al.*, "The clustering of the SDSS-IV extended Baryon Oscillation Spectroscopic Survey DR14 quasar sample: first measurement of baryon acoustic oscillations between redshift 0.8 and 2.2" *Mon. Not. Roy. Astron. Soc.* **473** no. 4, (2018) 4773–4794, arXiv:1705.06373 [astro-ph.CO].

[620] **DES** Collaboration, T. M. C. Abbott *et al.*, "Dark Energy Survey Year 1 Results: Measurement of the Baryon Acoustic Oscillation scale in the distribution of galaxies to redshift 1," *Mon. Not. Roy. Astron. Soc.* **483** no. 4, (2019) 4866–4883, arXiv:1712.06209 [astro-ph.CO].

[621] J. E. Bautista *et al.*, "The SDSS-IV extended Baryon Oscillation Spectroscopic Survey: Baryon Acoustic Oscillations at redshift of 0.72 with the DR14 Luminous Red Galaxy Sample," *Astrophys. J.* **863** (2018) 110, arXiv:1712.08064 [astro-ph.CO].

[622] J. F. Jesus, T. M. Gregório, F. Andrade-Oliveira, R. Valentim, and C. A. O. Matos, "Bayesian correction of $H(z)$ data uncertainties," *Mon. Not. Roy. Astron. Soc.* **477** no. 3, (2018) 2867–2873, arXiv:1709.00646 [astro-ph.CO].

[623] C. Zhang, H. Zhang, S. Yuan, T.-J. Zhang, and Y.-C. Sun, "Four new observational $H(z)$ data from luminous red galaxies in the Sloan Digital Sky Survey data release seven," *Res. Astron. Astrophys.* **14** no. 10, (2014) 1221–1233, arXiv:1207.4541 [astro-ph.CO].

[624] J. Simon, L. Verde, and R. Jimenez, "Constraints on the redshift dependence of the dark energy potential," *Phys. Rev. D* **71** (2005) 123001, arXiv:astro-ph/0412269.

[625] M. Moresco, "Raising the bar: new constraints on the Hubble parameter with cosmic chronometers at z $\sim$ 2," *Mon. Not. Roy. Astron. Soc.* **450** no. 1, (2015) L16–L20, arXiv:1503.01116 [astro-ph.CO].

[626] A. Oka, S. Saito, T. Nishimichi, A. Taruya, and K. Yamamoto, "Simultaneous constraints on the growth of structure and cosmic expansion from the multipole power spectra of the SDSS DR7 LRG sample," *Mon. Not. Roy. Astron. Soc.* **439** (2014) 2515–2530, arXiv:1310.2820 [astro-ph.CO].

[627] L. Anderson *et al.*, "The clustering of galaxies in the SDSS-III Baryon Oscillation Spectroscopic Survey: measuring D_A and H at z = 0.57 from the baryon acoustic peak in the Data Release 9 spectroscopic Galaxy sample," *Mon. Not. Roy. Astron. Soc.* **439** no. 1, (2014) 83–101, arXiv:1303.4666 [astro-ph.CO].

[628] N. G. Busca *et al.*, "Baryon Acoustic Oscillations in the Ly-α forest of BOSS quasars," *Astron. Astrophys.* **552** (2013) A96, arXiv:1211.2616 [astro-ph.CO].

[629] **BOSS** Collaboration, T. Delubac *et al.*, "Baryon acoustic oscillations in the Lyα forest of BOSS DR11 quasars," *Astron. Astrophys.* **574** (2015) A59, arXiv:1404.1801 [astro-ph.CO].

[630] **BOSS** Collaboration, A. Font-Ribera *et al.*, "Quasar-Lyman α Forest Cross-Correlation from BOSS DR11 : Baryon Acoustic Oscillations," *JCAP* **05** (2014) 027, arXiv:1311.1767 [astro-ph.CO].